



**HAL**  
open science

# Dynamique agéostrophique dans l'océan intérieur

Lia Siegelman

► **To cite this version:**

Lia Siegelman. Dynamique agéostrophique dans l'océan intérieur. Sciences de la Terre. Université de Bretagne occidentale - Brest, 2019. Français. NNT : 2019BRES0094 . tel-02998433

**HAL Id: tel-02998433**

**<https://theses.hal.science/tel-02998433>**

Submitted on 10 Nov 2020

**HAL** is a multi-disciplinary open access archive for the deposit and dissemination of scientific research documents, whether they are published or not. The documents may come from teaching and research institutions in France or abroad, or from public or private research centers.

L'archive ouverte pluridisciplinaire **HAL**, est destinée au dépôt et à la diffusion de documents scientifiques de niveau recherche, publiés ou non, émanant des établissements d'enseignement et de recherche français ou étrangers, des laboratoires publics ou privés.

# THESE DE DOCTORAT DE

L'UNIVERSITE  
DE BRETAGNE OCCIDENTALE  
COMUE UNIVERSITE BRETAGNE LOIRE

ÉCOLE DOCTORALE N° 598  
*Sciences de la Mer et du littoral*  
Spécialité : *Océanographie Physique et Environnement*

Par

**Lia SIEGELMAN**

**Ageostrophic dynamics in the ocean interior.**

**Thèse présentée et soutenue à Brest le 13 décembre 2019**

**Unité de recherche : UMR 6539 – Laboratoire des sciences de l'Environnement Marin - LEMAR**

## Rapporteurs avant soutenance :

Rosemary MORROW      Physicienne CNAP, OMP, LEGOS

Francesco d'OVIDIO      Chargé de recherche CNRS,  
LOCEAN

## Composition du Jury :

Alain COLIN De VERDIERE      Professeur des universités, UBO  
Président du Jury

Rosemary MORROW      Physicienne CNAP, OMP, LEGOS  
Francesco d'OVIDIO      Chargé de recherche CNRS, LOCEAN

Guillaume LAPEYRE      Directeur de recherche CNRS, ENS  
Paris

Jonathan GULA      Maître de conférences, UBO

Patrice KLEIN      Directeur de recherche CNRS,  
Directeur de thèse

Pascal RIVIERE      Maître de conférences, UBO,  
Co-directeur de thèse

---

# Ageostrophic dynamics in the ocean interior

---

Lia SIEGELMAN

*Supervisors*

M. Patrice KLEIN (Caltech/JPL)

M. Pascal RIVIÈRE (UBO)

## Acknowledgements

I deeply thank my main advisor, Patrice Klein, for his unlimited time and support, his boundless creativity and unabated enthusiasm over the past three years. I am looking forward to continuing our collaboration in the future.

I would also like to thank Pascal Rivière, my co-advisor, for his great kindness and support, Andrew F. Thompson, my unofficial co-advisor, for hosting me in the oceanography division at the California Institute of Technology (Caltech) and generously offering many insightful advice and suggestions, and Lee-Lueng Fu for hosting me in the general ocean circulation group at the Jet Propulsion Laboratory (JPL).

My thesis committee, Guillaume Lapeyre and Jonathan Gula for their generous time, comments, and questions. I am grateful that I was able to incorporate into my work groundbreaking observations for which many have invested considerable time and effort. I would particularly like to thank Christophe Guinet for giving me access to data collected by instrumented southern elephant seal and Fabien Roquet for providing help in understanding the capabilities and limitations of the instruments. I am also grateful to Clément Ubelmann for explaining the intricacies of processed SSH products, and to Frédéric Briol and Francesco d'Ovidio for providing the code to compute FSLE from satellite altimetry data.

Much support was also available for the computational work, in particular for the analysis of the LLC4320 simulation. Many thanks to Dimitris Menemenlis for running the simulation, colleagues at the NASA Supercomputing Division for making the outputs available, and Hector S. Torres for his computational expertise that prevented countless headaches.

I would also like to thank the administrative staff at both LEMAR and Caltech/JPL, that enabled my visits in California.

Thanks to my fellow students and postdocs at LEMAR and Caltech/JPL for their friendship and discussions that helped create a supportive and stimulating environment.

Special thanks are due to my friends and family for supporting me both overseas and locally.

My PhD was funded by a joint CNES-LabexMER doctoral fellowship and the CNES OSTST "Oceanic sub-mesoscales and internal gravity waves: an issue for SWOT" proposal.

# Contents

<b>Abstract</b>	<b>2</b>
<b>Acknowledgements</b>	<b>3</b>
<b>Publications</b>	<b>6</b>
<b>Scientific activity</b>	<b>7</b>
<b>Introduction</b>	<b>8</b>
Context . . . . .	8
Outline . . . . .	12
<b>1 Datasets</b>	<b>13</b>
1.1 Southern elephant seal data . . . . .	13
1.2 Satellite altimetry data . . . . .	34
1.2.1 Sea surface height . . . . .	34
1.2.2 Finite-size Lyapunov exponent . . . . .	37
1.3 Numerical simulation . . . . .	39
<b>2 Dynamical concepts on meso- and submesoscale turbulence</b>	<b>41</b>
2.1 Non-dimensional numbers . . . . .	41
2.2 Ertel potential vorticity . . . . .	43
2.3 Quasi-geostrophic dynamics ( $Ro \ll 1$ and $Ri \gg 1$ ) . . . . .	47
2.3.1 Production of submesoscales by mesoscale eddies . . . . .	48
2.3.2 Frontal dynamics in the QG regime . . . . .	52
2.4 Ageostrophic dynamics ( $Ro$ and $Ri$ of $O(1)$ ) . . . . .	55
2.4.1 Frontal dynamics in the ageostrophic regime . . . . .	56
2.4.2 Vertical velocities . . . . .	60
<b>3 Enhanced upward heat transport at deep submesoscale fronts</b>	<b>62</b>
<b>4 Ageostrophic dynamics of deep submesoscale fronts</b>	<b>84</b>
<b>5 Submesoscale fronts as biological hotspot</b>	<b>108</b>
<b>Conclusion and perspectives</b>	<b>122</b>
<b>References</b>	<b>128</b>
<b>Appendix A Klein et al. (2019)</b>	<b>135</b>
<b>Appendix B Torres et al. (2019)</b>	<b>159</b>

## List of Figures

0.1	VIIRS image in the Southern Ocean . . . . .	8
0.2	Surface relative vorticity . . . . .	9
0.3	Velocities at meso- and submesoscale . . . . .	10
1.1	Seal and satellite schematic . . . . .	13
1.2	MEOP profiles . . . . .	14
1.3	Instrumented seal . . . . .	15
1.4	CTD-SRDL . . . . .	15
1.5	Continuous CTD-SRDL deployment . . . . .	17
1.6	SSH map . . . . .	34
1.7	Satellite altimeters . . . . .	35
1.8	SLA time evolution . . . . .	36
1.9	FTLE versus strain . . . . .	37
1.10	FSLE snapshot . . . . .	38
1.11	Surface current speed in LLC4320 . . . . .	40
2.1	Vorticity conservation . . . . .	45
2.2	Ertel PV decomposition . . . . .	46
2.3	Time series of Ertel PV . . . . .	47
2.4	Geostrophic streamfunction . . . . .	49
2.5	Okubo-Weiss quantity . . . . .	50
2.6	Vortex stripping . . . . .	51
2.7	Ageostrophic circulation schematic . . . . .	53
2.8	Deformation vs vertical velocity schematic . . . . .	54
2.9	Boussinesq vs QG flows . . . . .	56
2.10	Ageostrophic streamfunction . . . . .	58
5.1	FSLE and Ertel PV . . . . .	124
5.2	Wavenumber-frequency spectrum . . . . .	125
5.3	Seismic reflection profiling . . . . .	127

## List of Tables

1	LLC spin-up hierarchy . . . . .	39
---	---------------------------------	----

# Publications associated with this dissertation

## Ageostrophic dynamics

- **Siegelman, L.**, Klein, P., Rivière, P., Thompson, A.F., Torres, H.S., Flexas, M. and Menemenlis, D. (2020). Enhanced upward heat transport at deep submesoscale ocean fronts. *Nature Geoscience*, 13(1), 50-55. (Chapter 3)
- **Siegelman, L.** (2020). Energetic submesoscale dynamics in the ocean interior. *Journal of Physical Oceanography*, 50(3), 727-749. (Chapter 4)
- **Siegelman, L.**, Klein, P., Torres, H., Thompson, A.F. and Menemenlis, D. (2020). Altimetry-based diagnosis of deep-reaching submesoscale ocean fronts. *Fluids*, 5(3), 145.
- Archer, M., Schaeffer, A., Keating, S., Roughan, M., Holmes, R. and **Siegelman, L.** (2020). Observations of submesoscale instability and frontal subduction within the mesoscale eddy field of the Tasman Sea. *Journal of Physical Oceanography*, 50(5), 1509-1529.

## Biological impact of ageostrophic dynamics

- **Siegelman, L.**, O’Toole, M., Flexas, M., Rivière, P. and Klein, P. (2019). Submesoscale ocean fronts act as biological hotspot for southern elephant seal. *Scientific reports*, 9(1), 2045-2322. (Chapter 5)
- Rivière, P., Jaud, T., **Siegelman, L.**, Klein, P., Cotté, C., LeSommer, J., Dencausse, G. and Guinet, C. (2019). Sub-mesoscale fronts modify elephant seals foraging behavior. *Limnology and Oceanography Letters*, 4(6), 193-204.

## Data processing

- **Siegelman, L.**, Roquet, F., Mensah, V., Rivière, P., Pauthenet, E., Picard, B. and Guinet, C. (2019). Correction and accuracy of high-and low-resolution ctd data from animal-borne instruments. *Journal of Atmospheric and Oceanic Technology*, 36(5), 745-760. (Chapter 1.1)
- Mensah, V., Roquet, F., **Siegelman, L.**, Picard, B., Pauthenet, E. and Guinet, C. (2018). A correction for the thermal mass-induced errors of CTD tags mounted on marine mammals. *Journal of atmospheric and oceanic technology*, 35(6), 1237-1252.
- Manucharyan, G., **Siegelman, L.** and Klein, P. (*in revision*). State estimation of surface and deep flows from sparse SSH observations of geostrophic ocean turbulence using Deep Learning. *Journal of Advances in Modeling Earth Systems*.

## Balanced motions and internal gravity waves from space

- Klein, P., Lapeyre, G., **Siegelman, L.**, Qiu, B., Fu, L.L., Torres, H.S., Su, Z., Menemenlis, D. and Le Gentil, S. (2019). Ocean-scale interactions from space. *Earth and Space Science*, 6(5), 795-817. (Appendix A)
- Torres, H.S., Klein, P., **Siegelman, L.**, Qiu, B., Chen, S., Ubelman, C., Wang, J., Menemenlis, D. and Fu, L.L. (2019). Diagnosing ocean-wave-turbulence interactions from space. *Geophysical Research Letters*., 46(15), 8933-8942. (Appendix B)

## Scientific activity during the PhD

### Field work

- **Kerguelen Islands, French Antarctic and Southern territories** *Nov 2016–Feb 2017*  
Program 109 IPEV, PI: C. Guinet. Data acquisition for the PhD. Southern elephant seal CTD-SRDL tag deployment and retrieval.

### International collaborations

- **Jet Propulsion Laboratory, California Institute of Technology** *2017–2019*  
NASA JPL Visiting Student Research Program in Lee-Lueng Fu's general ocean circulation group.
- **California Institute of Technology** *2017–2019*  
Visiting Graduate Student in Andrew F. Thompson's physical oceanography research group.

### Teaching

- **Université de Bretagne Occidentale** *Sep–Dec 2017*  
Teaching assistant. General physics, freshman year, 60 hours.

### International Meetings

- **AOGS Asia Oceania Geosciences Society Meeting, Singapore** *2019*  
Deep submesoscales: elephant seal and satellite unravel a major pathway connecting the ocean interior to the surface (presentation).
- **AOFD Atmospheric and Oceanic Fluid Dynamics Meeting, Portland, ME** *2019*  
Enhanced heat transport at deep ageostrophic ocean fronts (presentation).
- **SWOT Science Team Meeting, Bordeaux, France** *2019*  
Elephant seal and satellite provide insight towards reconstructing vertical velocities at submesoscale from space (presentation).
- **Ocean Sciences Meeting, Portland, OR** *2018*  
Mesoscale and sub-mesoscale dynamics in the Kerguelen region, Southern Ocean, revealed by Southern Elephant Seals (poster).



# Introduction

## Context

The ocean is the largest solar energy collector on Earth. It absorbs about 90% of Earth’s radiation imbalance (Hansen et al., 2011) and, as such, plays a crucial role in the regulation of our climate. The amount of heat the ocean can store is modulated by its complex circulation, which spans a broad range of spatial scales, from centimeters to thousands of kilometers. This dissertation focuses on the scale range 1–500 km, which encompasses two major physical structures: mesoscale eddies (100–300 km size), which account for most of the oceanic Kinetic Energy (KE), and submesoscale fronts ( $\leq 50$  km size), which capture most of the vertical velocity field.

Satellite altimetry of the past twenty-five years has revealed the existence of a strongly energetic mesoscale turbulent flow field in all the oceans (Klein et al., 2019). This oceanic mesoscale turbulence is characterized by cyclonic and anticyclonic eddies with an horizontal length scale of 100–300 km, a vertical length scale of 500–1000 m and a time scale ranging from a few days to several weeks (Chelton et al., 2011). At leading order, mesoscale eddies are in geostrophic balance, i.e., a balance between pressure and Coriolis forces. They are mostly energetic in turbulent regions such as the Gulf Stream, the

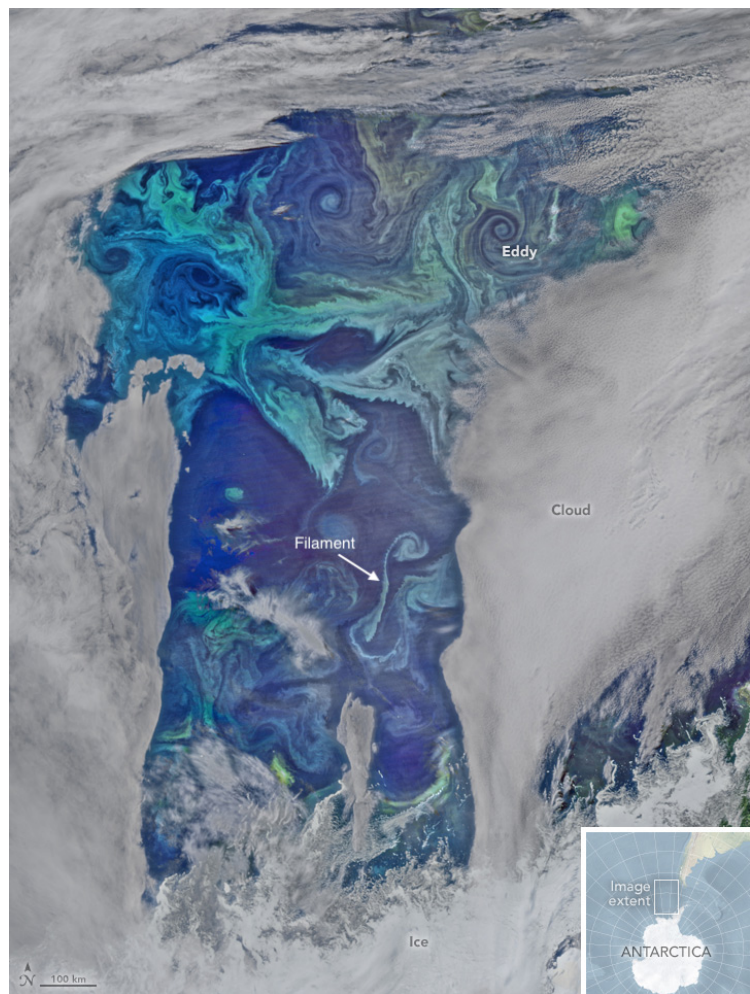


Figure 0.1: Visible Infrared Imaging Radiometer Suite on the Suomi satellite captures an extensive phytoplankton bloom just west of the Drake Passage, one of the most turbulent regions in the ocean. Mesoscale eddies and submesoscales filaments are noticeable on this image. From <https://earthobservatory.nasa.gov>.

Kuroshio Extension, and the Antarctic Circumpolar Current (Figures 0.1 and 0.2).

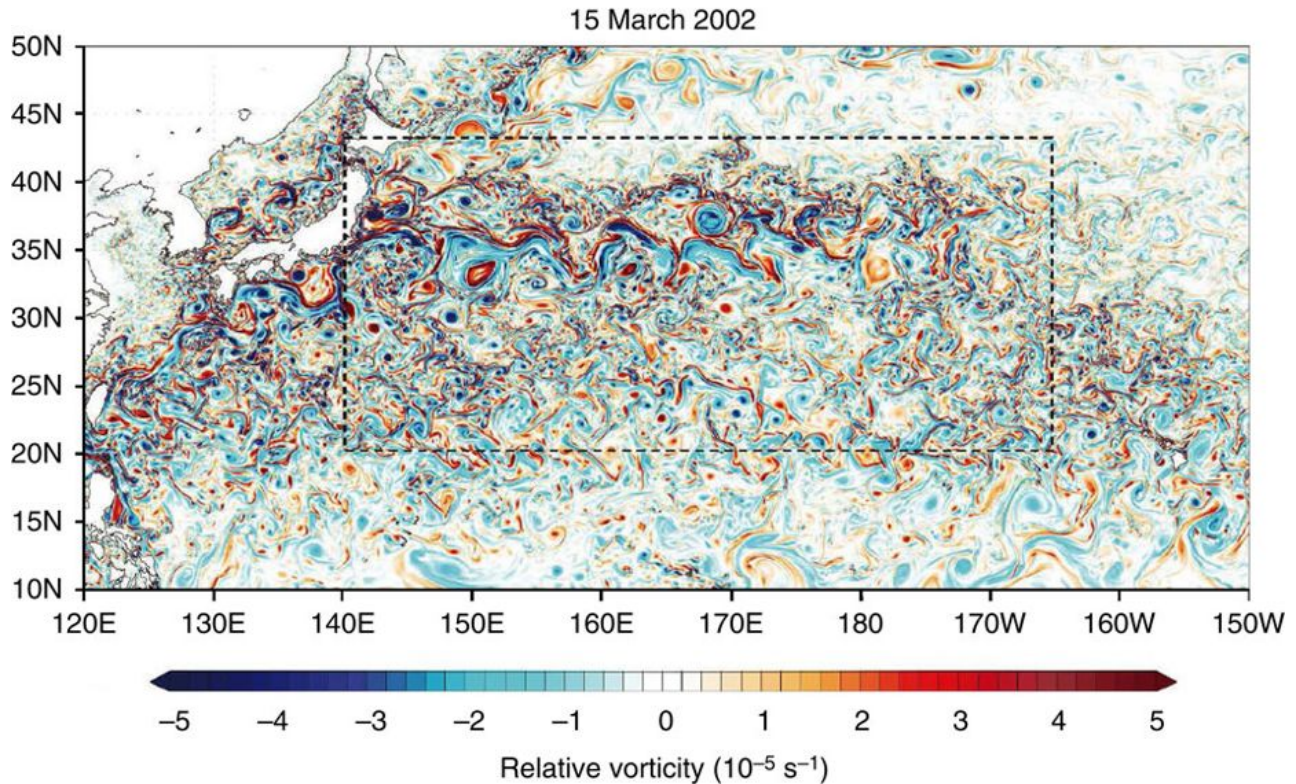


Figure 0.2: Surface relative vorticity in the Kuroshio Extension on March 15th 2002 from a high-resolution ( $1/30^\circ$  in the horizontal and 100 vertical levels) numerical simulation of the North Pacific using the ocean general circulation model for the Earth Simulator. From Sasaki et al. (2014).

Mesoscale eddies account for  $\sim 80\%$  of the total oceanic KE (Ferrari and Wunsch, 2009). In terms of KE budget, numerical and theoretical studies indicate that mesoscale eddies experience an inverse KE cascade, with KE fluxing from the source ( $\sim 50\text{--}100$  km), resulting from the baroclinic instability of large-scale currents, towards larger scales (Tulloch et al., 2011; Klein et al., 2019). In simple terms, this happens when two small eddies merge to form a larger one. This inverse KE cascade increases the total eddy KE and strengthens large geostrophic eddies as they become more coherent and their life time increases (Arbic et al., 2012; Qiu et al., 2014; Sasaki et al., 2014). Mesoscale eddies are a key component of the global ocean circulation and significantly impact, among others, carbon sequestration, biological productivity, heat transport and thus the Earth’s climate as a whole (Ferrari and Wunsch, 2009).

However, a new vision of ocean dynamics has emerged in the last two decades. It highlights the previously unsuspected importance of submesoscale motions, confined within the ocean surface mixed layer, for the general ocean circulation (Spall and Richards, 2000; Lévy et al., 2001). Submesoscales have an

horizontal length scale  $\leq 50$  km and a time scale ranging from hours to days. They lie intermediate to meso- and small-scale 3-D (0.1–100 m) motions and take the form of elongated fronts or filaments embedded within mesoscale eddies (Figures 0.1 and 0.2). Contrary to mesoscale eddies, submesoscale motions are not in geostrophic balance (Thomas et al., 2008), as such they are referred to as "ageostrophic" motions.

While mesoscales capture most of the horizontal eddy KE ( $u, v$ ), submesoscales capture most of the vertical eddy KE ( $w$ ) (Klein and Lapeyre, 2009; McWilliams, 2016), as illustrated in Figure 0.3. This figure shows that while most of the variance of  $(u, v)$  lies in the mesoscales, most of the variance of  $w$  is contained at submesoscales. Submesoscale dynamics are known to generate vertical velocities of  $\sim 100$  m/day that are typically an order of magnitude larger than those associated with the mesoscale. As such, submesoscale dynamics play an important role in the vertical transport of key properties such as climatically important gases, heat and nutrient (Klein and Lapeyre, 2009; Ferrari, 2011).

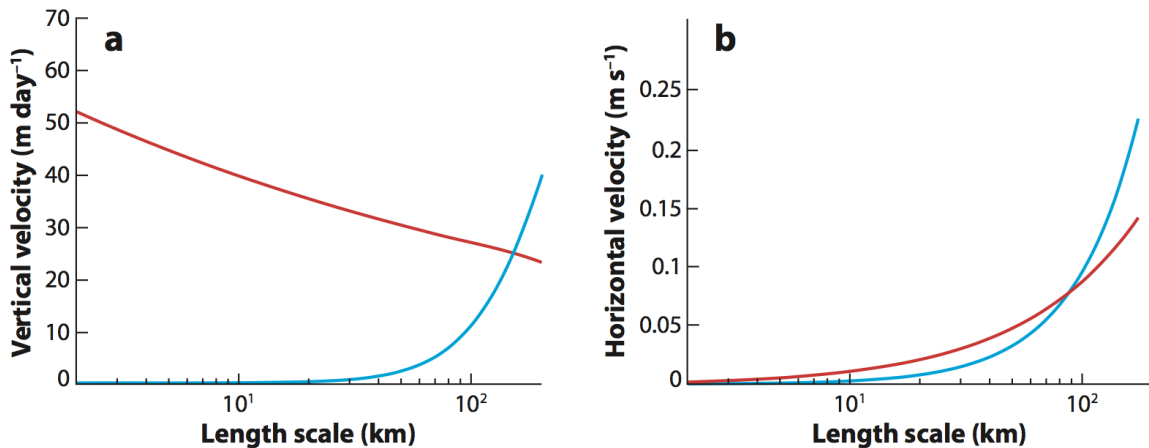


Figure 0.3: a) Vertical velocity and b) horizontal velocity at a 200-m depth as a function of the length scale for mesoscales (blue line) and submesoscales (red line), assuming equal KE for both regimes at the length scale of 100 km. From Klein and Lapeyre (2009).

To date, submesoscale dynamics have mainly been studied in the upper ocean, and in particular within the ocean mixed layer ( $\sim 50$ – $100$  m deep), where they are thought to be dominant due to the presence of horizontal density gradients, vertical shear, weak stratification, and a surface boundary conducive to frontogenesis. In contrast, submesoscales in the ocean interior are currently assumed to be weak. This is because the ocean interior is commonly assumed to be in geostrophic balance, preventing the formation of strong horizontal gradients. However, growing evidence suggests that the interior ocean

may depart from geostrophy and host energetic submesoscales. For instance, this has been proposed by Molemaker et al. (2010) in an idealized study, in which the authors demonstrate the presence of energetic frontogenesis driven by mesoscale eddies in the ocean interior. Seismic imaging has also long revealed the existence of energetic eddies in the ocean interior (Biescas et al., 2008; Menesguen et al., 2009; Barbosa Aguiar et al., 2015), such as the subsurface anticyclones of the North Atlantic known as "meddies" (Armi et al., 1988; Ménesguen et al., 2012) or the coherent eddies of the Gulf Stream (Gula et al., 2019). In addition, the recent *in situ* study of Yu et al. (2019) diagnosed strong upward vertical heat fluxes in the ocean interior that are believed to be produced by submesoscale dynamics.

Furthermore, mesoscale and submesoscale dynamics are often studied independently. To date, only a few studies (Fox-Kemper and Menemenlis, 2008; Klein and Lapeyre, 2009; Tulloch and Smith, 2009) have examined their interactions beyond the dynamics of stable/unstable submesoscale fronts embedded in a large-scale strain field. This dissertation addresses the question of the two-way interaction between mesoscale eddies and submesoscale structures in a fully turbulent flow field. More precisely, the focus of this work is on ageostrophic dynamics (see Chapter 2 for the precise definition) in the ocean interior, and in particular below the mixed layer, where little is known about their existence. The main purposes of this work are to show that ageostrophic motions (i) are generated by the background mesoscale eddy field via frontogenesis processes, and (ii) are not solely confined to the ocean surface mixed layer but, rather, can extend in the ocean interior down to depths of a thousand meters. As such, submesoscale fronts provide an important, yet unexplored, pathway for the transport of heat, chemical and biological tracers, between the ocean interior and the surface, with potential major implications for the biogeochemical and climate systems.

This dissertation focuses on one of the most energetic regions of the world's ocean: the Antarctic Circumpolar Current (ACC) (Hogg et al., 2015), from which numerous eddies emanates, making it prone to the generation of submesoscale motions. This region has been chosen because of availability of two groundbreaking datasets: (i) submesoscale-resolving *in situ* observations collected by instrumented elephant seals in the Kerguelen area (Indian sector of the Southern Ocean, Figure 1.2) and (ii) outputs from a realistic simulation at high-resolution that includes internal tides. In addition, this region benefits from a thorough satellite altimetry coverage, allowing to access the mesoscale activity of the area. As

such, the availability of these three independent datasets enabled the study of ageostrophic dynamics in the ocean interior from an observational and modeling perspective.

## Outline

- Chapter 1 describes the three datasets used in this dissertation:
  - Conductivity-Temperature-Depth data collected by instrumented southern elephant seals in the Kerguelen area (Figure 1.2), providing vertical sections of density at high-resolution, capable to resolve ageostrophic dynamics at depth.
  - Conventional satellite altimetry data, providing maps of sea surface height (SSH), a proxy for surface pressure, sufficient to resolve the mesoscale activity of the area. Finite size Lyapunov exponents are subsequently computed from SSH to retrieve the strain field.
  - A global and realistic numerical simulation with a  $1/48^\circ$  horizontal resolution, 90 vertical levels and tidal forcing, i.e., the so-called LLC4320 simulation.
- Chapter 2 introduces the theoretical concepts related to quasi-geostrophic and ageostrophic dynamics that will be used in Chapters 3–5. The aim of this chapter is to summarize the key theoretical results related to meso- and submesoscale turbulence. This chapter can be read independently from the others.
- Chapter 3 demonstrates the existence of submesoscale fronts in the ocean interior. These fronts generate enhanced upward vertical heat transport at depth. The results are based on an innovative methodology combining seal and satellite data, and are backed by an analysis of the high-resolution numerical simulation.
- Chapter 4 is in the continuity of Chapter 3; it confirms the presence of ageostrophic dynamics in the ocean interior and proposes a dynamical explanation for it, based on an analysis of the high-resolution numerical simulation.
- Chapter 5 presents a biological impact of ageostrophic dynamics for a top predator; the southern elephant seal. Its foraging activity is shown to be stimulated in the vicinity of submesoscale fronts.
- Lastly, the main results of this dissertation are summarized and some perspectives on questions that will need to be addressed in future work are presented.

# 1 Datasets

Three main datasets are used in this dissertation thesis; high-resolution observations collected by instrumented elephant seals in the Kerguelen area, satellite altimetry data, from which finite-size Lyapunov exponents are derived, and outputs from a realistic numerical simulation at high-resolution. The combination of the first two independent datasets (seal and satellite data) provides a synoptic 3-D view of the upper ocean, down to depths of  $\sim 500$  m (Figure 1.1). The numerical simulation is then used to confront and extend the observational results to the first thousand meters of the water column.

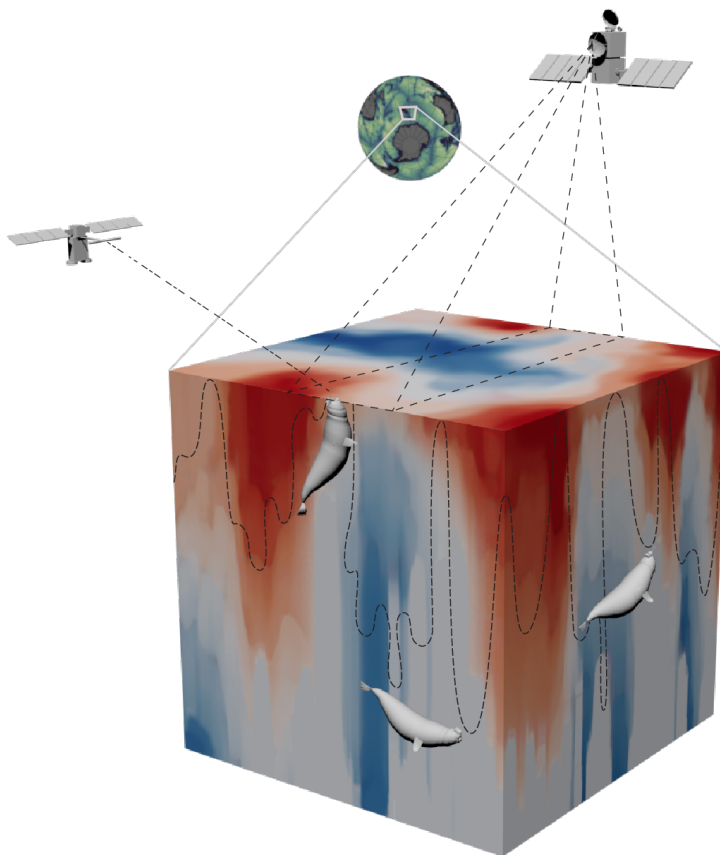


Figure 1.1: Schematic view of the upper 500 m of the ocean in the Kerguelen area (Indian sector of the Southern Ocean, see white polygon). Elephant seals sample mesoscale eddies. They are localized by the Argos satellite system (satellite on the left). Their dive trajectory is shown by the dashed curve. Satellite altimeter diagnoses sea surface height (satellite on the right). ©Tandi Reason Dahl.

## 1.1 High-resolution observations collected by instrumented southern elephant seals

Hydrographic data collected by marine mammals such as Southern Elephant Seals (*Mirounga leonina*) represent a consequent source of information, especially in the undersampled polar oceans where observa-

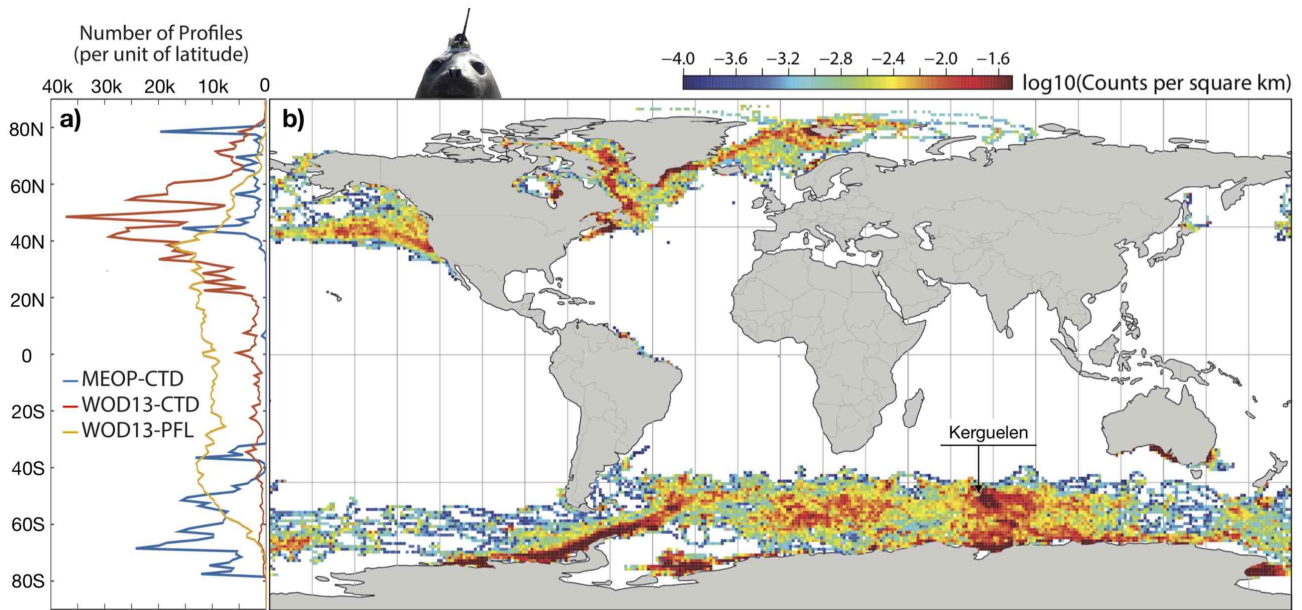


Figure 1.2: a) Zonal number of profiles from MEOP-CTD (blue), ship-based CTD (red) and ARGO floats (yellow) from the world ocean database 2013 (Boyer et al., 2013). Note the major contribution of MEOP south of 50°S. b) Density distribution of 529,373 CTD profiles from the MEOP-CTD database. From Pauthenet (2018).

tions are notoriously hard to acquire (Roquet et al., 2014; Treasure et al., 2017) (Figure 1.2). Since 2002, instrumented animals have been generating large datasets of oceanographic Conductivity-Temperature-Depth (CTD) casts ( $> 500\,000$  profiles), which are freely available to the scientific community through the Marine Mammals Exploring the Oceans Pole to Pole (MEOP) data portal (<http://meop.net>). Using marine mammals as data-collection platform has proved to be a powerful and cost-effective way to improve the ocean observing system for both physical and biological oceanographers. In fact, over 90% of CTD profiles south of 60°S have been collected by instrumented marine mammals (Treasure et al., 2017) (Figure 1.2).

Subantarctic and Antarctic islands, such as the Kerguelen, Macquarie, New South Wales, South Georgia, Bouvet or Falkland Islands, are home to large population of southern elephant seals. The southern elephant seal is a deep-diving ( $600 \pm 200$  m, with maxima around 2,000 m, Figure 1.3), wide-ranging marine predator species. It forages on mesopelagic fish in either one of three main habitats: the Antarctic continental shelf, the Kerguelen Plateau or deep open water regions (Hindell et al., 2016). Southern elephant seals spend  $\sim 8$  months per year at sea and come back to land twice a year for a cumulative period of  $\sim 4$  months; once to moult and once to breed.

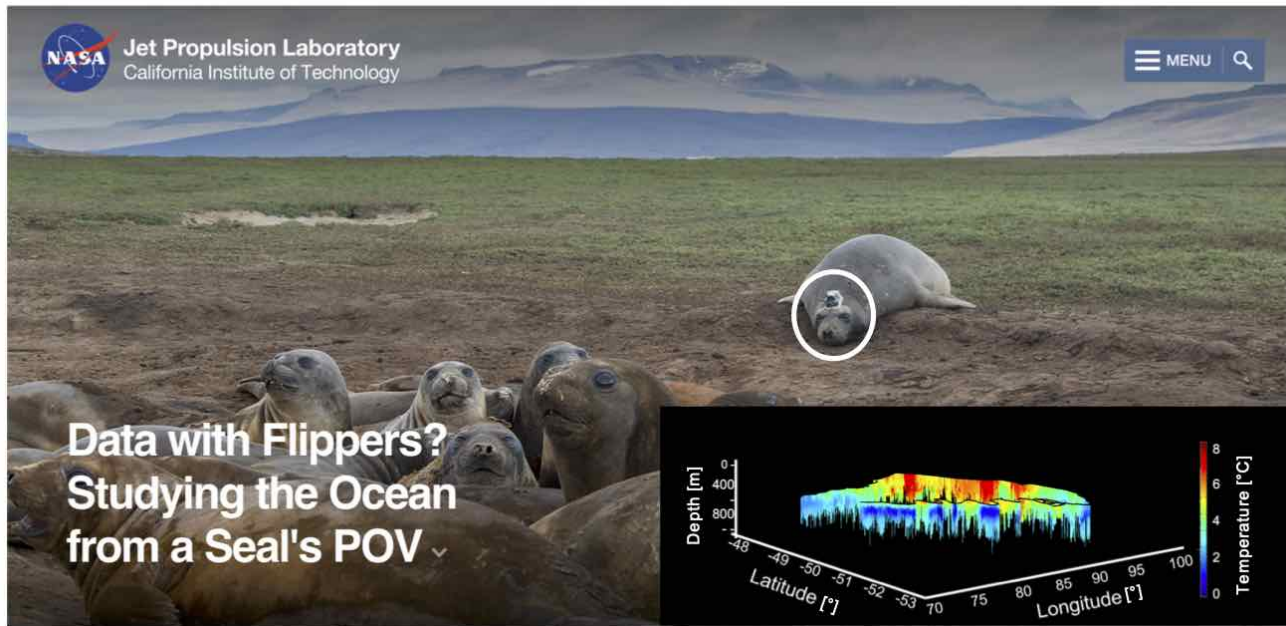


Figure 1.3: Colony of southern elephant seals at Kerguelen Islands during the molting season in December 2016, with an instrumented female in the background (white circle). Find out more about it in the NASA news release at <https://www.jpl.nasa.gov/news/news.php?feature=7392>. Picture ©Etienne Pauthenet, Sorbonne Université. The inset shows the trajectory of a southern elephant seal, with temperature profiles reaching depths of  $\sim 1000$  m. ©Thomas Jaud.

When they come back to land, elephant seals are equipped with CTD–Satellite Relay Data Logger (CTD-SRDL) tags (Figure 1.4), that are either retrieved at the end of the deployment or fall off with the animal’s dead skin during the next moulting season. CTD-SRDLs are built by the Sea Mammal Research Unit at the University of St Andrews in Scotland and incorporate a miniaturized CTD unit manufactured by Valeport Ltd. (Boehme et al., 2009). They record conductivity, temperature and pressure, from which salinity and, then, density are derived (Figure 1.4). In addition, the seal’s geographic position is tracked via the Argos satellite system.

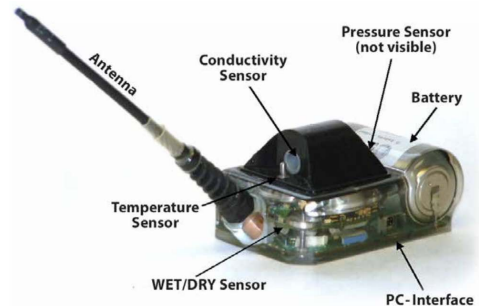


Figure 1.4: Photograph of a CTD-SRDL, with visible hardware components labeled. The miniaturized CTD unit samples the water column during the ascent phase of the seal’s dive. Data are then transmitted via the satellite transmission system Argos. From Treasure et al. (2017).

The data is traditionally compressed before being sent via Argos, due to limited battery and bandwidth capabilities. Approximately 5 profiles, made of  $\sim 15$  points each, are sent per day (Roquet et al., 2011).



However, thanks to recent improvements in battery capacity, a handful of CTD-SRDL have been set in continuous recording mode at the sampling frequency of 0.5 Hz, recording every dive realized by a seal during its journey. Since elephant seals typically perform more than 80 dives per day, this gives access to the density field at high-resolution over periods of several months, opening new horizons for the study of submesoscale physics in eddy-rich regions of the world oceans. Since 2014, twenty-eight such tags have been deployed at the Kerguelen Islands (French Southern Territories, Figure 1.2) and at Peninsula Valdes (Argentina) as part of the SO-MEMO program led by Christophe Guinet (CEBC/CNRS, France).

However, to be fitted on marine mammals, the tags are considerably smaller than a traditional CTD and often contain residual noise related to the miniaturized sensors capabilities (Roquet et al., 2017). Raw temperature and conductivity data are affected by a thermal lag effect, particularly pronounced across sharp thermoclines, and especially apparent on high-resolution profiles. Thus, we implemented an post-processing procedure aimed at improving the data quality, described in Siegelman et al. (2019b) and presented below. We build on papers published by Roquet et al. (2011) and Mensah et al. (2018). These authors developed initial corrections and accuracy estimates of animal-borne CTD data collected as part of the international MEOP consortium. Here, we take advantage of the newly available dataset of high-resolution profiles recorded, in continuous, at the sampling frequency of 0.5 Hz. More precisely, we make use of 7 tags deployed in the Southern Ocean from 2014 to 2018, allowing to access for the first time the ascent and descent of a dive. Thanks to this unique dataset, we develop and validate an autonomous post-processing procedure that considerably improves the quality all CTD-Satellite Relay Data Logger (CTD-SRDL) data, i.e. both high-resolution profiles recorded at the frequency of 0.5 Hz and compressed low-resolution ones transmitted in near-real time via satellite. The procedure corrects for the thermal lag effect on temperature and salinity and, subsequently, removes density inversions by adjusting salinity while leaving temperature unchanged. Overall, the procedure is applied to over 50 000 profiles (including high- and low-resolution profiles). In the process, we also refined accuracy estimates of CTD-SRDL data and, in particular, estimated for the first time the compression error associated to low-resolution data that, to date, represent 95% of the tags logged in the MEOP database. Thanks to recent progress in the field of bio logging, continuous high-resolution dataset are expected to become increasingly available. As such, the approaches proposed in this paper should gain increasing utility.

We refer the curious reader to Siegelman et al. (2019b) for technical details related to each tag’s own characteristics and associated errors. However, briefly, the final used in this dissertation has a post-correction accuracy of  $\pm 0.02^{\circ}\text{C}$  for temperature and  $\pm 0.03 \text{ g.kg}^{-1}$  for salinity, a median horizontal resolution of 700 m, a vertical resolution of 1 m and a mean temporal resolution of 25 min. Note that this resolution is greater than the one currently obtained from ocean gliders, which typically have a horizontal resolution of 2–4 km and a temporal resolution of 3–6 hours. In addition, and contrary to ocean gliders, elephant seals are endurance swimmers that can easily fight the current, painlessly crossing through, and thus sampling, mesoscale eddies and submesoscale fronts in the energetic ACC. In Chapter 3, we use of tag 48 deployed in a turbulent mesoscale area east of the Kerguelen Islands and in Chapter 5, we analyze tag 50 deployed west of the Kerguelen Islands in a less turbulent area (Figure 1.5). Both tags were deployed during the late austral spring–early austral summer of 2014.

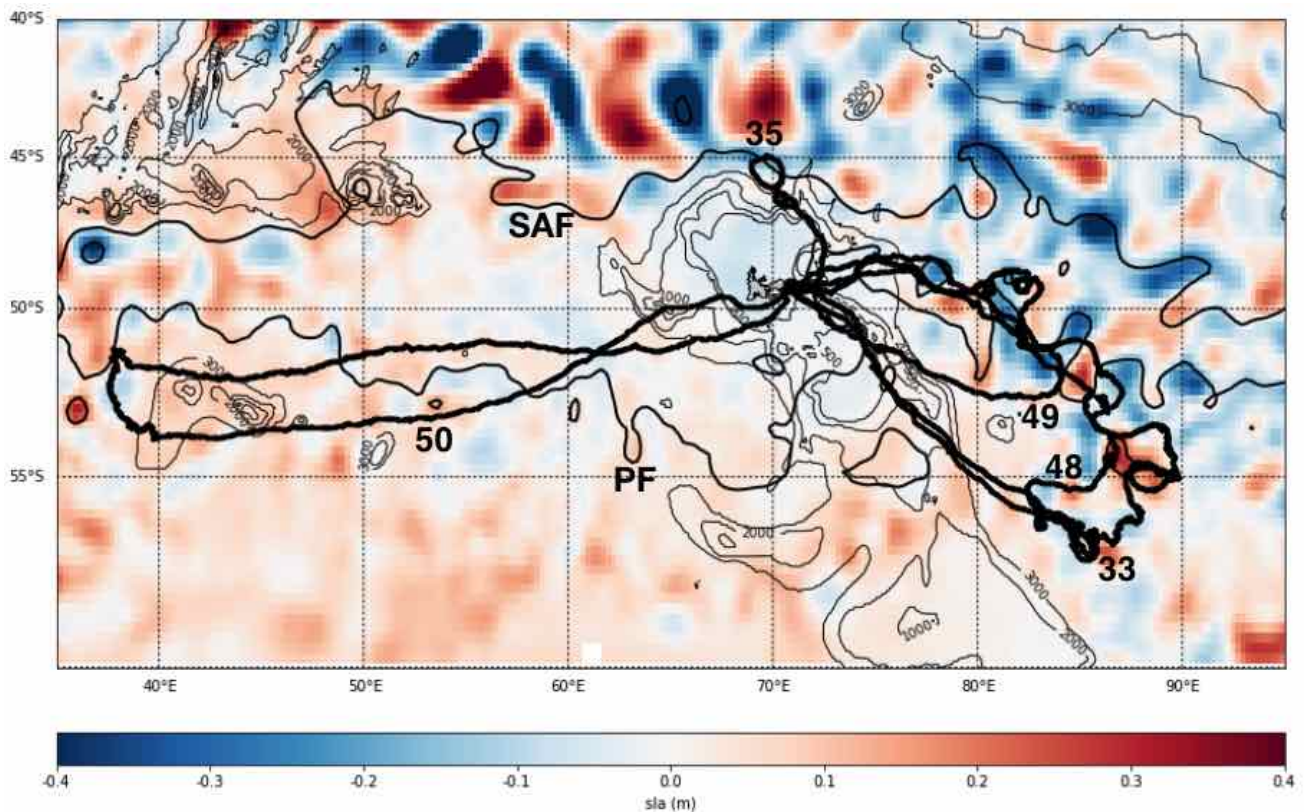


Figure 1.5: Continuous CDT-SRDL deployed on 5 southern elephant seals in 2014 at the Kerguelen Islands. The tag number is indicated. Sea level anomaly (sla) from AVISO is shown in the background for December 15, 2014. SSH contours corresponding to the Subantarctic (SAF; -0.25 m) and Polar (PF; -0.70 m) fronts are shown in black. Topography contours are plotted in grey.

## Correction and Accuracy of High- and Low-Resolution CTD Data from Animal-Borne Instruments

LIA SIEGELMAN,<sup>a,b,c</sup> FABIEN ROQUET,<sup>d</sup> VIGAN MENSAH,<sup>e</sup> PASCAL RIVIÈRE,<sup>a</sup>  
ETIENNE PAUTHENET,<sup>f</sup> BAPTISTE PICARD,<sup>g</sup> AND CHRISTOPHE GUINET<sup>g</sup>

<sup>a</sup> *Univ. Brest, CNRS, IRD, Ifremer, LEMAR, Plouzané, France*

<sup>b</sup> *Environmental Science and Engineering, California Institute of Technology, Pasadena, California*

<sup>c</sup> *NASA Jet Propulsion Laboratory, California Institute of Technology, Pasadena, California*

<sup>d</sup> *Department of Marine Sciences, University of Gothenburg, Gothenburg, Sweden*

<sup>e</sup> *Institute of Low Temperature Science, Hokkaido University, Sapporo, Japan*

<sup>f</sup> *Sorbonne Universités, UPMC Univ., Paris 06, UMR 7159, LOCEAN-IPSL, F-75005, Paris, France*

<sup>g</sup> *Centre d'Études Biologiques de Chizé, CNRS, Villiers-en-Bois, France*

(Manuscript received 28 September 2018, in final form 12 February 2019)

### ABSTRACT

Most available CTD Satellite Relay Data Logger (CTD-SRDL) profiles are heavily compressed before satellite transmission. High-resolution profiles recorded at the sampling frequency of 0.5 Hz are, however, available upon physical retrieval of the logger. Between 2014 and 2018, several loggers deployed on elephant seals in the Southern Ocean have been set in continuous recording mode, capturing both the ascent and descent for over 60 profiles per day during several months, opening new horizons for the physical oceanography community. Taking advantage of a new dataset made of seven such loggers, a postprocessing procedure is proposed and validated to improve the quality of all CTD-SRDL data: that is, both high-resolution profiles and compressed low-resolution ones. First, temperature and conductivity are corrected for a thermal mass effect. Then salinity spiking and density inversion are removed by adjusting salinity while leaving temperature unchanged. This method, applied here to more than 50 000 profiles, yields significant and systematic improvements in both temperature and salinity, particularly in regions of rapid temperature variation. The continuous high-resolution dataset is then used to provide updated accuracy estimates of CTD-SRDL data. For high-resolution data, accuracies are estimated to be of  $\pm 0.02^{\circ}\text{C}$  for temperature and  $\pm 0.03\text{ g kg}^{-1}$  for salinity. For low-resolution data, transmitted data points have similar accuracies; however, reconstructed temperature profiles have a reduced accuracy associated with the vertical interpolation of  $\pm 0.04^{\circ}\text{C}$  and a nearly unchanged salinity accuracy of  $\pm 0.03\text{ g kg}^{-1}$ .

### 1. Introduction

Hydrographic data collected by marine mammals such as southern elephant seals (SES; *Mirounga leonina*), Steller sea lions (*Eumetopias jubatus*), or ribbon seals (*Histiophoca fascia*) equipped with conductivity–temperature–depth Satellite Relay Data Logger (CTD-SRDL) tags (referred to as “tag”) represent a consequent

source of information, especially in the undersampled polar oceans where observations are notoriously hard to acquire (Roquet et al. 2014; Treasure et al. 2017). The temperature and conductivity sensors of these tags, manufactured by Valeport, Ltd., yield high precision ( $\pm 0.005^{\circ}\text{C}$  for temperature and  $\pm 0.01\text{ ms cm}^{-1}$  for conductivity; see Boehme et al. 2009) and reasonable accuracies ( $\pm 0.02^{\circ}\text{C}$  for temperature and  $\pm 0.03\text{ g kg}^{-1}$  for salinity) after delayed-mode calibration (Roquet et al. 2011). However, to be fitted on marine mammals, the tags are considerably smaller than a traditional CTD and often contain residual noise related to the miniaturized sensors capabilities (Roquet et al. 2017). Recent studies (Nakanowatari et al. 2017; Mensah et al. 2018) demonstrated that the tags are affected by a thermal mass error on their temperature and conductivity cells, particularly pronounced across sharp thermoclines.

Denotes content that is immediately available upon publication as open access.

Supplemental information related to this paper is available at the Journals Online website: <https://doi.org/10.1175/JTECH-D-18-0170.s1>.

Corresponding author: Lia Siegelman, [lsiegelman@caltech.edu](mailto:lsiegelman@caltech.edu)

DOI: 10.1175/JTECH-D-18-0170.1

© 2019 American Meteorological Society. For information regarding reuse of this content and general copyright information, consult the AMS Copyright Policy ([www.ametsoc.org/PUBSReuseLicenses](http://www.ametsoc.org/PUBSReuseLicenses)).

Correction of the thermal mass-induced error have been proposed and shown to work (Nakanowatari et al. 2017; Mensah et al. 2018) but only for salinity and not for temperature. Mensah et al. (2018) demonstrated that the thermal mass error on salinity is of  $O(10^{-2})$   $\text{g kg}^{-1}$  with maxima of  $O(10^{-1})$   $\text{g kg}^{-1}$ . These authors developed a correction, based on Lueck and Picklo (1990), which directly corrects salinity rather than conductivity and yields an error decrease of the salinity measure of up to 50% when using generic parameters values. However, due to the lack of thermal mass correction for temperature, density errors, some of them imputable to temperature, remain.

In addition, some aspects of the accuracy estimates of these data are insufficiently characterized. Indeed, besides the calibration errors discussed in Roquet et al. (2011), errors associated with the dynamical response of the tags and the reconstruction of profiles after compression also exist but have not been estimated.

In the present paper, we take advantage of a newly available continuous high-resolution dataset (described in section 2c) that advantageously contains the ascending and descending phase of dive, allowing to compare upcasts and downcasts for the first time. This unique dataset is used to tackle all the issues mentioned above, that is, the implementation of a thermal lag correction for temperature and conductivity, incorporation of a salinity correction to remove density inversions, and estimation of the dynamic response error of the tags and of the compression error associated with low-resolution data, all of which contribute to improving the post-processing and accuracy estimates of CTD-SRDL data.

Section 2 presents the datasets and method employed in this study. Section 3 introduces the correction procedure, which includes preliminary salinity and temperature adjustments and the thermal mass correction for conductivity and temperature as well as the density inversion removal algorithm. Section 4 describes the parameter estimation for the thermal mass correction. Section 5 presents the correction and accuracy estimates for high-resolution data. Section 6 presents the correction and accuracy estimates for compressed data. A summary and conclusions are proposed in section 7.

## 2. Datasets and method

### a. Satellite-transmitted compressed profile data

Compressed low-resolution profiles are transmitted in near-real time via the Argos satellite system for  $\sim 4$  profiles per day (among the  $\sim 60$  dives per day performed by SES) and are typically made of  $\sim 15$  points chosen via a broken-stick point selection algorithm (Boehme et al. 2009). To date, the majority of available

biologged data is made of low-resolution profiles. They represent 85% of the profiles and 95% of the tags in the Marine Mammals Exploring the Oceans Pole to Pole (MEOP) database, which is the largest database of biologged acquired hydrographic data with over 500 000 profiles collected since 2004 (Treasure et al. 2017). In particular, the heavy subsampling associated with the satellite-transmission method of low-resolution data implies the existence of a compression loss that will be evaluated for the first time in section 6c.

The low-resolution dataset employed in this study is made of 43 tags deployed on SES around the Kerguelen Islands from February 2011 to January 2018 (trajectories in black and red in Fig. 1a), amounting to a total of 14 762 CTD profiles. The environment in which SES dived is marked by temperatures of  $0^{\circ}$ – $4^{\circ}\text{C}$ , salinities of  $34$ – $34.9$   $\text{g kg}^{-1}$ , and densities of  $26.9$ – $27.8$   $\text{kg m}^{-3}$ , characteristic of the areas north of the polar front (PF), in the Antarctic zone (AAZ), which is defined as the area located between the PF and the southern Antarctic Circumpolar Current Front (SACCF) and south of the SACCF (Fig. 1).

### b. High-resolution profile data from retrieved tags

High-resolution profiles are recorded at the sampling frequency of 0.5 Hz for  $\sim 10$  profiles per day and are typically made of  $\sim 1000$  points. However, these data are only available after physical retrieval of the tag due to limited battery capabilities. Thus, compressed profiles are a subsample of high-resolution ones. The high-resolution dataset employed in this study corresponds to the high-resolution version of the low-resolution dataset, that is, the same 14 762 dives (trajectories in black and red in Fig. 1a) but recorded at the sampling frequency of 0.5 Hz. The high-resolution dataset is used to validate the proposed correction scheme for compressed low-resolution data and to derive the compression error (see section 6).

### c. Continuous high-resolution data

Thanks to recent progress in the field of miniaturization and satellite telemetry, tags can now record temperature, salinity, and pressure at the sampling frequency of 0.5 Hz for every dive of the seal's journey ( $>60$  dives per day), giving access, for the first time, to both the ascending and descending phase of a dive. Such tags can last for more than 3 months and cover large oceanic domains at a very high horizontal and vertical resolution (see sections of temperature and salinity in Fig. 2). These state-of-the-art data are opening new horizons for the physical oceanography community and in particular for the study of small-scale processes of  $O(1$ – $50)$  km, also called submesoscales. These submesoscale features,

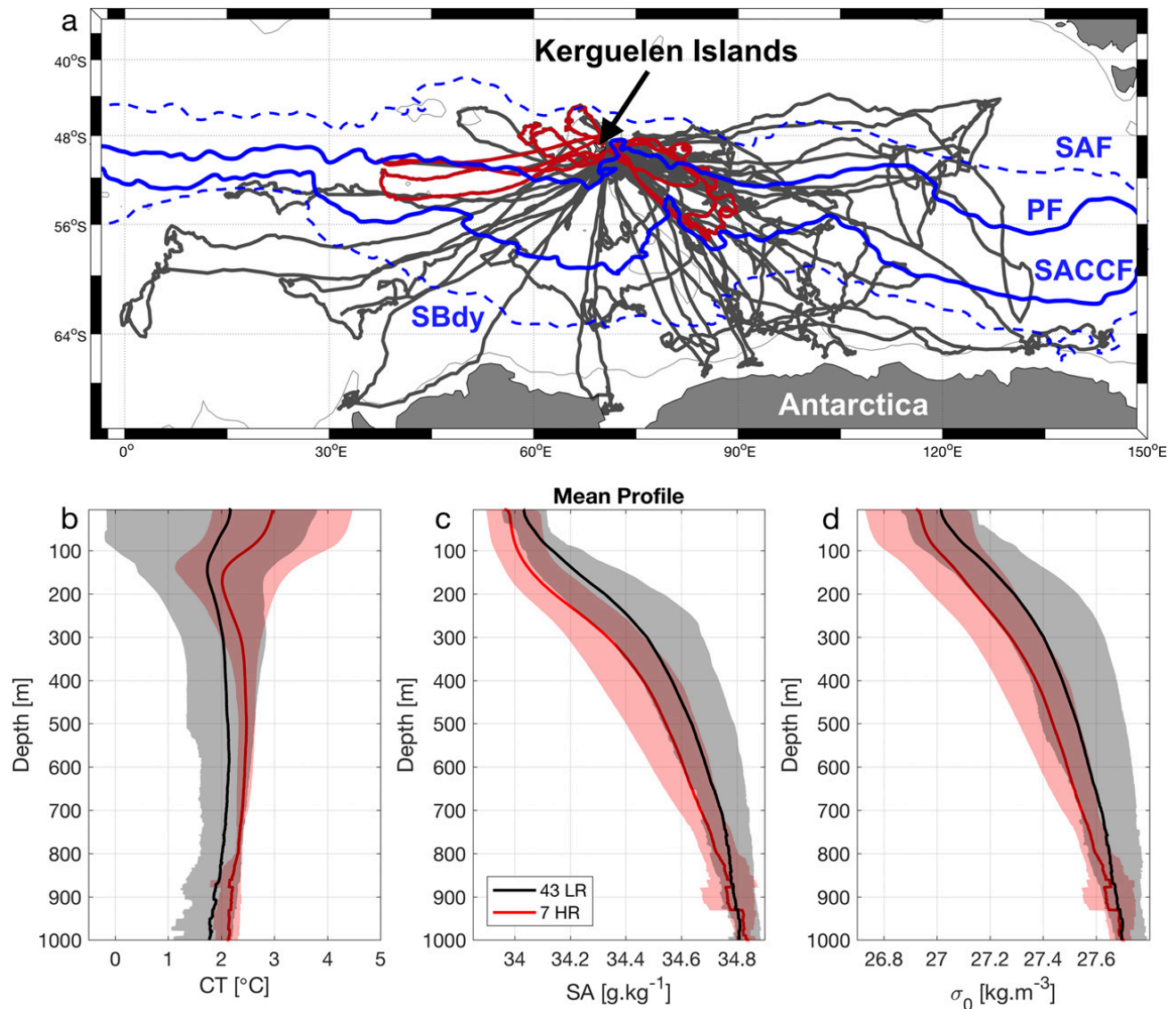


FIG. 1. (a) Spatial distribution of profiles collected by the 43 low-resolution tags (LR; black) among which 7 are also at continuous high resolution (HR; red), deployed from 2011 to 2018 on SES on the Kerguelen Islands. Climatological position of the Subantarctic Front (SAF), Polar Front (PF), Southern Antarctic Circumpolar Current Front (SACCF), and Southern Boundary Front (SBdy) are indicated in blue according to Kim and Orsi (2014). (b) Mean conservative temperature (CT) profile of the 43 LR tags (black) and 7 HR tags (red). (c) As in (b), but for absolute salinity (SA). (d) As in (b), but for potential density  $\sigma_0$ . In (b)–(d) the 20th and 80th percentiles are shaded.

characterized by elongated fronts and filamentary structures, are now captured by such observations, contrary to previous data obtained from animal-borne CTDs that were either of low resolution or only of high vertical (but not horizontal) resolution. To date, such data have only been briefly introduced in Mensah et al. (2018) to validate their salinity-based correction. In this paper, we fully exploit the potential of these new data, referred to as the “continuous high-resolution dataset,” that allows for direct comparison of upcasts and downcasts prior to and after correction.

The continuous high-resolution dataset employed in this study is made of seven tags (39 183 profiles) deployed

on SES around the Kerguelen Islands in the Indian Ocean sector of the Southern Ocean from October 2014 to January 2018 (trajectories in red on Fig. 1a). The environment in which the SES conducted profiles is marked by temperatures of  $1^{\circ}$ – $5^{\circ}$ C, salinities of  $33.9$ – $34.9$   $\text{g kg}^{-1}$ , and densities of  $26.7$ – $27.7$   $\text{kg m}^{-3}$ , characteristic of the area north of the SACCF (see Figs. 1 and 2).

#### d. General methodology

In addition to the temperature and salinity adjustments introduced in Roquet et al. (2011) and briefly recalled in section 3a, we propose an autonomous two-step

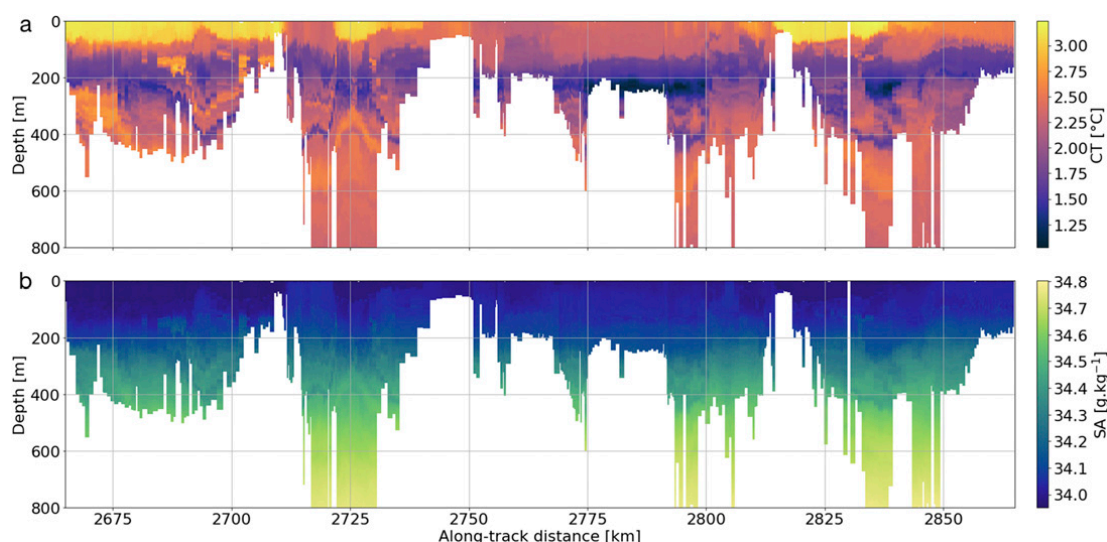


FIG. 2. Example of 200-km-long section of (a) conservative temperature and (b) absolute salinity at high resolution in the Southern Ocean from tag ct112–050–14 (red southwest trajectory from Kerguelen Islands in Fig. 1a). The tag recorded information at the sampling frequency of 0.5 Hz from 28 Oct 2014 to 21 Jan 2015, amounting to 6942 dives, or over 80 dives per day, and for a cumulative distance of 5665 km.

postprocessing procedure for the correction of MEOP's profiles also applicable to other hydrographic data acquired via biologging or with unpumped glider. We first implement a correction scheme for the thermal mass effect where temperature (Morison et al. 1994) and conductivity are simultaneously corrected (Lueck and Picklo 1990) instead of only and directly correcting salinity as is done in Mensah et al. (2018). This was, however, made possible by the theoretical framework delineated in Mensah et al. (2018) (see sections 3b and 4). We then aim at further refining the salinity correction regarding density inversions, which has not been addressed by previous works and is of particular importance for high-resolution profiles. To do so, hydrographic profiles are stabilized within the water column by minimally adjusting absolute salinity (SA) while leaving the values of in situ temperature unchanged with the method developed by Barker and McDougall (2017) (see section 3c).

The procedure is applied to the continuous high-resolution dataset as well as to the low-resolution dataset introduced in section 2. For high-resolution data, the effect of the correction is documented globally and then separately for the areas north and south of the PF (Fig. 1). The correction is then validated without relying on external data. Indeed, we use the continuous high-resolution dataset that advantageously contains both the ascending and descending phase of a dive, to validate the proposed correction by comparing upcast and downcast data before and after correction. Finally, the continuous high-resolution dataset is used to estimate the mean errors associated

with the tag's dynamical response, which are also estimated globally and separately north and south of the PF (see section 5).

For low-resolution data, the effect of the correction is documented for three oceanic zones: north of the PF, in the AAZ, and south of the SACCF (Fig. 1). The correction is then validated by comparing corrected high-resolution profiles to their low-resolution version prior to and after correction. Finally, the compression error associated with low-resolution data is estimated for the first time by comparing corrected low-resolution profiles to their high-resolution counterparts. The compression error is derived globally and then separately for the areas north of the PF, in the AAZ, and south of the SACCF (Fig. 1; see section 6).

Estimation of both the dynamic and compression errors enables us to provide updated accuracy estimates for high- and low-resolution data, which should be of prime importance to the physical oceanography community.

### 3. Correction procedure

#### a. Step 1: Salinity and temperature adjustments

In this section, we briefly recall the delayed-mode calibration designed by Roquet et al. (2011) and applied to the high- and low-resolution datasets before the correction scheme developed in this study (steps 2 and 3; Fig. 3). Temperature and salinity are first corrected for pressure-induced linear biases by comparing CTD-SRDL data to ship-based CTD measurements. An external field effect on the conductivity sensor is also detected, inducing an additional salinity offset.

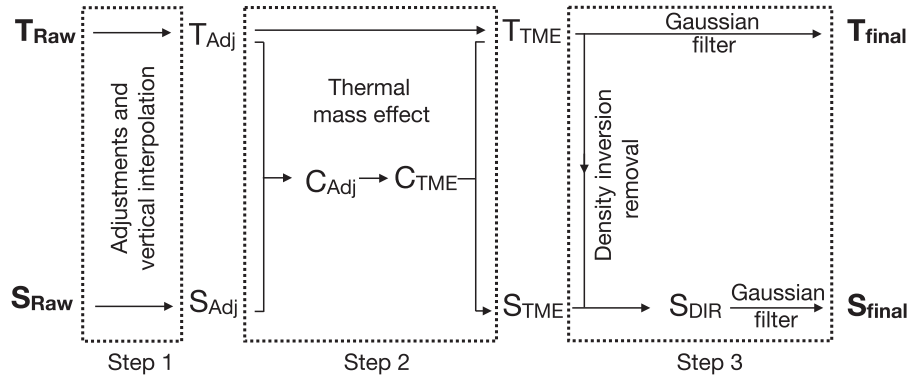


FIG. 3. Schematic summarizing the correction procedure implemented in the MEOP database. From the raw CTD data, temperature  $T_{\text{Raw}}$  and salinity  $S_{\text{Raw}}$  are first adjusted and vertically interpolated onto a regular grid according to the procedure described in Roquet et al. (2011) (step 1 detailed in section 3a). Then, adjusted conductivity  $C_{\text{Adj}}$  and temperature  $T_{\text{Adj}}$  are corrected for the thermal mass error (step 2 detailed in section 3b). Density inversions are then removed by minimally adjusting  $S_{\text{TME}}$  while leaving  $T_{\text{TME}}$  unchanged. Finally, a Gaussian filter with a 1-dbar window is applied to  $T_{\text{TME}}$  and  $S_{\text{DIR}}$  (step 3 detailed in section 3c).

This salinity offset is corrected with delayed-mode methods. The first method uses the stable salinity maximum characterizing the Lower Circumpolar Deep Water sampled by the seals foraging south of the SACCF and where this approach is not possible, a statistical method of cross comparison of CTD-SRDL measurements is used. For more details on the delayed-mode calibration methods, we refer the reader to Roquet et al. (2011). Finally, temperature and salinity are vertically interpolated onto a regular grid of 1-m resolution.

Note that the two-step correction procedure proposed in this paper can be implemented on hydrographic data acquired via biologging and unpumped glider without requiring step 1, which was specifically designed for the tags manufactured by Valeport, Ltd.

### b. Step 2: Thermal mass error

The thermal mass error (TME) is due to the transfer of heat from the sensor's walls to the sample being measured. This well-documented phenomenon (Lueck 1990) affects the conductivity cells of CTDs, which leads to a significant error in the estimation of salinity. This error is a function of the temperature gradient in space and time and has been widely documented for sharp thermocline (Lueck and Picklo 1990; Morison et al. 1994; Mensah et al. 2009; Liu et al. 2015). The tags considered in this study are particularly affected by the TME on their conductivity cells since they are unpumped. In addition, it appears that an error in temperature also related to the TME exists (Mensah et al. 2018). Building on Mensah et al. (2018), who only and directly corrected salinity, we implement a correction scheme for the TME that simultaneously corrects conductivity and temperature.

To correct the conductivity measure, we apply the procedure proposed by Lueck and Picklo (1990). The thermal mass error is modeled as an initial error  $\alpha_C$ , decaying within a relaxation time of  $1/\beta$  (Lueck 1990). Conductivity is then corrected via

$$C_T(n) = \Gamma_C \alpha_C (1 - 0.5\beta\Delta_t)^{-1} T_{\text{hp}}(n), \quad (1)$$

with  $C_T$  the conductivity correction added to the conductivity  $n$ th sample,  $T_{\text{hp}}(n)$  the high-pass-filtered sample's temperature, using a first-order discrete-time filter with a time constant  $\tau = \beta^{-1} - 0.5\Delta_t$ ,  $n$  the sample's index,  $\Gamma_C = (\partial C/\partial T)|_{S,p}$  the coefficient of sensitivity of conductivity to temperature at fixed salinity, and pressure and  $\Delta_t$  the sampling time interval, with  $\Delta_t = 2$  s for CTD-SRDLs. Note that Eq. (1), expressed as in Mensah et al. (2018), is equivalent to Lueck and Picklo's (1990) original formulation. Salinity is subsequently derived from the corrected conductivity.

Following Morison et al. (1994), temperature is corrected for the TME with a similar scheme according to

$$T_T(n) = \alpha_T (1 - 0.5\beta\Delta_t)^{-1} T_{\text{hp}}(n), \quad (2)$$

where the only difference with Eq. (1) is the absence of the sensitivity coefficient  $\Gamma_C$ . This second step is summarized in the schematic on Fig. 3. Adequate values for the three parameters  $\alpha_T$ ,  $\alpha_C$ , and  $\beta$  are estimated in section 4.

### c. Step 3: Density-inversion removal

Density inversions are commonly contained in oceanographic observations and are often due to instrumental noise and phenomena such as salinity spiking. While the

TME correction (step 1) suppresses part of this noise, most of the salinity spikes and density inversions persist after its application. [Barker and McDougall \(2017\)](#) propose a method to stabilize hydrographic profiles that removes part of this residual noise. The procedure minimally adjusts SA while leaving the values of conservative temperature (CT) unchanged. This density inversion removal (DIR) procedure adjusts the profiles such that they never exceed a minimum  $N^2$  threshold ( $N$  is the Brunt–Väisälä frequency), set here, and by default, to  $1 \times 10^{-9} \text{ s}^{-2}$ . Then a Gaussian filter with a 1-dbar window is applied to CT and SA to remove sharp and localized jumps induced by the DIR for SA profiles. These jumps occur at a frequency higher than the original sampling frequency and thus are not the reflection of a physical process. Furthermore, since experimental noise is observed in CT and in SA, which both contribute to the density estimate, smoothing CT in addition to SA ensures potential density  $\sigma_0$  free of density inversion or equivalently maintains a positive  $N^2$ . Indeed,  $N^2$  profiles can exhibit negative values when the filter is only applied to SA but not when it is applied to both SA and CT (not shown). The Gaussian filter also has the advantage to account for the irregular sampling in depth of the raw data that is dependent on the variable vertical speed of the animal. Last, the 1-dbar window does not alter the vertical resolution of the data since the original sampling frequency is of 0.5 Hz and the animal ascending speed is between 1 and  $2 \text{ m s}^{-1}$  ([Hindell and Lea 1998](#)). This third step is summarized in the schematic on [Fig. 3](#).

#### 4. Parameter estimation for the thermal mass error correction

To achieve an equivalent final salinity correction as the one obtained in [Mensah et al. \(2018\)](#), we use their generic parameters values of  $\beta = 0.06 \text{ s}^{-1}$  and  $\alpha_S = 0.04$ . Since [Mensah et al.'s \(2018\)](#) correction is based on the assumption that the correction of salinity is a linear combination of temperature and conductivity corrections, the initial error coefficients  $\alpha_C$ ,  $\alpha_T$ , and  $\alpha_S$  are related by  $\alpha_C = \alpha_T - \alpha_S$ , where  $\alpha_S$  is the initial error for salinity. The relaxation time  $1/\beta$  is assumed to be identical for both temperature and conductivity (thus also for salinity).

To derive an optimal  $\alpha_T$ , we use the continuous high-resolution dataset mentioned in [section 2](#). The temperature correction delineated by [Eq. \(2\)](#) is applied to the ascending and descending phases of every dive ranging from depths of a minimum of 150 m up to 1000 m and occurring within a 10-min interval in order to compare similar water masses, adding up to a total of 32 154 dives.

Differences in temperature between ascent and descent are not only due to the thermal mass effect; changes in the timing and geographic location between both phases actually account for a large part of this difference. However, the temperature difference between ascent and descent caused by natural variability should have no average bias. Consequently, the temperature correction scheme delineated by [Eq. \(2\)](#) is tested through a least squares regression scheme, in which we look for the optimal  $\alpha_T$  that minimizes the mean bias in temperature  $\sum_{z=0}^{400\text{m}} B(\alpha_T, z)$  between the ascending phase of dive  $i$  and the descending phase of dive  $i + 1$ , where

$$B(\alpha_T, z) = \frac{1}{n-1} \sum_{i=1}^{n-1} [T_a^{\alpha_T}(i, z) - T_d^{\alpha_T}(i+1, z)], \quad (3)$$

with  $z \in [0, 400]$  the depth of the measurements (m),  $i$  the  $i$ th dive,  $n$  the number of dives per tag, and  $T_a^{\alpha_T}$  and  $T_d^{\alpha_T}$  the temperature during ascent and descent, respectively, after application of the temperature correction with the coefficient  $\alpha_T$ . Note that below 400 m,  $T_{\text{hp}}$  is close to 0 such that the impact of the correction becomes negligible ([Fig. 4](#)), which justifies the choice of 400 m in  $\sum_{z=0}^{400\text{m}} B(\alpha_T, z)$ . Note also that we do not use the same dive for comparing ascending and descending phases but instead compare the ascending phase of dive  $i$  to the descending phase of dive  $i + 1$  because SES tend to station at the surface for only a few minutes ( $\sim 2$  min) while they swim underwater for longer periods of time ( $\sim 25$  min). It enables us to minimize the natural variability between ascents and descents.

The test is carried out separately for each of the seven tags, with resulting  $\alpha_T$  ranging from 0.07 to 0.10 (see [Table S1](#) in the online supplemental material). An optimal coefficient  $\alpha_T$  equal to 0.09 is then defined as the mean of the seven  $\alpha_T$  obtained for each tag. This optimal  $\alpha_T$  coefficient is used to implement the TME correction for temperature. A value of  $\alpha_C = \alpha_T - \alpha_S = 0.09 - 0.04 = 0.05$  is therefore used in combination with  $\beta = 0.06 \text{ s}^{-1}$ , which produces a salinity correction nearly identical to the one of [Mensah et al. \(2018\)](#). [Figure 4](#) presents the mean  $T_{\text{hp}}$  and temperature bias averaged for the seven tags. Noticeably, the mean temperature bias before correction is inversely proportional to the mean  $T_{\text{hp\_ascent}} - T_{\text{hp\_descent}}$  (black line), which confirms the appropriateness of the TME correction for the temperature field. Indeed, before correction, the mean temperature bias exhibits a significant positive (negative) bias between 0 and 200 m (200 and 400 m) (black line in [Fig. 4b](#)). However, after correction, the mean bias is centered around zero (blue line in [Fig. 4b](#)), indicating the suppression of a systematic bias throughout the water column. More importantly,



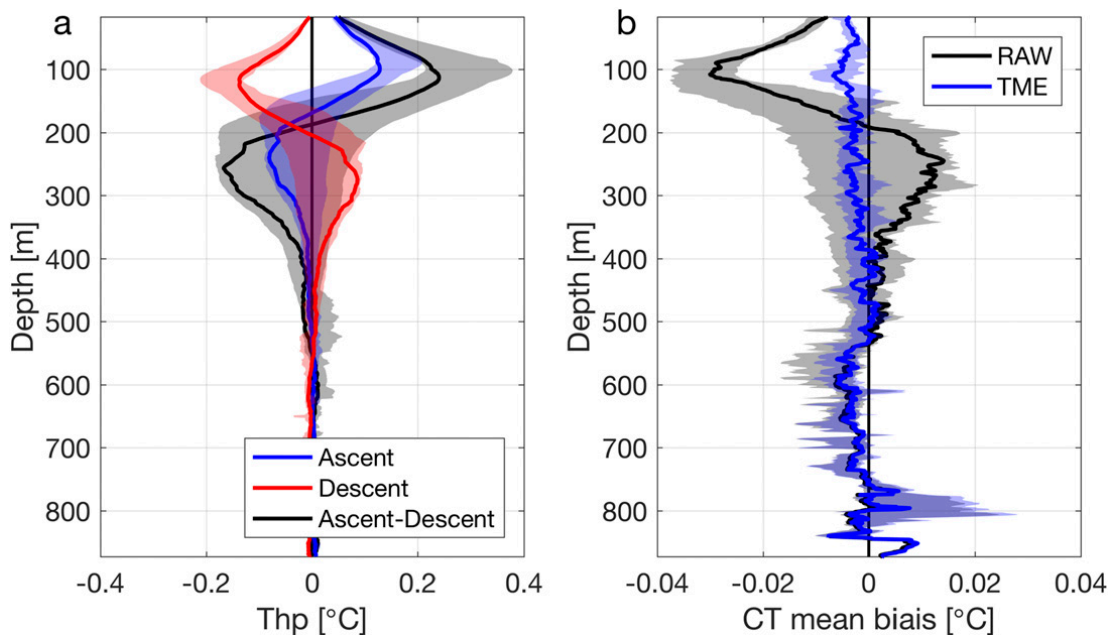


FIG. 4. (a) Mean high-pass filter of temperature  $T_{hp}$  during the ascent (blue line) and descent (red line) and mean  $T_{hp,ascent} - T_{hp,descent}$  (black line) for the 7 HR tags of the continuous high-resolution dataset used to implement the thermal mass error correction. (b) Mean bias prior to correction (black line) and after correction (blue line) for the 7 HR tags of the continuous high-resolution dataset. The 20th and 80th percentiles are shaded.

between 0 and 400 m, where the impact of the correction is the greatest due to the presence of the strongest  $T_{hp}$ , the mean temperature bias is reduced by 75% with an absolute value of  $0.01^{\circ}\text{C}$  before correction and only  $0.003^{\circ}\text{C}$  after correction, which is below the sensor's precision of  $\pm 0.005^{\circ}\text{C}$  (Boehme et al. 2009). Besides the averaged impact of the TME correction for temperature, Fig. 5a presents a typical ascent and descent profile prior to and after correction. The temperature difference between ascent and descent is reduced by  $0.08^{\circ}\text{C}$  at 112 m, a rather considerable improvement. In other words, application of the TME correction to the temperature field successfully removes the mean bias related to the thermal mass effect that is even maintained within the sensor's precision of  $\pm 0.005^{\circ}\text{C}$ .

## 5. Correction and accuracy of high-resolution profiles

### a. Effect of the correction scheme

Here we only consider the ascending phase of a dive since it is the one retained in the final MEOP database. We use the same continuous high-resolution dataset as in section 4 but with no restrictive criteria for depth or time. As a result, the two-step postprocessing correction is now implemented for the 39 183 high-resolution profiles of the continuous high-resolution dataset.

A typical pre- and postcorrection profile at high resolution is presented on the top panels of Fig. 6. The

TME (blue curve) first adjusts CT, SA, and  $\sigma_0$  on a low-frequency scale of  $O(100)$  m. Then salinity spikes and subsequent density inversions occurring at a scale of  $O(1)$  m are removed by the DIR (red curve).

Differences between raw and corrected data are computed at both steps and RMS values are presented on Fig. 7. Overall, the largest corrections take place between the surface and 300 m, that is, where stronger gradients of temperature are located (Fig. 4). As expected, the TME has a much larger contribution to the CT correction, whereas both TME and DIR contribute significantly to the correction of SA. Indeed, during the DIR the only effective correction applied to CT is the Gaussian filter. For CT, the root-mean-square (RMS) between raw and corrected data is  $5.9 \times 10^{-3}^{\circ}\text{C}$  after application of the TME and only  $6.1 \times 10^{-3}^{\circ}\text{C}$  after application of the additional DIR step (Fig. 7a). On the other hand, for SA, the RMS between raw and corrected data is of  $2.8 \times 10^{-3} \text{ g kg}^{-1}$  after the TME step and  $5.3 \times 10^{-3} \text{ g kg}^{-1}$  after the DIR. Likewise, for  $\sigma_0$ , the RMS is of 2.7 and  $4.5 \times 10^{-3} \text{ kg m}^{-3}$  after the TME and DIR, respectively. These results highlight the equally important impact of each step for the correction of SA and  $\sigma_0$  (Figs. 6 and 7). Furthermore, the order of the steps is important and applying the TME prior to the DIR considerably reduces the amplitude of the DIR (not shown here). In other words, the DIR has a lesser impact on the profiles when applied after the TME than directly on raw data, which points out the contribution

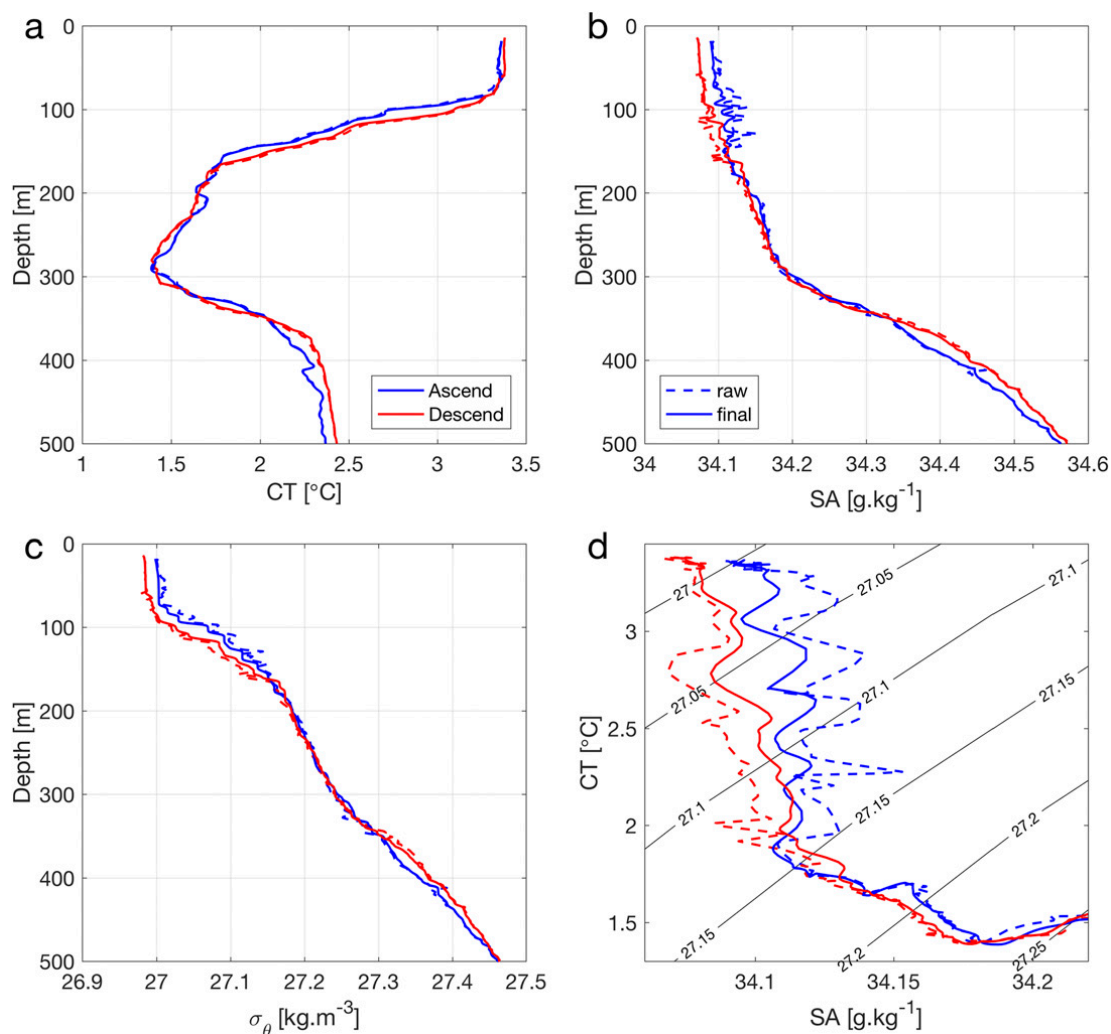


FIG. 5. Typical ascent (blue line) and descent (red line) profiles prior to correction (dashed line) and after correction (solid line), zoomed from 0 to 500 m. (a) Conservative temperature. (b) Absolute salinity. (c) Potential density. (d) CT-SA diagram.

of the thermal mass effect correction for reducing density inversions. The mean RMS between raw and corrected data is  $1.35 \times 10^{-2} \text{ }^\circ\text{C}$  for CT and  $1.17 \times 10^{-2} \text{ g kg}^{-1}$  for SA within the upper 300 m. These values are largely above the sensor's precision, and underscore the relative importance of the correction.

The impact of the correction for high-resolution profiles is now documented for two zones of the Southern Ocean: north and south of the PF, following the climatological definition of Kim and Orsi (2014). Unfortunately, the continuous high-resolution dataset used in this study does not contain enough profiles south of the SACCF (191 profiles or <0.05% of the dataset) to compute separate statistics for the AAZ and the area south of the SACCF. North of the PF, the profiles are marked by a mean temperature and salinity of  $2.50^\circ\text{C}$  and of  $34.42 \text{ g kg}^{-1}$ , while south of the PF, the means are of  $2.01^\circ\text{C}$  for temperature and  $34.57 \text{ g kg}^{-1}$  for salinity

(Table 1). RMSs between raw and corrected data are presented per area and depth range in Table 1. While below 300 m, the impact of correction is equivalent north and south of the PF, it differs between 0 and 300 m, where the correction is stronger by  $\sim 20\%$  south of the PF for both CT, SA, and  $\sigma_0$ . For CT, the mean RMS is  $1.4 \times 10^{-2} \text{ }^\circ\text{C}$  north of the PF and  $1.6 \times 10^{-2} \text{ }^\circ\text{C}$  south of the PF. For SA, the mean RMS is  $1.1 \times 10^{-2} \text{ g kg}^{-1}$  north of the PF and  $1.3 \times 10^{-2} \text{ g kg}^{-1}$  south of the PF. For  $\sigma_0$ , it is  $9 \times 10^{-3} \text{ kg m}^{-3}$  north of the PF and  $1.1 \times 10^{-2} \text{ kg m}^{-3}$  south of it (Table 1).

#### b. Validation of the correction scheme for high-resolution profiles

Following the same methodology as in section 4, the two-step correction is applied to the ascending and descending phases of the 39 183 dives that are deeper than 150 m and occur within a 10-min interval, which

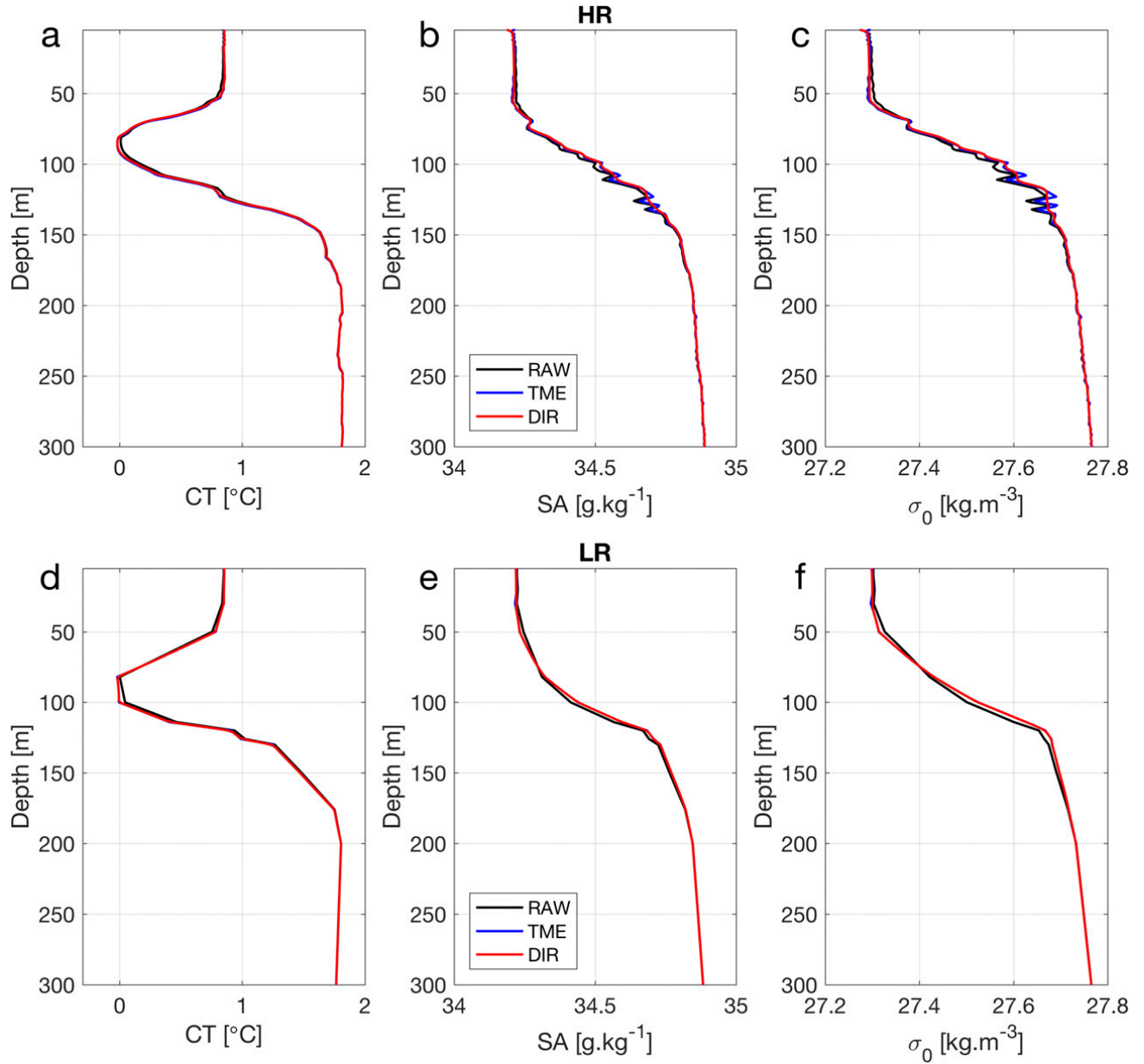


FIG. 6. Typical profile undergoing the correction scheme. High-resolution profiles of (a)–(c) conservative temperature, absolute salinity, and potential density, respectively. (d)–(f) As in (a)–(c), respectively, but showing low-resolution profiles.

amounts to 32 154 dives. Comparison between the ascending phase of dive  $i$  and the descending phase of dive  $i + 1$  is done before correction as well as at both steps of the procedure. For each tag, the RMS error of ascend versus descend is calculated at each depth  $z$  according to

$$\text{RMS}(z) = \sqrt{\frac{1}{n-1} \sum_{i=1}^{n-1} [X_a(z, i) - X_d(z, i+1)]^2}, \quad (4)$$

with  $n$  the total number of dives per tag,  $X_a$  and  $X_d$  the field (CT, SA, or  $\rho_0$ ) during the ascent and descent,

respectively. This RMS is calculated for the uncorrected ( $\text{RMS}_{\text{raw}}$ ) and corrected ( $\text{RMS}_{\text{cor}}$ ) CT, SA, and  $\rho_0$  at the TME and DIR steps. The performance of the correction is then evaluated through the difference  $D_{\text{cor}} = \text{RMS}_{\text{raw}} - \text{RMS}_{\text{cor}}$  at both steps, with positive values indicating a decrease of the RMS error due to a convergence of ascending and descending profiles post correction. All seven tags see a continuous and significant improvement at each step of the procedure for all three fields. The difference between the ascending and descending phases for both CT, SA, and  $\sigma_0$  is reduced after correction, as can be inferred from

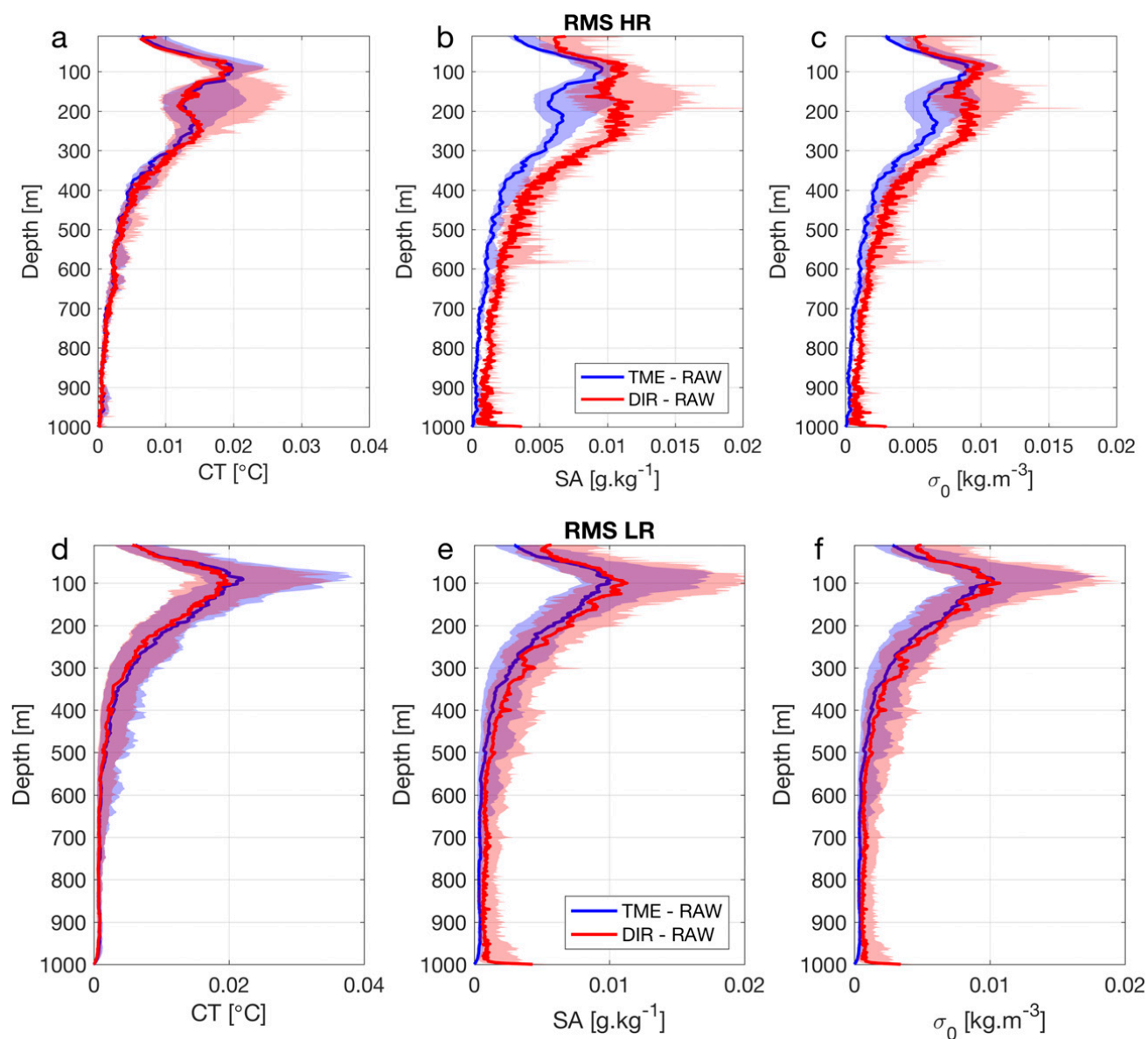


FIG. 7. Mean RMS between raw and corrected data for (top) the 7 HR tags for (a) CT, (b) SA, and (c)  $\sigma_0$  and (bottom) the 43 LR tags for (d) CT, (e) SA, and (f)  $\sigma_0$ . The 20th and 80th percentiles are shaded.

the positive  $D_{\text{cor}}$  presented on the upper panels of Fig. 8, even though between 200 and 400 m the difference is slightly negative for CT (but inferior to the sensor's precision). The TME reduces most the difference between ascents and descents for CT with mean  $|D_{\text{cor}}|$  over the water column of  $1.3 \times 10^{-3} \text{°C}$  at both steps. For SA and  $\sigma_0$ , the two steps incrementally contribute to reduce the difference between ascents and descents with a mean  $|D_{\text{cor}}|$  of 1.5 and  $3.0 \times 10^{-3} \text{g kg}^{-1}$  for SA at step TME and DIR, respectively, and 1.4 and  $2.9 \times 10^{-3} \text{kg m}^{-3}$  for  $\sigma_0$  at step TME and DIR, respectively.

Overall, the error difference  $D_{\text{cor}}$  is most reduced in areas of strong temperature gradients, that is, between the surface and 300-m depth (Figs. 4 and 8), which itself

coincides with the strongest impact of the correction procedure (Fig. 7), emphasizing the procedure's efficiency. Besides the effect of the correction scheme presented on Fig. 8 over the entire water column, a typical pre- and postcorrection profile, between the surface and 300 m, is shown on Fig. 5. The profile, which occurs in a region presenting sharp temperature variations and thus particularly prone to thermal mass and salinity spiking effects, sees its temperature difference between ascent and descent reduced by  $8 \times 10^{-2} \text{°C}$  at 112 m and its salinity by  $4 \times 10^{-2} \text{g kg}^{-1}$  at 130 m, two rather considerable improvements which are also reflected on the density profile (Fig. 5c) and in the TS plan (Fig. 5d).

TABLE 1. Statistics relative to high-resolution (HR) data per oceanic zone and depth range averaged for the seven tags of the continuous HR dataset used in this study. Mean CT, SA, and RMS between raw and final profiles are presented, as is the mean error bias defined by Eq. (5), for which 14 904 profiles are used north of the PF and 17 250 south of the PF, adding to a total of 32 154 profiles. The location of the PF is defined according to Kim and Orsi (2014).

Zone	No. of HR profiles	Depth (m)	CT (°C)	SA (g kg <sup>-1</sup> )	RMS of CT (°C)	RMS of SA (g kg <sup>-1</sup> )	RMS of $\sigma_0$ (kg m <sup>-3</sup> )	CT mean bias (°C)	SA mean bias (g kg <sup>-1</sup> )	$\sigma_0$ mean bias (kg m <sup>-3</sup> )
North of PF	17 592	0–300	2.64	34.04	0.014	0.011	0.009	0.004	0.005	0.005
		300–1000	2.45	34.58	0.003	0.003	0.002	0.003	0.004	0.004
		0–1000	2.50	34.42	0.006	0.006	0.004	0.003	0.005	0.004
South of PF	21 591	0–300	1.66	34.20	0.016	0.013	0.011	0.003	0.004	0.004
		300–1000	2.17	34.73	0.003	0.002	0.002	0.001	0.002	0.002
		0–1000	2.01	34.57	0.007	0.007	0.005	0.002	0.003	0.003
All	39 183	0–300	2.38	34.10	0.014	0.012	0.010	0.003	0.005	0.004
		300–1000	2.36	34.63	0.003	0.003	0.002	0.002	0.004	0.003
		0–1000	2.36	34.47	0.006	0.006	0.004	0.003	0.004	0.003

### c. Accuracy estimates

Besides calibration errors discussed in Roquet et al. (2011) and estimated to be of  $\pm 0.02^\circ\text{C}$  for temperature and  $\pm 0.03 \text{ g kg}^{-1}$  for salinity after delayed-mode calibration, the tags are also subject to a thermal lag response as documented in this study as well as in previous works (Nakanowatari et al. 2017; Mensah et al. 2018). Even after correction, a residual error imputable to thermal lag effects remains. In this section, we quantify this dynamical bias present in CTD-SRDL data, and also detail it north and south of the PF.

The mean dynamical error is estimated from the continuous high-resolution dataset through the calculation of  $B(\alpha_T, z)$  defined by Eq. (3) after application of the two-step correction. Results are presented for the entire water column on the top panels of Fig. 9 and summary statistics per zone can be found in Table 1, in which the mean dynamical error over the water column is defined by

$$M_{z_{\max}} = \frac{1}{z_{\max}} \sum_{z=0}^{z_{\max}} |B(\alpha_T, z)|, \quad (5)$$

where  $z_{\max}$  is the maximal depth, here, 1000 m. For both CT and SA, the mean dynamical bias  $M_{1000}$  is of  $2.7 \times 10^{-3}^\circ\text{C}$  and  $4.1 \times 10^{-3} \text{ g kg}^{-1}$ , respectively, which is well below the sensor's accuracies of  $\pm 0.005^\circ\text{C}$  for temperature and  $\pm 0.02 \text{ g kg}^{-1}$  for salinity. The  $\sigma_0$  also has a weak mean bias with a value of  $3.5 \times 10^{-3} \text{ kg m}^{-3}$ . For all three quantities  $M_{1000}$  is larger north than south of the PF by 75% for CT and 50% for SA and  $\sigma_0$ . Furthermore, across all areas, the mean dynamical bias is larger in the first 300 m by 45% for CT and 25% for SA and  $\sigma_0$ .

In conclusion, application of the TME and DIR considerably improves the final accuracy of CTD-SRDL data, with mean dynamical errors estimated to be below

the sensor's precision of  $\pm 0.005^\circ\text{C}$  for temperature and  $\pm 0.02 \text{ g kg}^{-1}$  for salinity. This means that after application of the correction procedure, dynamical errors are negligible compared to calibration errors such that the accuracies of  $\pm 0.02^\circ\text{C}$  for temperature and  $\pm 0.03 \text{ g kg}^{-1}$  for salinity presented in Roquet et al. (2011) are still valid for high-resolution data.

## 6. Correction and accuracy of compressed profiles

### a. Effect of the correction scheme

The low-resolution version of the high-resolution profile shown on Fig. 6a is presented on the bottom panels of the same figure. Overall, the correction procedure behaves similarly but with a few noticeable differences. Similarly to the high-resolution profile, CT is primarily affected by the TME. However, for SA and  $\sigma_0$ , only the effect of the TME is large while that of DIR has become insignificant. As mentioned before, the TME acts on scales of  $O(100)$  m while the DIR tends to act on scales of  $O(1)$  m. The strong (weak) impact of the TME (DIR) is thus consistent with the low resolution of the profile that does not have enough data points to generate salinity spiking. In addition, the Gaussian filter has a negligible impact for all three quantities (not shown), which is also coherent with the low resolution of the profile.

These observations can be generalized to the entire dataset and the application of the correction procedure to the 14 762 low-resolution profiles yields similar results as for high-resolution ones (Fig. 7, lower panels). The shape of the correction's impact within the water column is preserved, with the strongest corrections occurring once again between the surface and 300-m depth. However, as mentioned before, the TME now has the main impact for CT, SA, and  $\sigma_0$  with a mean

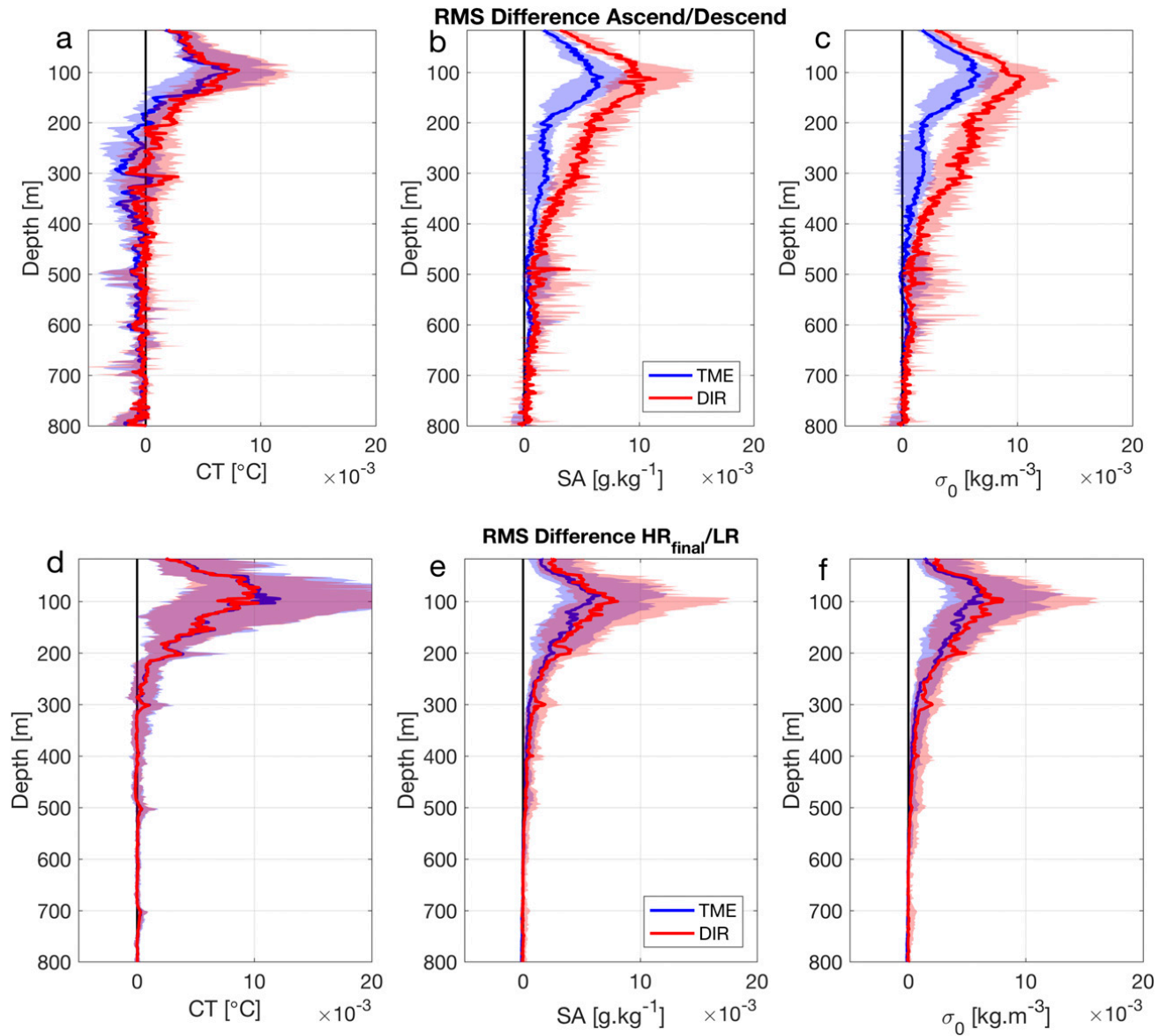


FIG. 8. Mean RMS difference between ascending and descending phases of a dive at each step of the correction procedure for (top) the 7 HR tags for (a) CT, (b) SA, and (c)  $\sigma_0$  and (bottom) the 43 LR tags for (d) CT, (e) SA, and (f)  $\sigma_0$ . The 20th and 80th percentiles are shaded.

RMS between raw and corrected data of  $4.9$  and  $4.5 \times 10^{-3} \text{ }^\circ\text{C}$  for CT at step TME and DIR, respectively,  $2.3$  and  $3.0 \times 10^{-3} \text{ g kg}^{-1}$  for SA, and  $2.3$  and  $2.7 \times 10^{-3} \text{ kg m}^{-3}$  for  $\sigma_0$ . Once again, the correction is noticeably stronger between 0 and 300 m with average RMS between raw and final data of  $11.9 \times 10^{-3} \text{ }^\circ\text{C}$  for CT,  $7.1 \times 10^{-3} \text{ g kg}^{-1}$  for SA, and  $6.6 \times 10^{-3} \text{ kg m}^{-3}$  for  $\sigma_0$ .

As for the high-resolution profiles, a regional analysis is conducted on the low-resolution dataset. Since a large amount of profiles are located south of the SACCF (5438 profiles or 37% of the dataset), three zones are now analyzed: the area north of the PF, the AAZ, and the area south of the SACCF, where the fronts are also defined according to [Kim and Orsi \(2014\)](#). Mean temperatures

are  $2.77^\circ$ ,  $2.17^\circ$ , and  $0.84^\circ\text{C}$  and mean salinities  $34.43$ ,  $34.52$ , and  $34.62 \text{ g kg}^{-1}$  for the areas north of the PF, in the AAZ, and south of the SACCF, respectively. The temperature correction is equivalent in all three zones regardless of the depth range. For SA and  $\sigma_0$ , the correction is equivalent in the three zones below 300 m but in the upper 300 m it is more important south of the PF (in both the AAZ and the area south of the SACCF), as for to the correction impact on high-resolution data. For SA, the mean RMS is  $0.005 \text{ g kg}^{-1}$  north of the PF and  $0.007$  and  $0.008 \text{ g kg}^{-1}$  in the AAZ and south of the SACCF, respectively. For  $\sigma_0$ , it is  $0.005 \text{ kg m}^{-3}$  north of the PF and  $0.007 \text{ kg m}^{-3}$  south of it ([Table 2](#)).

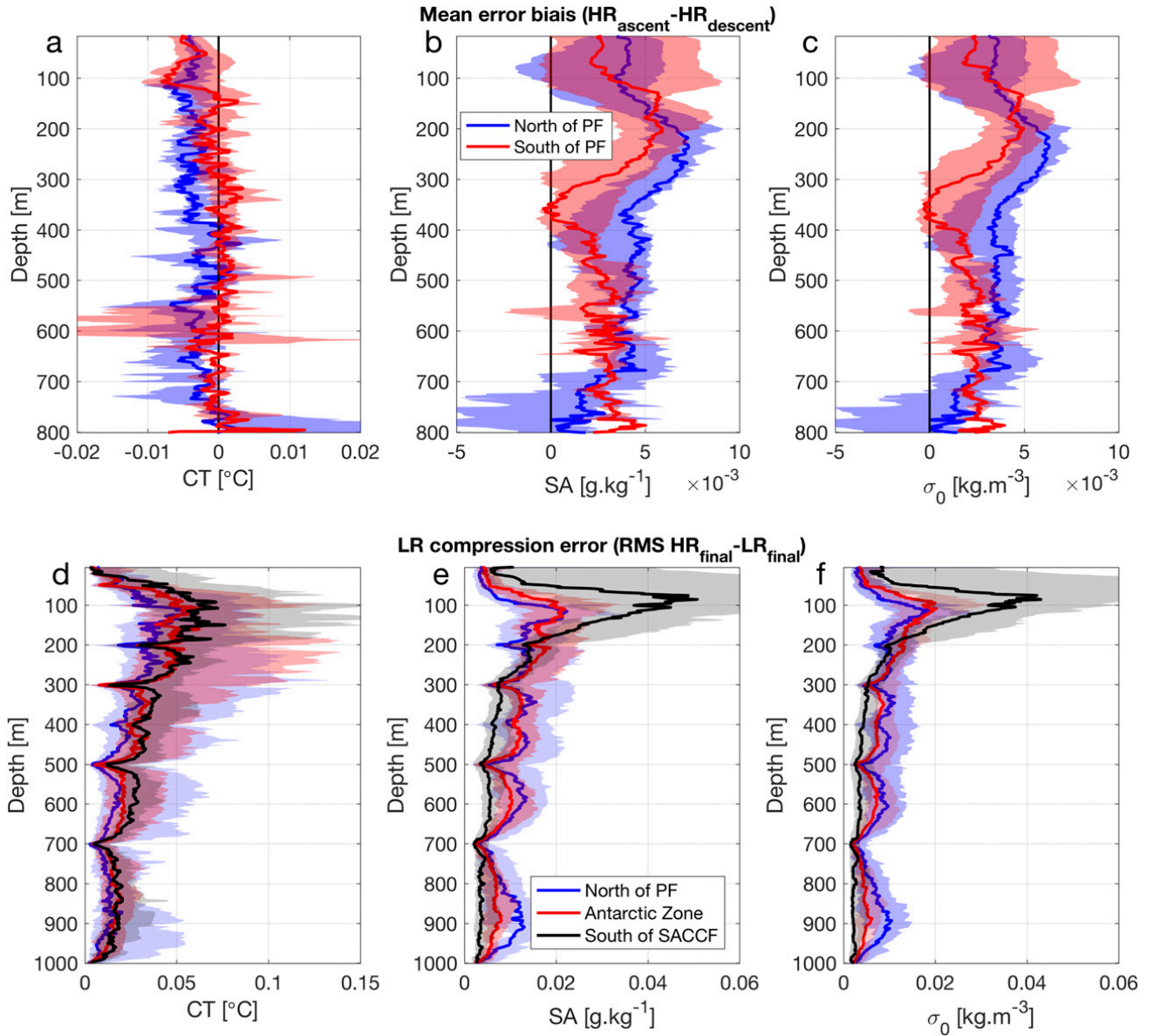


FIG. 9. (top) Mean error bias of high-resolution profiles related to the dynamical response of the tag. The mean error bias is calculated as the mean difference between the corrected ascents and descents [see Eq. (3)] for (a) CT, (b) SA, and (c)  $\rho_0$  averaged for the 7 HR tags of the continuous high-resolution dataset employed in this study and separated by frontal zones according to Kim and Orsi (2014). (bottom) Compression error associated with the low-resolution dataset. The compression error is calculated as the mean RMS difference between the corrected high- and low-resolution profiles for (d) CT, (e) SA, and (f)  $\rho_0$  averaged for the 43 tags and separated by oceanic zones according to Kim and Orsi (2014). The 20th and 80th percentiles are shaded.

### b. Validation of the correction scheme for compressed profiles

To validate the correction for low-resolution profiles, we undertake a comparison between the 14762 low-resolution profiles at each step of the correction procedure (raw, TME, DIR) and their available corrected high-resolution version. Similar to the validation of high-resolution data, the RMS error of high versus low resolution is calculated, for each tag, at each depth  $z$  according to

$$\text{RMS}(z) = \sqrt{\frac{1}{n} \sum_{i=1}^n [X_{\text{HR}_{\text{final}}}(z, i) - X_{\text{LR}}(z, i)]^2}, \quad (6)$$

with  $n$  the total number of dives,  $X_{\text{HR}_{\text{final}}}$  the high-resolution corrected field (CT, SA, or  $\rho_0$ ), and  $X_{\text{LR}}$  the low-resolution field (CT, SA, or  $\rho_0$ ). Note that in Eq. (6), the high-resolution profiles are those obtained after application of the correction scheme and referred to as  $X_{\text{HR}_{\text{final}}}$ . RMS is calculated for the uncorrected ( $\text{RMS}_{\text{raw}}$ ) and corrected ( $\text{RMS}_{\text{cor}}$ ) low-resolution profiles of CT,

TABLE 2. Statistics relative to low-resolution (LR) data per oceanic zone and depth range averaged for the 43 tags at low resolution considered in this study. Mean CT, SA, and RMS between raw and final profiles are presented, as is mean LR compression error defined by Eq. (6). The frontal zones are defined according to Kim and Orsi (2014).

Zone	No. of LR profiles	Depth (m)	CT (°C)	SA (g kg <sup>-1</sup> )	RMS of CT (°C)	RMS of SA (g kg <sup>-1</sup> )	RMS of $\sigma_0$ (kg m <sup>-3</sup> )	CT compression error (°C)	SA compression error (g kg <sup>-1</sup> )	$\sigma_0$ compression error (kg m <sup>-3</sup> )
North of PF	3333	0–300	3.05	34.09	0.012	0.005	0.005	0.031	0.011	0.009
		300–1000	2.65	34.58	0.001	0.001	0.001	0.015	0.010	0.007
		0–1000	2.77	34.43	0.003	0.002	0.002	0.020	0.010	0.008
Antarctic Zone	5991	0–300	2.04	34.14	0.013	0.007	0.007	0.040	0.014	0.011
		300–1000	2.22	34.68	0.001	0.001	0.001	0.019	0.008	0.005
		0–1000	2.17	34.52	0.004	0.003	0.002	0.025	0.010	0.007
South of SACCF	5438	0–300	0.19	34.36	0.012	0.008	0.007	0.046	0.021	0.017
		300–1000	1.12	34.73	0.001	0.001	0.001	0.022	0.005	0.003
		0–1000	0.84	34.62	0.004	0.003	0.003	0.029	0.010	0.007
All	14 762	0–300	1.91	34.21	0.012	0.007	0.007	0.048	0.015	0.012
		300–1000	2.06	34.66	0.001	0.001	0.001	0.025	0.009	0.006
		0–1000	2.02	34.53	0.004	0.003	0.003	0.032	0.011	0.008

SA, and  $\rho_0$  at both steps of the procedure. Similar to section 5b, the performance of the correction is then evaluated through the difference  $D_{\text{cor}} = \text{RMS}_{\text{raw}} - \text{RMS}_{\text{cor}}$  after application of the first step (TME) and second step (DIR). Positive  $D_{\text{cor}}$  indicates a decrease of the RMS error due to the convergence between the reference corrected high-resolution profile  $X_{\text{HR}_{\text{final}}}$  and the low-resolution profile undergoing the correction scheme. The results are presented on the lower panels of Fig. 8 for the averaged 43 tags and RMSs are of  $O(10^{-3})^\circ\text{C}$  for CT,  $O(10^{-3})\text{ g kg}^{-1}$  for SA, and  $O(10^{-3})\text{ kg m}^{-3}$  for  $\rho_0$ . Similarly to high-resolution profiles, there is a continuous decrease of the RMS error at each step of the procedure, validating the correction for low-resolution profiles. Once again, the strongest error decrease occurs in the first upper hundreds of meters of the water column. In contrast with high-resolution profiles, for which the first two steps have an equal impact, and in accordance with the correction impact on low-resolution profiles (see section 5a), it is now the TME that reduces most the RMS error. Indeed, for CT, the mean  $|D_{\text{cor}}|$  is  $1.0 \times 10^{-30}\text{C}$  after TME and  $1.3 \times 10^{-30}\text{C}$  after DIR. For SA, the mean  $|D_{\text{cor}}|$  is 0.9 and  $1.3 \times 10^{-3}\text{ g kg}^{-1}$  after TME and DIR, respectively and for  $\sigma_0$ , it is 1.4 and  $1.3 \times 10^{-3}\text{ kg m}^{-3}$  after TME and DIR, respectively.

### c. Compression error on low-resolution data

In this section, we estimate the compression error associated with the linear interpolation between transmitted data and quantify it for three major zones of the Southern Ocean: the area north of the PF, the AAZ, and the area south of the SACCF. The compression error is derived through the calculation of the RMS error between corrected high- and low-resolution profiles [see Eq. (6)]. The results are presented for the three zones on the lower panels of Fig. 9 and in Table 2. For CT, the compression error is important and has a mean value of  $\pm 0.032^\circ\text{C}$ , which is larger than the calibration error value of  $\pm 0.02^\circ\text{C}$  obtained after delayed-mode calibration (Roquet et al. 2011). This error increases from north to south with values of  $\pm 0.02^\circ\text{C}$  north of the PF,  $\pm 0.025^\circ\text{C}$  in the AAZ, and  $\pm 0.029^\circ\text{C}$  south of the SACCF. For SA, the compression error is overall relatively small, with a value of  $\pm 1.1 \times 10^{-2}\text{ g kg}^{-1}$  across all areas. However, south of the SACCF, the compression error in salinity is important in the first 200 m, with a maximal error of  $\pm 5 \times 10^{-2}\text{ g kg}^{-1}$  at 87 m. Furthermore, in the upper 300 m this compression error also increases from north to south with mean values of  $\pm 1.1 \times 10^{-2}\text{ g kg}^{-1}$  north of the PF,  $\pm 1.4 \times 10^{-2}\text{ g kg}^{-1}$  in the AZ, and  $\pm 2.1 \times 10^{-2}\text{ g kg}^{-1}$  south of the SACCF. However, from 300 to 1000 m this tendency is reversed with mean compression errors of  $\pm 1 \times 10^{-2}\text{ g kg}^{-1}$  north



of the PF,  $\pm 8 \times 10^{-3} \text{ g kg}^{-1}$  in the AZ, and  $\pm 5 \times 10^{-3} \text{ g kg}^{-1}$  south of the SACCF. Similar patterns are obtained for  $\sigma_0$ , with a mean compression error of  $\pm 0.008 \text{ kg m}^{-3}$  across all areas and a maximal error south of the SACCF of  $\pm 4 \times 10^{-2} \text{ kg m}^{-3}$  at 87 m. Note that the compression error profiles (Fig. 9) present lower values at fixed depths of 200, 300, 400, 500, 700, and 1000 m, which is due to the compression algorithm that picks these depth levels more often.

Overall, the compression error is important for CT but negligible for SA and  $\sigma_0$  with mean values of  $\pm 0.032^\circ\text{C}$ ,  $\pm 0.011 \text{ g kg}^{-1}$ , and  $\pm 0.008 \text{ kg m}^{-3}$ , respectively. Since the compression error can be assumed to be independent from the calibration error, new accuracy estimates for low-resolution data can be derived as  $\pm \sqrt{\text{Error}_{\text{compression}}^2 + \text{Error}_{\text{calibration}}^2}$ , which is equal to  $\pm 0.04^\circ\text{C}$  for temperature and  $\pm 0.03 \text{ g kg}^{-1}$  for salinity. These accuracy estimates can now be used to quantify the error associated with low-resolution data of the MEOP database ( $\sim 85\%$  of the profiles). However, if more precision is needed relative to a specific depth or oceanic zone, we encourage the users to refer to the compression error profiles of Fig. 9 as well as to Table 2.

## 7. Summary and conclusions

In this paper, we took advantage of the new generation of data available at the sampling frequency of 0.5 Hz to improve the quality of CTD-SDRL data. We provided evidence that the temperature sensors are affected by a thermal mass error. A correction scheme was therefore developed to improve temperature estimates by simultaneously correcting conductivity and temperature. This correction builds upon Mensah et al. (2018), who only and directly corrected salinity. In a second step, we refined salinity estimates by removing salinity spiking and density inversions according to Barker and McDougall (2017). This two-step postprocessing correction was implemented for two datasets collected by Kerguelen SES: a continuous high-resolution dataset made of 7 tags (39 183 profiles) deployed from 2014 to 2018 and a low-resolution dataset made of 43 tags (14 762 profiles) deployed from 2011 to 2018. The continuous high-resolution dataset was used to test the robustness and efficiency of the procedure for high-resolution data by comparing upcast and downcast data, which significantly converged after application of the correction. The correction scheme was then validated for low-resolution data by comparing corrected high- and low-resolution profiles, which showed similar improvements. To date, correction and validation of the profiles is mainly done by comparison with regional atlases of historical data and

ship-based CTDs (Roquet et al. 2011), thus relying on external observations acquired at a different date and location, and containing their own measure bias. A major advantage of this method is that it does not rely on external data and can be independently implemented. In addition to improving the tags' data quality, updated accuracy estimates were derived. Dynamical biases were found to be negligible in front of calibration errors such that the accuracy of high-resolution data is estimated to be  $\pm 0.02^\circ\text{C}$  for temperature and  $\pm 0.03 \text{ g kg}^{-1}$  for salinity. For the first time, the compression error associated with the interpolation of low-resolution data was quantified and found to be  $\pm 3.2 \times 10^{-2}^\circ\text{C}$  for temperature and  $\pm 1.1 \times 10^{-2} \text{ g kg}^{-1}$  for salinity (Table 2). This implies that the accuracies of low-resolution data are  $\pm 0.04^\circ\text{C}$  for temperature and  $\pm 0.03 \text{ g kg}^{-1}$  for salinity (section 6c). This analysis is of prime importance for users of the MEOP database, as it will enable them to carefully quantify the error associated with the MEOP data and ultimately refine their analyses.

Both datasets used in this study are located in the Southern Ocean. This suggests that the TME coefficients derived in section 3 may not be optimal for datasets located in other areas, in particular in regions marked by stronger thermoclines. Hence, we encourage users to determine their own optimal coefficient in the areas of deployment following the same methodology as the one presented in section 3 whenever possible. Nevertheless, our results have shown that the TME parameters provide satisfactory results for the Southern Ocean, which is where most of the MEOP data are located. In addition, this method should yield similar results for the polar areas of the Northern Hemisphere that are characterized by similar temperature gradients and where most of the remaining MEOP data are located.

Another potential drawback of this method is that it removes all density inversions within the water column yet they may occur on scales of order 1–5 m as the result of physical instabilities such as gravitational or Kelvin–Helmholtz's ones (Kundu and Cohen 1990). This is particularly the case during winter when these instabilities are known to be more frequent (Haine and Marshall 1998) and will become a growing concern with the advent of continuous high-resolution tags capable of detecting such density inversions. To refine the correction, an option would be to use, when available, accelerometry sensors deployed on marine mammals in conjunction with CTD tags to detect the animal's head movements, speed, and direction variations. These motions recorded by the accelerometer, and often linked to the apex predator's foraging effort (Viviant et al. 2010),

may cause the water to flow in a reverse direction within the unpumped cell of the tag. This may in turn generate thermal mass and salinity spiking effects. Being able to discriminate density inversions resulting from the animal's behavior and physical processes is key to perfect the correction procedure. Incorporation of such biological data in the correction of biologged profiles in conjunction with sensor accuracy improvements appears as the next step forward to refine the quality and accuracy of animal tag oceanographic data.

In conclusion, we have presented a new postprocessing method that yields conclusive results for the improvement of CTD-SDRL data. This technique may also be useful for unpumped glider data. Given the recent technological advances in biologging, continuous high-resolution dataset are expected to become increasingly available such that the approaches proposed here should have increasing utility.

*Acknowledgments.* The present study is a contribution to the Observing System—Mammals as Samplers of the Ocean Environment (SO-MEMO) with funding and logistic support from CNES-TOSCA, IPEV, and CORIOLIS in situ ocean observation program. The authors wish to thank Paul Barker and Trevor McDougall for the use of their correction scheme. L.S. is supported by a CNES and LabexMer doctoral fellowship.

#### REFERENCES

- Barker, P. M., and T. J. McDougall, 2017: Stabilizing hydrographic profiles with minimal change to the water masses. *J. Atmos. Oceanic Technol.*, **34**, 1935–1945, <https://doi.org/10.1175/JTECH-D-16-0111.1>.
- Boehme, L., P. Lovell, M. Biuw, F. Roquet, J. Nicholson, S. E. Thorpe, M. P. Meredith, and M. Fedak, 2009: Animal-borne CTD-satellite relay data loggers for real-time oceanographic data collection. *Ocean Sci.*, **5**, 685–695, <https://doi.org/10.5194/os-5-685-2009>.
- Haine, T. W., and J. Marshall, 1998: Gravitational, symmetric, and baroclinic instability of the ocean mixed layer. *J. Phys. Oceanogr.*, **28**, 634–658, [https://doi.org/10.1175/1520-0485\(1998\)028<0634:GSABIO>2.0.CO;2](https://doi.org/10.1175/1520-0485(1998)028<0634:GSABIO>2.0.CO;2).
- Hindell, M. A., and M.-A. Lea, 1998: Heart rate, swimming speed, and estimated oxygen consumption of a free-ranging southern elephant seal. *Physiol. Biochem. Zool.*, **71**, 74–84, <https://doi.org/10.1086/515890>.
- Kim, Y. S., and A. H. Orsi, 2014: On the variability of Antarctic Circumpolar Current fronts inferred from 1992–2011 altimetry. *J. Phys. Oceanogr.*, **44**, 3054–3071, <https://doi.org/10.1175/JPO-D-13-0217.1>.
- Kundu, P., and L. Cohen, 1990: *Fluid Mechanics*. Academic Press, 638 pp.
- Liu, Y., R. H. Weisberg, and C. Lembke, 2015: Glider salinity correction for unpumped CTD sensors across a sharp thermocline. *Coastal Ocean Observing Systems*, Elsevier, 305–325.
- Lueck, R. G., 1990: Thermal inertia of conductivity cells: Theory. *J. Atmos. Oceanic Technol.*, **7**, 741–755, [https://doi.org/10.1175/1520-0426\(1990\)007<0741:TIOCCT>2.0.CO;2](https://doi.org/10.1175/1520-0426(1990)007<0741:TIOCCT>2.0.CO;2).
- , and J. J. Picklo, 1990: Thermal inertia of conductivity cells: Observations with a sea-bird cell. *J. Atmos. Oceanic Technol.*, **7**, 756–768, [https://doi.org/10.1175/1520-0426\(1990\)007<0756:TIOCCO>2.0.CO;2](https://doi.org/10.1175/1520-0426(1990)007<0756:TIOCCO>2.0.CO;2).
- Mensah, V., M. Le Menn, and Y. Morel, 2009: Thermal mass correction for the evaluation of salinity. *J. Atmos. Oceanic Technol.*, **26**, 665–672, <https://doi.org/10.1175/2008JTECHO612.1>.
- , F. Roquet, L. Siegelman-Charbit, B. Picard, E. Pauthenet, and C. Guinet, 2018: A correction for the thermal mass-induced errors of CTD tags mounted on marine mammals. *J. Atmos. Oceanic Technol.*, **35**, 1237–1252, <https://doi.org/10.1175/JTECH-D-17-0141.1>.
- Morison, J., R. Andersen, N. Larson, E. D'Asaro, and T. Boyd, 1994: The correction for thermal-lag effects in sea-bird CTD data. *J. Atmos. Oceanic Technol.*, **11**, 1151–1164, [https://doi.org/10.1175/1520-0426\(1994\)011<1151:TCFTLE>2.0.CO;2](https://doi.org/10.1175/1520-0426(1994)011<1151:TCFTLE>2.0.CO;2).
- Nakanowatari, T., and Coauthors, 2017: Hydrographic observations by instrumented marine mammals in the Sea of Okhotsk. *Polar Sci.*, **13**, 56–65, <https://doi.org/10.1016/j.polar.2017.06.001>.
- Roquet, F., J.-B. Charrassin, S. Marchand, L. Boehme, M. Fedak, G. Reverdin, and C. Guinet, 2011: Delayed-mode calibration of hydrographic data obtained from animal-borne satellite relay data loggers. *J. Atmos. Oceanic Technol.*, **28**, 787–801, <https://doi.org/10.1175/2010JTECHO801.1>.
- , and Coauthors, 2014: A southern Indian Ocean database of hydrographic profiles obtained with instrumented elephant seals. *Sci. Data*, **1**, 140028, <https://doi.org/10.1038/sdata.2014.28>.
- , and Coauthors, 2017: Ocean observations using tagged animals. *Oceanography*, **30** (2), 139, <https://doi.org/10.5670/oceanog.2017.235>.
- Treasure, A. M., and Coauthors, 2017: Marine mammals exploring the oceans pole to pole: A review of the MEOP consortium. *Oceanography*, **30** (2), 132–138, <https://doi.org/10.5670/oceanog.2017.234>.
- Viviant, M., A. W. Trites, D. A. Rosen, P. Monestiez, and C. Guinet, 2010: Prey capture attempts can be detected in Steller sea lions and other marine predators using accelerometers. *Polar Biol.*, **33**, 713–719, <https://doi.org/10.1007/s00300-009-0750-y>.

## 1.2 Satellite altimetry data

The Antarctic Circumpolar Current hosts an energetic field of mesoscale eddies that are routinely monitored from space. The Kerguelen area is representative of such a turbulent mesoscale eddy field (Figure 1.6). As elephant seals principally evolve within these eddy-rich regions (Figures 1.2 and 1.6), it is particularly relevant to use a combination of satellite and seal data in the Kerguelen area to study ageostrophic dynamics in the real ocean.

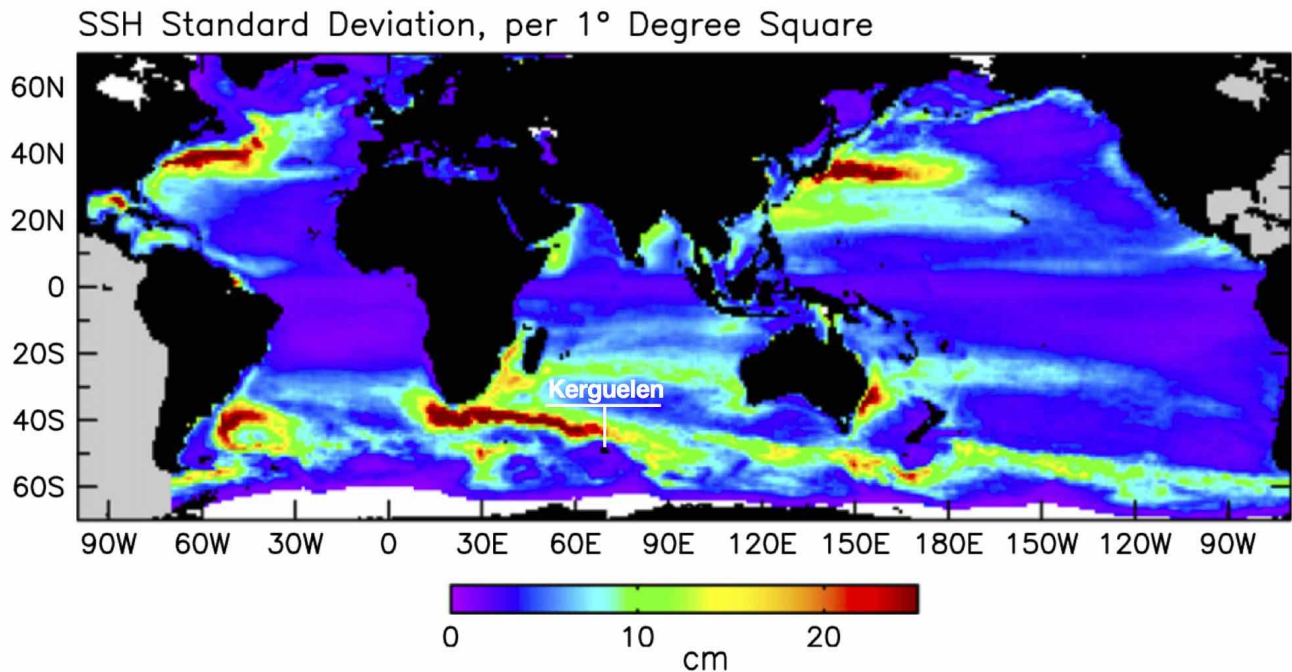


Figure 1.6: Map of the standard deviation of eddy Sea Surface Height (SSH) amplitude, from the 16-year period from October 1992 to December 2008, and for eddy lifetimes  $>16$  weeks. From Chelton et al. (2011).

### 1.2.1 Sea surface height

Satellites equipped with high-precision altimeters have been observing Sea Surface Height (SSH) across the globe, at spatial scales of 100 to more than 5,000 km, for the past twenty-five years (Klein et al., 2019). SSH observations obtained from these altimeters (Figure 1.7) have a resolution sufficient to resolve mesoscale eddies (100–300 km size), and as such, have led to a major breakthrough emphasizing the existence of a strongly energetic mesoscale turbulent eddy field in all the oceans (Chelton et al., 2011).

In this dissertation thesis, we use the delayed-time global ocean gridded L4 SSH and derived variables reprocessed product (1993–ongoing) distributed by Copernicus Marine Environment Monitoring Service (CMEMS, <http://marine.copernicus.eu/>). This product processes data from all altimeter missions: Jason-3, Sentinel-3A, HY-2A, Saral/AltiKa, Cryosat-2, Jason-2, Jason-1, T/P, ENVISAT, GFO, ERS1/2 (Figure 1.7). It provides a consistent and homogeneous product suitable for both near-real-time applications and offline studies. Multimission altimeter satellite gridded SSH and derived variables are computed with respect to a twenty-year mean. All the missions are homogenized with respect to a reference mission which is currently OSTM/Jason-2. The final horizontal effective resolution of this product is  $1/4^\circ$  (Figure 1.8) and the time resolution is daily.

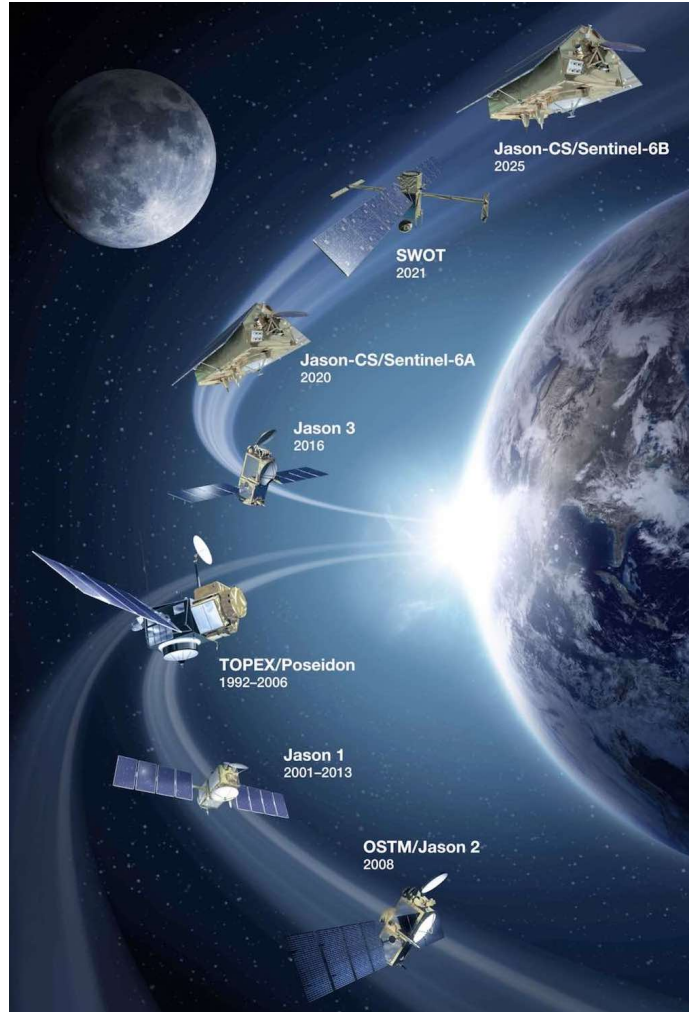


Figure 1.7: Artist’s concept of seven altimeters orbiting Earth: Jason-CS/Sentinel-6B, SWOT, Jason-CS/Sentinel-6A, Jason 3, TOPEX/Poseidon, Jason 1 and OSTM/Jason 2. From <https://swot.jpl.nasa.gov/>.

A thorough description of the processing method can be found in Rio et al. (2016). However, briefly, Sea Level Anomaly (SLA) is computed with an optimal and centered computation time window (6 weeks before and after the date). For delayed-time SLA, the system acquires and then synchronizes altimeter data; each mission is homogenized using the same models and corrections, and the best altimeter data is used. The multi-mission cross-calibration process removes any residual orbit error, as well as large scale biases and discrepancies between various data flows; all altimeter fields are interpolated at crossover locations and dates. After a repeat-track analysis, a mean profile, which is peculiar to each mission, or a Mean Sea Surface (MSS, when the orbit is non repetitive) is subtracted to com-

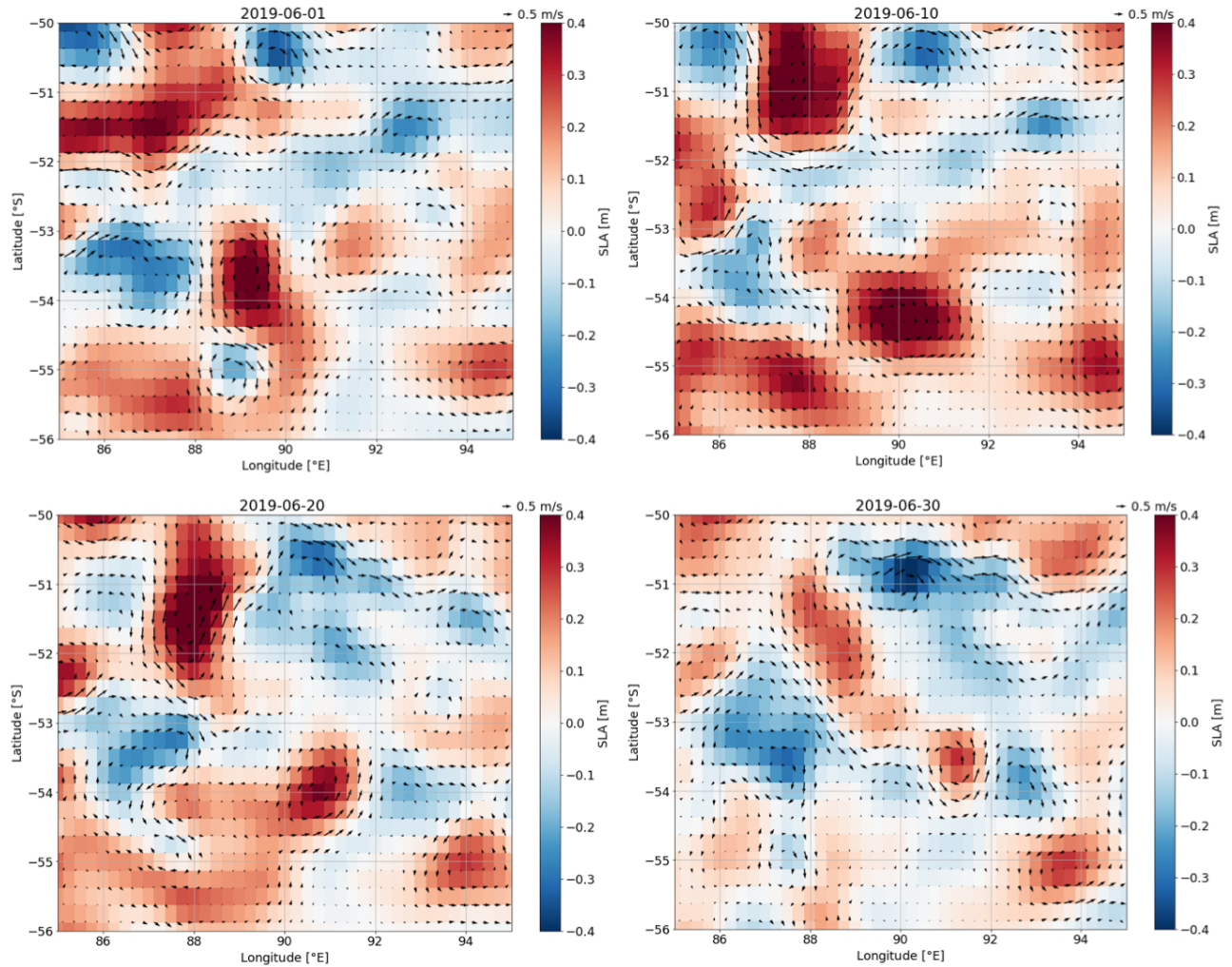


Figure 1.8: Evolution of Sea Level Anomaly (SLA) in the Kerguelen area from the global ocean gridded L4 SSH product distributed by CMEMS.

pute SLA. The MSS is available via the Aviso+ dissemination (<http://www.aviso.altimetry.fr/en/data/products/auxiliary-products/mss.html>). Data are then cross validated, filtered from residual noise and small scale signals, and then sub-sampled. Finally, an optimal interpolation is made merging all the flying satellites in order to compute gridded SLA. The Absolute Dynamic Topography (ADT, or equivalently SSH) is then computed as follows:  $ADT = SLA + MDT$  where MDT is the Mean Dynamic Topography distributed by Aviso+ (<http://www.aviso.altimetry.fr/en/data/products/auxiliary-products/mdt.html>). Geostrophic currents (black arrows in Figure 1.8) are derived from SLA using the geostrophic approximation (Vallis, 2017).

The mesoscale eddy field of the Kerguelen area considerably evolves over periods of a few days, as can be

seen in Figure 1.8. Indeed, within ten days, i.e., the time between each snapshot in Figure 1.8, mesoscale eddies have either merged, vanished or changed shape due to the strong deformation field generated by their co-interaction. Thus, in this dissertation thesis, we use daily snapshots of SLA in order to retrieve the optimal time evolution of the mesoscale turbulence (Ubelmann et al., 2015). Note that, within 10 days, elephant seals travel  $\sim 700$  km, which corresponds roughly to the domain-size of Figure 1.8. Thus, elephant seals are able to capture the evolution of mesoscale eddies, with no synopticity issues. While satellite data are sufficient to resolve the mesoscale activity on the horizontal plane, seal data give access to smaller-scales along a vertical section. As such, these two independent datasets contain different but complementary information that can be combined to retrieve a synoptic 3-D view of the deformation field. This information is used to study ocean scale interactions, and more specifically the formation of submesoscale fronts generated by the mesoscale background eddy field.

### 1.2.2 Finite-size Lyapunov exponent

Finite-Size Lyapunov Exponent (FSLE) are used as a proxy for the strain rate generated by mesoscale eddies. Unlike the Okubo-Weiss criterion, FSLE takes into account the rotation of the strain tensor axis (Lapeyre et al., 1999). FSLE corresponds to the Lagrangian integration of the strain field over a given length scale and allows to characterise both the direction and intensity of the strain field. An empirical relation between FSLE and the strain field has been established by Waugh and Abraham (2008) (Figure 1.9).

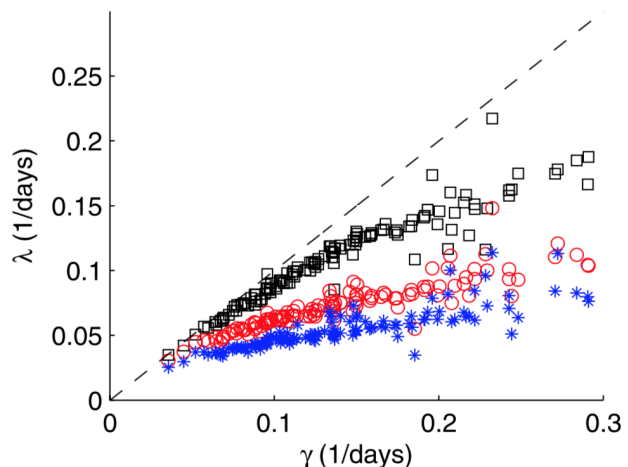


Figure 1.9: Variation of the spatial-mean finite time Lyapunov exponent  $\lambda$  with spatial-mean strain rate  $\gamma$  for several different  $20^\circ$  by  $20^\circ$  regions in different oceans, for 5 (black), 10 (red) and 20 (blue) days of integration times. From Waugh and Abraham (2008).

More precisely, FSLE measures the separation rate of the trajectories of close initial particles (1–10km). As such, it quantifies dispersion processes (Haza et al., 2012) and maps coherent structures (d’Ovidio

et al., 2004). FSLE is defined as:

$$\lambda(\delta_0, \delta_f) = \frac{1}{\tau} \log\left(\frac{\delta_f}{\delta_0}\right), \quad (1)$$

where  $\delta_0$  and  $\delta_f$  are the initial and final separation distances and  $\tau$  the first time at which a separation  $\delta_f$  is reached. FSLE has the dimension of  $\text{time}^{-1}$ . FSLE define directions where stretching or compressing processes are dominant, by providing exponential rates of deformation of water parcels. When computed backward in time, they identify parcels that have undergone strong stretching, which typically occurs along fronts and at the periphery of eddies (Figure 1.10).

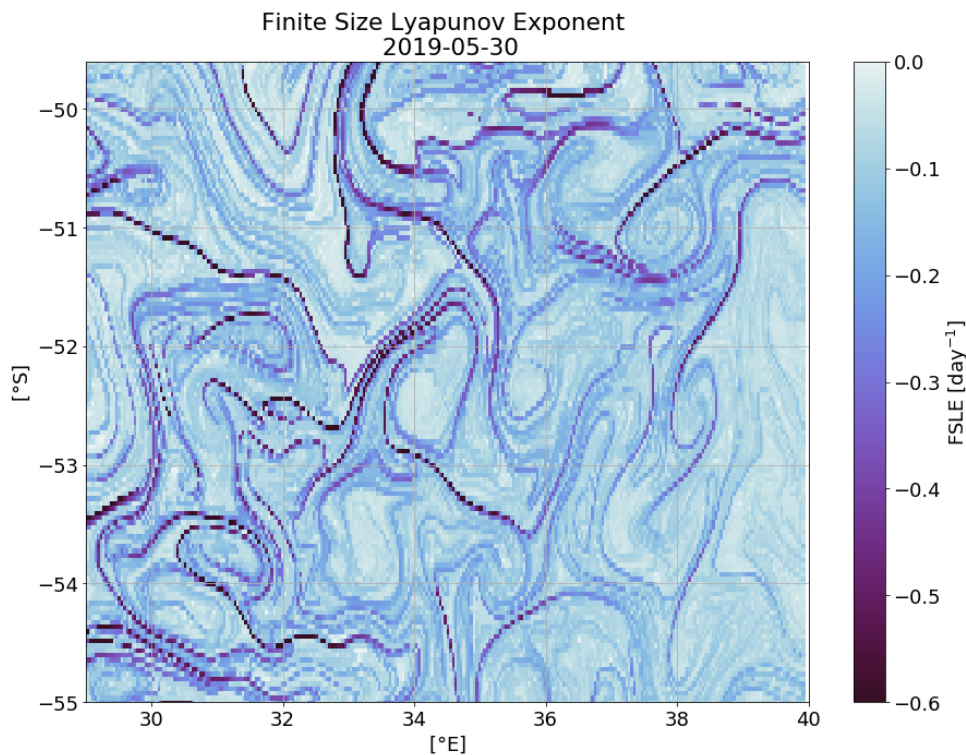


Figure 1.10: Snapshot of backward in time Finite-Size Lyapunov Exponent (FSLE) on 2019-05-30 in the Antarctic Circumpolar Current, computed from satellite altimetry data and distributed by AVISO.

When computed forward in time, they identify parcels that have undergone strong compression. The intersections of stretching and compressing lines identify Lagrangian hyperbolic points leading to strong filamentation of tracers along the stretching direction following an exponential growth rate. Particles spread while moving toward hyperbolic points along repelling ridges, whereas they aggregate while moving away from hyperbolic points along attracting ridges (Lehahn et al., 2007; Haller and Sapsis, 2011). Areas surrounding hyperbolic points are particularly prone to frontogenesis and chaotic advection. That is, in between co-rotating mesoscale eddies, where mesoscale density gradients are stirred by the deformation field yielding the production of strong density gradients at submesoscale.

### 1.3 High-resolution realistic numerical simulation

A numerical simulation, the so-called LLC4320, enabled by NASA Advanced Supercomputing Division, is used to investigate ocean dynamics down to the submesoscale. The LLC4320 simulation is based on a global, full-depth ocean and sea ice configuration of the Massachusetts Institute of Technology general circulation model (MITgcm) (Marshall et al., 1997; Hill et al., 2007) and uses a Latitude–Longitude–polar Cap (LLC) grid (Forget et al., 2015). The MITgcm was spun up in a hierarchy of increasing horizontal resolutions with 90 vertical levels (details in Table 1). The simulation analyzed here is the highest resolution, the LLC4320 at  $1/48^\circ$  (0.75 km near Antarctica, 2.3 km at the equator, and 1 km in the Arctic Ocean), with a time step of 25 s. The prognostic variables are saved as instantaneous snapshots at hourly intervals. Control files and details of the high-resolution LLC model setups and forcing files are available at [http://mitgcm.org/viewvc/MITgcm/MITgcm\\_contrib/llc\\_hires](http://mitgcm.org/viewvc/MITgcm/MITgcm_contrib/llc_hires). This simulation uses primitive equations and resolves mesoscale eddies, internal tides, and other hydrostatic processes at scales as small as about 10 km. As an illustration, an instantaneous snapshot of surface current speed from the simulation is presented in Figure 1.11, where numerous mesoscale eddies can be seen.

Table 1: Details of the LLC spin-up hierarchy adapted from Rocha et al. (2016a). In this dissertation thesis, two subsets of the LLC4320 are analyzed (Figure 1.11).

Simulation	Resolution [ $^\circ$ ]	Time step [s]	Period	Tides
ECCO2	1/6	1,200	January 2009 – December 2011	No
LLC1080	1/12	90	January 2010 – July 2012	No
LLC2160	1/24	45	January 2011 – April 2013	Yes
LLC4320	1/48	25	September 2011 – November 2012	Yes

Surface fluxes are from the  $0.14^\circ$  European Centre for Medium-range Weather Forecasting (ECMWF) atmospheric operational model analysis, starting in 2011. The surface fields include 10-m wind velocity, 2-m air temperature and humidity, downwelling long and shortwave radiation, and atmospheric pressure load. These fields are converted to surface fluxes using the bulk formulae of Large and Yeager (2004) and the dynamic/thermodynamic sea ice model of Losch et al. (2010). Thanks to this prescribed reanalysis of atmospheric state and the fact that the model’s global SST distribution lies in a realistic range, LLC4320’s air–sea fluxes are of comparable magnitude to climatological’s ones (Large and Yeager, 2009). The model also includes tidal forcing for the 16 most significant components that are applied as additional atmospheric pressure forcing (Chaudhuri et al., 2013). Vertical mixing is parameterized based



on the critical value of Richardson number and is implemented using the K-Profile Parameterization (KPP) scheme (Large et al., 1994) that has been extensively used and evaluated in ocean modeling studies (Large et al., 1997; Fernández-Castro et al., 2014).

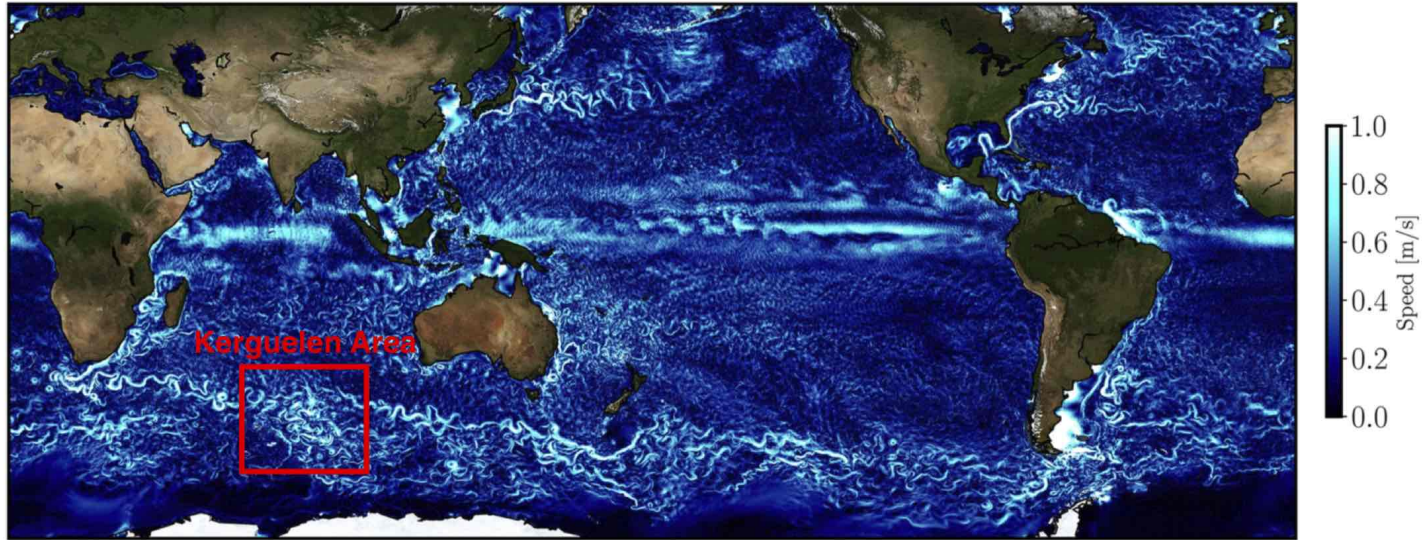


Figure 1.11: Snapshot of surface current speed from LLC4320. The Kerguelen region (red rectangle) is considered in this dissertation. Adapted from Klein et al. (2019).

Horizontal wavenumber spectra suggest that the effective resolution of LLC4320 is about 10 km in terms of wavelength (Rocha et al., 2016b). The LLC4320 has also been evaluated and validated via the comparison with *in situ* observations of kinetic energy at different wavelengths and frequencies (Rocha et al., 2016b,a).

This dissertation focuses on ageostrophic dynamics and, hence, on submesoscales in a subset of the LLC4320 in the Kerguelen area (red rectangle in Figure 1.11). The current integration time of LLC4320 is able to reach the equilibrium state for submesoscale dynamics because of their short timescales ( $< 1$  week). Note that while the simulation does not reach the equilibrium state for the larger-scale ocean dynamics in the global ocean (Lévy et al., 2010), which is beyond the current capability of the most powerful computers, it should resolve, to a large extent, some key sources of submesoscale generation, such as mixed layer instabilities (Boccaletti et al., 2007; Callies et al., 2016; Callies and Ferrari, 2013; Sasaki et al., 2014; Fox-Kemper et al., 2008), wind-front interactions (Thomas and Ferrari, 2008), and strain-induced frontogenesis (McWilliams, 2016; Capet et al., 2008).

## 2 Dynamical concepts on meso- and submesoscale turbulence

The purpose of this chapter is to introduce some key theoretical concepts used to discriminate quasi-geostrophic dynamics from ageostrophic dynamics, and upon which the results of this dissertation are based. Section 2.1 introduces several key non-dimensional numbers, section 2.2 presents the Ertel potential vorticity that is used throughout this dissertation to characterize meso- and submesoscale dynamics. Section 2.3 discusses the dynamics of the quasi-geostrophic regime and section 2.4 the dynamics of the ageostrophic regime. These dynamical concepts are key to understand the results presented in Chapters 3–5, and in particular the presence of energetic submesoscale fronts in the ocean interior, associated with large vertical velocities and strong upward vertical heat and buoyancy fluxes. Note that this chapter is intended to serve as an in-depth glossary of the physical concepts used throughout this dissertation. It can be read independently from Chapters 3–5, which are self-sufficient.

### 2.1 Key non-dimensional numbers for a stratified fluid in rotation

The ocean is essentially a shallow layer of fluid on a sphere, whose total mean depth of  $\sim 5000$  m is much smaller than its horizontal basin scale extent of  $\sim 6000$  km, and whose motions are strongly influenced by two effects: rotation, via the Coriolis force, and stratification. The latter meaning that the mean vertical gradient of density is often large compared to the horizontal one. This dissertation focuses on the interactions between mesoscale eddies and submesoscale structures at mid- to high-latitudes. Such meso- and submesoscale turbulence can be characterized by four key non-dimensional numbers, that have distinct meanings and allow to non-dimensionalise the equations of momentum and density for a Boussinesq and hydrostatic flow. These non-dimensional numbers are:

- the Reynolds number  $\text{Re} \equiv \frac{UL}{\nu}$ , where  $U$  is the velocity scale,  $L$  the horizontal length scale, and  $\nu$  the viscosity.  $\text{Re}$  is the ratio of the advective terms to the viscous terms present in the momentum equations. A large  $\text{Re}$  emphasizes the turbulent character of a flow field as the advective terms are larger than the viscous ones. Typically,  $\text{Re} \gg 10\,000$  for the oceanic scales considered in this dissertation, i.e., from 1 to 6000 km (Gill, 1982).
- the Rossby number  $\text{Ro} \equiv \frac{U}{fL}$  is the ratio of the advective terms to the Coriolis terms in the momentum equations. Altimeter data emphasize that mesoscale eddies, with a size of 100–300 km, are characterized by  $\text{Ro} \leq 0.05$  (Chelton et al., 2011). For these low  $\text{Ro}$ , the flow is in quasi-

geostrophic (QG) equilibrium, i.e., it is at leading order in geostrophic balance; a balance between pressure and Coriolis forces (Pedlosky, 2013). This indicates a dominance of geostrophic motions,  $\mathbf{u}_g$ , over ageostrophic motions,  $\mathbf{u}_a$ , since motions,  $\mathbf{u}$ , can be approximated by  $\mathbf{u} \sim \mathbf{u}_g + \text{Ro } \mathbf{u}_a$  (Pedlosky, 2013). Since geostrophic motions are non-divergent, the resulting QG regime is weakly divergent and it is adequately described by a set of equations presented in section 2.3. Furthermore, recent studies indicate that submesoscale structures, with a size  $\leq 50$  km, can be associated with Ro of  $O(1)$ , indicating that ageostrophic motions have the same order of magnitude as geostrophic motions at these scales (McWilliams, 2016). This ageostrophic regime is adequately described by a set of equations that differs from the QG equations, and is presented in section 2.4. As this regime significantly departs from geostrophic, it involves large vertical velocities. In this dissertation, typically Ro are of  $\sim 0.05$  for QG flows and  $\sim 0.3\text{--}0.5$  for ageostrophic flows (Molemaker et al., 2010).

- the Burger number  $\text{Bu} \equiv \frac{N^2 H^2}{f^2 L^2}$ , where  $H$  is the depth scale of the mesoscale–submesoscale structures and  $N^2 = \frac{\partial b}{\partial z}$  is the squared Brunt–Väisälä frequency, which characterizes the vertical stratification, with  $b$  is the buoyancy. Typically, Bu is close to one for meso- and submesoscales, indicating that the aspect ratio between the horizontal and vertical scales is similar for meso- and submesoscales (Thomas et al., 2008).
- the Richardson number  $\text{Ri} \equiv \frac{N^2 f^2}{(\nabla_H b)^2}$ , where  $\nabla_H$  is the horizontal gradient operator. Ri can be interpreted as the steepness of the isopycnal’s slope:  $\text{Ri} \sim \frac{f^2}{N^2} \left( \frac{\partial b / \partial z}{\partial b / \partial x} \right)_{b=\text{cst}}^2$  in the x–direction. For  $\text{Bu} \sim 1$ ,  $\text{Ro} = \text{Ri}^{-1/2}$  (Molemaker et al., 2005). As such,  $\text{Ri} \gg 1$ , or equivalently  $\text{Ro} \ll 1$ , correspond to the QG regime, characterized by a small isopycnal’s slope, whereas Ri and Ro of  $O(1)$  correspond to the ageostrophic regime, characterized by a steep isopycnal’s slope and therefore strong lateral gradients of buoyancy at submesoscale.

Let us now introduce the term "Balanced Motions" (BMs) that will be extensively used throughout this dissertation. Balanced motions are characterized by  $\text{Ro} \leq 1$  and exclude internal gravity waves (IGWs), whose frequencies are larger than the Coriolis frequency. Both classes of motions, i.e., balanced motions and IGWs, are governed by the primitive equations, i.e., the Boussinesq equations in hydrostatic balance (the non-hydrostatic regime is not considered in this dissertation). Given  $\text{Ro} \leq 1$ , the divergence equation becomes a diagnostic equation (Gent and McWilliams, 1983), implying that balanced motions

do not propagate, whereas IGWs do (Gent and McWilliams, 1983). As a result, the dynamics of balanced motions and IGWs greatly differ. This chapter exclusively considers the dynamics of balanced motions, which include mesoscale eddies and submesoscale structures.

## 2.2 Ertel potential vorticity

In this section, we introduce a key physical quantity, the Ertel Potential Vorticity (PV), that can be considered as the cornerstone for the study of a stratified fluid in rotation, such as the ocean. The Ertel PV is used to infer the properties of meso- and submesoscale turbulence (Deremble et al., 2014), from the surface of the ocean down to depths of  $\sim 1\,000$  m, i.e., well below the mixed layer (see Chapter 4).

The equation governing the Ertel PV evolution can be derived from the primitive equations (PE), which describe the properties of a Boussinesq flow in hydrostatic balance (Pedlosky, 2013). Assuming an  $f$ -plane for the sake of simplicity, i.e.,  $f = \text{cst}$ , these PE read:

$$\frac{D\mathbf{u}}{Dt} + f \mathbf{k} \times \mathbf{u} = -\frac{1}{\rho_0} \nabla_H p, \quad (2)$$

$$\frac{Db}{Dt} = 0, \quad (3)$$

$$\nabla_H \cdot \mathbf{u} + \partial_z w = 0, \quad (4)$$

$$b = \partial_z P, \quad (5)$$

$$\frac{D}{Dt} = \partial_t + \mathbf{u} \cdot \nabla_H + w \partial_z, \quad (6)$$

where  $\mathbf{u}$  is the horizontal velocity vector,  $p$  is pressure,  $b$  is buoyancy and  $\mathbf{k}$  is the vertical unit vector.

For this set of equations and neglecting the spatial derivatives of  $w$ , the Ertel PV is:

$$q = (f \mathbf{k} + \nabla \times \mathbf{u}) \cdot \nabla b, \quad (7)$$

where  $\nabla \times \mathbf{u}$  is the three-dimensional curl, with  $\nabla$  the 3D gradient operator, applied to the horizontal velocity vector  $\mathbf{u}$ , i.e., the 3-D vorticity vector associated with the horizontal velocity field (Pedlosky, 2013). A key property of the Ertel PV, which is derived from equations (2)–(6), is that it is conserved

along a Lagrangian trajectory in the absence of sources or sinks (see Haynes and McIntyre (1990) for a derivation), such that:

$$\frac{Dq}{Dt} = 0. \quad (8)$$

The conservation of Ertel PV places a strong constraint on the flow field and imparts additional information for the study of meso- and submesoscale turbulence. Indeed, the dynamics of a given balanced flow can be entirely retrieved through the inversion of this conserved scalar (Hoskins et al., 1985; Davis, 1992). Another major consequence, particularly relevant for this dissertation work, is that Ertel PV, as any other tracer conserved on a Lagrangian trajectory, experiences a direct cascade in which numerous submesoscale filaments of Ertel PV are generated by co-interacting mesoscale eddies (Pedlosky, 2013). As such, it is possible to discriminate meso- and submesoscale dynamics from the analysis of the Ertel PV field.

Indeed, the Ertel PV can be written as:

$$q = (f + \zeta) \partial_z b + (\mathbf{k} \times \partial_z \mathbf{u}) \cdot \nabla_H b, \quad (9)$$

with  $\zeta$  the vertical component of the relative vorticity defined as  $\zeta = \partial_x v - \partial_y u$ . From equation (9), the Ertel PV can be decomposed into three main components:  $(f + \zeta) \partial_z b$ ,  $-\partial_z v \partial_x b$  and  $\partial_z u \partial_y b$ . Each component can be interpreted as a quasi-equilibrium between vortex stretching and vorticity in the Lagrangian framework. This is illustrated in Figure 2.1 for the first component, i.e., for the vertical vortex stretching,  $\partial_z b$ , and the vertical absolute vorticity,  $f + \zeta$ . Similarly, the second and third components,  $-\partial_z v \partial_x b$  and  $\partial_z u \partial_y b$ , can be interpreted as the relationship between horizontal stretching and horizontal vorticity in the  $x$  and  $y$ -direction, respectively. They can also be understood with the schematic of Figure 2.1 but instead of being in the  $z$ -plane, the competition between stretching and vorticity is now in the  $x$  and  $y$ -plane, respectively. For simplicity's sake, the last two components are combined into one, i.e.,  $-\partial_z v \partial_x b + \partial_z u \partial_y b$ , in this dissertation.

Following Thomas et al. (2013), the Ertel PV can also be expressed in terms of the non-dimensional

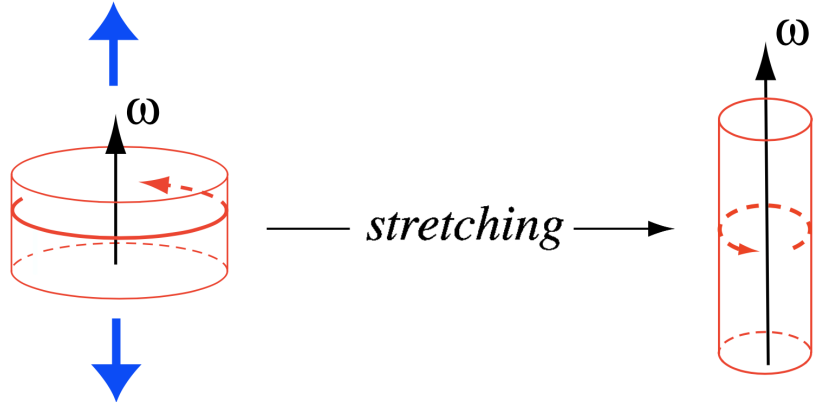


Figure 2.1: Quasi-equilibrium between vertical vortex stretching and absolute vorticity  $\omega = f + \zeta$ . Because of the conservation of the volume of fluid and of the angular momentum, vorticity is amplified in the direction of the stretching. From Vallis (2017).

Rossby number<sup>1</sup>,  $Ro \equiv \zeta/f$ , and Richardson number,  $Ri \equiv f^2 N^2 / (\nabla b)^2$ , as:

$$q \approx f N^2 (1 + Ro - Ri^{-1}). \quad (10)$$

Using  $|Ro| = Ri^{-1/2}$  (Molemaker et al., 2010),  $q$  becomes:

$$q \approx f N^2 (1 + Ro - Ro^2), \quad (11)$$

indicating that in the QG regime the terms associated with the horizontal buoyancy gradients can be neglected.

The Ertel PV field diagnosed from the LLC4320 simulation is presented in Figure 2.2. It allows to discriminate meso- and submesoscale structures. In the Southern Hemisphere ( $f < 0$ ), the Ertel PV is principally negative when it is dominated by its first component because  $\partial_z b$  is mostly positive and  $\zeta/f > -1$ , as can be seen in Figure 2.2a,b,d. Furthermore, numerous submesoscale structures related to lateral gradients of buoyancy can be seen in Figure 2.2 c. The contribution of the strongest submesoscale features (panel c) to the Ertel PV is actually of the same order of magnitude as the contribution of the first component (panel b). From equations (10) and (11), it indicates that submesoscales are characterized by large  $Ro$ , implying a departure from the QG regime and the presence of an ageostrophic regime. The comparison between panels b and c further highlights that these submesoscale buoyancy

<sup>1</sup>from now on, we use  $Ro \equiv \zeta/f$ , such that  $Ro$  can be positive or negative.

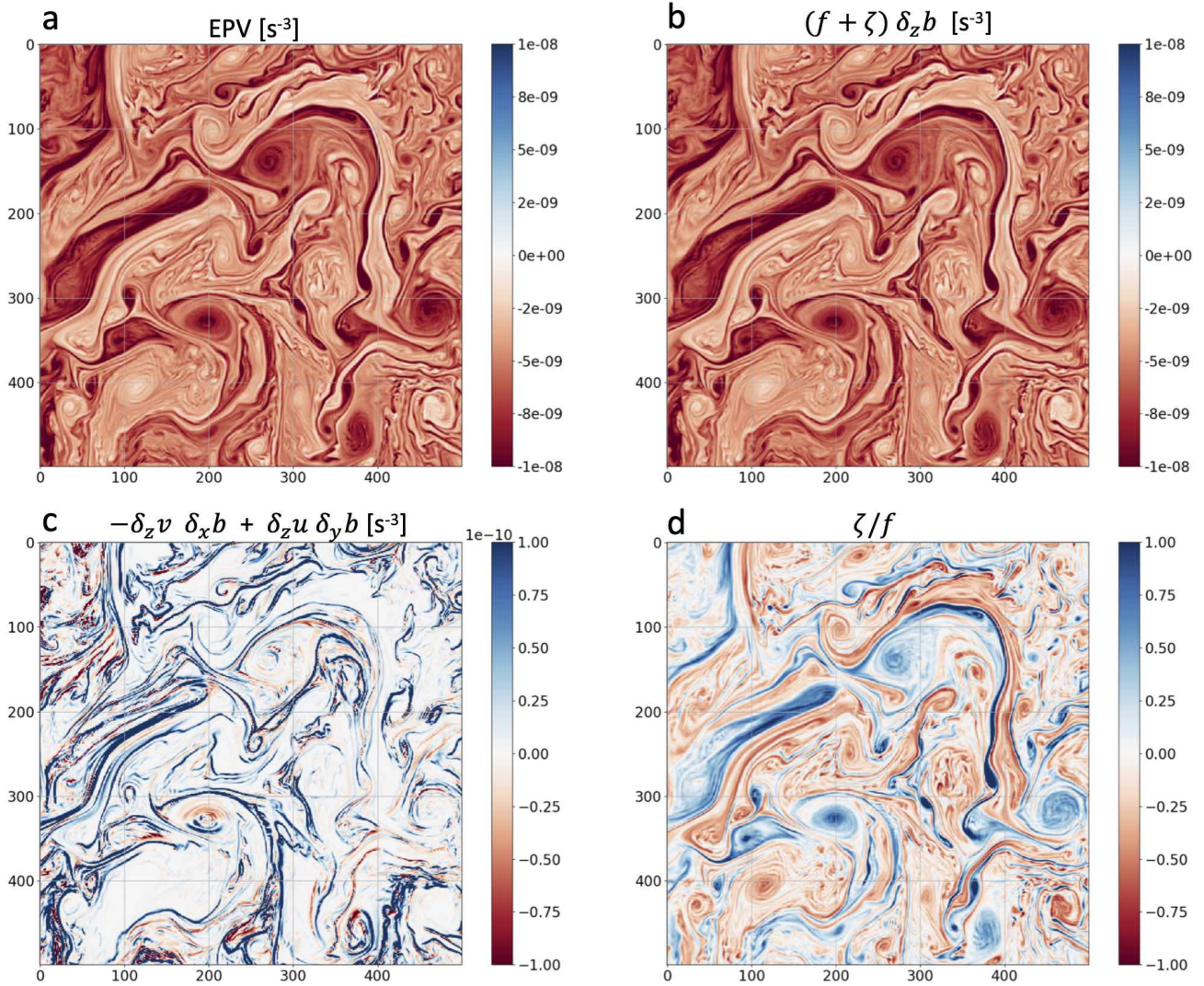


Figure 2.2: Decomposition of a snapshot of Ertel PV according to equation (9) at 39 m in the Kerguelen area (Southern Hemisphere, see Figure 1.11) on 2012-12-202 02:00:00 UTC, from the LLC4320 simulation at  $1/48^\circ$  ( $\sim 1.7$  km horizontal resolution in the Kerguelen area). The  $x$  and  $y$ -axes are shown in model grid points. Note the different colorbar scale in panels a–b and c.

gradients are mostly filamentary structures located around and in-between mesoscale eddies. As such, these submesoscale structures act as dynamical barriers encircling mesoscale eddies. These dynamical barriers prevent Lagrangian particles to cross strong gradients of Ertel PV, therefore trapping fluid parcels within eddies (Mariotti et al., 1994).

Equation (10) indicates that when the first and second component of the Ertel PV are of comparable magnitude,  $Ri$  is small, implying a steep isopycnal's slope. In this case, the Ertel PV exhibits thin vertical structures on the vertical, as can be seen in the upper 200 m of the water column, especially

when the ML is shallow, such as in the beginning of fall as well as during spring- and summertime (day 20–60 and 270–350 in Figure 2.3 for instance). These characteristic of the Ertel PV are extensively used in Chapter 4, in both physical and spectral space, to characterize the respective contribution of meso- and submesoscale dynamics in the ocean interior.

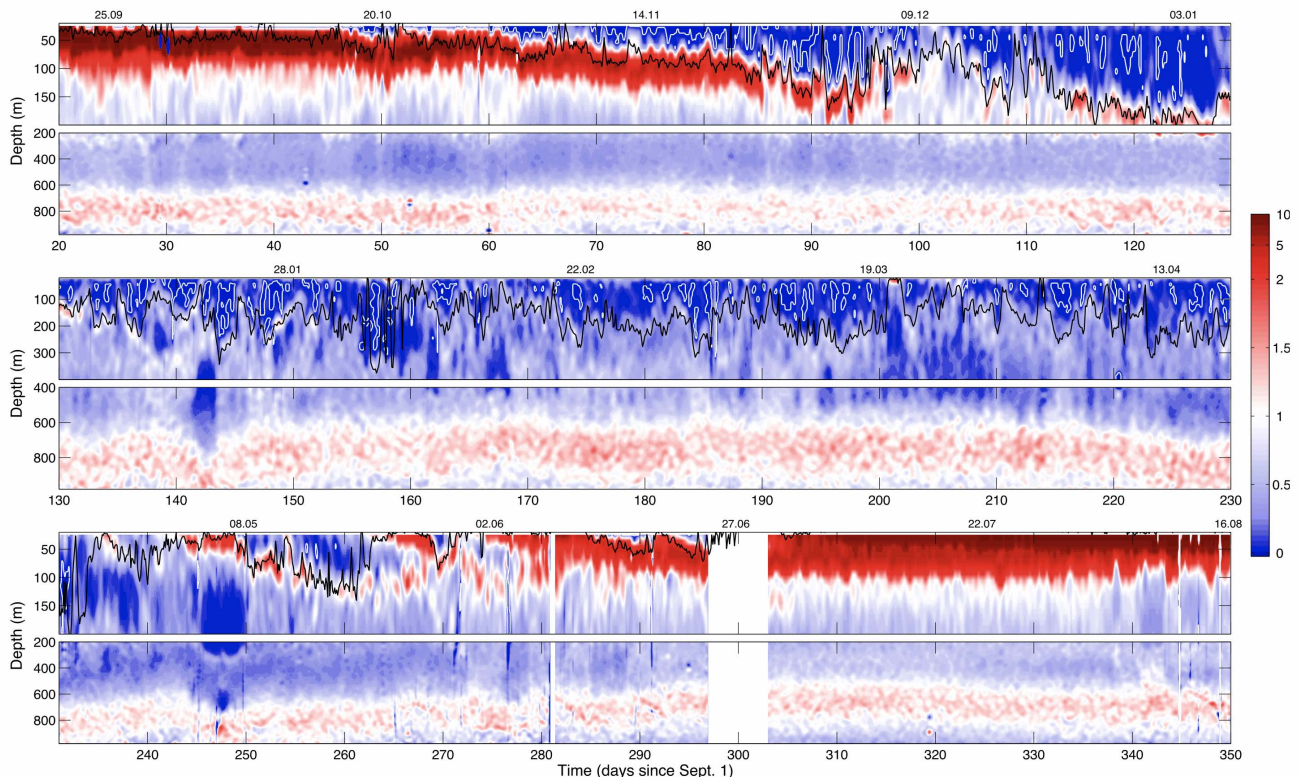


Figure 2.3: Year-long time series of Ertel PV [ $10^{-9} \text{ s}^{-3}$ ], calculated from glider data in the subtropical northeast Atlantic. The time series is divided into (top) fall, (middle) winter and (bottom) spring–summer periods; calendar dates (dd.mm) are provided along the top of the panels. The white contour indicates Ertel PV = 0, while the black contour is the mixed layer depth. From Thompson et al. (2016).

### 2.3 Quasi-geostrophic dynamics ( $\text{Ro} \ll 1$ and $\text{Ri} \gg 1$ )

Mesoscale eddies, associated with  $\text{Ro} \ll 1$  and  $\text{Ri} \gg 1$ , are at leading order in geostrophic balance: a balance between Coriolis and horizontal pressure forces. As such, they can be characterized by a streamfunction  $\psi(x, y)$  (Figure 2.4), from which horizontal motions can be retrieved via  $\mathbf{u}_g = \mathbf{k} \times \nabla \psi$ , with  $\mathbf{u}_g$  the geostrophic horizontal velocity vector. SSH, introduced in section 1.2, can be considered as a streamfunction at the ocean surface. Consequently, horizontal motions  $\mathbf{u}_g$  and the KE associated with mesoscale eddies can be retrieved via the first order spatial derivatives of  $\psi$ . However, mesoscale eddies are far from stationary; they evolve quickly, within a few days (Figure 1.8). In order to retrieve the time



evolution of the mesoscale eddy field, one needs to know the Lagrangian acceleration of the flow field, i.e.,  $d_g \mathbf{u}_g / dt$ , with  $d_g / dt = \partial / \partial t + \mathbf{u}_g \cdot \nabla_H$  (see Hua et al. (1998) and Muraki et al. (1999) for a derivation).

In the QG regime, any given variable can be decomposed in a Taylor series where only the first order terms are kept. For horizontal motions, this decomposition yields:

$$\mathbf{u} \sim \mathbf{u}_g + \text{Ro } \mathbf{u}_a,$$

with  $\mathbf{u}_g$  ( $\mathbf{u}_a$ ) the (a)geostrophic part of the flow. The QG equations can be derived from the primitive equations (2) to (6) using a similar Taylor series decomposition, where advection by ageostrophic motions  $\mathbf{u}_a$  is neglected. In addition, since Ri is large in the QG regime, the vertical advection term in the buoyancy equation,  $w b_z$ , can be replaced by  $w \bar{N}^2$ , with  $\bar{N}^2 = \bar{b}_z$  and  $\bar{b}$  the buoyancy averaged over the domain. In the QG framework, the Ertel PV is replaced by the QG PV, which includes only the first component of the Ertel PV, and the Ertel PV equation is solely advected by geostrophic motions. In summary, the QG equations differ from the PE ones as the advection by ageostrophic motions  $\mathbf{u}_a$  is neglected. As these ageostrophic motions are weak and geostrophic motions are non-divergent, the flow is weakly divergent in a QG regime. However, a question that arises concerns the connection between the production of submesoscale structures, that are not necessarily in geostrophic balance, within a mesoscale eddy field. This is explored in the QG regime in the following section.

### 2.3.1 Production of submesoscales by mesoscale eddies

The production of submesoscale features embedded within a mesoscale eddy field can be understood by analyzing the advection of a tracer by a geostrophic flow in the QG regime. Let us consider a tracer  $c$  that obeys the conservation equation:

$$\frac{d_g c}{dt} = 0. \tag{12}$$

Its gradient will obey:

$$\frac{d_g \nabla c}{dt} = -\mathbf{A} \nabla c, \tag{13}$$

where  $\mathbf{A}$  is the velocity gradient tensor, that can be written as:

$$\mathbf{A} \equiv \frac{1}{2} \begin{pmatrix} \sigma_n & \sigma_s + \zeta \\ \sigma_s - \zeta & -\sigma_n \end{pmatrix} \quad (14)$$

with  $\zeta = \partial_x v_g - \partial_y u_g$  the relative vorticity,  $\sigma_n = \partial_x u_g - \partial_y v_g$  the normal strain rate, and  $\sigma_s = \partial_x v_g + \partial_y u_g$  the shear strain rate (Okubo, 1970). Note that  $\sigma_n$  can be recovered from  $\sigma_s$  by a rotation of the axes of  $\pi/4$ , and vice versa.

From equation (13), one can see that the production of tracer gradients depends on the eigenvalues of  $\mathbf{A}$ . A commonly used criterion to infer the production of tracer gradients is the Okubo-Weiss (OW) quantity  $\lambda$ , derived by Okubo (1970) and Weiss (1991, 1981).  $\lambda$  is the squared eigenvalues of  $\mathbf{A}$ :

$$\lambda = \frac{1}{4}(\sigma_n^2 + \sigma_s^2 - \zeta^2). \quad (15)$$

$\lambda$  is used to partition the fluid into elliptic regions dominated by  $\zeta$ , and hyperbolic regions dominated by  $\sigma_n$  and  $\sigma_s$  (Figure 2.4). Under the assumption that the velocity gradient is slowly varying along a Lagrangian trajectory, the behavior of the tracer gradient can be determined by  $\lambda$ : tracer gradients do not grow in vortex cores where  $\lambda < 0$  since the eigenvalues of  $\mathbf{A}$  are purely imaginary. In this case, the gradient vector experiences a simple rotation. On the other hand, in strain-dominated areas where  $\lambda > 0$ , the eigenvalues of  $\mathbf{A}$  are real and tracer gradients exponentially grow. Thus, strain-dominated areas are particularly

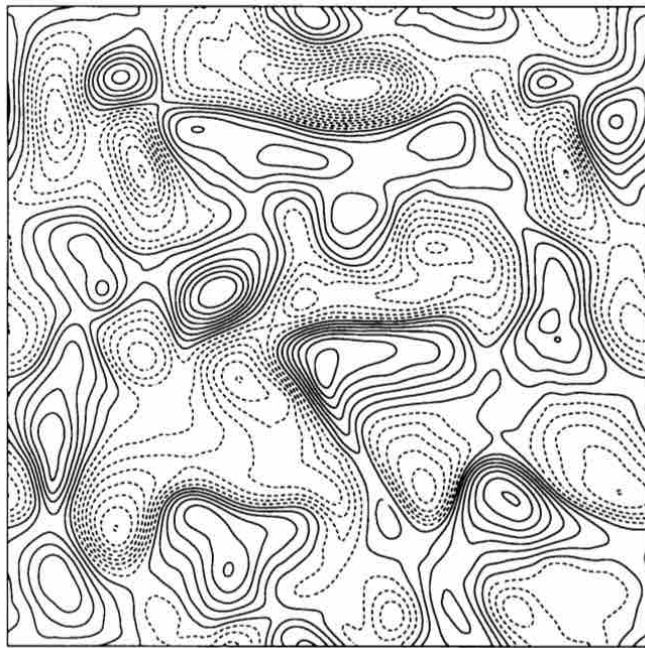


Figure 2.4: Field of geostrophic streamfunction  $\psi$ . From Hua et al. (1998).

prone to the formation of submesoscale fronts. These mechanisms are further detailed in many insightful studies (Gent and McWilliams, 1983; Basdevant and Philipovitch, 1994; Hua et al., 1998; Muraki et al.,

1999; Lapeyre et al., 1999).

Following Hua and Klein (1998), the OW quantity can also be written as:

$$\lambda = -J_{xy}(\partial_x\psi, \partial_y\psi). \quad (16)$$

Relation (16) indicates that the OW quantity, and therefore the production of strong tracer gradients, principally depends on the curvature of the stream function associated with the geostrophic flow. This remark points to the strong potential of future spatial altimeter missions, such as the upcoming NASA-CNES Surface Water Ocean Topography (SWOT) satellite mission, that will resolve the curvature of the SSH field, i.e., the second order derivatives of the surface streamfunction  $\psi$ , thanks for a ten-times improved spatial resolution compared to conventional altimeters, in addition to a large swath.

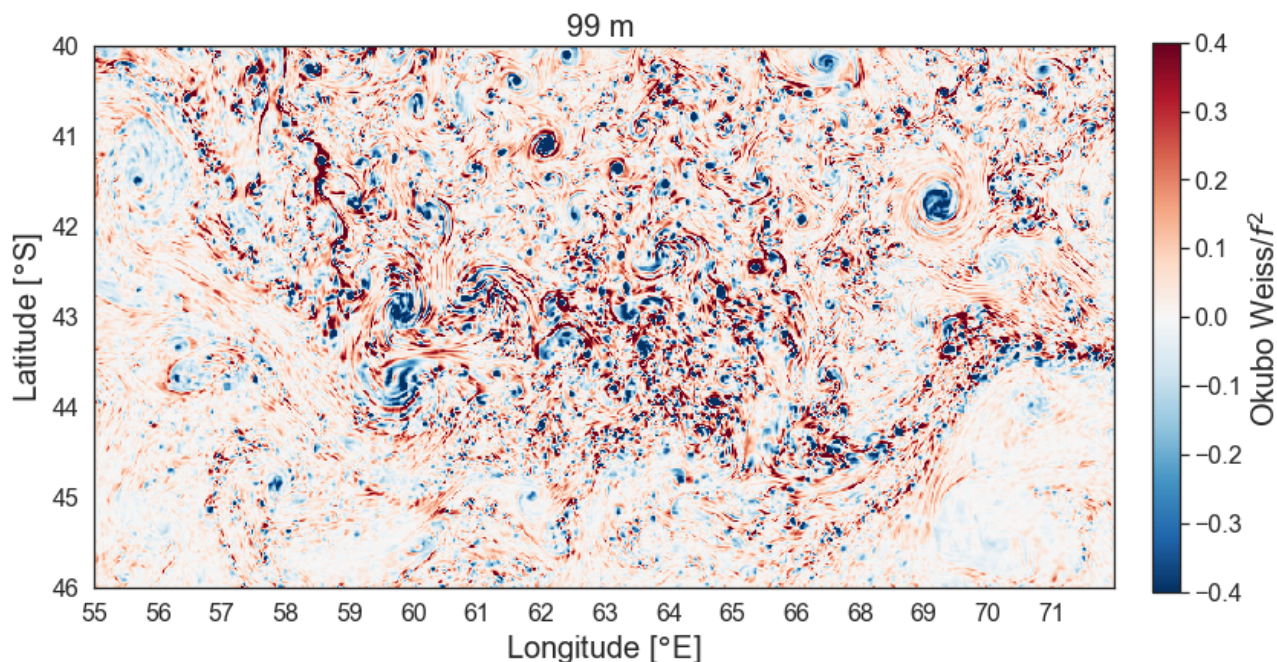


Figure 2.5: Okubo–Weiss quantity, defined as  $\lambda$  in the main text, normalized by  $f^2$ , computed at 99 m in the ACC in the LLC4320 simulation at  $1/48^\circ$  resolution (see section 1.3).

Figure 2.5 displays a snapshot of the OW quantity in the energetic ACC. On one hand,  $\lambda$  is mostly negative within eddy cores, highlighting the dominance of vorticity in these regions of the flow. On the other hand,  $\lambda$  is mostly positive around mesoscale eddies, highlighting the dominance of the strain field. Around mesoscale eddies, both relative and potential vorticity as well as buoyancy gradients are increased, as can be seen in Figure 2.2. These gradients act as dynamical barriers (Mariotti et al.,

1994; Lapeyre et al., 2001), as discussed in section 2.2 and Chapter 4. The strain field is also dominant in-between eddies, such as at  $\psi$ -saddle points. Submesoscale fronts and filaments that build up in these regions are the signature of chaotic advection (Aref, 1984; Lapeyre, 2002; Ollitrault et al., 2005). Chaotic advection refers to the action of stretching and folding by mesoscale eddies, creating long and thin filaments of tracers, as can be seen in the ocean on chlorophyll or Ertel PV maps; see Figures 0.1 and 2.2. Ultimately, these filaments eventually mix with their surrounding environment (Ledwell et al., 1993; Pierrehumbert et al., 1994). Chaotic advection renders mixing much more efficient than what would be expected based on the classical diffusion paradigm used in 3-D turbulence, by at least 2 to 3 orders of magnitude (Garrett, 1983).

The combination of these two opposite submesoscale effects, i.e., dynamical barriers and chaotic advection, strengthens mesoscale eddies. Indeed, an elliptic region, such as a vortex, displays two saddle points from which vorticity filaments can get expelled via the so-called "vortex stripping" (Mariotti et al., 1994). Figure 2.6 presents the vorticity distribution of such a two-dimensional vortex submitted to the action of an external strain field. The vorticity initially located at the periphery of the vortex is torn away through the ejection of filaments. While the eddy is eroded during this process, the ejection of vorticity filaments also allows the eddy to regain an axisymmetric shape.

As a consequence, the vorticity gradient is significantly increased around the eddy (see the inset in Figure 2.6) and acts as a barrier that prevents the eddy from getting destroyed by the external strain field. This situation also applies to the Ertel PV and buoyancy in the presence of strong gradients.

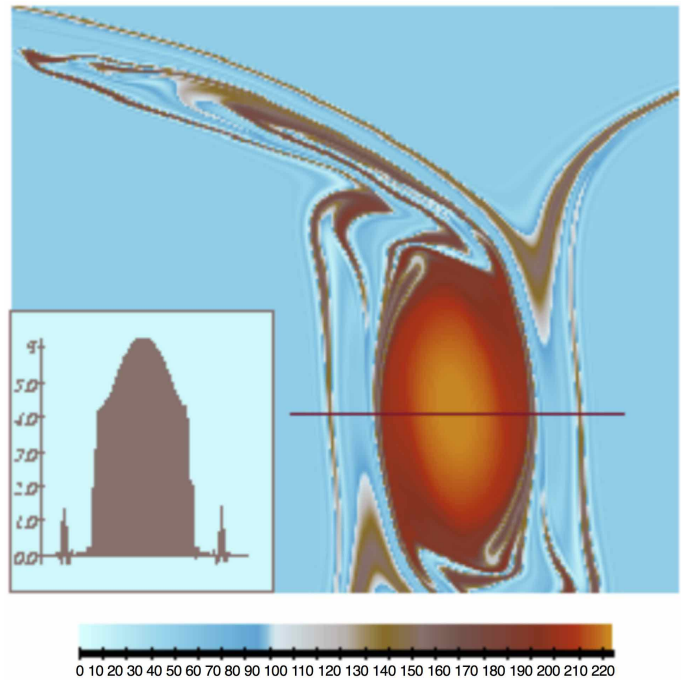


Figure 2.6: Vorticity field of an isolated vortex submitted to an externally prescribed strain field at a late stage after stripping has started; filaments surround the vortex and a sharp boundary develops as shown in the vorticity cross section in the inset figure. From Mariotti et al. (1994).

### 2.3.2 Frontal dynamics in the QG regime

In the QG regime, the weakness of the ageostrophic motions prevents the formation of strong lateral gradients of buoyancy at submesoscale. This property is related to  $|\text{Ro}| \ll 1$ , i.e., weak ageostrophic motions, and  $\text{Ri} \gg 1$ , i.e., weak buoyancy gradients. This inhibition becomes apparent when looking at the time evolution of the thermal wind balance's components, which reads:

$$\nabla_H b = -f \mathbf{k} \times \frac{\partial \mathbf{u}_g}{\partial z}. \quad (17)$$

The time evolution of these components is affected by geostrophic motions, and in particular by the geostrophic strain field, but also by the weak ageostrophic motions as:

$$\frac{d_g \nabla_H b}{dt} = -\mathbf{A} \nabla_H b - \overline{N^2} \nabla_H w, \quad (18)$$

$$\frac{d_g}{dt} \left( -f \mathbf{k} \times \frac{\partial \mathbf{u}_g}{\partial z} \right) = \mathbf{A} \left( -f \mathbf{k} \times \frac{\partial \mathbf{u}_g}{\partial z} \right) - f^2 \frac{\partial}{\partial z} (\mathbf{u}_a), \quad (19)$$

Equations (18) and (19) reveal that each component of the thermal wind balance reacts differently to geostrophic motions, leading to a destruction of the thermal wind balance. Indeed, the matrix  $\mathbf{A}$ , defined by equation (14), appears in equation (18) and with the opposite sign in equation (19). Consequently, in areas where the eigenvalues of  $\mathbf{A}$  are real ( $\lambda > 0$ ), like in strain-dominated areas, the geostrophic term involving  $\mathbf{A}$  will induce an exponential growth of lateral buoyancy gradients and an exponential decay of the corresponding vertical gradients of horizontal velocity, leading to a rapid destruction of the thermal wind balance. This thermal wind imbalance causes motions to depart from geostrophy and, subsequently, induces ageostrophic motions  $(\mathbf{u}_a, w)$ . In the QG approximation, the role of these ageostrophic motions, through the second terms on the right-hand sides (RHS) of equations (18) and (19) is to instantaneously reestablish geostrophy. In other words, the thermal wind balance is destroyed by geostrophic dynamics but is instantaneously restored by ageostrophic motions. These ageostrophic motions counter the formation of strong horizontal buoyancy gradients and adjust the vertical gradients of the horizontal velocity such that equation (17) still holds. As a result, the flow generates an ageostrophic 3D circulation  $(\mathbf{u}_a, w)$  aimed at restoring thermal wind balance.

Note that a diagnostic equation for these ageostrophic motions can be derived by eliminating the time derivative from equations (18) and (19), yielding the so-called QG Omega equation (Hoskins et al., 1978; Hua et al., 1998; Hakim and Keyser, 2001):

$$\bar{N}^2 \nabla_H^2 w + f^2 \partial_z^2 w = 2 \nabla_H \cdot Q, \quad (20)$$

where  $Q$  is the frontogenetic vector derived by Hoskins et al. (1978) and defined as:

$$Q = (Q_1, Q_2) = -\mathbf{A} \cdot \nabla_H b \quad (21)$$

The classical frontogenesis process emphasizes that the increase tendency of buoyancy gradients embedded in a strain field is balanced by ageostrophic motions ( $\mathbf{u}_a, w$ ) that tend to decrease these gradients (Hoskins and Bretherton, 1972), as schematized in Figure 2.7.

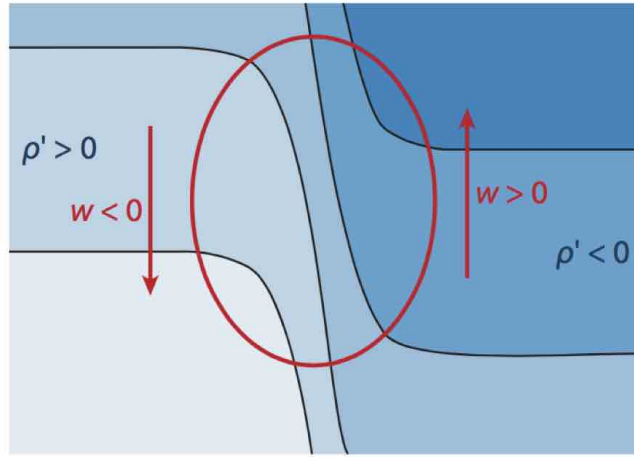


Figure 2.7: Schematic illustration of the ageostrophic circulation that develops in response to strengthening of a horizontal density/buoyancy front. The figure corresponds to a vertical cross section through a submesoscale front. Black lines are isopycnals. The red arrows correspond to the ageostrophic circulation. Lighter fluid (dark blue) is on the right of the figure and denser fluid (light blue) is on the left. From Klein and Lapeyre (2009).

This can be understood by multiplying equation (18) by  $[\nabla_H b]^T$ , yielding the equation for the buoyancy gradient magnitude's time evolution:

$$\frac{1}{2} \frac{d_g |\nabla_H b|^2}{dt} = -[\nabla_H b]^T \cdot \mathbf{A} \cdot \nabla_H b - \bar{N}^2 \cdot [\nabla_H b]^T \cdot \nabla_H w. \quad (22)$$

Equation (22) captures the balance between the gradient production by geostrophic strain, i.e.,  $-\nabla_H b]^T$ .

$\mathbf{A} \cdot \nabla_H b$ , and the gradient destruction by ageostrophic motions, i.e.,  $-N^2 \cdot [\nabla_H b]^T \cdot \nabla_H w$ . Figure 2.8 illustrates these two effects, i.e., the frontogenetic nature of geostrophic strain and the frontolytic nature of vertical velocity.

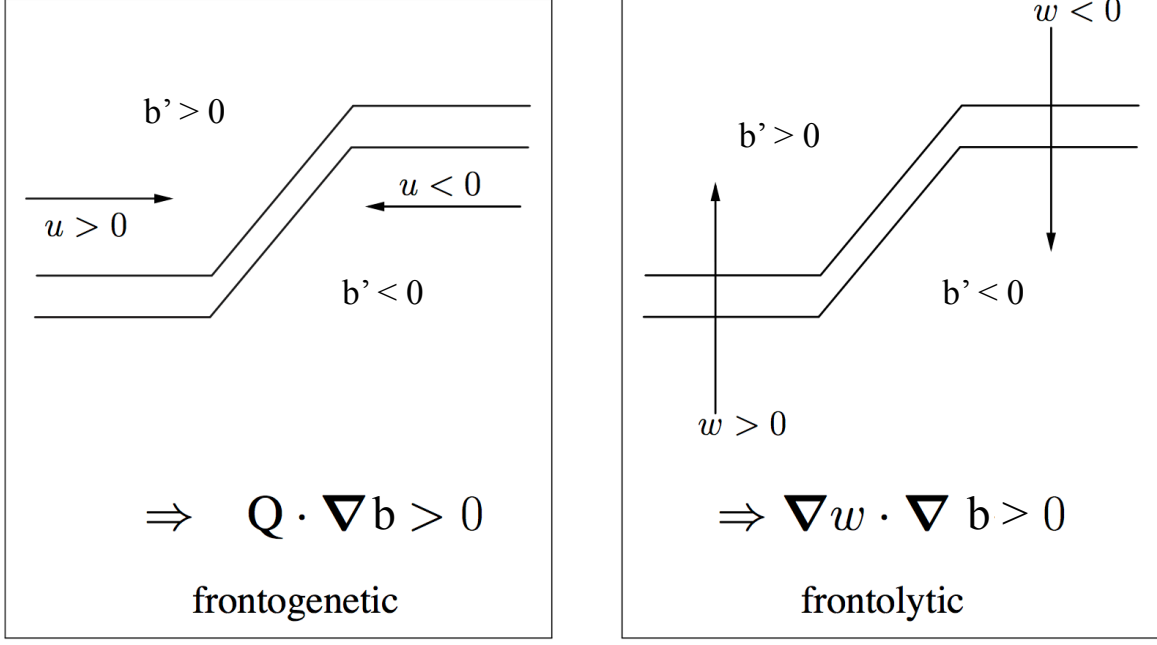


Figure 2.8: Schematic illustration of the effect of deformation and vertical velocity on buoyancy gradient. Adapted from the personal communication of Guillaume Lapeyre (Laboratoire de Météorologie Dynamique, École Normale Supérieure) and Patrice Klein (Caltech/JPL).

A dimensional analysis based on the thermal wind balance and the approximation  $w \propto \frac{H}{L} \text{Ro} \mathbf{u}_g$ , derived from  $\mathbf{u} \sim \mathbf{u}_g + \text{Ro} \mathbf{u}_a$  and from a dimensional analysis of the continuity equation, i.e.,  $\nabla_H \mathbf{u}_a + w_z = 0$  (Pedlosky, 2013), yields:

$$\frac{1}{2} \left| \frac{d_g |\nabla_H b|^2}{dt} \right| \propto |\nabla_H u_g| |\nabla_H b|^2 (1 + \text{Ri} \cdot \text{Ro}^2). \quad (23)$$

Thus, the equilibrium between frontolytic and frontogenetic processes is consistent with the relation  $\text{Ri}^{-1/2} \sim |\text{Ro}|$ . When  $|\text{Ro}| \ll 1$  and  $\text{Ri} \gg 1$ , as in the QG regime, ageostrophic motions and buoyancy gradients are small. One can see, from equation (23) and from the conservation of buoyancy along a Lagrangian trajectory, that strong buoyancy gradients at submesoscale cannot emerge in this regime because of the weak ageostrophic motions, and *vice versa*. This explains why the buoyancy wavenumber spectrum displays a  $k^{-5}$  slope at depth in the QG regime, with  $k$  the horizontal wavenumber (Smith and Ferrari, 2009). As a result, buoyancy gradients at depth are characterized by a  $k^{-3}$  spectral slope,

emphasizing the mesoscale character of these gradients. Note that this is however not the case for temperature and salinity. Indeed, since their gradient evolution equation is closer to equation (13) than equation (22) (Klein et al., 1998; Smith and Ferrari, 2009), strong, density compensated, submesoscale gradients of temperature and salinity may emerge in the QG regime. However, when the regime departs from QG, i.e., for  $Ro$  and  $Ri$  of  $O(1)$  satisfying  $|Ro| \sim Ri^{-1/2}$  (section 2.1), equation (23) indicates that both terms on the RHS of equation (22) are of comparable magnitude, permitting the production of vigorous buoyancy gradients at submesoscale. Yet, equation (22) is derived from the QG equations and, thus, does not take into account all the physics captured by the primitive equations, which are better suited for ageostrophic dynamics. The primitive equations yield a more complex solution as well as an intensified production of buoyancy gradients at submesoscale, as developed in the next section.

## 2.4 Ageostrophic dynamics ( $Ro$ and $Ri$ of $O(1)$ )

In the ageostrophic regime, the advection of a given quantity takes into account not only geostrophic motions but also ageostrophic motions, as the latter now have the same order of magnitude as the former, again using  $\mathbf{u} \sim \mathbf{u}_g + Ro \mathbf{u}_a$ . The momentum and density equations appropriate for this regime are the primitive equations. Associated dynamics greatly differ from that of the QG regime where  $Ro \ll 1$  and  $Ri \gg 1$ . Indeed, Molemaker et al. (2010) showed that relaxing the QG hypotheses in an idealized model of the ocean interior lead to the emergence of large  $Ro$  and energetic frontogenesis at submesoscale driven by mesoscale eddies. These authors compared two idealized numerical simulations at high-resolution; one using the Boussinesq equations and one using the QG ones. As expected, in the QG run, strong buoyancy gradients at submesoscale are confined to the surface, as  $w = 0$  there and therefore the formation of strong gradients is not inhibited, whereas submesoscale buoyancy gradients at depth are much weaker. In contrast, the Boussinesq simulation exhibits a totally different solution in the ocean interior; submesoscale gradients have large magnitude, leading to an enhanced frontogenesis in the ocean interior (Figure 2.9).

In addition, Molemaker et al. (2010) found that the Boussinesq solution is energetically dominated by flows in gradient-wind balance, i.e., a balance between the Coriolis force, pressure gradients force and the nonlinear terms in the momentum equations, and even more so by flows in hydrostatic balance. These results strongly challenge the well accepted QG paradigm for the ocean interior. As such, the



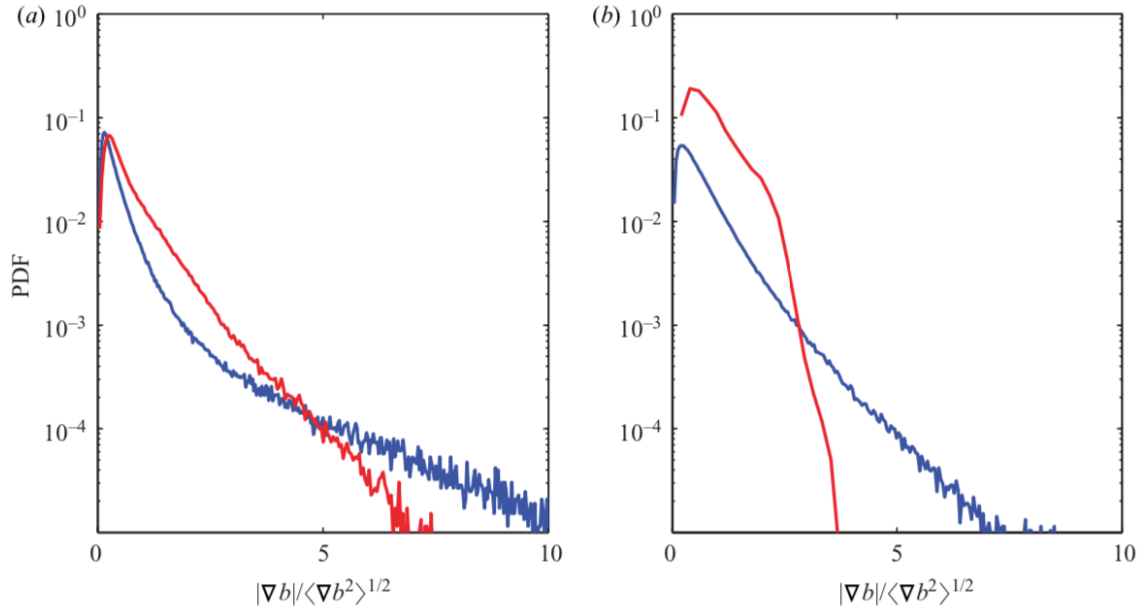


Figure 2.9: PDF of  $|\nabla b|$  in the ocean interior (red) and near the surface (blue) for the Boussinesq run (a) and the QG one (b). From Molemaker et al. (2010).

purpose of this section is to understand the mechanisms that are not present in the QG regime, but that can lead to enhanced frontogenesis at submesoscale in the ocean interior in the ageostrophic regime. For simplicity's sake, we restrict ourselves to a 2-D situation.

### 2.4.1 Frontal dynamics in the ageostrophic regime

Let us consider the case of a 2-D semi-geostrophic front in the  $y$ - $z$  plane, where semi-geostrophy refers to geostrophy in the  $x$ -direction and ageostrophy in the  $y$ - $z$  -direction (Holton, 1973). We further assume that all derivatives in the  $x$ -direction are zero, which leads to  $\partial b/\partial x = 0$ , but  $\partial b/\partial y \neq 0$ . The along-front velocity is purely geostrophic, i.e.,  $u = u_g$ , and in thermal wind balance, i.e.,  $f \partial u_g/\partial z = -\partial b/\partial y$ . This situation is well suited for the study of submesoscale fronts generated by a strain field that is elongated in one direction. The Lagrangian derivative is:

$$\frac{d}{dt} = \frac{d_g}{dt} + \left( v_a \frac{\partial}{\partial y} + w \frac{\partial}{\partial z} \right), \quad (24)$$

where,  $\frac{d_g}{dt} = \frac{\partial}{\partial t} + u_g \frac{\partial}{\partial x} + v_g \frac{\partial}{\partial y}$  is the material derivative following the geostrophic wind balance,  $v_a$  is the  $y$ -component of the ageostrophic velocity and  $w$  its vertical component. The terms not present in the QG material derivative are shown in blue.

Since ageostrophic motions are related to  $w$  through the continuity equation, i.e.,  $\partial v_a/\partial y + \partial w/\partial z = 0$ , equations (18) and (19) become:

$$\frac{d}{dt} \left( \frac{\partial b}{\partial y} \right) = Q_2 - \frac{\partial v_a}{\partial y} \frac{\partial b}{\partial y} - \frac{\partial w}{\partial y} \left( N^2 + \frac{\partial b}{\partial z} \right), \quad (25)$$

$$\frac{d}{dt} \left( -f \frac{\partial u_g}{\partial z} \right) = -Q_2 - f \frac{\partial v_a}{\partial z} \left( f - \frac{\partial u_g}{\partial y} \right) - \frac{\partial w}{\partial z} \frac{\partial b}{\partial y}, \quad (26)$$

with  $Q_2$  given by (21). The terms present in equations (25) and (26) but not in equations (18) and (19) are shown in blue. The impact of the blue terms on frontal dynamics can be understood through the equation of the buoyancy gradient magnitude's time evolution, deduced from (25) with  $Q_2 = -\frac{\partial v_g}{\partial y} \frac{\partial b}{\partial y}$ .

This equation reads:

$$\frac{1}{2} \frac{d}{dt} \left| \frac{\partial b}{\partial y} \right|^2 = -\frac{\partial v_g}{\partial y} \left| \frac{\partial b}{\partial y} \right|^2 - \frac{\partial v_a}{\partial y} \left| \frac{\partial b}{\partial y} \right|^2 - \frac{\partial w}{\partial y} \frac{\partial b}{\partial y} \left( N^2 + \frac{\partial b}{\partial z} \right), \quad (27)$$

Equation (27) is similar to equation (22) except for the blue terms. These terms, and in particular the first one, explain the strong asymmetry in the  $y$ -direction, displayed in Figure 2.10, which is not observed in the QG framework (Hakim and Keyser, 2001). This asymmetry, in the upper part of the front in Figure 2.10c, is characterized by intensified (subdued) buoyancy gradients on the cold (warm) side of the front. Let us now consider the first and second terms on the RHS of (27);  $\frac{\partial v_g}{\partial y}$  is related to the large-scale strain field whose negative sign is the same on the cold and warm sides of the front and which tend to increase buoyancy gradients. In contrast,  $\frac{\partial v_a}{\partial y}$  is negative (positive) on the cold (warm) side of the front. This means that  $\frac{\partial v_a}{\partial y}$  will increase (decrease) the buoyancy gradients on the cold (warm) side of the front, leading to a significant asymmetry, as displayed in Figure 2.10. This asymmetry due to  $\frac{\partial v_a}{\partial y}$  has also been reported in Capet et al. (2008) (see their Figure 7). The intensification of buoyancy gradients on the cold side should lead to an increased  $\text{Ri}^{-1}$ , since the latter is proportional to the isopycnal's slope. Furthermore, because of the thermal wind balance,  $f \partial u_g/\partial z = -\partial b/\partial y$ , the geostrophic jet,  $u_g$ , will increase on the cold side of the front, leading to enhanced relative vorticity, as displayed in Figure 2.10b, and thus to an increased Ro. As illustrated in Figure 2.10a, the asymmetric ageostrophic circulation is associated with intensified vertical velocities on the cold side of the front. The reverse situation is observed in the lower part of the front.

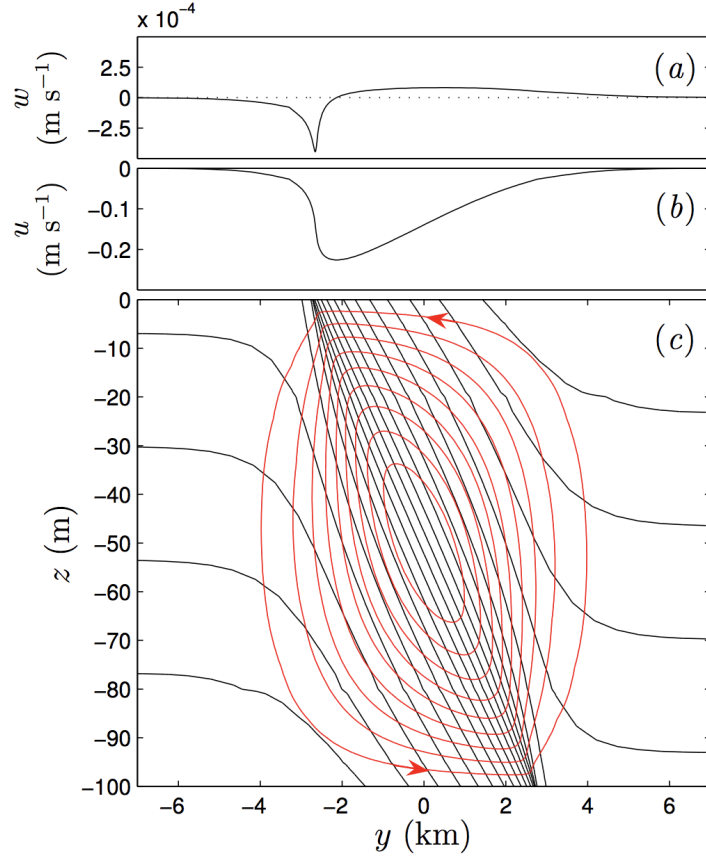


Figure 2.10: Ageostrophic secondary circulation at a submesoscale front. a)  $w$  and b)  $u$  at  $z = -2.5$  m, and c) overturning streamfunction  $\psi_M$  (red contours) and buoyancy  $b$  (black contours), corresponding to the solution of equations (25) and (26). From Thomas et al. (2008).

The omega equation resulting from (25) and (26) further helps to understand this asymmetry and the intensification of the vertical velocity field. In the case of a 2-D semi-geostrophic front, the ageostrophic circulation in the  $y$ - $z$  plane can be represented in terms of a meridional streamfunction  $\psi_M$  defined as:

$$v_a = -\frac{\partial\psi_M}{\partial z}, \quad w = \frac{\partial\psi_M}{\partial y}, \quad (28)$$

which satisfies the continuity equation. Adding equations (25) and (26), and using the thermal wind balance to eliminate the time derivative and equation (28) to eliminate  $v_a$  and  $w$ , we obtain the so-called *Sawyer-Eliassen* omega equation:

$$N_s^2 \frac{\partial^2 \psi_M}{\partial y^2} + F^2 \frac{\partial^2 \psi_M}{\partial z^2} + 2 S^2 \frac{\partial^2 \psi_M}{\partial y \partial z} = 2 Q_2, \quad (29)$$

where

$$N_s^2 \equiv \bar{N}^2 + \frac{\partial b}{\partial z}, \quad F^2 \equiv f \left( f - \frac{\partial u_g}{\partial y} \right), \quad S^2 \equiv -\frac{\partial b}{\partial y}. \quad (30)$$

Equation (29) can be compared to the QG version of the omega equation (equation (20)) obtained by neglecting advection by the ageostrophic circulation. This equation reads in its  $\psi_M$ -formulation form:

$$\bar{N}^2 \frac{\partial^2 \psi_M}{\partial y^2} + f^2 \frac{\partial^2 \psi_M}{\partial z^2} = 2 Q_2. \quad (31)$$

Thus, in the QG case, the coefficients in the differential operator on the LHS only depend on the standard Brunt–Väisälä frequency  $N$  and the planetary vorticity  $f$ , whereas in the semi-geostrophic case (29), they depend on the deviation of buoyancy from its standard profile through the  $N_s$  and  $S$  terms and the absolute vorticity through the  $F$  term. Again, the terms involved in the *Sawyer-Eliassen* equation but not in the QG one are shown in blue in equations (29) and (30).

Provided that  $N_s^2 F^2 - S^4 > 0$ , the *Sawyer-Eliassen* equation (29) is an elliptic boundary value problem, which admits a real solution. The solution can be found using the method of the Green's function, as detailed in Hakim and Keyser (2001). The Green's function  $G$  for  $\psi_M$  satisfies the following equation:

$$N_s^2 \frac{\partial^2 G}{\partial y^2} + F^2 \frac{\partial^2 G}{\partial z^2} + 2 S^2 \frac{\partial^2 G}{\partial y \partial z} = \delta(y - Y, z - Z), \quad (32)$$

which, for any  $Q_2$ -vector distribution, yields the ageostrophic circulation  $\psi_M = -2 \iint G(y - Y, z - Z) Q_2(Y, Z) dY dZ + \psi_H$  where  $\psi_H$  is a homogeneous solution to  $\nabla \cdot \mathbf{u}_a = 0$ , which ensures  $\psi_M$  satisfies the boundary conditions. The solution to equation (32) is given by:

$$G = \frac{1}{4\pi\sqrt{f} q_{2D}} \log|Arg|, \quad (33)$$

where

$$Arg = \frac{[(y - Y) - (z - Z)S^2/F^2]^2}{L_{SG}^2} + \frac{(z - Z)^2}{H^2}$$

and

$$L_{SG} = H \frac{\sqrt{f} q_{2D}}{F^2} \quad (34)$$

is the semi-geostrophic Rossby radius of deformation, and  $H$  is the vertical length scale of the flow. The 2-D Ertel PV,  $q_{2D}$ , is given by:

$$q_{2D} = \frac{1}{f}(N_s^2 F^2 - S^4) = f N_s^2(1 + \text{Ro} - \text{Ri}^{-1}). \quad (35)$$

The condition  $N_s^2 F^2 - S^4 > 0$  can thus be written as  $f^2 N_s^2 (1 + \text{Ro} - \text{Ri}^{-1}) > 0$ . From the dependence of equation (33) on the Ertel PV, it can be seen that a real solution does not exist when  $f q_{2D} \leq 0$ , indicating that equation (29) has a real solution if and only if  $f q_{2D} > 0$ . This places a strong constraint on  $\text{Ri}^{-1}$ , which is positive and has to be smaller than  $|1 + \text{Ro}|$ . In turn, it leads to a limitation of the steepness of the front and also to a limitation of the importance of  $S^2$  relatively to the other terms in the *Sawyer-Eliassen* equation (29).

#### 2.4.2 Vertical velocities

The vertical velocity field associated with equation (33) is given by:

$$w = -\frac{F^4}{2\pi(f q_{2D})^{3/2} H^2} \frac{(y - Y)}{\text{Arg}}. \quad (36)$$

From equation (36), one can see that the magnitude of  $w$  is inversely proportional to the Ertel PV. The spatial variation of the coefficients in equation (30) and the presence of the cross-derivative term produce a distortion of the secondary circulation, as shown in Figure 2.10 (Thomas et al., 2008). The ageostrophic secondary circulation cell (red ellipses in Figure 2.10c) is tilted along isopycnals (black contours in Figure 2.10c) and has an asymmetrical shape. This is because, at the surface for instance, the relative vorticity,  $-\partial u_g / \partial y$ , is positive on the left side of the front and negative on the right side (Figure 2.10b), leading to a larger  $F^2$  on the left side of the front than on the right. As a consequence, for a given Ertel PV,  $L_{SG}$  (equation (34)) is smaller and  $|w|$  greater on the left side of the front than on the right. This is consistent with the fact that an increase in relative vorticity coincides with an increase in lateral density gradient, as previously discussed and as can be seen from equation (35). Thus, an increase in  $\text{Ro}$  is associated with an increase in  $\text{Ri}^{-1} \propto (b_y/b_z)^2$ , indicating that lateral buoyancy gradients are increased, or stratification destroyed. This implies that on the cold side of the front ( $w < 0$ ),  $w$  has a narrower width but greater amplitude than on the warm side ( $w > 0$ ). This asymmetry considerably enhances vertical buoyancy flux and restratification processes compared to the QG regime.

In the context of this dissertation, and in particular in Chapter 3, it is important to note that many studies, starting with Hoskins (1982) and more recently confirmed by Hakim and Keyser (2001), have emphasized that the *Sawyer-Eliassen* and QG solutions are qualitatively similar when the condition  $F^2 N^2 - S^4 > 0$  is satisfied. In particular, the *Sawyer-Eliassen* and weak QG ageostrophic circulations, and therefore the  $w$ -field, have the same sign. Indeed, the sense of the ageostrophic secondary circulation cell (red ellipses in Figure 2.10c) is thermally direct in both cases, i.e., it tends to flatten isopycnals and restore the thermal wind balance. This is because the Green's function is forced by a RHS in equation (29) such that  $Q_2 \cdot \nabla b > 0$ , corresponding to the case of frontogenetic deformation (Figure 2.8). Overall, the main differences between the *Sawyer-Eliassen* and QG ageostrophic circulations are:

- the shape of the ageostrophic circulation, which is more tilted and oriented parallel to the isopycnals in the *Sawyer-Eliassen* solution.
- the amplitude of the  $w$ -field, which is larger in the *Sawyer-Eliassen* solution for  $Ri$  of  $O(1)$  than in the QG case.

The qualitative similitude between the two omega equations is useful when the blue terms in equation (29) are unknown, as it is the case in Chapter 3. In this situation, the difference in  $w$ -magnitude can be retrieved using the analytical solutions for the QG and *Sawyer-Eliassen* (SE) versions of the omega equation derived in Hakim and Keyser (2001). These authors show that  $w_{SE} \sim w_{QG} \left( \frac{PV_{QG}}{PV_{PE}} \right)^{1/2}$  with  $w_{SE}$  and  $w_{QG}$  the solutions of the SE and QG omega equation, respectively, and  $PV_{PE}$  and  $PV_{QG}$  the Ertel and QG PV, respectively. Following Thomas et al. (2008), using the approximations  $PV_{QG} \sim fN^2$  and  $PV_{PE} \sim fN^2(1 - Ri^{-1})$  leads to  $PV_{QG}/PV_{PE} = (1 - Ri^{-1})^{-1}$ . This relation is used in Chapter 3 to quantify the vertical velocity's underestimation at low  $Ri$ .

Overall, the intensification of frontogenesis mechanisms in the ageostrophic regime explains the idealized results of Molemaker et al. (2010), emphasizing the existence of strong submesoscale buoyancy gradients in the ocean interior. These dynamical concepts also explain the observational and numerical results of Chapters 3 and 4, highlighting the existence of the strong buoyancy gradients in the ocean interior that are associated with intense vertical velocities and enhanced upward vertical fluxes of heat and buoyancy.

### 3 Enhanced upward heat transport at deep submesoscale fronts

In this chapter, we apply the dynamical concepts presented in Chapter 2 to two observational datasets (seal and satellite observations) collected in the energetic ACC in late spring/early summer, i.e., when the mixed layer depth is  $\sim 100$  m deep. Finite-Size Lyapunov Exponent (FSLE) derived from satellite altimetry are used as a proxy for the mesoscale strain field (see section 1.2.2). Frontogenesis is studied by comparing the mesoscale strain field, given by FSLE, to the production of lateral gradient of buoyancy, provided by the seal data. The two independent datasets are then combined into a QG omega equation, yielding important vertical velocities reaching  $\pm 100$  m/day, but which should attain  $\pm 140$  m/day had the full *Sawyer-Eliassen* equation been used (see Supplementary Materials below). Lateral buoyancy gradients and their associated intense vertical velocities are primarily located on the periphery of mesoscale eddies, consistent with the theoretical results presented in Chapter 2. Both extend down to depths of at least 400 m, i.e., well below the mixed-layer, highlighting the presence of ageostrophic dynamics in the ocean interior. Enhanced vertical heat transport at these deep submesoscale ocean fronts is subsequently diagnosed, with local values reaching  $\pm 2000$  W/m<sup>2</sup> and average values reaching  $+100$  W/m<sup>2</sup> at 200 m. This effect is argued to remarkably alter oceanic heat uptake and exacerbate restratification processes. It will be strongest in eddy-rich regions such as the ACC, the Kuroshio Extension, and the Gulf Stream, all of which are key players in the climate system.

**Siegelman, L.**, Klein, P., Rivière, P., Thompson. A.F., Torres, H.S., Flexas, M. and Menemenlis, D. (2019). Enhanced upward heat transport at deep submesoscale ocean fronts. *Nature Geoscience*. doi:10.1038/s41561-019-0489-1

# Enhanced upward heat transport at deep submesoscale ocean fronts

Lia Siegelman<sup>1,2,3\*</sup>, Patrice Klein<sup>1,2,4</sup>, Pascal Rivière<sup>3</sup>, Andrew F. Thompson<sup>1</sup>, Hector S. Torres<sup>2</sup>, Mar Flexas<sup>1</sup> and Dimitris Menemenlis<sup>2</sup>

**The ocean is the largest solar energy collector on Earth. The amount of heat it can store is modulated by its complex circulation, which spans a broad range of spatial scales, from metres to thousands of kilometres. In the classical paradigm, fine oceanic scales, less than 20 km in size, are thought to drive a significant downward heat transport from the surface to the ocean interior, which increases oceanic heat uptake. Here we use a combination of satellite and in situ observations in the Antarctic Circumpolar Current to diagnose oceanic vertical heat transport. The results explicitly demonstrate how deep-reaching submesoscale fronts, with a size smaller than 20 km, are generated by mesoscale eddies of size 50–300 km. In contrast to the classical paradigm, these submesoscale fronts are shown to drive an anomalous upward heat transport from the ocean interior back to the surface that is larger than other contributions to vertical heat transport and of comparable magnitude to air–sea fluxes. This effect can remarkably alter the oceanic heat uptake and will be strongest in eddy-rich regions, such as the Antarctic Circumpolar Current, the Kuroshio Extension and the Gulf Stream, all of which are key players in the climate system.**

Vertical heat transport (VHT) is one of the key mechanisms by which the ocean regulates Earth's climate. Munk and Wunsch<sup>1</sup> first postulated that VHT is balanced by an upward component due to the large-scale mean flow (>300 km) and a downward component explained by fine-scale diffusive processes (<20 km). However, recent studies<sup>2,3</sup> highlighted the importance of mesoscale eddies (50–300 km) for VHT. Thus, global VHT by mean flow and diffusion are now thought to be both downward and balanced by an upward eddy heat flux, with the mean and eddy components generally being the largest contributors<sup>2</sup>.

Mesoscale eddies are intensified in energetic areas such as the Antarctic Circumpolar Current (ACC), Kuroshio Extension and Gulf Stream<sup>4</sup>. They are known to drive the production of submesoscale fronts (<20 km), that is, regions that separate waters of different densities<sup>5–9</sup>, which are ubiquitous on satellite images of ocean colour (Fig. 1). To date, submesoscale fronts were mainly thought to be confined to the ocean surface mixed layer (~100 m deep)<sup>8,9</sup>. This is because, in the classical model, motions below the mixed-layer are broadly assumed to be in geostrophic balance (a balance between Coriolis and horizontal pressure forces), which prevents the formation of strong density gradients<sup>10</sup>. As a consequence, fine scales below the mixed-layer are still principally associated with diffusive processes that drive downward heat transport. However, a handful of studies suggest that submesoscale fronts associated with upward heat transport may also penetrate below the mixed layer<sup>11–14</sup>. Yet, these studies do not explain the formation mechanism of these submesoscale fronts because they are confined to small domains (<50 km). Observational evidence over domains sufficiently large to capture multiple mesoscale eddies and their associated submesoscale fronts are needed for the closure of oceanic VHT. Such measurements are still lacking because capturing fine spatial and temporal scales over extended domains lie at the edge of our observational capabilities.

Here we meet this observational challenge by analysing a unique dataset collected by an instrumented elephant seal in the ACC. The seal data revealed the presence of numerous deep-reaching submesoscale fronts that extend well below the mixed-layer and are principally found on eddies' edges. We then developed a pioneering methodology that combines satellite and seal observations to retrieve a three-dimensional (3D) synoptic view of ocean dynamics from the meso- to submesoscale. The results explicitly demonstrate that deep-reaching submesoscale fronts are generated by the strain field associated with co-interacting mesoscale eddies. By invoking the properties of mesoscale turbulence, we explain why deep-reaching fronts, counterintuitively, drive an enhanced VHT below the surface mixed layer that is directed upward; this is also supported by a numerical model analysis (Supplementary Information). The associated VHT is larger than the mean flow and eddy contributions<sup>2</sup>, and of similar magnitude to air–sea fluxes<sup>15</sup>. This effect is argued to crucially limit oceanic heat uptake and therefore to alter the ocean heat storage capacity.

## Frontal region sampled by elephant seal and satellite

Measurements were collected by a southern elephant seal (*Mirounga leonina*) in the Kerguelen area (Indian sector of the Southern Ocean, Fig. 1) during the austral spring and summer. The dataset has a horizontal resolution of 1 km, a vertical resolution of 1 m and extends from the surface down to 400 m in the ocean interior. Over a period of more than three months and a distance that exceeded 5,000 km, the seal continuously recorded temperature, conductivity and pressure, from which the buoyancy  $b$  (opposite sign to density) was derived (Methods). An example of the buoyancy field is shown in Fig. 2a–c. In addition, satellite altimeter observations supply daily horizontal fields of sea surface height (SSH), a proxy of surface pressure, with an effective resolution sufficient to resolve mesoscale eddies of size of 50–100 km.

<sup>1</sup>Environmental Science and Engineering, California Institute of Technology, Pasadena, CA, USA. <sup>2</sup>Jet Propulsion Laboratory, California Institute of Technology, Pasadena, CA, USA. <sup>3</sup>Université de Brest, CNRS, IRD, Ifremer, LEMAR, Plouzané, France. <sup>4</sup>Université de Brest, CNRS, IRD, Ifremer, LOPS, Plouzané, France. \*e-mail: [lsiegelman@caltech.edu](mailto:lsiegelman@caltech.edu)



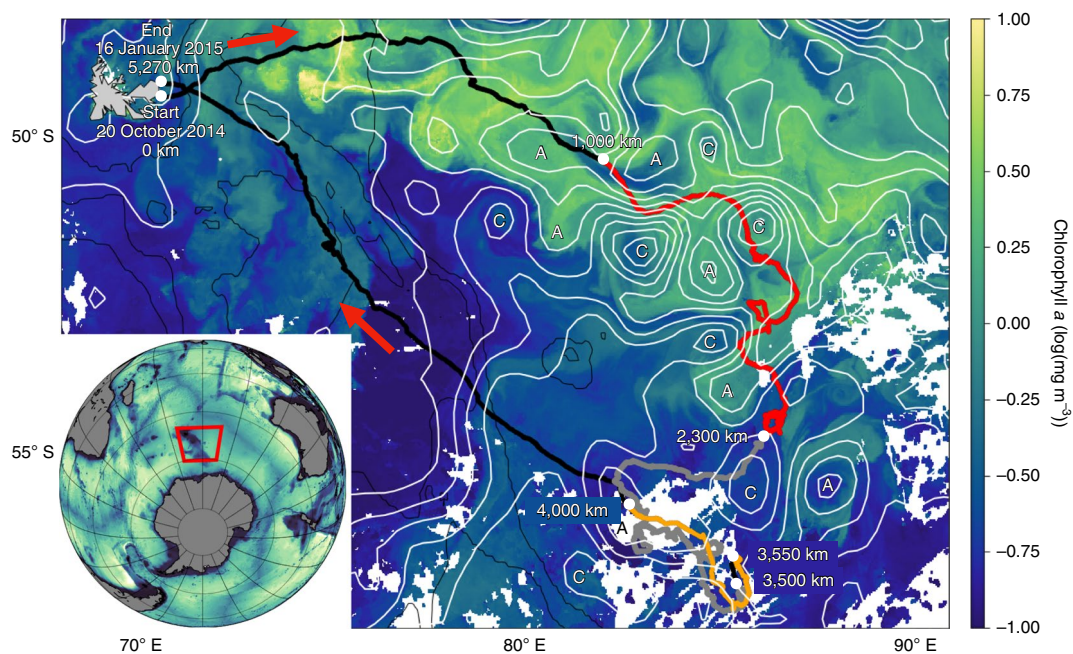


**Fig. 1 | Study region (22 December 2014).** A three-month seal trajectory (black line) superimposed with a snapshot of chlorophyll *a* and SSH (white contours). Three regions are highlighted: the highly turbulent area (red), the weakly turbulent area (grey) and the southern eddy edge (orange). Cyclones (C) and anticyclones (A) are identified from elliptic SSH contours. Hyperbolic SSH contours located in-between eddies identify the strain field (Fig. 3a). Red arrows indicate the direction of the seal. Bathymetry contours of 0.5, 2 and 3 km (thin black lines) from NOAA ETOPO5 (National Oceanic and Atmospheric Administration's Earth topography five minute grid) outline the Kerguelen plateau. Inset: Kerguelen region (red polygon).

The area sampled by the seal from 1,000 to 2,300 km (red line in Fig. 1), that is, from 2 November to 24 November 2014, is rich in eddies and lies within the energetic ACC<sup>16</sup>, as illustrated by the SSH contours in Fig. 1. The seal crossed numerous co-interacting cyclonic (low SSH) and anticyclonic (high SSH) mesoscale eddies. Geostrophic currents, derived from the SSH, reach values of  $1 \text{ m s}^{-1}$  around the eddy edges (Fig. 2a) and are similar to those found in the Gulf Stream and the Kuroshio Extension, the two other most energetic ocean currents<sup>4</sup>. This area is thus representative of the flow field encountered within eddy-rich regions of the world oceans, and will receive particular emphasis in this study. The other areas crossed by the seal (Fig. 1) are much less energetic (Extended Data Fig. 1).

A comparison between the satellite SSH and buoyancy anomalies sampled by the seal in the turbulent area (Fig. 2a–c and Supplementary Fig. 1a–c) highlights the expected vertical structure of the mesoscale eddies<sup>10</sup>: buoyancy anomalies are positive and bowl shaped in anticyclonic eddies (high SSH) and negative and reversed bowl shaped in cyclonic eddies (low SSH, Fig. 2a–c and Extended Data Fig. 1a–c). The combination of satellite observations of SSH and seal measurements of buoyancy provides a synoptic 3D view of the flow field encountered by the seal, and, in particular, of the eddy field, which can extend down to depths of at least 400 m. Supplementary Information gives a more detailed analysis of the consistency at mesoscale between these two independent datasets.

Frontal structures, or buoyancy fronts, are identified by the along-track derivative of buoyancy and are defined as  $b_s = \partial b / \partial s$ , where  $s$  is the curvilinear abscissa, that is, the along-track direction. The fronts, shown in Fig. 2d, have a width between 5 and 20 km and are thus submesoscale features. Indeed, the Rossby radius of deformation in the Kerguelen area is  $\sim 15 \text{ km}$  (ref. <sup>17</sup>), which corresponds to an eddy radius of  $\sim 50 \text{ km}$  (refs. <sup>17,18</sup>), consistent with the SSH observations (Fig. 2a). These fronts are well-resolved by the seal's 1 km horizontal resolution measurements. They are more numerous below the mixed layer and extend down to at least 400 m.

Large buoyancy gradients are preferentially found at the edges of the mesoscale eddies and in-between them. Buoyancy gradient magnitudes reach values larger than  $5 \times 10^{-7} \text{ s}^{-2}$ . The root mean squared (r.m.s.) of the lateral gradient of buoyancy, used as an indicator of the gradient magnitude, is larger than  $0.5 \times 10^{-7} \text{ s}^{-2}$ , regardless of depth (Extended Data Fig. 2a). Compared to the few other existing submesoscale-resolved datasets<sup>19–21</sup>, these values are of the same order of magnitude, which highlights the important frontal activity of the area.

### Frontal dynamics in the ocean interior

Figure 3 illustrates how the production of horizontal gradients of buoyancy is driven by a pure strain field, which corresponds to the hyperbolic regions in-between co-interacting eddies<sup>5</sup>, as can be seen in Fig. 1. In the schematic Fig. 3a, the strain field (black arrows) stretches a tracer patch in the  $y$  direction and compresses it in the  $x$  direction. This leads to the formation of strong horizontal gradients of buoyancy, or fronts, at submesoscale that are associated with a growth rate related to the strain rate  $u_x = \frac{\partial u}{\partial x}$  (Fig. 3b).

To assess the relevance of this mechanism in the Kerguelen area, we analysed the background strain field in relation to the observed buoyancy gradients. We used daily finite size Lyapunov exponents (FSLEs)<sup>22</sup> computed from satellite-derived geostrophic velocities to characterize the strain field properties (Methods). FSLEs indicate both the orientation and timescale (colour bar in Fig. 4a) of the stretching and compression induced by the strain field (respectively, the red and blue curves in Figs. 3a and 4a). As illustrated in Fig. 3a, we expect a tracer patch, or equivalently a buoyancy anomaly, to be aligned with stretching FSLE<sup>22</sup>. The spatial distribution of FSLE (Fig. 4a and Extended Data Fig. 3) confirms that regions in-between eddies and on eddy edges are prone to the formation of strong horizontal buoyancy gradients ( $|b_x|$ ). However, the seal's trajectory is often oblique rather than perpendicular to the buoyancy fronts, which may lead to an underestimation of the front's magnitude. Therefore, to correct for the seal's orientation with respect

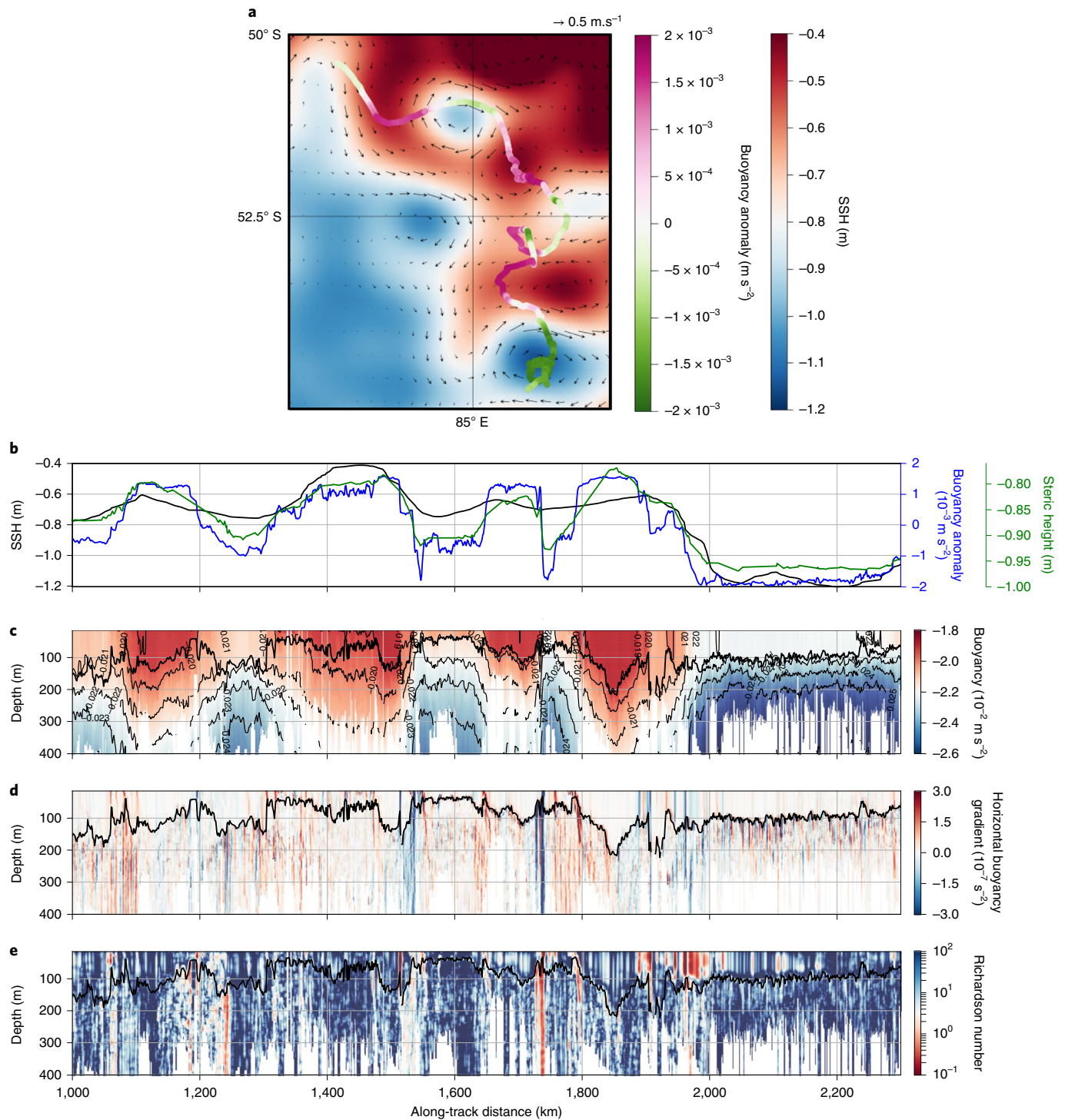


**Fig. 2 | Characteristics of the strongly turbulent area (red in Fig. 1).** **a**, A snapshot (13 December 2014) of SSH and geostrophic currents (black arrows) superimposed with the surface buoyancy anomaly measured by the seal from 2 November 2014 to 24 November 2014. **b**, An along-seal-track time series of SSH (black line), seal-measured buoyancy anomaly (blue line) and steric height (green line) (Supplementary Information). **c**, The seal's vertical section of buoyancy. The thin black lines are isopycnals. **d**, The seal's vertical section of lateral buoyancy gradients,  $b_x$ . **e**, The seal's vertical section of the Richardson number. The mixed layer depth (MLD) is shown by a thick black line in **c-e**.

to the FSLE it encounters, buoyancy gradients were first normalized by the angle between the seal's trajectory and the FSLE direction (Methods). Note that the normalized buoyancy gradients are now referred to as  $b_x$ , where the subscript  $x$  refers to the direction normal to the stretching FSLE (Fig. 3a). We then compared the along-track time series of stretching FSLE estimated along the seal's

path with the normalized buoyancy gradients at 300 m (a comparison with buoyancy gradients at different depths below the mixed layer produces similar results). There is good agreement between the FSLE and normalized buoyancy gradients at 300 m (Fig. 4 and Extended Data Fig. 4a), as well as a consistent relationship that links the two (Fig. 4b). The two time series are strongly intermit-

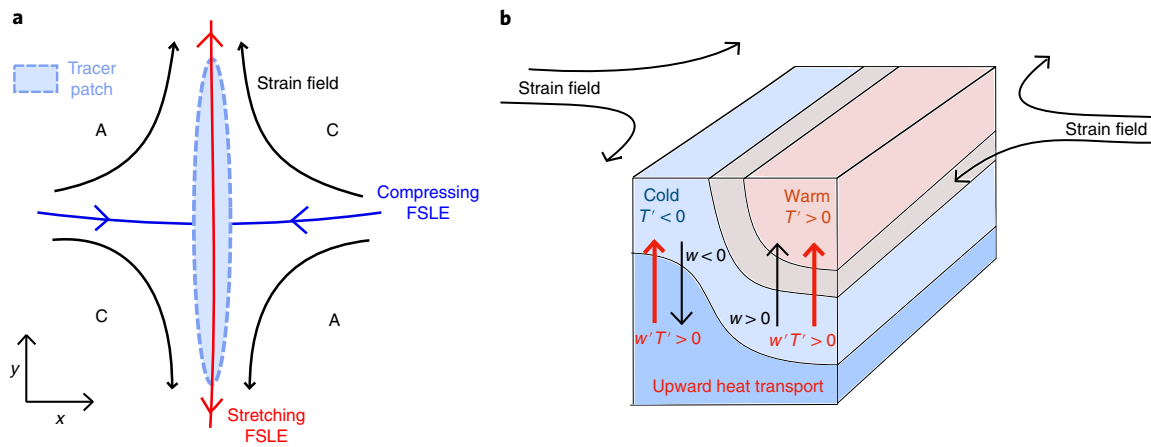


**Fig. 3 | Strain field, frontogenesis and VHT. a**, A horizontal slice ( $x,y$ ) of a tracer patch (light blue) in a strain field (black arrows). The strain elongates (compresses) the tracer in the  $y$  ( $x$ ) direction<sup>10</sup>. Red (blue) FSLE (proxy of strain) arrows identify horizontal stretching (compressing) directions. The fronts are aligned with the stretching FSLE. **b**, A 3D slice of the strain-induced submesoscale front. The thin black lines are isotherms. Vertical velocities ( $w$ , straight black arrows) develop in response to the front intensification. As the temperature and  $w$  anomalies are positively correlated, frontogenesis-induced VHT is upward (see Methods for a full description).

tent. Peaks of FSLE and buoyancy gradients are often co-located (Fig. 4a,b and Extended Data Fig. 4a). Note that similar results are obtained with non-normalized gradients, which demonstrates that no bias is added via the normalization. Combined together, these two datasets provide observational evidence of how an eddy strain field, diagnosed at the sea surface, drives strong buoyancy gradients at a submesoscale in the ocean interior.

A comparison between panels c and d in Fig. 2 further reveals that, whereas mesoscale buoyancy anomalies are slanted on the vertical, as evidenced by the bowl-shaped structures of buoyancy (panel c), buoyancy fronts at the submesoscale are almost vertical (panel d). This density slope property is related to the dynamical regime that drives these structures and can be quantified by the non-dimensional Richardson number  $Ri$  (Methods). The small  $Ri$  values observed in Fig. 2d suggest an energetic ageostrophic regime associated with intense vertical currents. The emergence of these vertical currents,  $w$ , counterbalances the formation of sharp submesoscale fronts generated by the ambient strain field. This mechanism is referred to as frontogenesis<sup>23</sup> and is sketched in Fig. 3b. It leads to an equilibrium that is captured by the classical omega equation, which involves the vertical current field  $w$ , the strain field  $u_x$  and the lateral gradient of buoyancy field  $b_x$ . Here we diagnose the vertical currents  $w$  by solving the 2D ( $x,z$ ) quasi-geostrophic (QG) version of the omega equation<sup>23</sup> (Methods), with  $b_x$  obtained from seal observations and  $u_x$  estimated from stretching FSLE (Fig. 4). However, compared to the full omega equation, there is a tendency for the vertical currents diagnosed here to be underestimated by  $\sim 1.4$  (Methods).

The vertical section of  $w$  shown in Fig. 5b reveals positive and negative  $w$  values with large magnitudes of up to  $100 \text{ m d}^{-1}$ , that is, almost an order of magnitude greater than that attributed to mesoscale eddies alone<sup>24</sup>. Vertical currents have a width of 5–10 km. They are intensified in the ocean interior, below the mixed layer down to at least 400 m, and do not necessarily penetrate into the mixed layer. The continuous vertical extent of these vertical currents highlights the crucial role played by deep-reaching submesoscale fronts in connecting the ocean interior to the surface. The  $w$  field is characterized by the same intermittency present in the FSLE and buoyancy gradient fields (Figs. 2d, 4c, 5b and Extended Data Fig. 4b). Large  $w$  magnitudes are co-located with strong buoyancy gradients and intense FSLE, and are therefore mostly found on the edges of, and in-between, eddies.

The analysis of the vertical currents presented here is supported by a comparison with a realistic regional numerical model with a 1.5 km horizontal resolution (Supplementary Information gives more details on the model). The values of  $w$  derived from the observations are comparable to, although smaller than, those obtained in the model (Extended Data Fig. 5a). Overall, these results suggest that the vertical pathway provided by deep ocean fronts in the spring and summer is likely a generic mechanism throughout the ocean. This deep-reaching vertical pathway has important consequences for the vertical transfer of heat between the ocean interior and the surface mixed layer, as explored in the next section.

### VHT at deep submesoscale fronts

Oceanic heat transport was estimated from temperature and vertical velocity anomalies, from the surface down to 400 m depth (Fig. 5a,b). A vertical section of this transport (Methods gives the calculation) is shown in Fig. 5c, in which a positive (negative) value indicates an upward (downward) heat transport. Positive values result from frontogenesis processes, that is, the production of fronts, as illustrated in Fig. 3b. Negative values arise from frontolysis processes, that is, the destruction of fronts (Supplementary Information). Heat transport is strongly enhanced at the location of submesoscale fronts generated by the background strain field and has a local amplitude that reaches  $2,000 \text{ W m}^{-2}$  below the surface mixed layer, and extends down to at least 400 m, consistent with the high-resolution regional model (Extended Data Figs. 5b and 6) and, surprisingly, of the same order of magnitude as instantaneous air–sea heat fluxes<sup>19</sup>.

We explored the contribution of fine oceanic scales to the domain-averaged VHT. Averaged VHT within the eddy-rich area of the ACC sampled by the seal (1,000–2,000 km, in red in Fig. 1) is directed upward, that is, from the ocean interior back to the surface (Fig. 5f). This direction is strikingly opposite to that induced by the diffusive processes used in the classical paradigm. However, this result can be understood in terms of the direct cascade of potential energy, a well-known property of mesoscale eddy turbulence<sup>25</sup>. The direct cascade implies that frontogenesis statistically dominates frontolysis, and thus that the net VHT associated with submesoscale fronts is positive (Supplementary Information), which is also striking in the model outputs (Extended Data Fig. 6). Furthermore, the heat transport magnitude reached an averaged value of  $\sim 100 \text{ W m}^{-2}$  at 200 m (Fig. 5f). Remarkably, this value is an order of magnitude larger than

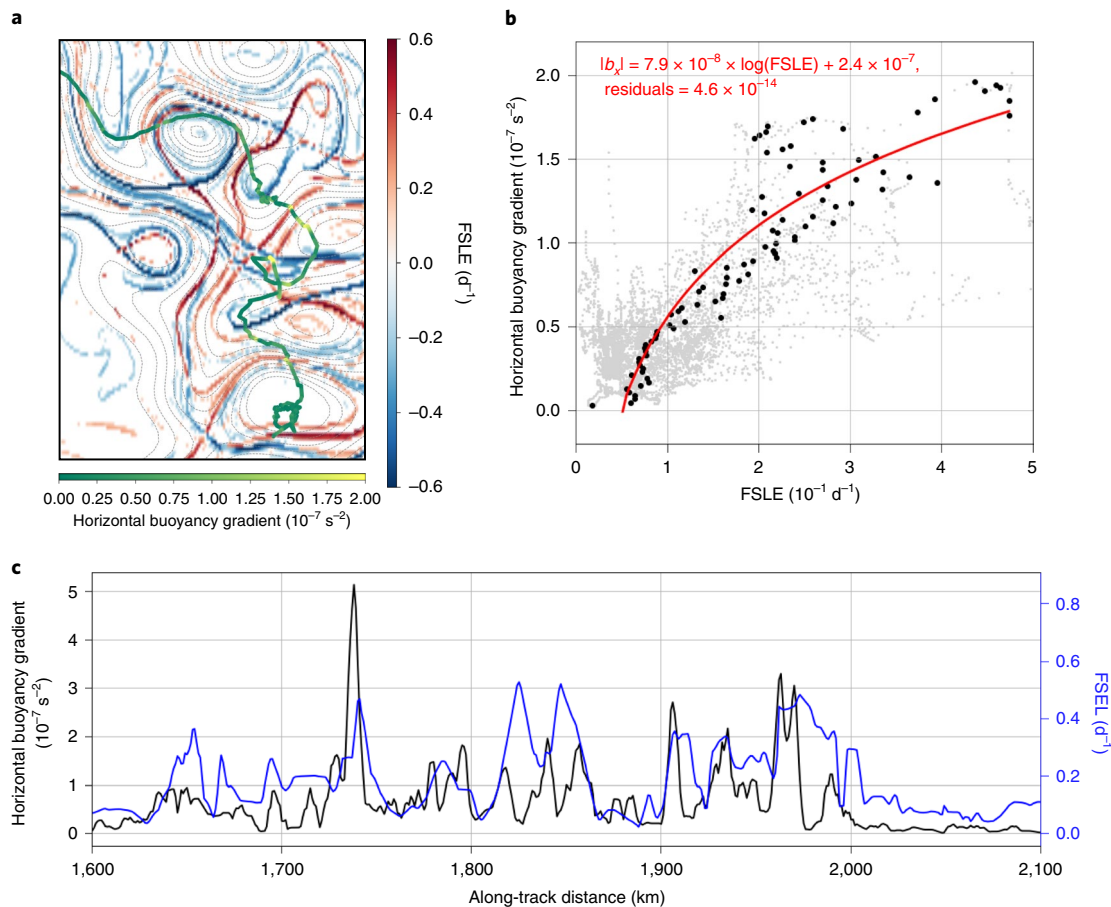


**Fig. 4 | FSLE and horizontal buoyancy gradients ( $|b_x|$ ).** **a**, A snapshot of FSLE and SSH contours (dashed grey) for 13 November 2014 in the strongly turbulent region (red line in Fig. 1), with surface  $|b_x|$  from 2 November to 24 November 2014. **b**, A scatter plot of along-seal-track stretching FSLE and  $|b_x|$  at 300 m, over the entire trajectory, after a 30 km moving average and averaging the y axis over 100 bins (black dots), with unaveraged data in grey. The relationship obtained between FSLE and  $|b_x|$  is given in red. **c**, Along-seal-track time series of stretching FSLE (blue) and  $|b_x|$  at 30 m (black) after a 5 km moving average.

that associated with mesoscale eddies alone<sup>26</sup>, which is, along with the mean flow, traditionally thought to be the main contributor to VHT<sup>2</sup>. It is also of comparable magnitude to domain-averaged air-sea heat fluxes<sup>15</sup>, which illustrates a potential coherent pathway that links the ocean interior to the atmosphere. Note that the percentage of seal dives decreases with depth (grey line in Fig. 5f), from 100 to 40% between 200 and 400 m. This probably accounts for a part of the r.m.s. decrease (stagnation) of temperature (velocity) anomalies below 200 m, as one would have expected<sup>5</sup> (Fig. 5d,e). As a consequence, the already unexpected strong heat transport (Fig. 5c,f) is likely to be underestimated because of it, in addition to the conservative estimate of the vertical currents discussed in the previous section. Indeed, the domain-integrated heat transport from the high-resolution numerical simulation yields a similar—although stronger—positive VHT (Extended Data Fig. 7) with, for instance, a value of  $\sim 140 \text{ W m}^{-2}$  at 200 m. As such, these results strongly contrast with the classical paradigm based on diffusive heat transport, as they emphasize the existence of an intense and upward heat transport in the ocean interior well below the ocean surface mixed layer that is preferentially localized in strain-dominated areas (Extended Data Fig. 6).

The data presented here provide the first observational evidence of a large and anomalous, that is, upward, heat transport associated with deep-reaching submesoscale fronts in an eddy-rich area of the world ocean. The observations, supported by a high-resolution regional model (Supplementary Information), highlight the crucial

role played by submesoscale frontal dynamics in the ocean interior, well below the ocean surface mixed layer, for oceanic heat transport.

In summary, the deep-reaching frontal dynamics and its associated large positive VHT, observed here in numerous sharp fronts of the ACC, are driven by mesoscale eddies and are likely to occur widely in the ocean, such as in the eddy-rich Gulf Stream and Kuroshio Extension, all of which are key players in the climate system. It potentially plays an important role by, for instance, exacerbating restratification processes as warm (cold) waters become warmer (colder). Furthermore, a first-order estimation indicates that these deep ocean fronts lead to an additional increase of the sea surface temperature that ranges between  $\sim 0.2$  and  $\sim 0.6^\circ\text{C}$  within a month (Methods gives the calculation and caveats), which illustrates the potential impact of deep-reaching ocean fronts on air-sea fluxes and how they can substantially limit oceanic heat uptake from the atmosphere.

These observational results suggest revisiting current estimates of the Earth's heat budget and stress the need to account for small-scale physics, not only within, but also below, the ocean surface mixed layer, in the prediction of future climate states. Inaccurate representation of such physics could considerably underestimate the amount of heat transferred from the ocean interior back to the surface and, as a consequence, potentially overestimate the amount of heat the ocean can absorb. Finally, these results may have a far greater scope as the evidence for intense vertical currents associated

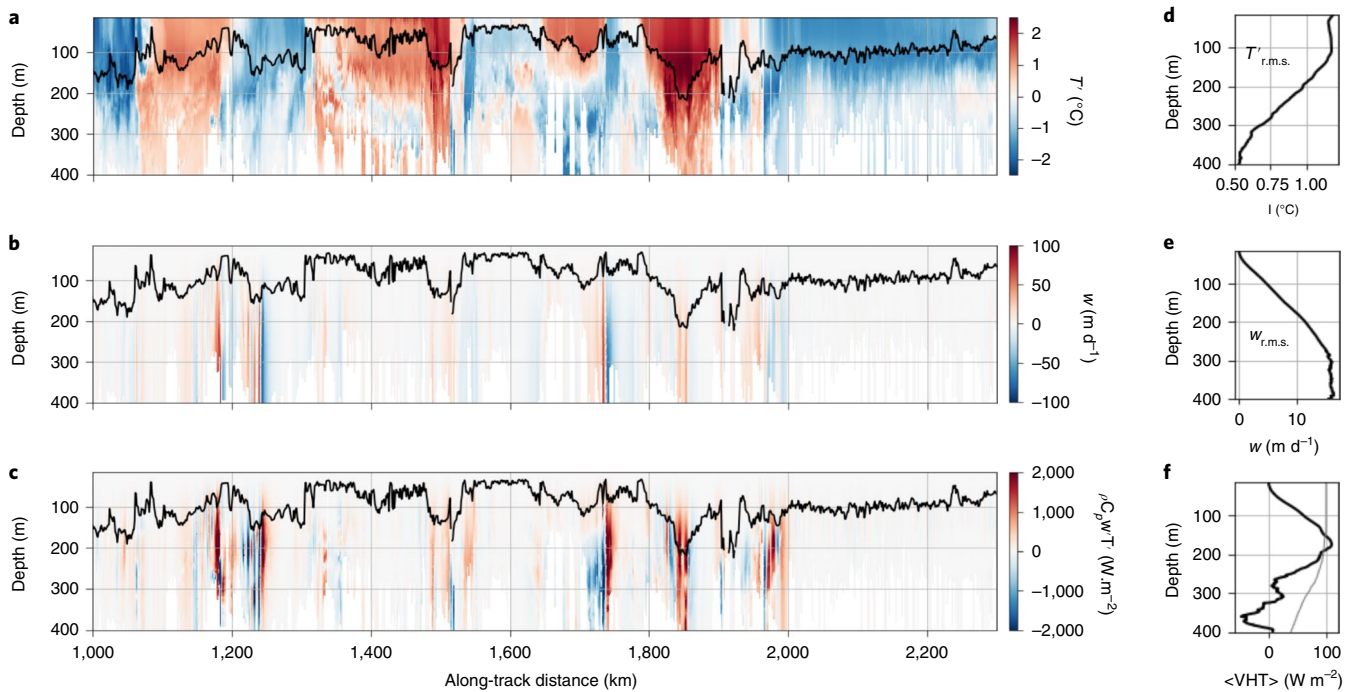


**Fig. 5 | Temperature anomaly, vertical velocity and VHT.** **a–c**, The vertical section of the seal-sampled temperature anomaly ( $T$ ) (**a**), vertical velocity derived from the seal and satellite data with equation (3) (**b**) and VHT (**c**), as defined in Methods. In **a–c**, the MLD is in bold black. **d,e**, The r.m.s. ( $z$ ) from 1,000 to 2,000 km of the temperature anomaly (**d**) and the vertical velocity (**e**). **f**, Averaged VHT ( $\langle \text{VHT} \rangle$ ) (black line).  $\langle \text{VHT} \rangle$  reaches  $\sim +110 \text{ W m}^{-2}$  at 200 m. The percentage of profiles (grey line) goes from 100% at 20 m to 40% at 400 m.

with the deep-reaching ocean fronts presented here also indicates an efficient pathway for the transport of chemical and biological tracers, with potential major implications for biogeochemical systems.

### Online content

Any methods, additional references, Nature Research reporting summaries, source data, extended data, supplementary information, acknowledgements, peer review information; details of author contributions and competing interests; and statements of data and code availability are available at <https://doi.org/10.1038/s41561-019-0489-1>.

Received: 18 June 2019; Accepted: 16 October 2019;

### References

- Munk, W. & Wunsch, C. Abyssal recipes II: energetics of tidal and wind mixing. *Deep Sea Res. Part I* **45**, 1977–2010 (1998).
- Wolfe, C., Cessi, P., McClean, J. & Maltrud, M. Vertical heat transport in eddy ocean models. *Geophys. Res. Lett.* **35**, L23605 (2008).
- Griffies, S. M. et al. Impacts on ocean heat from transient mesoscale eddies in a hierarchy of climate models. *J. Clim.* **28**, 952–977 (2015).
- Ferrari, R. & Wunsch, C. Ocean circulation kinetic energy: reservoirs, sources, and sinks. *Annu. Rev. Fluid Mech.* **41**, 253–282 (2009).
- Klein, P. & Lapeyre, G. The oceanic vertical pump induced by mesoscale and submesoscale turbulence. *Annu. Rev. Mar. Sci.* **1**, 351–375 (2009).
- Ferrari, R. A frontal challenge for climate models. *Science* **332**, 316–317 (2011).
- Mahadevan, A. The impact of submesoscale physics on primary productivity of plankton. *Annu. Review Mar. Sci.* **8**, 161–184 (2016).
- McWilliams, J. C. Submesoscale currents in the ocean. *Proc. R. Soc. A* **472**, 20160117 (2016).
- Lévy, M., Frank, P. J. & Smith, S. K. The role of submesoscale currents in structuring marine ecosystems. *Nat. Commun.* **9**, 4758 (2018).
- Vallis, G. K. *Atmospheric and Oceanic Fluid Dynamics* (Cambridge Univ. Press, 2017).
- Taylor, J. R. & Ferrari, R. Ocean fronts trigger high latitude phytoplankton blooms. *Geophys. Res. Lett.* **38**, 23 (2011).
- Thomas, L. N., Taylor, J. R., Ferrari, R. & Joyce, T. M. Symmetric instability in the Gulf Stream. *Deep. Sea Res. Pt II* **91**, 96–110 (2013).
- Bachman, S. D. & Taylor, J. R. Modelling of partially-resolved oceanic symmetric instability. *Ocean Model.* **82**, 15–27 (2014).
- Yu, X. et al. An annual cycle of submesoscale vertical flow and restratification in the upper ocean. *J. Phys. Oceanogr.* **49**, 1439–1461 (2019).
- Large, W. G. & Yeager, S. The global climatology of an interannually varying air–sea flux data set. *Clim. Dynam.* **33**, 341–364 (2009).
- Hogg, A. M. et al. Recent trends in the Southern Ocean eddy field. *J. Geophys. Res. Ocean* **120**, 257–267 (2015).
- Chelton, D. B., DeSzoeke, R. A., Schlax, M. G., El Naggar, K. & Siwertz, N. Geographical variability of the first baroclinic Rossby radius of deformation. *J. Phys. Oceanogr.* **28**, 433–460 (1998).
- Chelton, D. B., Schlax, M. G., Freilich, M. H. & Milliff, R. F. Satellite measurements reveal persistent small-scale features in ocean winds. *Science* **303**, 978–983 (2004).
- Thompson, A. F. et al. Open-ocean submesoscale motions: a full seasonal cycle of mixed layer instabilities from gliders. *J. Phys. Oceanogr.* **46**, 1285–1307 (2016).
- duPlessis, M., Swart, S., Ansgore, I. J. & Mahadevan, A. Submesoscale processes promote seasonal restratification in the Subantarctic Ocean. *J. Geophys. Res. Ocean* **122**, 2960–2975 (2017).
- Vigilione, G. A., Thompson, A. F., Flexas, M. M., Sprintall, J. & Swart, S. Abrupt transitions in submesoscale structure in southern Drake Passage: glider observations and model results. *J. Phys. Oceanogr.* **48**, 2011–2027 (2018).
- d’Ovidio, F. & Fernández, V. Hernández-García, E. & López. Mixing structures in the Mediterranean Sea from finite-size Lyapunov exponents. *Geophys. Res. Lett.* **31**, L17203 (2004).
- Hoskins, B. J., Draghici, I. & Davies, H. C. A new look at the  $\omega$ -equation. *Q. J. R. Meteorol. Soc.* **104**, 31–38 (1978).
- McGillicuddy Jr, D. J. Mechanisms of physical–biological–biogeochemical interaction at the oceanic mesoscale. *Annu. Review Mar. Sci.* **8**, 125–159 (2016).
- Salmon, R. Baroclinic instability and geostrophic turbulence. *Geophys. Astrophys. Fluid Dyn.* **15**, 167–211 (1980).
- Su, Z., Wang, J., Klein, P., Thompson, A. F. & Menemenlis, D. Ocean submesoscales as a key component of the global heat budget. *Nat. Commun.* **9**, 775 (2018).

**Publisher’s note** Springer Nature remains neutral with regard to jurisdictional claims in published maps and institutional affiliations.

This is a U.S. government work and not under copyright protection in the U.S.; foreign copyright protection may apply 2019

## Methods

**SSH and geostrophic currents.** The SSH used to retrieve the mesoscale dynamics of the Kerguelen area (67–91°E, 48–58°S) is composed of the mean dynamic topography CNES/CLS 2015<sup>27</sup> and the sea level anomaly maps produced by the DUACS (data unification and altimeter combination system) processing chain that merges the multi-altimeter along-track data. This specific regional dataset was produced in the context of the DUACS-HR project, which aimed to increase the resolution of altimetry maps by applying recently developed methods, such as dynamic interpolation<sup>28</sup>. The period from October 2014 to January 2015 benefits from an extremely favourable satellite coverage of four altimeters (AltiKa, Jason-2, Cryosat-2 and HY-2), which allowed a very good spatial and temporal sampling. The temporal resolution is daily and, as estimated in Ballarotta et al.<sup>29</sup>, the spatial effective resolution of the gridded anomalies approaches 40 km in wavelength. Using the geostrophic approximation, geostrophic surface currents ( $u, v$ ) are derived from SSH following<sup>10</sup>:

$$u = -\frac{g}{f} \frac{\partial \text{SSH}}{\partial y}, \quad v = \frac{g}{f} \frac{\partial \text{SSH}}{\partial x} \quad (1)$$

where  $g$  is gravity and  $f$  the Coriolis parameter.

**FSLE.** Instead of using a direct estimate of the strain rate (that is,  $du/dx$  calculated directly from SSH, Fig. 3) that only describes the buoyancy gradient's growth rate, we use FSLEs. Indeed, FSLEs have the advantage of exploiting both the spatial and temporal variability of the velocity field deduced from SSH, and consequently provide information about both the growth rate and orientation of elongated buoyancy gradients<sup>30,31</sup>. FSLE is a Lagrangian diagnostic that measures the separation of close initial particles embedded in a given flow field. The separation's growth rate is defined as:

$$\lambda(d_0, d_f) = \frac{1}{\tau} \log\left(\frac{d_f}{d_0}\right) \quad (2)$$

where  $d_0$  and  $d_f$  are the initial and final separation distances, respectively, and  $\tau$  the first time at which a separation  $d_f$  is reached. FSLE has the dimension of time<sup>-1</sup>. FSLE is particularly suited to diagnose the properties of a strain field. Positive (negative) FSLE indicate that patches of particles are being stretched (compressed) in a given direction determined by the background strain field. As such, large positive (negative) FSLE values indicate regions of strong stretching (compression) (Fig. 3a and Supplementary Information give more details). Here, positive (negative) FSLE are computed backward (forward) in time<sup>22</sup>.

For the Kerguelen area, 88 daily maps of altimetry-based FSLEs were computed following d'Ovidio et al.<sup>22</sup> and using the geostrophic velocities derived from the SSH. The parameters were chosen close to those of d'Ovidio et al.<sup>22</sup> with  $d_0 = 0.04^\circ$  and  $d_f = 1^\circ$ , that is, a final separation distances of about 110 km.

An along-track time series of stretching (that is, positive) FSLE was extracted along the seal's path to capture the stretching direction and intensity of the strain field. A subsequent 5 km window moving average was applied to remove the strong intermittency present in the raw data (Fig. 4 and Extended Data Fig. 4a). Stretching FSLEs were then compared to lateral gradients of buoyancy sampled by the seal.

**Southern elephant seal measurements.** A newly released in situ dataset collected in the austral summer by a female southern elephant seal during her three-month post-breeding trip (20 October 2014 to 16 January 2015) east of the Kerguelen Islands (Indian sector of the Southern Ocean, Fig. 1) was analysed. Compared to previous tags mounted on elephant seals, this one recorded every single dive realized by the animal (> 80 dives per day) at high-resolution as opposed to 2–5 dives per day for previous tags. The seal was localized through the Argos satellite system and was equipped with sensors that recorded conductivity, temperature and pressure (CTD-Satellite Relay Data Logger) at a continuous frequency of 0.5 Hz. Only the ascending phase of a dive was used because it is more uniform in speed and direction compared to the descent when the seal dives sinusously to forage<sup>32</sup>. The dataset comprised 6,333 dives, which corresponds to a cumulative length of 5,270 km with a median spacing between two dives of 700 m (Extended Data Fig. 8a). Dives, which could be as deep as 500–1,000 m, lasted less than 25 min and were separated by intervals of a few minutes during which the seal breathes but does not transit. More than 80% of the dives reached a depth of at least 200 m, 50% reached 300 m and 35% reached 400 m or deeper.

To ensure a better accuracy of the temperature- and conductivity-derived salinity data, two additional steps were applied: first, a thermal cell effect correction was applied to the temperature and conductivity fields. A density inversion removal algorithm, which seeks the minimum adjustment of the salinity profile to achieve neutral stability, was subsequently applied to the salinity field. The accuracy of the final postprocessed data was  $\pm 0.02^\circ\text{C}$  for the temperature and  $\pm 0.03 \text{ g kg}^{-1}$  for salinity. More details on the postprocessing method and final data accuracy are given in Siegelman et al.<sup>32</sup>. Potential density was calculated from the corrected conservative temperature and absolute salinity with the TEOS-10 equation<sup>33</sup>.

The animal in this study was handled in accordance with the Institut polaire francais Paul-Emile Victor (IPEV) ethical and Polar Environment Committees

guidelines as part of the SNO-MEMO and IPEV program 109 (principle investigator H. Weimerskirch). The experimental protocols were approved by the Ethics Committee of IPEV and the Polar Environment Committees.

**Buoyancy.** Along-track time series of buoyancy,  $b = g(1 - \rho/\rho_0)$ , where  $g$  is gravity,  $\rho$  is potential density and  $\rho_0 = 1,025 \text{ kg m}^{-3}$  is a reference density, revealed a variability that covers both the meso- and submesoscales. For the analysis, in particular the calculation of lateral buoyancy gradients  $b_x = \partial b/\partial x$ , buoyancy was first linearly interpolated along the seal's path onto a regular grid of 100 m resolution, which corresponds to the shortest along-track distance between two dives (Extended Data Fig. 8a). A moving average with a 1 km window was then applied such that the final dataset had a horizontal resolution of 1 km and a vertical resolution of 1 m. Buoyancy anomalies were resolved by multiple vertical profiles, such that the structures were not related to aliasing of the along-track data. The surface buoyancy anomalies in Fig. 2a,b were defined by the time series of the mean buoyancy from 15 to 50 m minus its mean value calculated from 15 to 50 m along the entire trajectory.

**MLD.** The MLD was defined as the level of a  $0.03 \text{ kg m}^{-3}$  density increase from 15 m depth.

**Normalization of buoyancy gradients.** As the seal's trajectory was more often oblique to the stretching FSLEs (it crossed rather than ran perpendicular to them (Extended Data Fig. 8b)) and buoyancy fronts were assumed to be aligned with the stretching FSLE, buoyancy gradients sampled by the seal needed to be corrected to account for the seal's orientation with respect to the FSLE it encountered. To do so, the buoyancy gradients were divided by the sine of the angle  $\theta$  between the seal's trajectory and the FSLE direction. More precisely,  $\theta$  is the angle between the FSLE eigenvector and the seal's path. To focus on the regions prone to the formation of submesoscales, only  $b_x$  associated with large FSLE (>  $0.15 \text{ d}^{-1}$ ) were normalized and are referred to as  $b_x$ . However, a sensitivity analysis (which ranged from 0.1 to  $0.3 \text{ d}^{-1}$ , not shown here) to this threshold value led to similar results.

**Link between strain, frontogenesis and VHT.** The ambient strain field in Fig. 3a acts to elongate the tracer patch in the stretching direction ( $y$  direction) and to compress it in the  $x$  direction because the area of the tracer patch is conserved to the leading order<sup>10</sup>. This increases the tracer gradient in the  $x$  direction. The orientation and timescale of the strain field can be captured by FSLE. In Fig. 3a, the red (blue) FSLE lines identify the horizontal stretching (compressing) direction. This mechanism is particularly relevant for the formation of submesoscale fronts, which are thus aligned with the stretching FSLE (red line). Figure 3b shows a schematic illustration of the frontogenesis process. It corresponds to a 3D slice through a submesoscale front generated by a background mesoscale strain field (curved black arrows), like that in Fig. 3a. Warmer (or equivalently lighter) fluid (light red) is on the right of the Fig. 3b and colder (or equivalently heavier) fluid (light blue) is on the left. As a consequence, the VHT associated with frontogenesis is directed upward because of the positive correlation between the temperature and vertical velocity anomalies.

**Richardson number.** The non-dimensional Richardson number  $Ri$ , estimated from the seal measurements, is defined as  $Ri \equiv f^2 N^2 / b_x^2$ , with  $N^2 = \partial b/\partial z$  the Brunt-Väisälä frequency and  $b_x = \partial b/\partial x$  the normalized along-track lateral gradient of buoyancy.  $Ri$  characterizes the dynamic regime and can be interpreted as the steepness of the isopycnal slopes relatively to  $N/f$ , as  $Ri = \frac{f^2}{N^2} \left(\frac{\partial b/\partial z}{\partial b/\partial x}\right)^2 = \frac{f^2}{N^2} \left(\frac{\partial x}{\partial z}\right)^2$ . Thus, for  $Ri > 1$ , which corresponds to the QG regime<sup>34,35</sup>, the steepness of the isopycnal slope,  $\frac{\partial b/\partial x}{\partial b/\partial z}$ , is small. For  $Ri$  close to one (that is,  $Ri \leq 4$ ), which corresponds to the ageostrophic regime<sup>34,35</sup>, the steepness of the isopycnal slope,  $\frac{\partial b/\partial x}{\partial b/\partial z}$ , is large. Seal observations suggest a strong ageostrophic regime, as instances of strong  $b_x$ ,  $|b_x| \geq 2.5 \times 10^{-7} \text{ s}^{-2}$ , coincide with  $Ri < 2$  (Fig. 2 and Extended Data Fig. 2b). Small  $Ri$  values ( $Ri < 2$ ) indicate an ageostrophic regime in which the vertical currents are large<sup>34,35</sup>.

**Vertical velocities.** Classical methods to diagnose vertical velocities are based on the Q-vector version of the omega equation<sup>23,36</sup>. In this study, we used the QG version of the omega equation (Supplementary Information discusses this choice). Buoyancy fronts are assumed to be elongated along a stretching direction (red FSLE in Fig. 3a) such that the along-front gradient of buoyancy in the  $y$  direction is negligible with respect to the cross-front one ( $x$  direction). Thus, we considered the 2D version ( $x, z$ ) of the QG omega equation. This equation assumes that the trajectory is normal to the front, that is, that the front is embedded in a pure strain field, which is achieved through the buoyancy gradient normalization mentioned above. This equation is:

$$N^2 w_{xx} + f^2 w_{zz} = -2 (u_x b_x)_x \quad (3)$$

where the subscripts indicate the derivatives.  $u_x$  is estimated from stretching FSLE derived from satellite altimetry and  $b_x$ ,  $N^2$  and  $f^2$  are from the seal's measurements.

Equation (3) is solved using the flexible framework for spectrally solving differential equations provided by Dedalus<sup>37</sup>.

Note that when the Richardson number is close to one, equation (3) underestimates the vertical velocities. When  $Ri \approx 2$ , the magnitude of this underestimation is of  $\sim 0.7$ , which implies that the vertical velocities  $w$  diagnosed at sharp fronts should be closer to  $1.4w$  (Supplementary Information gives more details).

Note also that this study focuses on strain-dominated regions. However, in other regions, for instance, within mesoscale eddies, the strain rate is weaker and its impact on the formation of horizontal gradients is counterbalanced by the impact of the relative vorticity, which leads to the formation of weaker gradients of buoyancy. In such regions, even though the 2D version of the omega equation is no longer appropriate and a 3D version needs to be used, the resulting vertical velocities are 7.5 times weaker than those associated to submesoscale fronts in strain-dominated regions<sup>5</sup>, like the ones considered in the present study.

**VHT.** The VHT is defined as  $\rho C_p w' T'$ , where  $C_p = 3,985 \text{ J kg}^{-1} \text{ K}^{-1}$  is the specific heat capacity of seawater,  $\rho = 1,025 \text{ kg m}^{-3}$  is the density of the fluid, and  $w'$  and  $T'$  are the vertical velocity and temperature anomalies, respectively.

**Impact of deep-reaching ocean fronts on the mixed-layer temperature.** The impact of the deep-reaching ocean fronts on the mixed-layer temperature, and therefore the sea surface temperature, is derived from a thermodynamic equation that captures the evolution of the mixed-layer temperature  $T$ . This approach has already been used and validated at leading order<sup>26</sup>. The equation, integrated over the mixed-layer depth, is:

$$C \frac{dT}{dt} = S - \lambda T \quad (4)$$

where  $C = \rho C_p H$  is the total heat capacity of the mixed layer,  $H$  is the mixed-layer depth,  $S$  is the heat transport at the base of the mixed layer due to deep-reaching fronts and  $-\lambda T$  is the negative feedback from the air–sea heat fluxes. From equation (4), a positive  $S$  causes a higher temperature  $T$ , and hence a larger upward air–sea heat exchange  $\lambda T$ .

A sensitivity analysis was carried out to assess the range of the mean mixed-layer temperature change due to submesoscales over a period of one month, which corresponds to the time spent by the seal in the turbulent region and the time span of the high-resolution model. We set  $S$  to vary between 50 and  $100 \text{ W m}^{-2}$ , as obtained from both the observational (Fig. 5f) and model (Extended Data Fig. 7) results,  $\lambda$  to vary between 15 and  $2 \text{ W m}^{-2} \text{ K}^{-1}$ , according to Vallis<sup>38</sup> and the mixed-layer  $H$  to vary between 100 and 200 m, which implies that  $C$  varies between  $\sim 4 \times 10^8$  and  $\sim 8 \times 10^8 \text{ J m}^{-2} \text{ K}^{-1}$ . As a consequence, equation (4) integrated over one month indicates that the mean mixed-layer temperature increase ranges between  $\sim 0.2$  and  $\sim 0.6^\circ \text{C}$ .

Note this is a first-order estimation that includes several caveats. In particular, this estimation does not take into account any subsequent atmospheric feedback on the ocean that may arise in response to these surface heat fluxes ( $\lambda T$ ). For instance, such a feedback may include interactions between the wind stress and SST anomalies at submesoscales<sup>39</sup>, which may limit the mean temperature increase.

## Data availability

The marine mammal data were collected and made freely available by the International MEOP Consortium and the national programs that contribute to it, and is available at [www.meop.net/database/meop-databases/meop-sms-database-submesosc.html](http://www.meop.net/database/meop-databases/meop-sms-database-submesosc.html). The Ssalto/Duacs altimeter products were produced and distributed by the Copernicus Marine and Environment Monitoring Service with support from CNES, and is available at <http://marine.copernicus.eu/services-portfolio/access-to-products/>.

## References

- Rio, M. H. et al. Improving the altimeter-derived surface currents using high-resolution sea surface temperature data: a feasibility study based on model outputs. *J. Atmos. Ocean. Technol.* **33**, 2769–2784 (2016).
- Ubelmann, C., Klein, P. & Fu, L. L. Dynamic interpolation of sea surface height and potential applications for future high-resolution altimetry mapping. *J. Atmos. Ocean. Technol.* **32**, 177–184 (2015).
- Ballarotta, M. et al. On the resolutions of ocean altimetry maps. *Ocean Sci.* **15**, 1091–1109 (2019).
- Waugh, D. W., Abraham, E. R. & Bowen, M. M. Spatial variations of stirring in the surface ocean: a case study of the Tasman Sea. *J. Phys. Oceanogr.* **36**, 526–542 (2006).
- d'Ovidio, F., Isern-Fontanet, J., López, C., Hernández-García, E. & García-Ladona, E. Comparison between Eulerian diagnostics and finite-size Lyapunov exponents computed from altimetry in the Algerian Basin. *Deep. Sea Res. Pt I* **56**, 15–31 (2009).
- Siegelman, L. et al. Correction and accuracy of high-and low-resolution CTD data from animal-borne instruments. *J. Atmospheric Ocean. Technol.* **36**, 745–760 (2019).
- Intergovernmental Oceanographic Commission *The International Thermodynamic Equation of Seawater—2010: Calculation and Use of Thermodynamic Properties (Includes Corrections up to 31st October 2015)* (UNESCO, 2015); [https://www.oceanbestpractices.net/bitstream/handle/11329/286/TEOS-10\\_Manual.pdf?sequence=1](https://www.oceanbestpractices.net/bitstream/handle/11329/286/TEOS-10_Manual.pdf?sequence=1)
- Molemaker, J., McWilliams, J. & Yavneh, I. Baroclinic instability and loss of balance. *J. Phys. Oceanogr.* **35**, 1505–1517 (2005).
- Thomas, L. N., Tandon, A. & Mahadevan, A. in *Ocean Modeling an Eddy Regime* (eds Hecht, M. W. & Hasumi, H.) 17–38 (Geophysical Monograph Series Vol. 177, American Geophysical Union, 2008).
- Giordani, H., Prieur, L. & Caniaux, G. Advanced insights into sources of vertical velocity in the ocean. *Ocean. Dyn.* **56**, 513–524 (2006).
- Burns, K. J., Vasil, G. M., Oishi, J. S., Lecoanet, D. & Brown, B. Dedalus: Flexible Framework for Spectrally Solving Differential Equations (Astrophysics Source Code Library, 2016).
- Vallis, G. K. *Climate and the Oceans* (Princeton Univ. Press, 2012).
- Foussard, A., Lapeyre, G. & Plougonven, R. Response of surface wind divergence to mesoscale SST anomalies under different wind conditions. *J. Atmos. Sci.* **76**, 2065–2082 (2019).

## Acknowledgements

We thank K. Richards for his insightful comments, F. d'Ovidio for providing the code to compute FSLE. The elephant seal work was supported as part of the SNO-MEMO and by the CNES-TOSCA project Elephant seals as Oceanographic Samplers of submesoscale features led by C. Guinet with support of the French Polar Institute (programmes 109 and 1201). This research was carried out, in part, at the Jet Propulsion Laboratory, California Institute of Technology, under a contract with the National Aeronautics and Space Administration (NASA). High-end computing resources for the numerical simulation were provided by the NASA Advanced Supercomputing Division at the Ames Research Center. This work was partly funded by the CNES (OSTST-OSIW) and the Laboratoire d'Excellence LabexMER (ANR-10-LABX-19). L.S. is a NASA-JVSRP affiliate and is supported by a joint CNES-Région Bretagne doctoral grant. P.K. is supported by the NASA-CNES SWOT mission and a NASA Senior NPP Fellowship. A.F.T. is supported by the David and Lucille Packard Foundation and NASA grant NNX16AG42G. M.F. is supported by NASA grant NNX15AG42G.

## Author contributions

L.S. and P.K. conceived the experiments, analysed the results and wrote the manuscript. D.M. and H.S.T. ran the numerical simulations. H.S.T. helped with analysing the regional simulation. L.S., P.K., P.R., A.F.T., H.S.T. and M.F. reviewed the manuscript.

## Competing interests

The authors declare no competing interests.

## Additional information

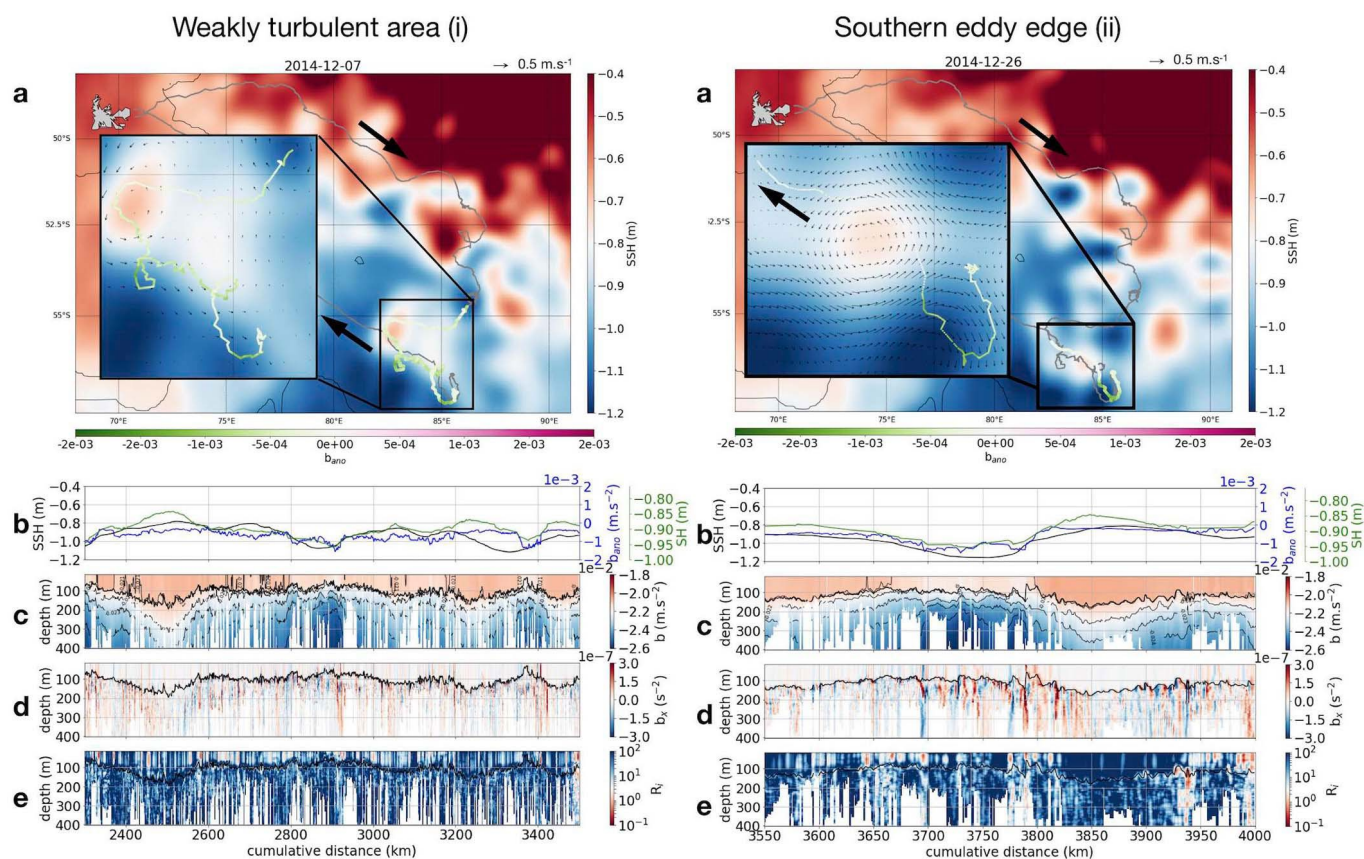
**Extended data** is available for this paper at <https://doi.org/10.1038/s41561-019-0489-1>.

**Supplementary information** is available for this paper at <https://doi.org/10.1038/s41561-019-0489-1>.

**Correspondence and requests for materials** should be addressed to L.S.

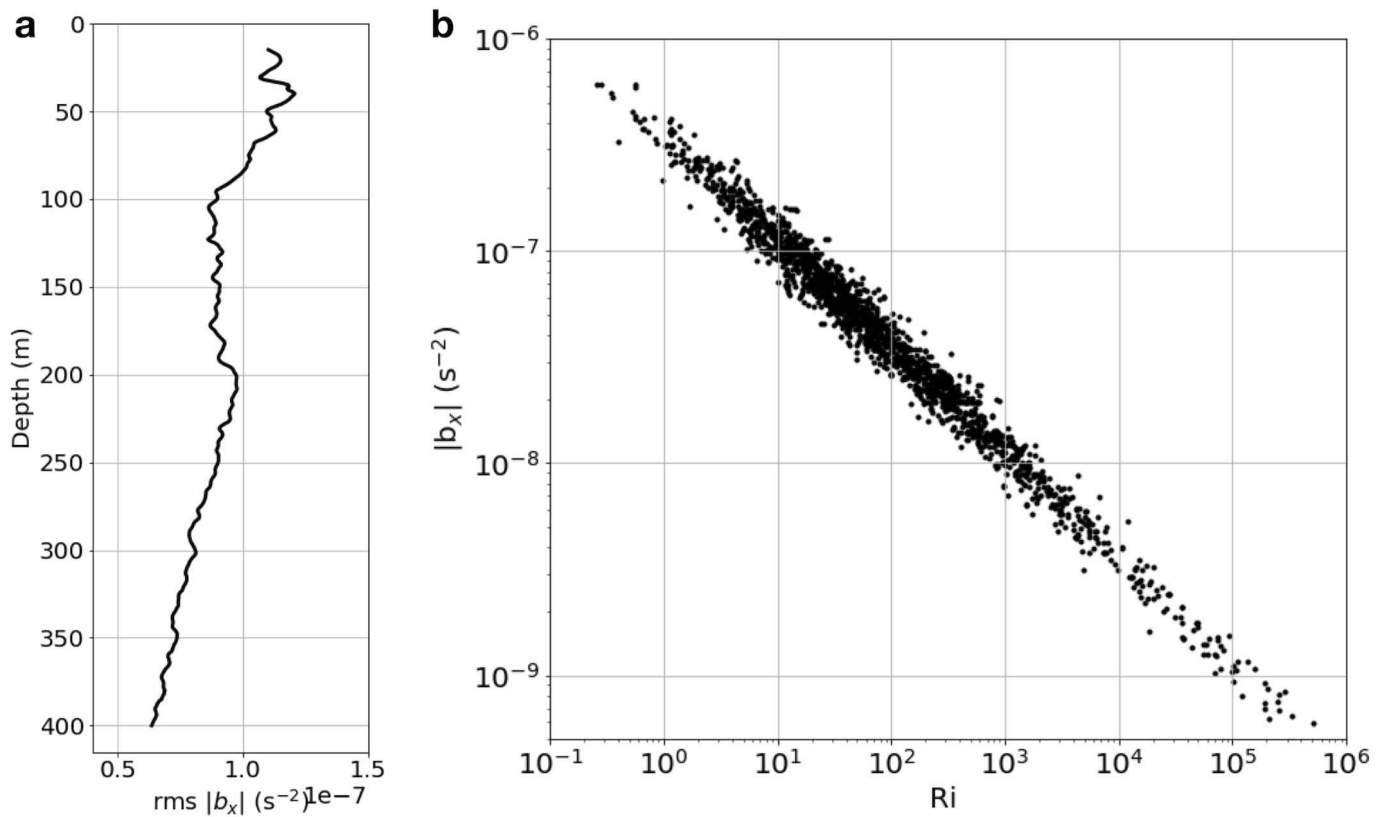
**Peer review information** Primary Handling Editor(s): Heike Langenberg.

**Reprints and permissions information** is available at [www.nature.com/reprints](http://www.nature.com/reprints).

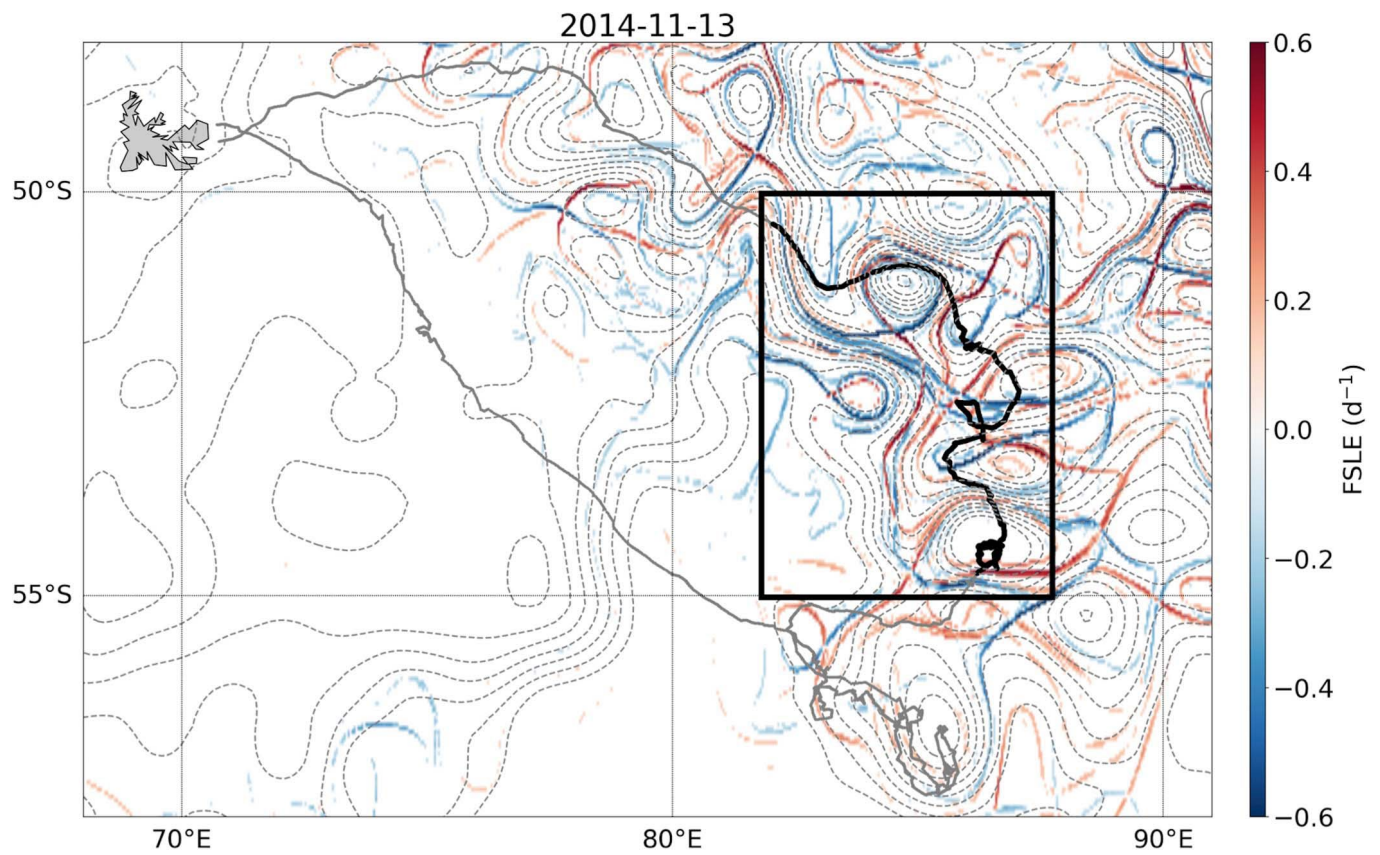


**Extended Data Fig. 1 | Weakly turbulent and southern eddy edge areas.** Same as Fig. 2 but for i) 2014/11/24 to 2014/12/20 with the SSH snapshot in **a**) taken on 2014/12/07. The seal crosses a large anti-cyclonic region (grey trajectory in Fig. 1) characterized by weaker currents (smaller SSH anomalies) and referred to as the weakly turbulent area. ii) 2014/12/22-29 with the SSH snapshot in **a**) taken on 2014/12/26. The seal follows the edges of mesoscale eddies over a distance of ~600 km. This region is referred to as the southern eddy (in orange in Fig. 1). Bold black arrows indicate the direction of the seal.

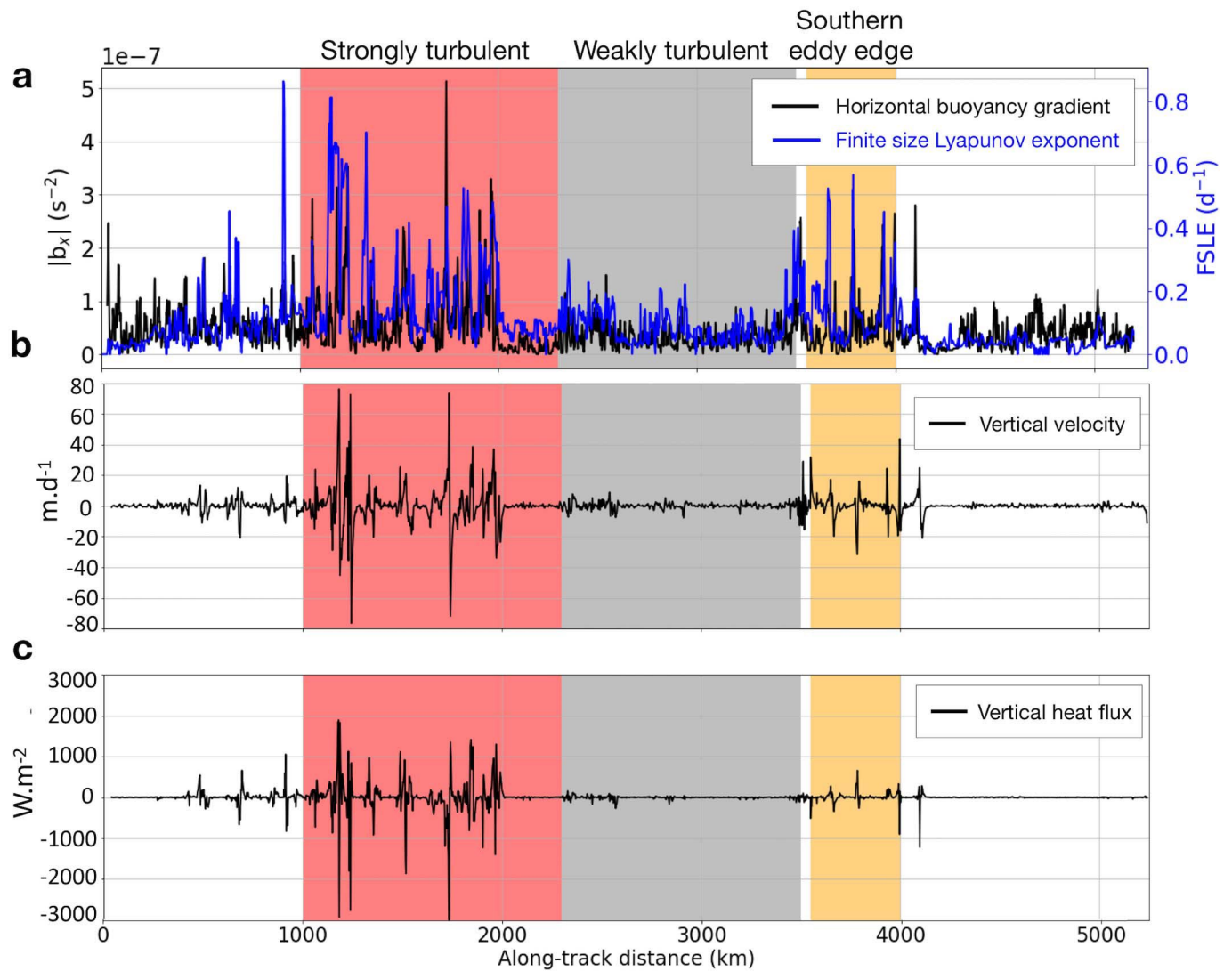




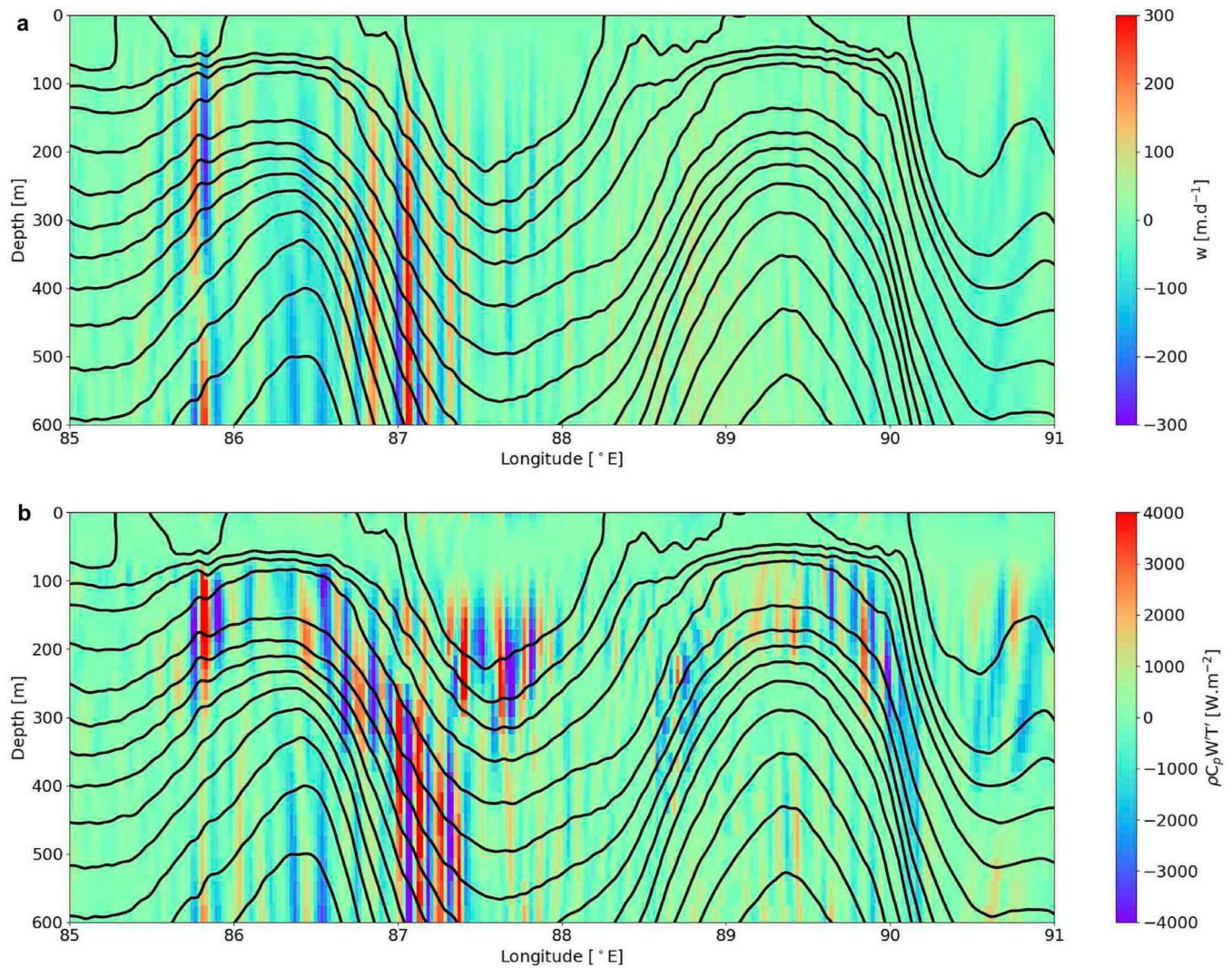
**Extended Data Fig. 2 | Lateral gradient of buoyancy and Richardson number in the strongly turbulent area. a)** RMS of lateral gradients of buoyancy,  $|b_x|$ , as a function of depth in the strongly turbulent area. **b)** Scatter plot between lateral gradients of buoyancy,  $|b_x|$ , and Richardson number,  $Ri$ , in the strongly turbulent area.  $Ri < 2$  coincide with strong buoyancy gradients ( $|b_x| > 2.5 \times 10^{-7} \text{ s}^{-2}$ ), highlighting the ageostrophic character of the dynamical regime encountered by the seal and the expected strong frontogenesis processes at play.



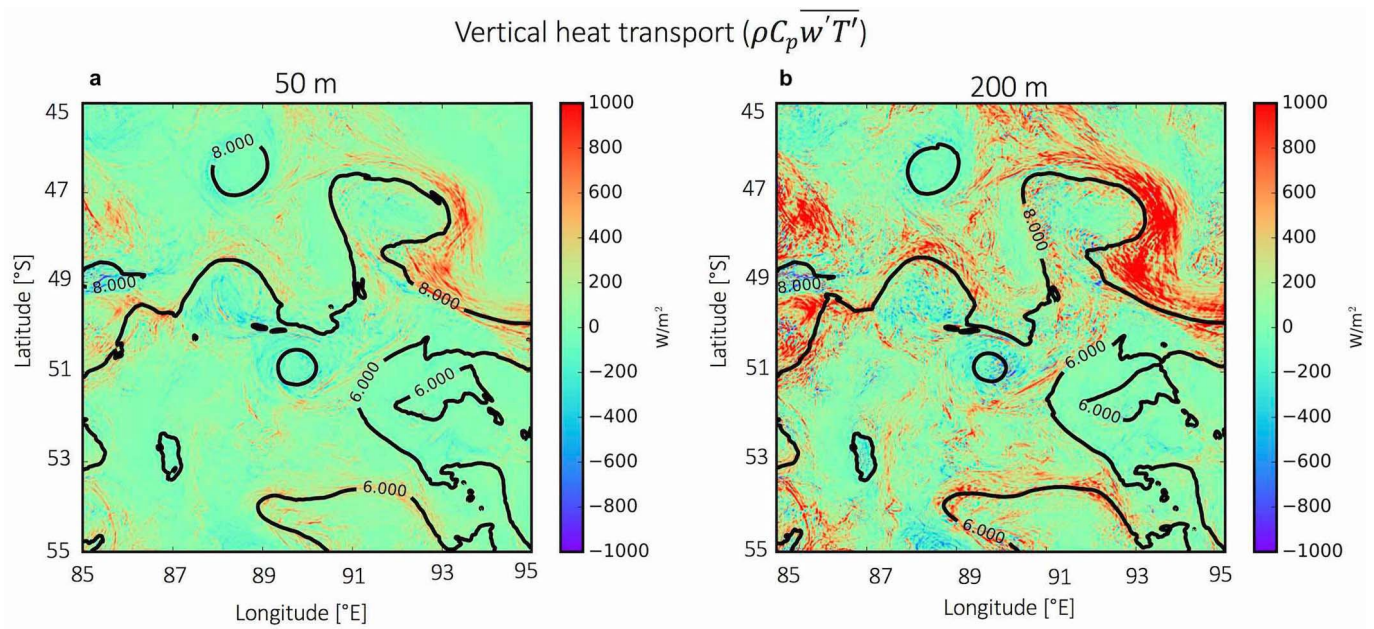
**Extended Data Fig. 3 | Map of finite size Lyapunov exponents.** Map of FSLE over the entire domain on 13 November 2014. FSLE are greatly enhanced in the strongly turbulent region (black rectangle and in red in Fig. 1) compared to the rest of the domain.



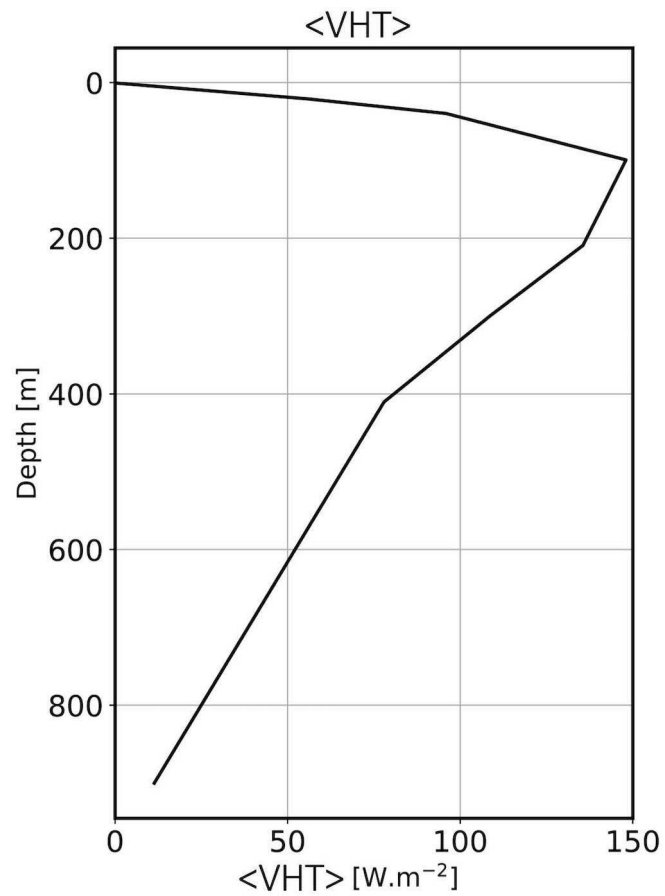
**Extended Data Fig. 4 | Finite size Lyapunov exponents and horizontal gradient of buoyancy, vertical velocities and vertical heat transport at 300 m.** Times series of **a**) Horizontal gradients of buoyancy at 300 m sampled by the seal (in black) and FSLE derived from satellite altimetry along the seal's track (in blue). **b**) Vertical velocities at 300 m derived from the seal and satellite data by solving the omega equation (see main text and Methods). **c**) Vertical heat transport (see Methods). The areas described in the main text and in Fig. 1 are highlighted by the colored rectangles.



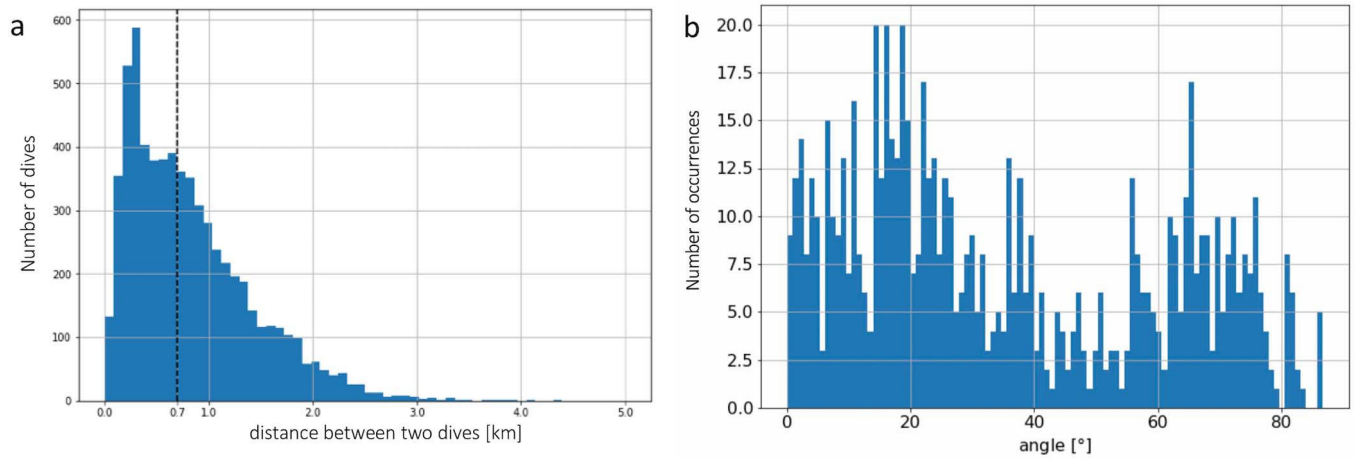
**Extended Data Fig. 5 | Daily averaged vertical velocities and vertical heat transport from the high-resolution numerical simulation.** Daily averaged vertical section from the high-resolution numerical simulation for November 22, 2011 at 52°S of **a**) Vertical velocities **b**) Vertical heat transport. Isopycnals are shown by the black lines. Enhanced vertical velocities and heat transport with a width of 5-10 km are found in the ocean interior and, in particular, below the mixed layer, similar to the observation presented in the main text.



**Extended Data Fig. 6 | Averaged vertical heat transport from the high-resolution numerical simulation.** 2-D (x,y) view of 10-day averaged vertical heat transport (VHT) at a) 50 m and b) 200 m. Isotherms are shown in black. Domain averaged values are respectively 92 and 197  $W/m^2$ . VHT is enhanced at depth and follows the isotherms on the eddy edges, and its averaged value is directed upward (positive value), all of which is consistent with the observational results presented in the main text.



**Extended Data Fig. 7 | Domain averaged vertical heat transport from the high-resolution numerical simulation.** Monthly averaged vertical heat transport (<VHT>) as a function of depth over the entire domain from the high-resolution numerical simulation. VHT is directed upwards (positive values) and its magnitude is similar - although even higher - than what is derived from the observational data presented in the main text.



**Extended Data Fig. 8 | Distance between two dives and angle between the seal's trajectory and the fronts. a)** Histogram of the distance between two dives. Median distance between two dives is 700 m (dotted line) and the shortest distance is 100 m. **b)** Histogram of the angle between the seal's trajectory and the stretching FSLE it encounters for FSLE > 0.15 day<sup>-1</sup>. Oblique crossings are most frequent and a normalization is implemented to correct for it (see Methods).

# Enhanced upward heat transport at deep submesoscale ocean fronts - Supplementary Information

Lia Siegelman<sup>1,2,3\*</sup>, Patrice Klein<sup>1,2,4</sup>, Pascal Rivière<sup>3</sup>, Andrew F. Thompson<sup>1</sup>, Hector S. Torres<sup>2</sup>, Mar Flexas<sup>1</sup>, and Dimitris Menemenlis<sup>2</sup>

<sup>1</sup>Environmental Science and Engineering, California Institute of Technology, Pasadena, CA, USA

<sup>2</sup>Jet Propulsion Laboratory, California Institute of Technology, Pasadena, CA, USA

<sup>3</sup>Univ. Brest, CNRS, IRD, Ifremer, LEMAR, Plouzané, France

<sup>4</sup>Univ. Brest, CNRS, IRD, Ifremer, LOPS, Plouzané, France

\*lsiegelman@caltech.edu

## Consistency between seal and satellite observations at meso- and submesoscale

The contribution of the vertical stratification to the SSH can be estimated by integrating the hydrostatic equation  $dp/dz = -\rho g$ . The SSH ( $\eta$ ) referenced from  $z = 0$  is then given by<sup>1</sup>

$$\eta = \frac{p'_b}{\rho_0 g} - \frac{p_a}{\rho_0 g} - \int_{-H}^0 \frac{\rho'}{\rho_0} dz, \quad (1)$$

where  $p$  is the pressure,  $\rho$  the potential density,  $\rho_0$  the reference potential density ( $1025 \text{ kg m}^{-3}$ ),  $\rho'$  the potential density anomaly ( $\rho = \rho_0 + \rho'$ ),  $g$  the gravity of Earth,  $p_a$  the atmospheric surface pressure,  $H$  the depth of the ocean and  $p'_b = p_b - \rho_0 g H$  the bottom pressure anomaly with  $p_b$  the ocean bottom pressure. The term  $\int_0^\eta \rho'/\rho_0 dz$  has been neglected because  $\eta \ll H$ . The three terms on the right hand side of equation (1) represent respectively the contributions from the bottom pressure, the atmospheric pressure loading, and the steric height. The steric height ( $\zeta$ ) is computed with the seal dataset from the surface down to  $H = 400$  m for dives reaching at least 400 m (3100 dives) as  $\zeta_{400} = \int_{-400}^0 \rho'/\rho_0 dz$ .  $\zeta_{400}$  is then compared to the SSH observed by altimetry.

SSH obtained from satellite data and mixed layer depth (MLD) and buoyancy anomalies, sampled by the seal, have a larger magnitude in the strongly turbulent region (Fig. 2) than in the weakly turbulent one (Extended Data Fig. 1i). Anticyclonic structures, or positive SSH anomalies, are associated with an increase in MLD and bowl-shaped positive buoyancy anomalies from the surface down to 400 m depth (Fig. 2 and Extended Data Fig. 1). Shallow MLD and negative buoyancy anomalies are associated with cyclonic structures, or negative SSH anomalies, confirming the fact that buoyancy anomalies compensate SSH anomalies. To further quantify this compensation over the water column, we have compared SSH with the depth-integrated buoyancy also called steric height. Since seal observations mostly sample the upper ocean, the steric height contribution has been estimated from surface down to 400 m (which concerns at least 35% of the dives) as  $\zeta_{400} = \int_{-400}^0 b dz$  with  $b$  the buoyancy (see Methods). As emphasized by the time-series in Fig. S1a (SSH in black and  $\zeta_{400}$  in blue), SSH and steric height fluctuations correlate well over the entire trajectory, but only for scales smaller than 100 km. SSH reveals a large-scale signal ( $\sim 1000$  km) not present for  $\zeta_{400}$ . This indicates that SSH at larger scales is likely compensated by the buoyancy field below 400 m and/or by bottom pressure. The contribution of  $\zeta_{400}$  to SSH is no more than 30% as revealed by the linear regression coefficient of 3.58 linking the two-time series (not shown).

To remove this large-scale contribution and focus only on the meso/sub-mesoscale band, time-series of the horizontal gradients of SSH and  $\zeta_{400}$  are computed (a gradient operator overemphasizes contribution of smaller scales). This is the equivalent of comparing horizontal currents from SSH using the geostrophic approximation, with those explained by the buoyancy field contribution in the water column using the thermal wind balance<sup>1</sup>. The two time-series are now closer in terms of amplitude differences (Fig. S1b).  $\zeta_{400}$  gradients statistically explain almost 75% of the SSH gradients as revealed by the linear regression coefficient of 1.35 linking the two time-series (not shown). This further emphasizes the consistency between the two independent datasets at meso/sub-mesoscale despite their different spatial resolution. The main differences concern the extrema of SSH gradients (mostly located on the eddy edges) that overcome those of  $\zeta_{400}$  gradients by a factor of two to three. This suggests the steric height is not integrated deep enough to capture SSH in the upper mesoscale band and therefore that dynamics of this band affects at least the first 400 m below the surface.



## Link between the strain field, Finite Size Lyapunov Exponents and lateral gradients of buoyancy

As illustrated in Fig. 3a, buoyancy anomalies embedded in a strain field are elongated in one direction and compressed in the perpendicular direction. This mechanism can be understood in terms of particle dispersion, and thus in terms of Finite Size Lyapunov Exponents (FSLE); two particles, initially close and embedded in a strain field, become quickly separated in one particular direction (the stretching direction, in red in Figs 3a and 4a). As such, the time scale of their separation can be characterized by  $\lambda^{-1}$  (see equation 2 in Methods), with large  $\lambda$  being indicative of an intense strain field. More precisely, FSLE characterize both the time scale (via the largest FSLE eigenvalue  $\lambda$ ) and the direction (via the FSLE eigenvector associated to  $\lambda$ ) of the elongation of buoyancy anomalies.

Thus, the time scale  $\lambda$  (shown in the colorbar of Fig. 4a for instance) can be used to characterize the production of buoyancy gradient expressed in the RHS of the omega equation (equation 3 in Methods). In particular, the intersection of intense compressing and stretching FSLE lines, respectively in blue and red in Figs 3a and 4a, identify Lagrangian hyperbolic points, where particles (or tracers) are simultaneously being stretched along one direction and compressed along the other one. Areas surrounding hyperbolic points are particularly prone to frontogenesis.

## Vertical velocities underestimation

At steeply tilted isopycnals' fronts, the vertical velocity field is more accurately captured by the full omega equation, known as the Sawyer-Eliassen (SE) equation, than by its QG version<sup>2,3</sup>. The 2-D (x,z) SE equation, assuming the front is embedded in a pure strain field and diffusive processes are negligible, reads<sup>2</sup>:

$$N^2 \frac{\partial^2 \psi}{\partial x^2} + F^2 \frac{\partial^2 \psi}{\partial z^2} + 2S^2 \frac{\partial^2 \psi}{\partial z \partial x} = 2u_x b_x, \quad (2)$$

with  $\psi$  a meridional streamfunction related to the ageostrophic circulation (i.e. defined as  $v_a = -\frac{\partial \psi}{\partial z}$ ,  $w = \frac{\partial \psi}{\partial x}$ , with  $v_a$  the ageostrophic component of the meridional component of the horizontal velocity field.  $N^2 = N^2(x, z)$ ,  $S^2 = -b_x$  and  $F^2 = f(f + \frac{\partial v}{\partial x})$ , where  $\frac{\partial v}{\partial x}$  is the relative vorticity associated with the front<sup>3</sup>.

Compared with the QG version (equation 3 in Methods) rewritten in the form of the ageostrophic stream function, equation (2) involves  $F^2 = f(f + \frac{\partial v}{\partial x})$  instead of  $f^2$  as well as  $N^2(x, z)$  instead of  $N^2(z)$ . In addition, equation (2) involves the extra term  $2S^2 \frac{\partial^2 \psi}{\partial z \partial x}$ . A dimensional analysis, using  $L$  and  $D$  as respectively the horizontal and depth scales of the front, indicates that this extra term is of the order of  $Ri^{-1}$ , with  $Ri$  the Richardson number, compared to the other two terms on the LHS<sup>2,3</sup>. Since  $Ri^{-1}$  is not small but close to one at locations of sharp fronts, this term should not be ignored. Nevertheless, a real solution for equation (2) exists if and only if  $F^2 N^2 - S^4 > 0$ . This condition can be written as  $f^2 N^2 (1 + Ro - Ri^{-1}) > 0$ , with  $Ro$  the Rossby number. As such, it places a strong constraint on  $Ri^{-1}$ , which is positive and has to be smaller than  $1 + Ro$ . This leads to a limitation of the steepness of the front and also to a limitation of the importance of the  $S^2$  term relatively to others.

However, we do not have access to  $F^2$  and in particular to  $\frac{\partial v}{\partial x}$ , the along-front relative vorticity, that can be of order  $f$ . SSH observations have a spatial resolution too low to resolve  $\frac{\partial v}{\partial x}$  at these scales. This is why we use the QG version (equation 3 in Methods). Nevertheless, many studies, starting with Hoskins (1982)<sup>4</sup> and more recently confirmed by Hakim and Keyser (2001)<sup>2</sup>, emphasize that the SE and QG solutions are qualitatively similar when the condition  $F^2 N^2 - S^4 > 0$  is met. In particular, the SE and QG ageostrophic circulation, and therefore the w-field, have the same sign. What differs is the amplitude of the w-field, which is larger in the SE solution, as well as the shape of the ageostrophic circulation, which is more tilted and oriented parallel to the isopycnals in the SE solution. Thus, the QG omega solution gives the correct sign for w but the magnitude may be underestimated at low  $Ri$ .

This underestimation can however be quantified using the analytical solutions for the QG and SE versions of the omega equation derived in Hakim and Keyser (2001)<sup>2</sup>. These authors show that  $w_{SA} \sim w_{QG} [\frac{PV_{QG}}{PV_{PE}}]^{1/2}$  with  $w_{SA}$  and  $w_{QG}$  respectively the solution of the QG and SA equations and  $PV_{QG}$  and  $PV_{PE}$  respectively the QG potential vorticity and the Ertel potential vorticity. Using the approximations  $PV_{QG} \sim fN^2$  and  $PV_{PE} \sim fN^2[1 - Ri^{-1}]$ , as detailed by Thomas et al. 2008<sup>3</sup>, leads to  $[\frac{PV_{QG}}{PV_{PE}}]^{1/2} = [\frac{1}{1 - Ri^{-1}}]^{1/2}$ . When  $Ri = 2$ , which corresponds to the strongest fronts in the seal measurements (see main text), we get  $w_{SA} \sim 1.4 \times w_{QG}$ . In other words, the maximum w-values found in our study should be closer to 140 m/day than to 100 m/day.

## Dominance of frontogenesis versus frontolysis understood via the direct cascade of potential energy

The classical frontogenesis process<sup>5</sup> emphasizes that the increase tendency of a buoyancy gradient embedded in a strong strain field is balanced by a vertical velocity field that tends to decrease this buoyancy gradient (black arrows in Fig. 3b). The reason is that a buoyancy gradient increase destroys the thermal wind balance and this balance is restored by the emergence of the vertical velocity field. These mechanisms lead to the omega equation (see Methods section “Vertical velocities”). As illustrated in Fig. 3b, the frontogenesis process leads to an upward vertical heat flux (red arrows in Fig. 3b) because of the positive correlation between temperature and vertical velocities anomalies.

On the other hand, the frontolysis process, or the destruction of front, occurs when the strain rate decreases and/or changes its direction. As a consequence, the buoyancy gradient relaxes, which is then balanced by a vertical velocity field (and therefore a vertical heat flux) in the opposite direction for the same reason as before (thermal wind balance). The frontolysis process is also captured by the omega equation and is associated with a downward vertical heat flux because of the negative correlation between temperature and vertical velocities anomalies (Fig. 5c). Frontogenesis (frontolysis) processes explain occurrences of positive (negative) vertical heat fluxes displayed in Fig. 5c and Extended Data Fig. 5b.

However, a well-known property of mesoscale eddy turbulence is the direct cascade of potential energy driven by the background strain field. The direct cascade refers to the creation of buoyancy anomalies at smaller and smaller scales and thus to the continuous production of submesoscale fronts<sup>6</sup>. This is why frontogenesis processes statistically dominate frontolysis ones, as can be seen in Fig. S2c where positive buoyancy fluxes are more numerous and of greater magnitude than negative ones. As a consequence, we propose that the dominance of positive vertical heat fluxes at submesoscale as demonstrated in the main text is consistent with the strong background eddy field (Fig. 5f).

## Numerical simulation comparison

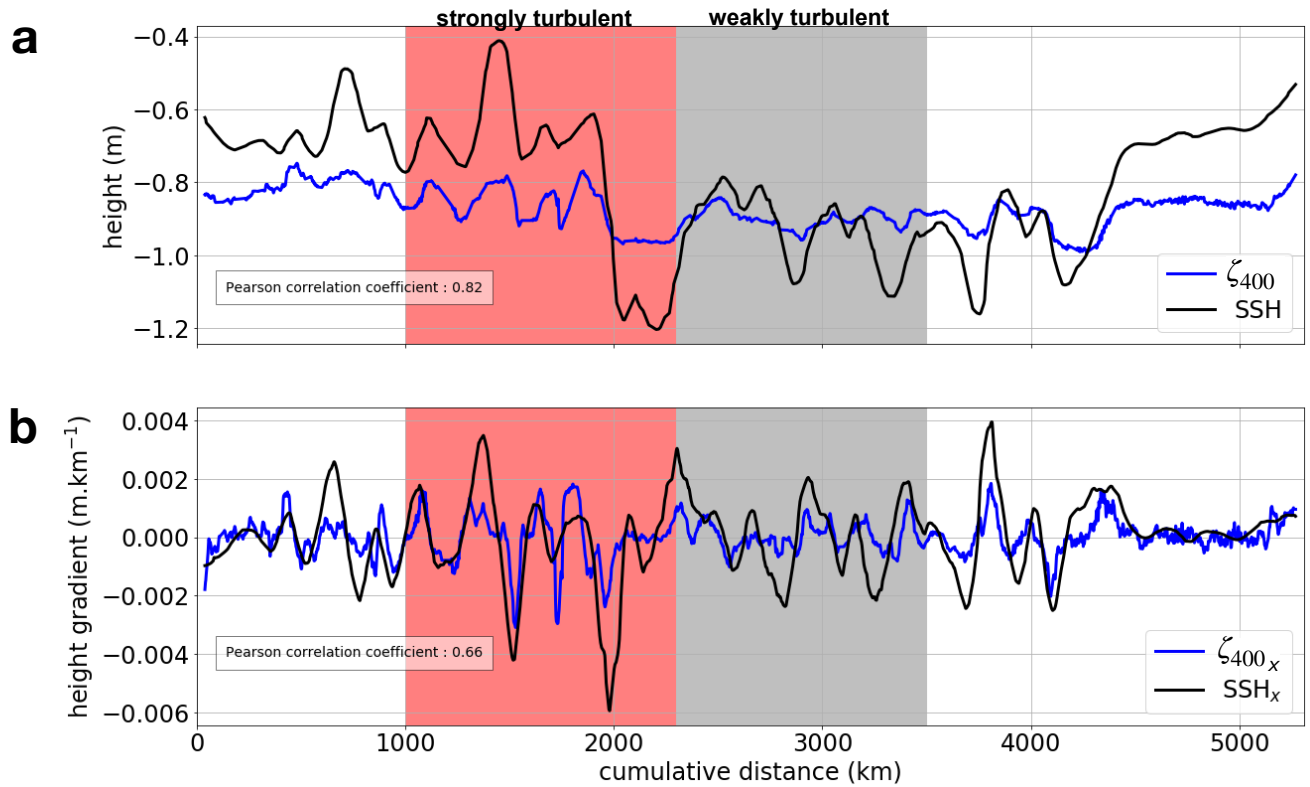
The vertical velocity field and vertical heat transport (VHT) calculated from the observations are compared to the same fields obtained from a high-resolution numerical simulation in the Kerguelen area in late spring-early summer (November 2011) performed with the Massachusetts Institute of Technology general circulation model (MITgcm). This high-resolution simulation has a horizontal resolution of  $1/48^\circ$ , 90 vertical levels and 10 minute outputs and is described in many papers (see for example Su *et al.* (2018)<sup>7</sup>). The model domain is  $45^\circ\text{S}$ – $55^\circ\text{S}$ /  $85^\circ\text{E}$ – $95^\circ\text{E}$  (or  $\sim 1000 \times 1000$  km). This domain is embedded in the MITgcm LLC 4320 global numerical simulation performed at the same resolution but with hourly outputs<sup>7</sup>. Boundary conditions and forcings are supplied by the global simulation.

Vertical sections of daily averaged vertical velocities and vertical heat transport obtained from this simulation are presented in Extended Data Fig. 5. At depths of 100–600 m, intense vertical velocities with a width of 5–10 km are present below the mixed layer and reach 300 m/day. Similar features are observed for vertical heat transport with values locally reaching  $4000 \text{ W/m}^2$ . Two-dimensional slices (x,y) of vertical heat transport averaged over 10 days are shown in Extended Data Fig. 6 at 50 and 200 m. This Fig. clearly highlights that the organization of VHT is driven by the background mesoscale strain field, intensified on the eddy edges. This Fig. also shows the dominance of positive VHT in the domain as well as its intensification at depth. Finally, Extended Data Fig. 7 presents the domain-averaged VHT over one month, which reveals similar - although larger - values than the ones derived from the observational data. Overall, the similar shape, distribution within the water column, and magnitude of both quantities in the model and in the observations strengthen the results presented in this study, and further highlight the impact of deep reaching ocean fronts on oceanic heat transport.

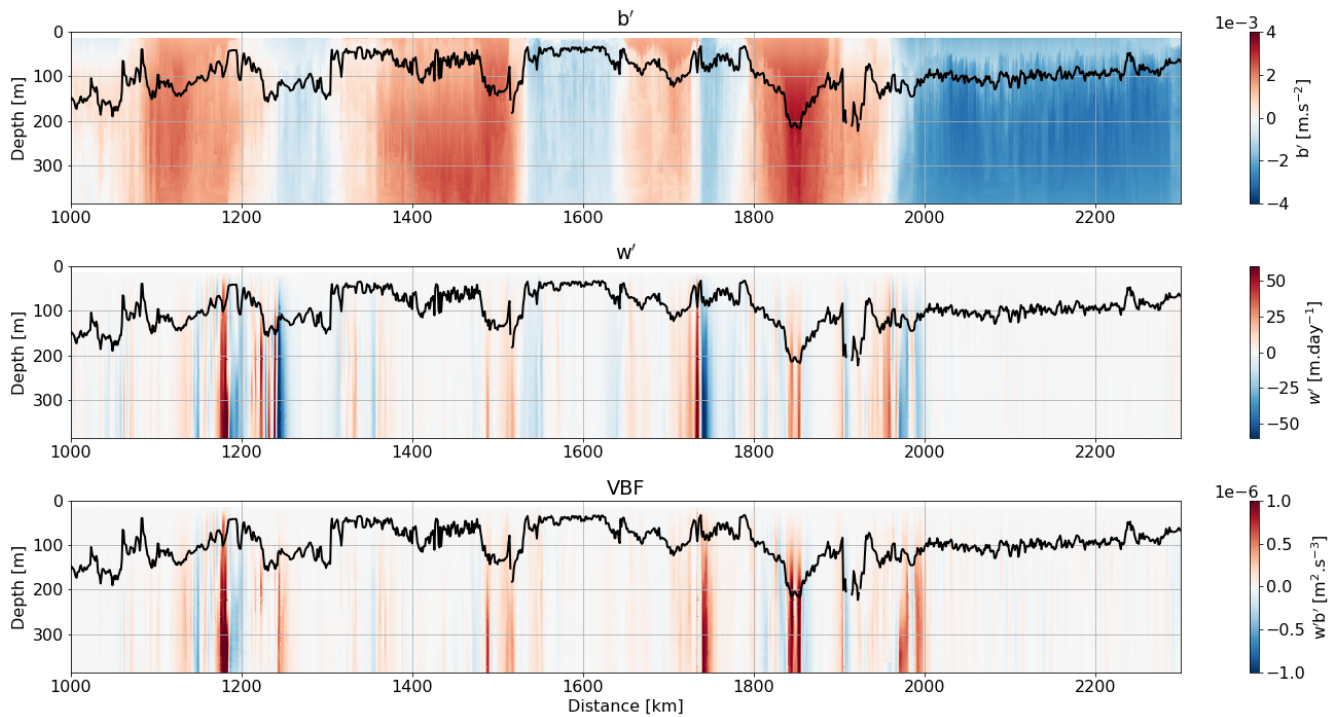
## References

1. Vallis, G. K. *Atmospheric and oceanic fluid dynamics* (Cambridge University Press, 2017).
2. Hakim, G. & Keyser, D. Canonical frontal circulation patterns in terms of green’s functions for the sawyer-eliassen equation. *Q. J. Royal Meteorol. Soc.* **127**, 1795–1814 (2001).
3. Thomas, L. N., Tandon, A. & Mahadevan, A. Submesoscale processes and dynamics. *Ocean. modeling an Eddy Regime* **177**, 17–38 (2008).
4. Hoskins, B. J. The mathematical theory of frontogenesis. *Annu. review fluid mechanics* **14**, 131–151 (1982).
5. Hoskins, B. J. & Bretherton, F. P. Atmospheric frontogenesis models: Mathematical formulation and solution. *J. Atmospheric Sci.* **29**, 11–27 (1972).

6. Salmon, R. Baroclinic instability and geostrophic turbulence. *Geophys. & Astrophys. Fluid Dyn.* **15**, 167–211 (1980).
7. Su, Z., Wang, J., Klein, P., Thompson, A. F. & Menemenlis, D. Ocean submesoscales as a key component of the global heat budget. *Nat. communications* **9**, 775 (2018).



**Supplementary Fig. S1. SSH and steric height ( $\zeta_{400}$ ).** a) Time series of satellite SSH (black line) along the seal's path and steric height ( $\zeta_{400}$ , blue line) calculated from the SES dataset down to 400 m. b) Time series of the lateral gradients of SSH (SSH<sub>x</sub>, black line) and steric height ( $\zeta_{400,x}$ , blue line). On both panels, the red (grey) zone corresponds to the strongly (weakly) turbulent area of Fig. 2(S1i).



**Supplementary Fig. S2. Buoyancy and temperature anomalies and vertical buoyancy fluxes from seal and satellite data** Same as Fig. 5 but for buoyancy. a) Vertical section of buoyancy anomaly sampled by the seal. b) Vertical section of vertical velocity anomaly derived from the seal and satellite data by solving the omega equation (see main text and Methods). c) Vertical section of vertical buoyancy flux (or transport, VBF) defined as  $w'b'$ , with  $w'$  and  $b'$  are the anomalies of vertical velocity and buoyancy, respectively. The mixed layer depth is shown in bold black. From panel c) it is clear that frontogenesis (positive VBF, in red) dominates frontolysis (negative VBF, in blue).

## 4 Ageostrophic dynamics of deep submesoscale fronts

In this chapter, we offer a dynamical explanation for the observational results presented in Chapter 3. A subset of the global realistic LLC4320 simulation, with a  $1/48^\circ$  horizontal resolution and tidal forcing (see section 1.3), is used in the ACC to demonstrate that the ocean interior departs from the quasi-geostrophic regime down to depths of 900 m, i.e., well below the mixed-layer. Results highlight that, contrary to the classical paradigm, the ocean interior is strongly ageostrophic, with a pronounced cyclone-anticyclone asymmetry and a dominance of frontogenesis over frontolysis. Numerous vortices and filaments, from the surface down to 900 m, are characterized by large Rossby and low Richardson numbers, strong lateral gradients of buoyancy and vigorous ageostrophic frontogenesis. These deep submesoscale fronts are only weakly affected by internal gravity waves and drive intense upward vertical heat fluxes, consistent with recent observations in the ACC (Siegelman et al., 2019a) and the Gulf Stream (Yu et al., 2019). As such, deep submesoscale fronts provide an efficient pathway for the transport of heat from the ocean interior to the surface, suggesting the unexpected presence of deep oceanic restratification.

**Siegelman, L..** (2020). Energetic submesoscale dynamics in the ocean interior. *Journal of Physical Oceanography*.

# 🔗 Energetic Submesoscale Dynamics in the Ocean Interior ✍️

LIA SIEGELMAN

*Environmental Science and Engineering, and Jet Propulsion Laboratory, California Institute of Technology, Pasadena, California*

(Manuscript received 24 October 2019, in final form 28 December 2019)

## ABSTRACT

Submesoscale ocean processes, characterized by order-1 Rossby and Richardson numbers, are currently thought to be mainly confined to the ocean surface mixed layer, whereas the ocean interior is commonly assumed to be in quasigeostrophic equilibrium. Here, a realistic numerical simulation in the Antarctic Circumpolar Current, with a  $1/48^\circ$  horizontal resolution and tidal forcing, is used to demonstrate that the ocean interior departs from the quasigeostrophic regime down to depths of 900 m, that is, well below the mixed layer. Results highlight that, contrary to the classical paradigm, the ocean interior is strongly ageostrophic, with a pronounced cyclone–anticyclone asymmetry and a dominance of frontogenesis over frontolysis. Numerous vortices and filaments, from the surface down to 900 m, are characterized by large Rossby and low Richardson numbers, strong lateral gradients of buoyancy, and vigorous ageostrophic frontogenesis. These deep submesoscale fronts are only weakly affected by internal gravity waves and drive intense upward vertical heat fluxes, consistent with recent observations in the Antarctic Circumpolar Current and the Gulf Stream. As such, deep submesoscale fronts are an efficient pathway for the transport of heat from the ocean interior to the surface, suggesting the presence of an intensified oceanic restratification at depth.

## 1. Introduction

Oceanic mesoscale and submesoscale turbulence has been extensively studied in the past decade (Klein and Lapeyre 2009; Mahadevan 2016; McWilliams 2016). Results emphasize the existence of submesoscale fronts ( $\leq 50$ -km width), predominantly confined to the surface mixed layer (ML) and particularly energetic in winter when ML instabilities are active (Fox-Kemper et al. 2008; Callies et al. 2015). These fronts, mostly produced by co-interacting mesoscale eddies (50–300 km size), are associated with important positive vertical heat fluxes (Su et al. 2018). In contrast, submesoscale vertical heat fluxes in the ocean interior are thought to be small. This is because, in the classical paradigm, motions below the ML are broadly assumed to be in quasigeostrophic

(QG) balance, preventing the formation of strong density gradients at depth.

However, growing evidence suggests that interior ocean dynamics significantly depart from quasigeostrophy and may be strongly ageostrophic, as proposed by Molemaker et al. (2010). These authors show that relaxing the QG assumptions in an idealized model of the ocean interior leads to the emergence of large Rossby number and energetic frontogenesis driven by mesoscale eddies. Seismic imaging has also long revealed the existence of ageostrophic mesoscale eddies (50–100 km) in the ocean interior (Biescas et al. 2008; Menesguen et al. 2009; Barbosa Aguiar et al. 2015), such as the subsurface anticyclones of the North Atlantic Ocean known as “meddies” (Armi et al. 1988) or the coherent eddies of the Gulf Stream (Gula et al. 2019). In addition, two recent in situ studies diagnosed strong upward vertical heat fluxes in the ocean interior (Siegelman et al. 2020; Yu et al. 2019), believed to be produced by ageostrophic dynamics. In particular, Siegelman et al. (2020) reported an enhanced vertical heat flux at deep submesoscale ocean fronts in the Kerguelen region in spring and summer, seasons traditionally associated with weak submesoscales (Sasaki et al. 2014; Callies et al. 2015).

---

🔗 Denotes content that is immediately available upon publication as open access.

---

✍️ Supplemental information related to this paper is available at the Journals Online website: <https://doi.org/10.1175/JPO-D-19-0253.s1>.

---

*Corresponding author:* Lia Siegelman, [lsiegelman@caltech.edu](mailto:lsiegelman@caltech.edu)

DOI: 10.1175/JPO-D-19-0253.1

© 2020 American Meteorological Society. For information regarding reuse of this content and general copyright information, consult the [AMS Copyright Policy \(www.ametsoc.org/PUBSReuseLicenses\)](https://www.ametsoc.org/PUBSReuseLicenses).

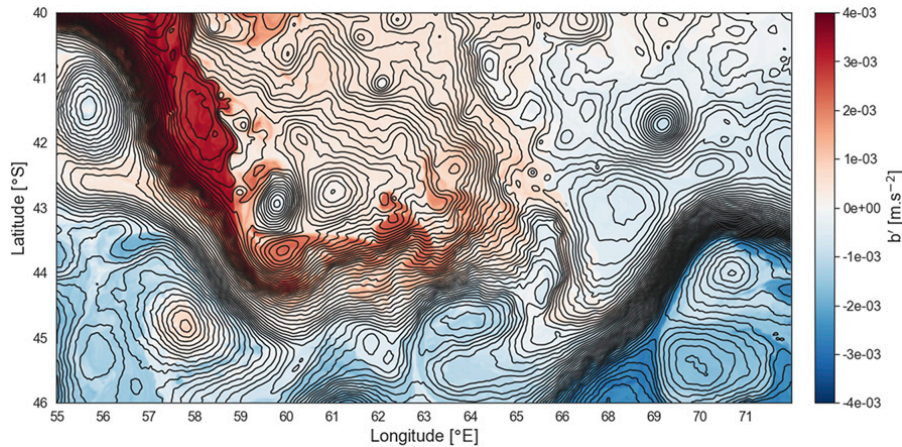


FIG. 1. Map of buoyancy anomaly (shading; the “e” in the values indicates that the numeral preceding the e should be multiplied by 10 raised to the sign and numerals following it), defined as the anomaly with respect to the domain-averaged value, at 99 m superimposed with contours of SSH ranging from  $-0.9$  to  $1.15$  m at  $0.03$ -m interval. The map is a randomly selected snapshot taken at 0200 UTC 28 Oct 2012, which is representative of the time period considered in this study.

Here, ageostrophic dynamics of deep submesoscale ocean fronts are studied in the Antarctic Circumpolar Current (ACC), offering a dynamical explanation for the observational results of Siegelman et al. (2020). The numerical simulation is described in section 2. The Ertel potential vorticity (PV), used to characterize meso–submesoscale turbulence and therefore ocean-scale interactions, is briefly introduced in section 3 in terms of nondimensional numbers. The ageostrophic character of this turbulence, along with frontal dynamics and vertical heat fluxes are analyzed in section 4. Some conclusions and perspectives are provided in section 5.

## 2. Realistic numerical simulation

A primitive equation global ocean simulation with a horizontal resolution of  $1/48^\circ$ , 90 vertical levels and internal tides (appendix A) is used to study ocean-scale interactions over a broad range of scales, from 10 km to basin scales. A subdomain of the ACC, just north of the Kerguelen Islands, that spans  $55^\circ$ – $73^\circ$ E,  $40^\circ$ – $46^\circ$ S ( $\sim 1300$  km  $\times$  700 km) is analyzed. The domain size is sufficiently large to capture part of the large-scale Subantarctic Front (SAF; Fig. 1) (Kim and Orsi 2014), and the model resolution is sufficiently high to resolve multiple mesoscale eddies and to permit the emergence of submesoscale features such as elongated fronts and submesoscale vortices (Fig. 2).

The time period ranges from 15 October to 15 November 2012, that is, late spring in the Southern Hemisphere. This season lies intermediate to the submesoscale-energetic winter and summertime, when submesoscales are thought to be inhibited by shallow ML (Sasaki et al. 2014; Callies et al. 2015). Here, the mixed layer depth

(MLD) is relatively shallow with an average value of 50 m but having local maxima of 100 m within cyclonic eddies.

## 3. Ertel potential vorticity as a tracer of ocean-scale interactions

The Ertel PV is a key dynamical quantity for the study of a stratified fluid in rotation. It is conserved along a Lagrangian trajectory and is only modified by sources, sinks, and friction. As such, the Ertel PV experiences a direct cascade in which numerous submesoscale filaments are generated by co-interacting mesoscale eddies, the latter emerging from baroclinic instabilities of large-scale flows (Pedlosky 2013a). The Ertel PV is used here to characterize the flow field in terms of mesoscale and submesoscale turbulence.

The Ertel PV can be expressed as

$$q = (f + \zeta)b_z + (\mathbf{k} \times \mathbf{u}_z) \cdot \nabla_H b, \quad (1)$$

where  $b = g(1 - \rho/\rho_0)$  is buoyancy, with  $g$  being Earth’s gravitational acceleration,  $\rho$  being potential density, and  $\rho_0$  being a reference density of  $1027.5 \text{ kg m}^{-3}$ ,  $f$  is the Coriolis parameter,  $\zeta = v_x - u_y$  is the vertical component of the 3D vorticity vector (i.e., the relative vorticity),  $\mathbf{k} \times \mathbf{u}_z = (-v_z, u_z)$  is its horizontal component, and the spatial derivatives of  $w$  are neglected (Holton 1973). Subscripts denote partial derivatives.

The Ertel PV can thus be decomposed into two main components:  $(f + \zeta)b_z$  and  $-v_z b_x + u_z b_y$ . It can also be expressed in terms of the nondimensional Rossby number  $\text{Ro}$  ( $\equiv \zeta/f$ ) and Richardson number  $\text{Ri}$  [ $\equiv f^2 N^2 / (\nabla b)^2$ ] (assuming thermal wind balance) as

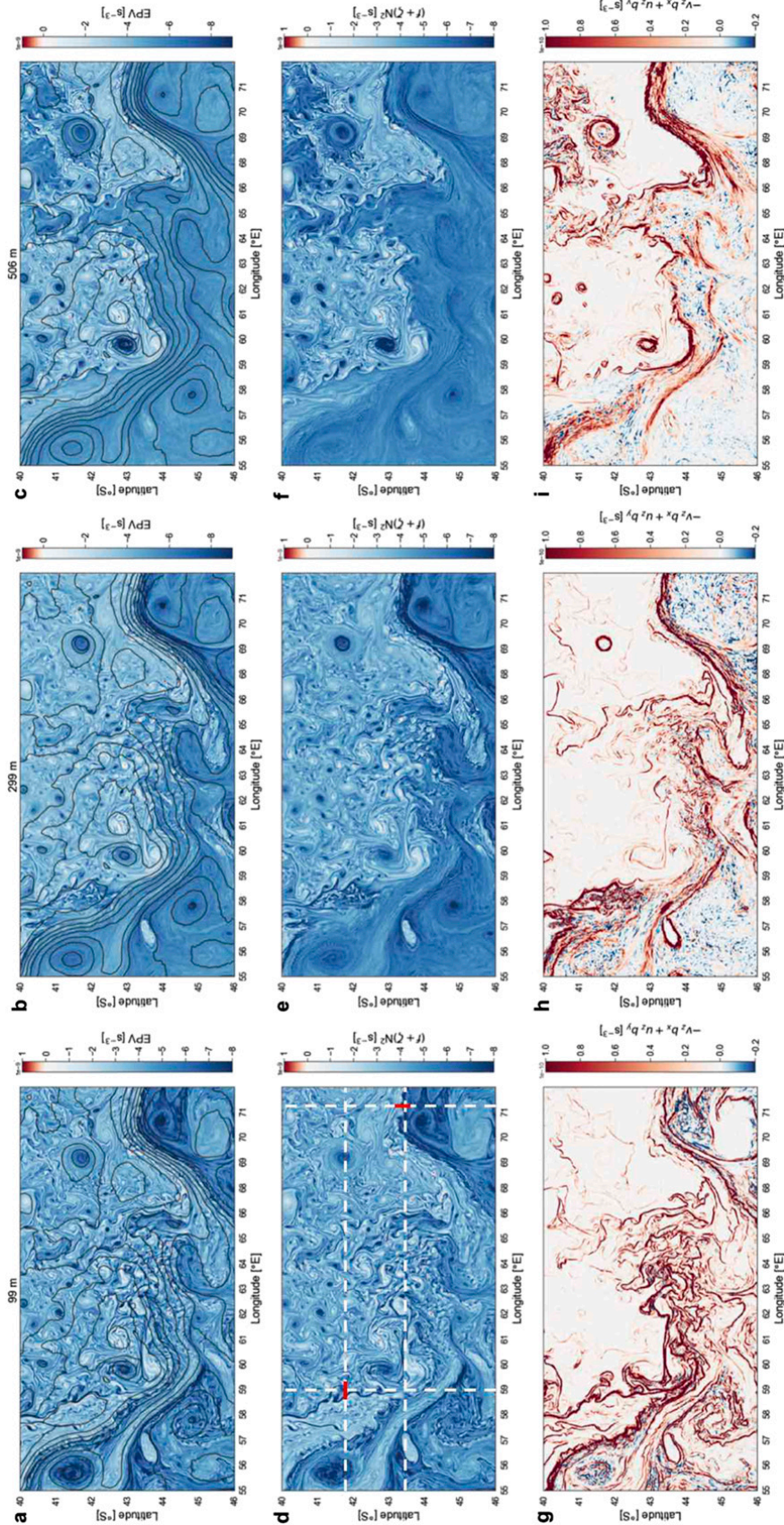


FIG. 2. Maps of (a)–(c) Ertel PV, superimposed with SSH contours (in black) ranging from  $-0.9$  to  $1.15$  m at  $0.1$ -m interval, and Ertel PV's (d)–(f) first component  $(f + \zeta)N^2$  and (g)–(i) second component  $-v_z b_x + u_z b_y$  at (left) 99, (center) 299, and (right) 506 m. All maps are for the same randomly selected snapshot taken at 0200 UTC 28 Oct 2012. The white dashed lines in (d) correspond to the vertical sections presented in Figs. 3, 4, 7, and 14, below. The red lines in (d) correspond to the two submesoscale fronts presented in Fig. 13, below.



$$q \approx fN^2(1 + \text{Ro} - \text{Ri}^{-1}), \quad (2)$$

where  $N^2 \equiv b_z$  is the Brunt–Väisälä frequency squared (Thomas et al. 2008).

For QG flows,  $\text{Ro} \ll 1$  and  $\text{Ri} \gg 1$ , which corresponds to a balance between pressure and Coriolis forces at leading order and a small isopycnal slope, respectively. For ageostrophic flows,  $\text{Ro} = O(1)$  and  $\text{Ri} \leq 1$ , indicating a break of geostrophic balance and a large isopycnal slope, respectively. Commonly accepted values for  $\text{Ro}$  in an ageostrophic regime start at  $\sim 0.3$ – $0.5$ , corresponding to  $\text{Ri}^{-1}$  of  $\sim 0.1$ – $0.2$ . This is because  $\text{Ro}^2 = \text{Ri}^{-1}$  when the horizontal length scale of the flow is close to the first Rossby radius of deformation (Molemaker et al. 2005). In the next sections, ageostrophy is explored in terms of the Ertel PV,  $\text{Ro}$ , and  $\text{Ri}$ .

## 4. Results

### a. Ocean-scale interactions in the Antarctic Circumpolar Current

#### 1) LARGE-SCALE BACKGROUND FLOW

The large-scale meandering SAF has a width of  $O(100\text{ km})$  and strong currents reaching  $1.5\text{ ms}^{-1}$  and separates dense waters in the south from light waters in the north (Fig. 1). This geostrophic jet, is, to leading order, in thermal wind balance within the permanent thermocline, which exhibits a sharp stratification gradient;  $N^2$  increases from  $3 \times 10^{-5}$  to  $5.5 \times 10^{-5}\text{ s}^{-2}$  over just 50 km from south to north and the permanent thermocline's depth deepens from 200 to 700 m (see at  $43.5^\circ\text{S}$  in Fig. 3a). This is reflected in the large-scale features of Ertel PV that are essentially governed by  $fN^2$  [Eq. (2)] and follow contours of sea surface height (SSH; Fig. 2). North of the SAF and down to 506 m, the Ertel PV has a low magnitude of  $\sim 3 \times 10^{-9}\text{ s}^{-3}$ , indicating the presence of moderately stratified fluid ( $N/f \sim 160$ ) sitting above the permanent thermocline. South of the SAF and starting from 99 m, the Ertel PV has a high magnitude of  $\sim 5 \times 10^{-9}\text{ s}^{-3}$ , indicating the presence of strongly stratified fluid within the permanent thermocline ( $N/f \sim 215$ ). Large-scale patterns of Ertel PV become more prominent with depth (Fig. 2), covering the quasi totality of the domain at 900 m (not shown).

Numerous mesoscale cyclones and anticyclones are released through baroclinic instabilities of the SAF. The eddies have a size of  $\sim 150$  and 50 km south and north, respectively, of the SAF (Fig. 1). This striking size difference is a consequence of the stratification difference that is reflected in the first Rossby radius of deformation,  $L_d = NH/f$ , with  $H$  being the depth scale of the flow, corresponding to the depth of the main thermocline, and

$f$  being the Coriolis frequency. Mesoscale buoyancy anomalies (in color in Fig. 1) are mostly present in the vicinity of the SAF and are consistent with the thermal wind balance, that is, positive within anticyclones and negative within cyclones. However, there is a slight phase shift between these mesoscale buoyancy anomalies and large-scale SSH contours, as can be seen at  $43^\circ\text{S}$ ,  $62^\circ\text{E}$  (Fig. 1). This offset is key to the generation of sub-mesoscale buoyancy fronts and filaments, because the strain field will then be able to stretch and compress these background anomalies (Klein et al. 2019). These large- and mesoscale characteristics are common to the two other most energetic currents: the Kuroshio Extension (Sasaki et al. 2014) and the Gulf Stream (Chassignet and Xu 2017).

#### 2) MESO- AND SUBMESOSCALE TURBULENCE

Meso- and submesoscale turbulence is characterized by the spontaneous emergence of numerous small-scale filaments and vortices with a horizontal size of tens of kilometers (McWilliams 2016), not directly identifiable in SSH (Fig. 1) but evident in tracer fields, such as the Ertel PV (Klein et al. 2019).

Meso- and submesoscale features are strongly heterogeneous throughout the domain, as can be seen in the maps of Ertel PV (Figs. 2a–c). North of the SAF, numerous small eddies ( $\sim 50\text{ km}$  in size) are associated with negative Ertel PV anomalies extending down to at least 506 m. These eddies are surrounded by filaments of Ertel PV at their periphery and in between them, elongated over distances of tens of kilometers. Instances of depth-intensified turbulence also occurs, such as at 506 m around  $41.5^\circ\text{S}$ ,  $69^\circ\text{E}$  (Fig. 2c). South of the SAF, that is, in the large-scale-dominated and high-Ertel-PV region, few large mesoscale eddies ( $\sim 200\text{ km}$  size) are mostly confined to the first 200–300 m. They are associated with elongated filaments over distances greater than 100 km.

The Ertel PV is mostly explained by its first component, that is,  $(f + \zeta)N^2 = fN^2(1 + \text{Ro})$ , as can be seen on the Ertel PV decomposition shown in Fig. 2, highlighting the dominant contribution of the relative vorticity at meso and submesoscale. The second component, that is,  $-v_z b_x + u_z b_y \approx -fN^2\text{Ri}^{-1}$ , is generally an order of magnitude lower than the first one, except at the location of strong submesoscale fronts where they become comparable (see section 4b). This latter component is mostly dominant in the vicinity of the SAF and its width increases with depth (Figs. 2g–i).

The ageostrophic character of the ocean interior becomes obvious on vertical sections of Ertel PV (Figs. 3 and 4), especially north of the SAF where the permanent thermocline can be deeper than 500 m. Three classes of eddy emerge. First, surface-trapped mesoscale eddies

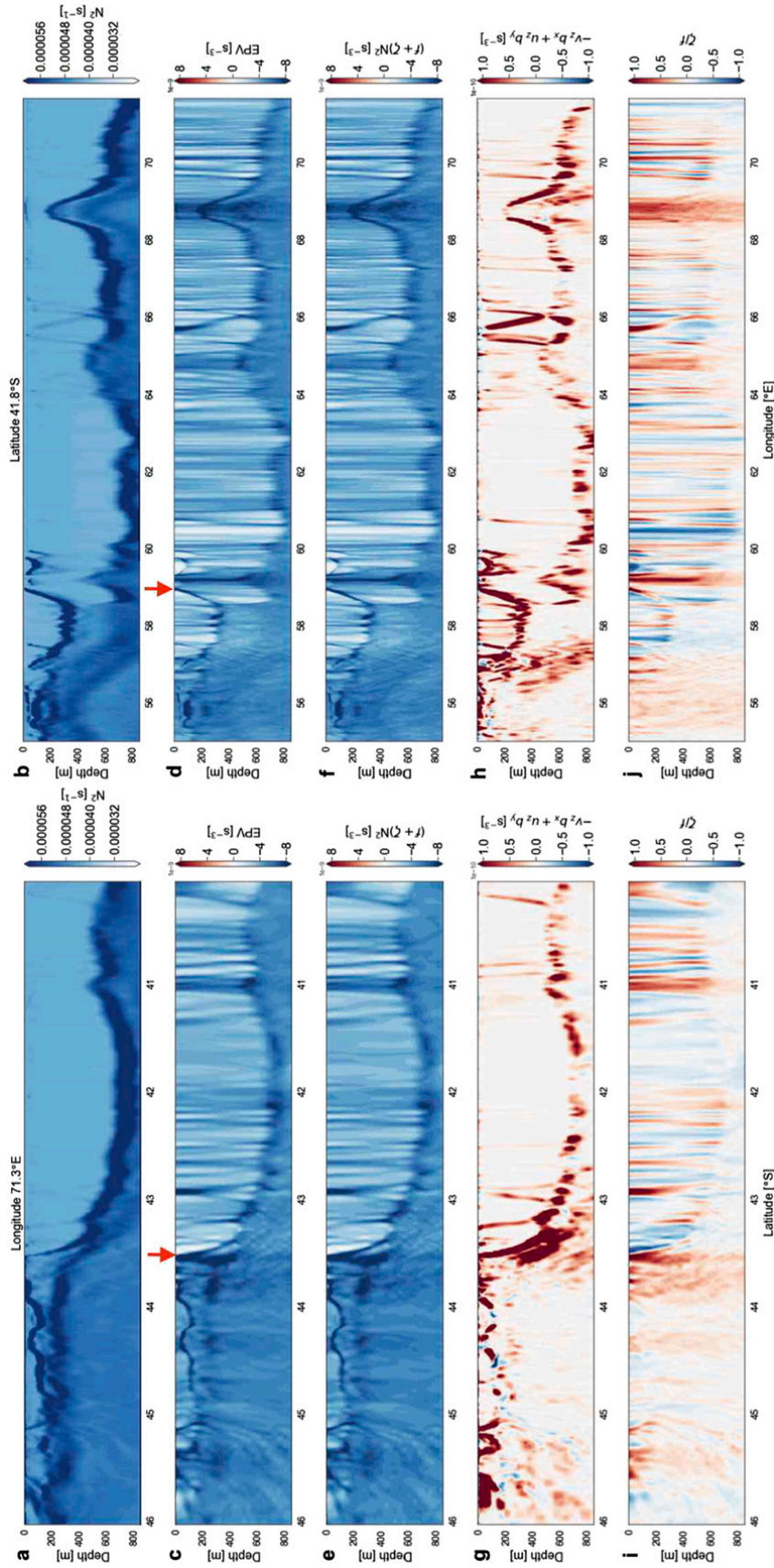


FIG. 3. (left) Meridional and (right) zonal vertical sections at 0200 UTC 28 Oct 2012 of (a), (b) vertical stratification  $N^2$ , (c), (d) Ertel PV's first component  $(f + \zeta)N^2$ , (e), (f) Ertel PV's second component  $-v_z b_x + u_z b_y$ , and (g), (h) relative vorticity normalized by  $\zeta/f$ . The two sections are highlighted by the white dashed lines in Fig. 2d. The red arrows in (c) and (d) correspond to the two submesoscale fronts presented in Fig. 13, below.

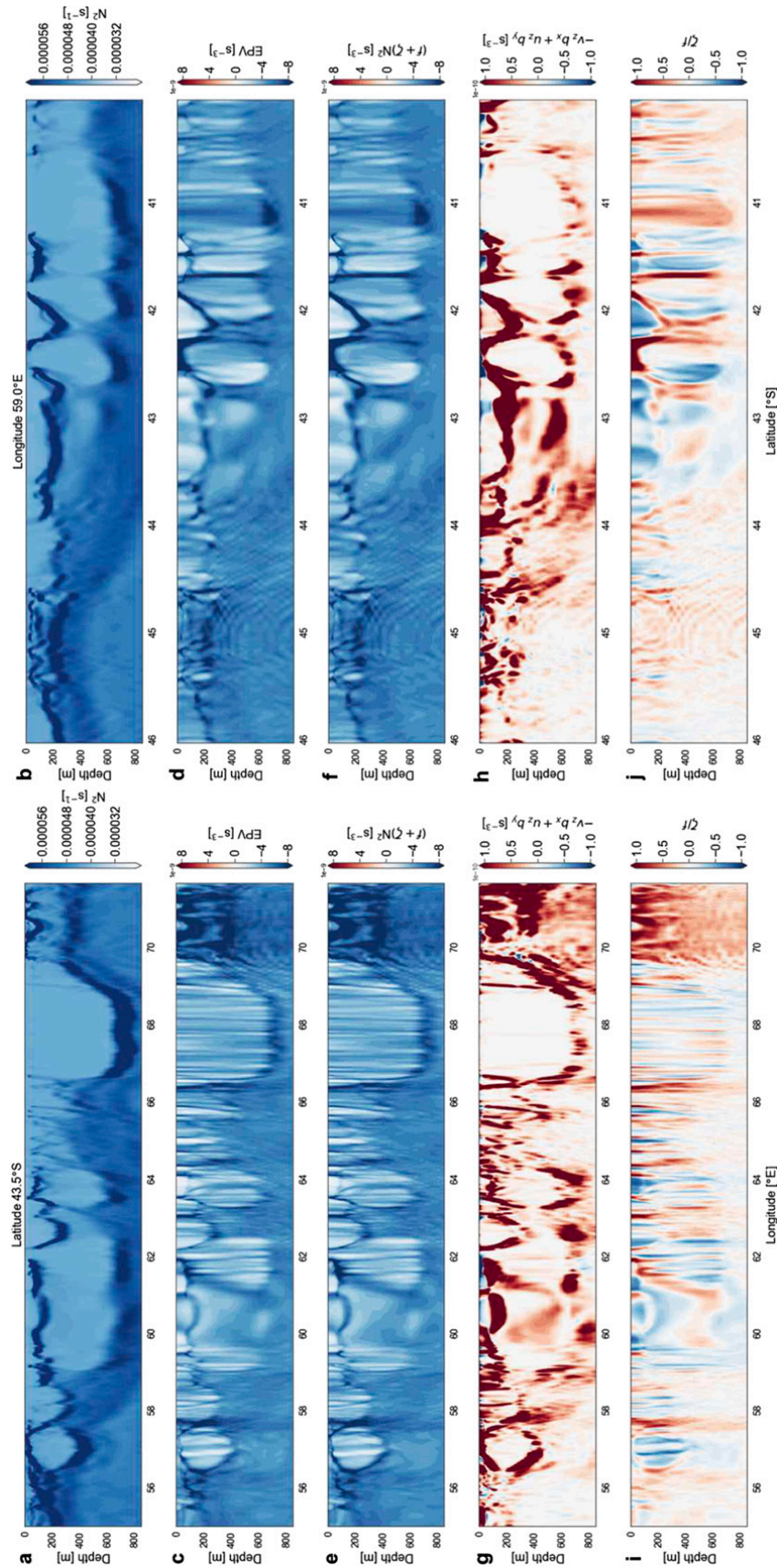


FIG. 4. As in Fig. 3, but for the other zonal and meridional transects highlighted by the white dashed lines in Fig. 2d.

are conspicuous in the domain, see at 62.5°E in Fig. 4a for instance. They extend down to 100–200 m, have a horizontal size of about 50 km, and are associated with low Ertel PV (Figs. 4c,d). They are mostly anticyclones ( $\zeta/f < 0$ ), characterized by  $|\text{Ro}| \geq 0.5$  and surrounded by positive rings of  $\zeta/f$  (Figs. 4i,j), which explains the high-Ertel-PV rings located at their periphery. Strikingly, these eddies are encircled by strong vertical and horizontal gradients of buoyancy, apparent in both  $N^2$  (Figs. 4a,b) and the second component of the Ertel PV (Figs. 4g,h). Since the Ertel PV and buoyancy fields are conserved along a Lagrangian trajectory, these submesoscale fronts should act as dynamical barriers that prevent mesoscale eddies from getting destroyed by their interaction with neighboring ones. As a consequence, mesoscale eddies become more coherent and energetic and their lifetime increases (Mariotti et al. 1994).

Second, subsurface mesoscale eddies are ubiquitous throughout the domain—see at 57°E in Fig. 4a or at 41.8° and 42.5°S in Fig. 4b for instance. Their vertical extent is of 400–600 m, and their horizontal size is 50–100 km. They have a less pronounced surface signature than surface-trapped ones (Fig. 2). Once again, these eddies are mostly anticyclones associated with low Ertel PV anomalies and surrounded by rings of  $\zeta$  of opposite sign as well as enhanced buoyancy gradients, explaining the contours of high Ertel PV located at their edges. High  $|\text{Ro}|$  ( $\geq 0.5$ ) is found both in their core and at their periphery. These subsurface eddies may result from the subduction of low buoyancy waters located south of the SAF below higher buoyancy waters north of the SAF (Fig. 1). These eddies are also reminiscent of those recently observed in the Gulf Stream (Gula et al. 2019) as well as of the well-known meddies encountered in the North Atlantic (Menesguen et al. 2009; Barbosa Aguiar et al. 2015).

Third, deep mesoscale eddies with almost no surface signature are present, see for example at 41°S in Fig. 3a and 69°E in Fig. 3b. These eddies appear to emerge from the instabilities of the permanent thermocline north of the SAF, contributing to inject deep and strongly stratified fluid in upper oceanic layers (see at 69°E in Fig. 3b where waters at 600 m are injected up to 200 m). Contrary to the previous two types, they are mostly cyclones ( $\zeta/f > 0$ ) associated with anomalies of high Ertel PV that is explained by its first component (Fig. 3h). Yet, similar to surface-trapped and subsurface eddies, they are surrounded by intense submesoscale buoyancy gradients and rings of relative vorticity of opposite sign (Figs. 3i,j).

The ageostrophic character of the flow field down to 506 m, that is, well below the mixed layer, also occur away from the SAF, in the northern part of the domain (e.g., at 60°–66°E in Fig. 3b); high  $|\text{Ro}| \geq 0.5$  is associated

with numerous submesoscale structures above the permanent thermocline (600–800 m; Figs. 3b,j). These submesoscale features exhibit alternating low and high Ertel PV anomalies (Fig. 3d), mostly explained by the relative vorticity (Fig. 3j). Indeed, they have a very weak signature on buoyancy gradients (Fig. 3h).

South of the SAF, shallow eddies above the permanent thermocline ( $\sim 200$  m, Fig. 3a) have similar characteristics as surface-trapped ones north of the SAF (Fig. 3b); they are surrounded by filaments of  $\zeta$  of opposite sign and enhanced buoyancy gradients. Within the permanent thermocline, an unexpected signature of internal gravity waves (IGWs) is present on the Ertel PV and relative vorticity fields. IGWs exhibit patterns of radial and crisscross beams, as can be seen at 43.5°–45.5°S in Figs. 4d, 4f, and 4j. However, they should not impact the spatial distribution of Ertel PV because linear waves do not transport material or tracer (Kundu and Cohen 2004). Nevertheless, these IGWs can have a local and transient signature as their high vertical velocity (Pedlosky 2013b; Kundu and Cohen 2004) may affect the buoyancy field. This interesting feature is further developed below.

The simulation includes energetic IGWs, comprising internal tides, near-inertial motions and a large IGWs continuum at higher frequencies. As such, it is essential to be able to disentangle them from balanced motions, that is, flows in thermal or gradient wind balance that encompass meso and submesoscales (Klein et al. 2019). To do so, we use frequency–wavenumber ( $\omega$ – $k$ ) spectra following the methodology described in Torres et al. (2018). The dispersion relation curve associated with the highest baroclinic mode resolved by the model (10th baroclinic mode, curved dashed line in Fig. 5) partitions IGWs, located above the curve, and balanced motions, located below the curve [see appendix B and Torres et al. (2018) for more details]. The  $\omega$ – $k$  spectra of KE, Ertel PV,  $\zeta$ , and  $\nabla b$  are shown at 39, 299, and 900 m (Fig. 5). However they have a similar shape from the surface down to 506 m and decrease linearly with depth (partially shown for 39 and 299 m). As expected, most of the KE is contained at mesoscale ( $>50$  km) and low frequencies at both 39, 299, and 900 m (Figs. 5a,e,i). While the impact of IGWs is visible, especially for M2 tidal motions and near-inertial waves, their relative contribution is weak compared to that of balanced motions. The Ertel PV exhibits a different distribution. At 39 m, most of the variance is contained at submesoscales ( $<50$  km, Fig. 5b). At 900 m, the Ertel PV is less energetic and the variance is contained at both meso and submesoscale (Fig. 5j). Once again, the impact of IGWs on the Ertel PV is substantially weaker than that of balanced motions. The relative vorticity field is even less affected by IGWs. At 39 m (Fig. 5c), most of the variance is

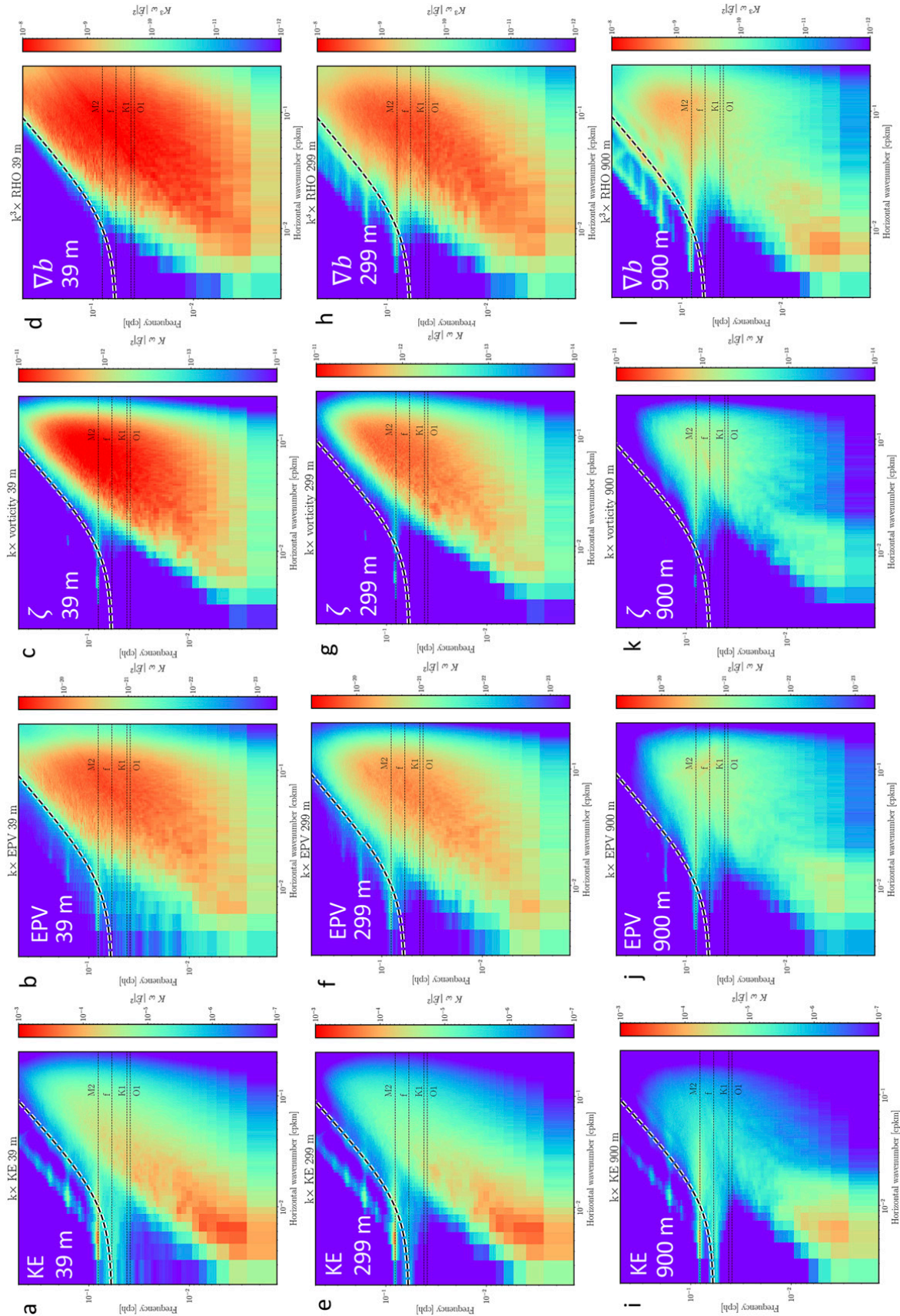


FIG. 5. Frequency-wavenumber spectra computed from 15 Oct to 15 Nov 2012 at (top) 39, (middle) 299, and (bottom) 900 m of (a),(e),(i) kinetic energy (KE), (b),(f),(j) Ertel PV (EPV), (c),(g),(k) relative vorticity  $\zeta$ , and (d),(h),(l) lateral gradients of buoyancy  $\nabla b$ . These spectra are presented in a variance-preserving form, which allows one to directly compare the relative contribution of different time and spatial scales with the total variance (appendix B).

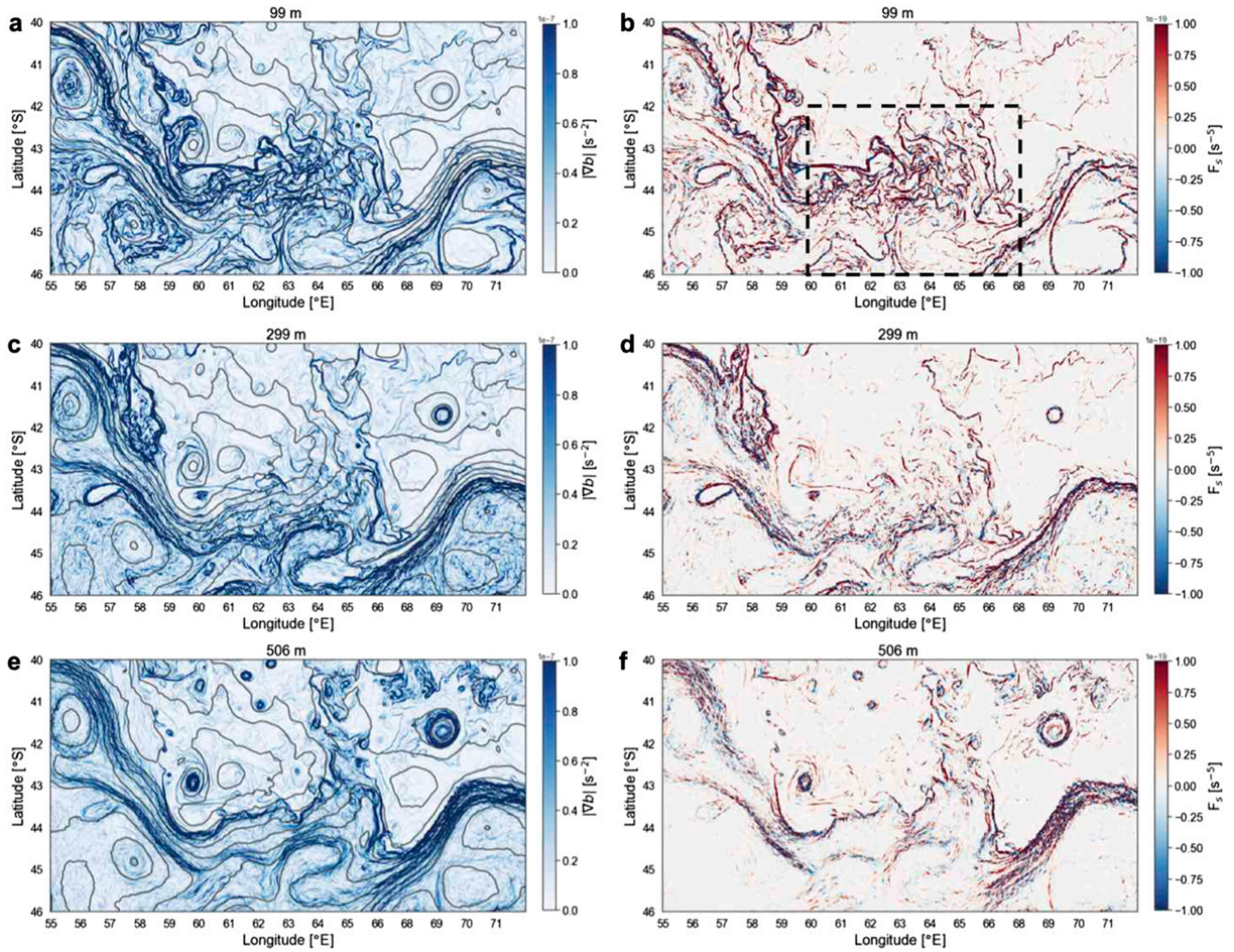


FIG. 6. Maps of (left) lateral gradients of buoyancy  $|\nabla b|$  superimposed with SSH contours ranging from  $-0.9$  to  $1.15$  m at  $0.1$ -m interval and (right) the frontogenesis function  $F_s$  at (a),(b) 99, (c),(d) 299, and (e),(f) 506 m. The maps are a randomly selected snapshot taken at 0200 UTC 28 Oct 2012. The dashed rectangle in (b) corresponds to an active submesoscale area used in Fig. 15 (below) to compute vertical heat fluxes.

contained at high wavenumbers, whereas at 900 m (Fig. 5k) the variance is distributed between meso and submesoscales, similar to the Ertel PV. Consistent with the features observed in physical space,  $\omega-k$  spectra of  $\zeta$  are similar to those of Ertel PV's first component  $(f + \zeta)N^2$  (Figs. S1a–c in the online supplemental material). Lateral gradients of buoyancy  $|\nabla b|$  are not affected by IGWs down to 506 m (Figs. 5d,h) but they are at 900 m (Fig. 5l). Down to 506 m, the variance is principally captured by submesoscales. At 900 m, the variance distribution is similar to the Ertel PV. Consistent with the features observed in physical space,  $\omega-k$  spectra of  $|\nabla b|$  are remarkably similar to those of Ertel PV's second component  $-v_z b_x + u_z b_y$  (Figs. S1b–d in the online supplemental material). The variance of  $\nabla b$  is mostly explained by submesoscales down to 506 m. At 900 m, the variance of  $\nabla b$  is smaller. Overall,  $\omega-k$  spectra

highlight that the Ertel PV and its components are principally explained by scales  $\leq 50$  km and that IGWs have only a weak impact. As such, these results emphasize the existence of energetic submesoscales in the ocean interior, and in particular of energetic frontal dynamics over the domain and time period considered in this study.

*b. Ageostrophic dynamics in terms of lateral gradients of buoyancy,  $Ro$ , and  $Ri$*

1) LATERAL GRADIENT OF BUOYANCY

Lateral gradients of buoyancy  $|\nabla b|$  are of particular interest because of their link with frontogenesis processes associated with large vertical buoyancy and heat fluxes (Hoskins and Bretherton 1972). Strong  $|\nabla b|$  are mostly at submesoscale (Figs. 6a,c,e). They are found from the surface down to 900 m along the SAF as well as

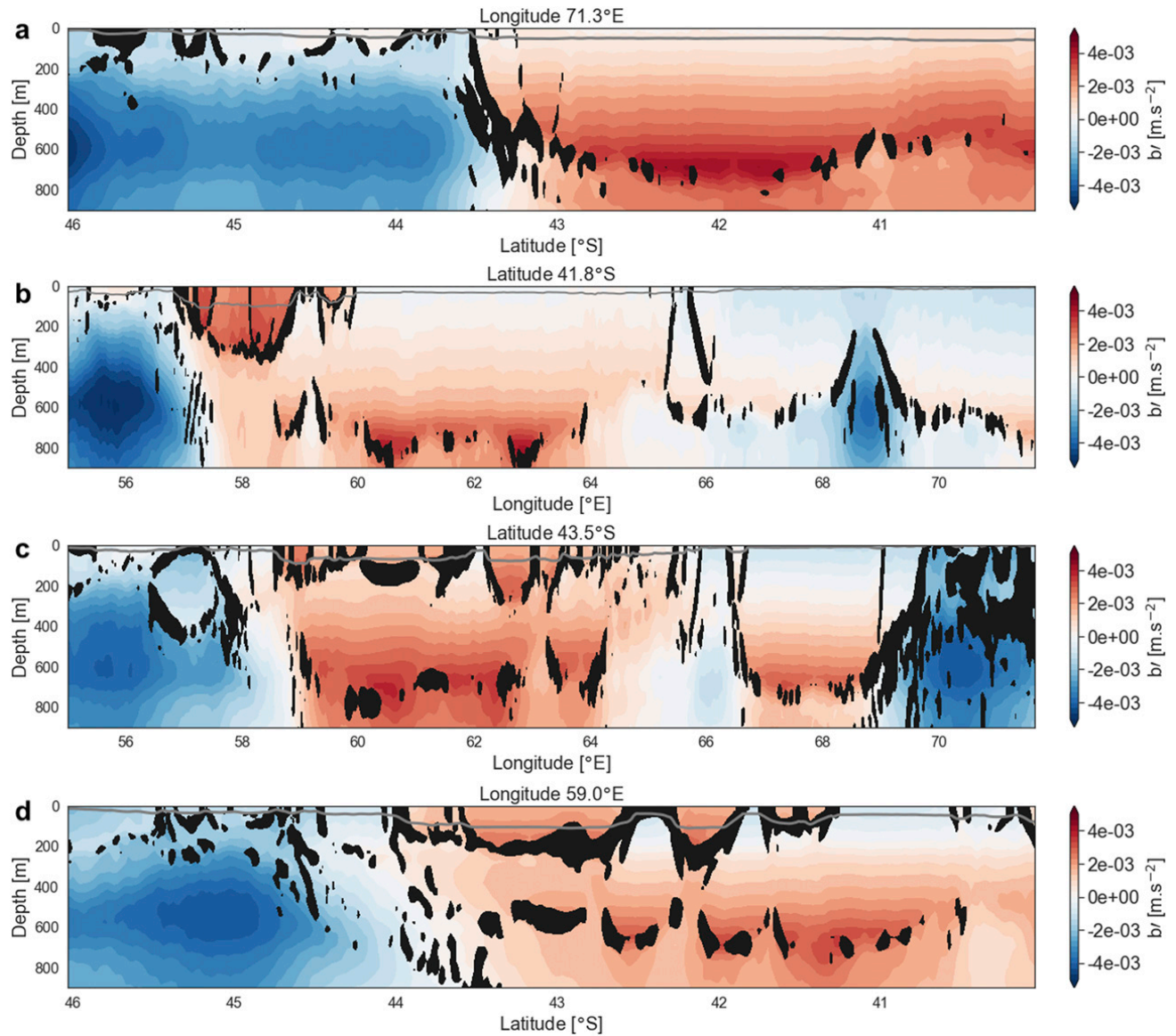


FIG. 7. Four vertical sections of buoyancy anomaly  $b'$  (shading; the “e” in the values indicates that the numeral preceding the e should be multiplied by 10 raised to the sign and numerals following it), superimposed with  $|\nabla b| > 5 \times 10^{-8} \text{ s}^{-2}$  (black contours) corresponding to the dashed white lines in Fig. 2d. The mixed layer depth is shown in gray and corresponds to a density increase of  $0.03 \text{ kg m}^{-3}$  from the density at 10 m. Shown is a randomly selected snapshot taken at 0200 UTC 28 Oct 2012.

at the periphery and in between mesoscale eddies, that is, in strain dominated regions, as inferred from SSH contours (Figs. 6a,c,e). They have a width of  $\sim 10 \text{ km}$  and are meandering over length scales ranging from 50 km, in the intense submesoscale area located at the center of the domain ( $43^\circ\text{S}$ ,  $63.5^\circ\text{E}$ ), to several hundreds of kilometers along the SAF. The typology of  $|\nabla b|$  is very rich; whereas  $|\nabla b|$  in the intense submesoscale area tend to be concentrated in the upper hundred meters of the water column, other  $|\nabla b|$  have an enhanced subsurface signature, which is especially the case for subsurface eddies located north of the SAF (Figs. 6a,c,e and 7). Overall,  $|\nabla b|$  are similarly distributed as Ertel PV's

second component  $-v_z b_x + u_z b_y$  (Figs. 2g-i, 3g-h and 4g-h) as most of  $|\nabla b|$  are in thermal wind balance in the alongfront direction (in red in Figs. 2g-i).

Furthermore, the 3D distribution of  $|\nabla b|$  is remarkably consistent with that of mesoscale buoyancy anomalies. A striking relation between mesoscale buoyancy anomalies and submesoscale  $|\nabla b|$  emerges (Fig. 7). One can observe the classical bowl shape of the buoyancy field within anticyclone, such as between  $57^\circ$  and  $59^\circ\text{E}$  from 0 to 350 m, and reverse bowl shape within cyclone, such as at  $69^\circ$ – $70^\circ\text{E}$  between 300 and 800 m (Fig. 7b). Intense  $|\nabla b|$ , highlighted by the black contours in Fig. 7, are located at the periphery of mesoscale eddies, both

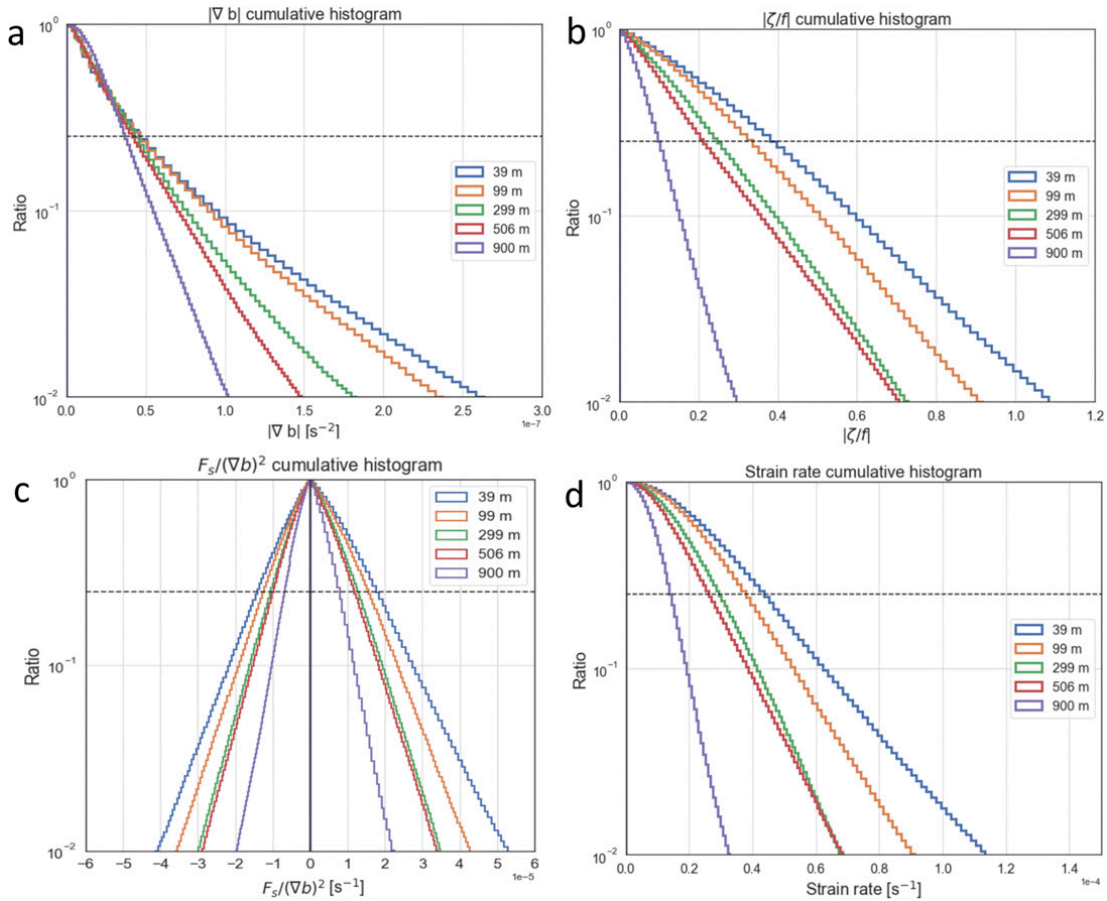


FIG. 8. Cumulative distribution of (a)  $|\nabla b|$ , (b)  $|\zeta/f|$ , (c)  $F_s/(\nabla b)^2$  and (d) strain rate at different depths over the entire domain for a randomly selected snapshot taken at 0200 UTC 28 Oct 2012. The horizontal dashed line corresponds to  $y = 0.25$ .

within and below the MLD, consistent with the maps of  $|\nabla b|$  (Figs. 6a,c,e). While some  $|\nabla b|$  extend from the surface down to depths of 700 m, following deep reaching buoyancy anomalies (at  $66.5^\circ\text{E}$  in Fig. 7c for instance), other  $|\nabla b|$  are only present at depth with a weak—or no—surface signature. This is the case for deep eddies (Figs. 7b–d).  $|\nabla b|$  are slanted and follow the bowl-shaped buoyancy anomalies. Such slanted  $|\nabla b|$  are known to result from the competition between horizontal strain and vertical shear (Haynes and Anglade 1997; Klein et al. 1998; Meunier et al. 2015).

Statistics over the domain indicate that  $|\nabla b|$  at 39 m, that is, mostly within the ML, reaches values of up to  $2.6 \times 10^{-7} \text{ s}^{-2}$  (Fig. 8a). These values are close to, although smaller than, what is found in the literature in both observational and numerical studies. Indeed, Siegelman et al. (2019, 2020) reported values of up to  $4 \times 10^{-7} \text{ s}^{-2}$  using in situ observations collected by southern elephant seals in this region in spring and summer, whereas Rosso et al. (2014) documented  $|\nabla b|$  of up to  $5 \times 10^{-7} \text{ s}^{-2}$  at 50 m in a high-resolution model at  $1/80^\circ$  also in this region. Note that the lower  $|\nabla b|$  obtained here compared to

Rosso et al. (2014) is likely due to the lower resolution of our model. However, a key and surprising result concerns the quasi-constant magnitude of  $|\nabla b|$  with depth. Indeed,  $|\nabla b|$  still reach values greater than  $2 \times 10^{-7} \text{ s}^{-2}$  below the ML and cumulative distributions of  $|\nabla b|$  at different depths are broadly similar down to 506 m:  $|\nabla b| > 5 \times 10^{-8} \text{ s}^{-2}$  account for 25% of the domain at 39 and 99 m, 20% at 299 and 506 m, and 15% at 900 m (Fig. 8a). This weak depth dependence of  $|\nabla b|$ , once again, strongly contrasts with QG dynamics. Indeed, buoyancy anomalies in the QG regime have a spectral slope in  $k^{-2}$  near the surface and  $k^{-5}$  in the ocean interior, that is, a  $k^{-3}$  difference between surface and depth (Hua and Haidvogel 1986; Smith and Ferrari 2009; Molemaker et al. 2010). Here, the wavenumber spectrum of buoyancy displays a slope in  $k^{-2}$  down to 99 m and in  $k^{-2.5}$  below (Fig. 9), which highlights the ageostrophic character of the dynamics at depth. The  $k^{-3}$  difference in spectral slope between the QG and ageostrophic regimes also applies to  $|\nabla b|$ . This implies that, if a mesoscale buoyancy gradient with a size of 100 km is similar at surface and depth,  $|\nabla b|$  with a size of 10 km should be smaller by a



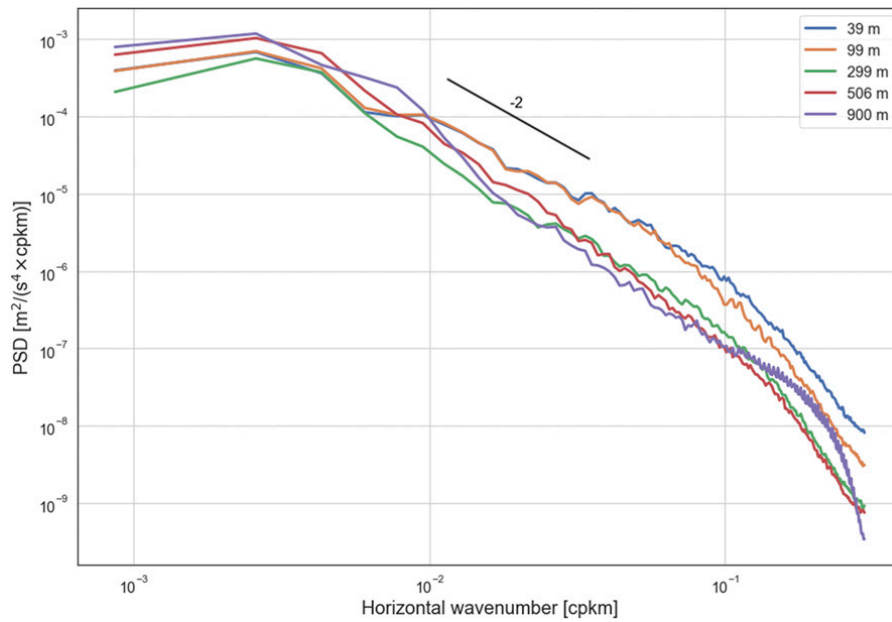


FIG. 9. Wavenumber spectrum of buoyancy at different depths over the entire domain for a randomly selected snapshot taken at 0200 UTC 28 Oct 2012.

factor of 30 at depth than at the surface, or smaller by a factor of 1000 in terms of variance. This is clearly not the case here (Figs. 5d,h,l), highlighting the striking departure from QG dynamics in the ocean interior. The  $\omega$ - $k$  spectra of  $|\nabla b|$  also emphasize the importance of scales  $< 50$  km and the weak impact of IGWs (Figs. 5d,h,l), consistent with the features in physical space.

## 2) ROSSBY NUMBER

The signature of many submesoscale eddies and filaments is apparent in  $\zeta/f$ , at 39 (not shown), 99 (Fig. 10a), 299 (Fig. 10c), and 506 m (Fig. 10e). Similar to the maps of Ertel PV (Figs. 2a-c), larger eddies are found south of the SAF, whereas deeper subsurface eddies are mostly found north of the SAF, starting at 299 m. Filaments of  $\zeta/f$  have a deep vertical extent reaching 500 m, as can be seen in Figs. 3i,j and 4i,j, consistent with Ertel PV's vertical structure (Figs. 3c,d and 4c,d). Interestingly, deep-reaching filaments of  $\zeta/f$  are collocated with weak vertical stratification (Figs. 3a,b,i,j and 4a,b,i,j), highlighting the almost two-dimensional character of oceanic turbulence in this region and season (McWilliams 1984).

Large  $|\text{Ro}|$  are found not only near the surface but also in the ocean interior, down to 900 m. Ro ranges from  $-1.8$  to  $3.5$  at 39 m (not shown), between  $-1.7$  and  $3.1$  at 99 m (Fig. 11a), between  $-1.4$  and  $2.1$  at 299 m (Fig. 11b), between  $-1.4$  and  $1.8$  at 506 m (Fig. 11c), and between  $-0.7$  and  $0.7$  at 900 m (not shown), highlighting the rare occurrence of inertial instability ( $\zeta/f < -1$ ) down to 506 m. Cumulative histograms indicate that 20% of  $|\text{Ro}|$  are larger than 0.45 at 39 m, 0.3 at 299 m and even

0.25 at 506 m (Fig. 8b). These values are remarkably large given the relatively moderate model resolution ( $\sim 1.7$ -km horizontal resolution). As suggested by the results of the previous section, the distribution of Ro is positively skewed down to 299 m, with skewness values of 0.66 at 39 m, 0.42 at 99 m, 0.19 at 209 m, 0.07 at 299 m,  $-0.05$  at 506 m, and  $-0.53$  at 900 m. These skewness values indicate a dominance of cyclones ( $\zeta/f > 0$ ) down to 299 m and a dominance of anticyclones ( $\zeta/f > 0$ ) from 506 to 900 m, consistent with the idealized results of Roulet and Klein (2010). These domain-wide statistics further confirm the strong departure from QG, not only within the mixed layer, but also in the ocean interior.

Filaments and vortices of Ro (Figs. 10a,c,e) can be separated with the Okubo-Weiss quantity (appendix C). Using this partition, Roulet and Klein (2010) showed that filaments of vorticity have a larger positive skewness than vortices, said to be due to ageostrophic frontogenesis. This is quantified over the entire domain using the same Okubo-Weiss partitioning as Roulet and Klein (2010), aimed at excluding vortices of Ro. Results show that the relationship between  $|\nabla b|$  and filaments of Ro is asymmetric and positively correlated down to 506 m; negative or positive filaments of Ro are collocated with weak or strong  $|\nabla b|$ , respectively (Figs. 12a-c). At 900 m, the relation becomes symmetrical, suggesting a quasigeostrophic regime with the absence of cyclone-anticyclone asymmetry (Fig. 12d).

## 3) INVERSE RICHARDSON NUMBER

Similar to Ro, the signature of many submesoscale vortices and filaments is apparent in the inverse Richardson

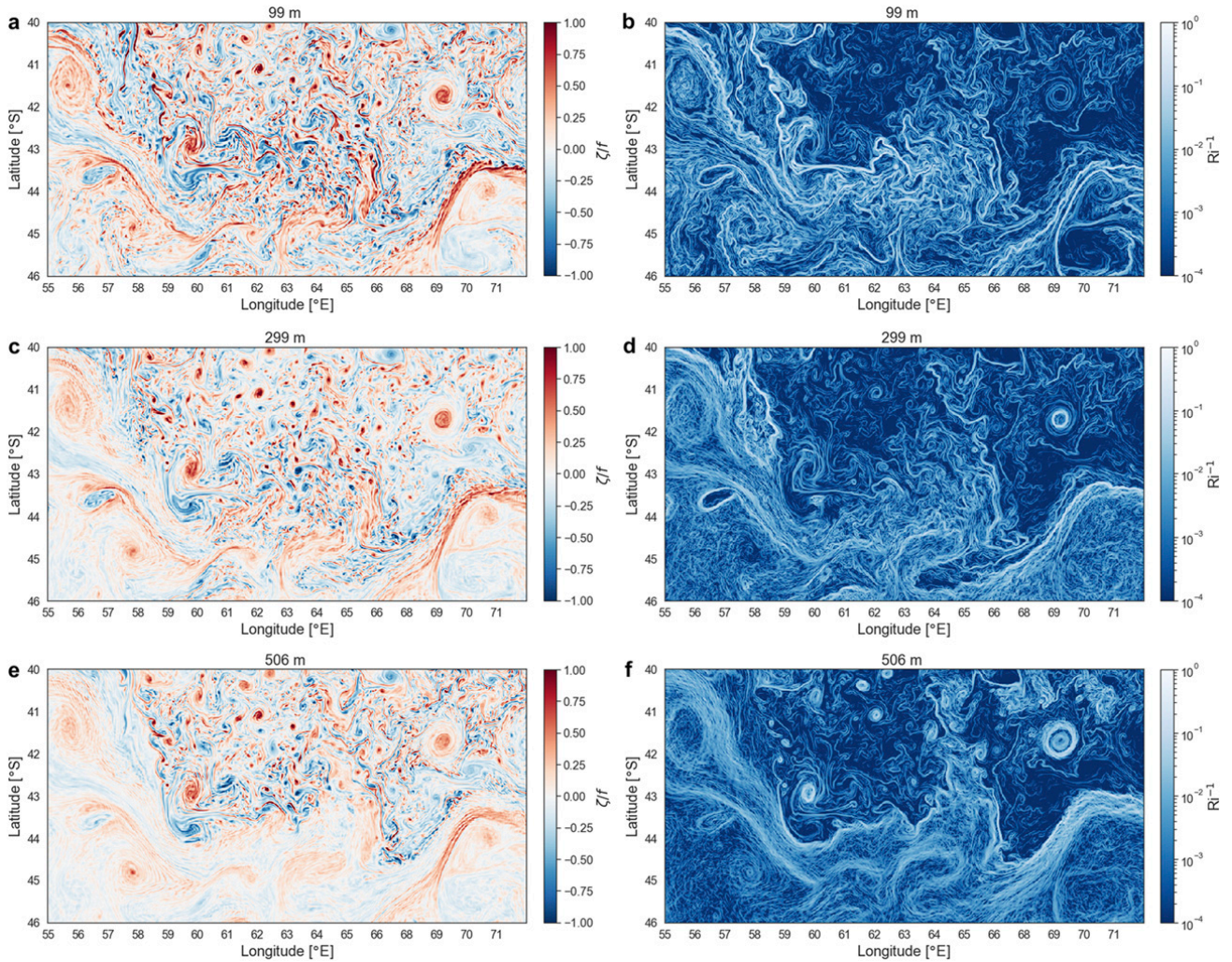


FIG. 10. As in Fig. 6, but for the (left) Rossby number  $\zeta/f$  and (right) inverse Richardson number  $Ri^{-1}$ .

number, defined by  $Ri^{-1} \equiv (\nabla b/fN)^2$  assuming thermal wind balance, down to 506 m (Figs. 10b,d,f). The 3D distribution of  $Ri^{-1}$  closely resembles that of  $|\nabla b|$  (Figs. 6a,c,e), and large  $Ri^{-1}$  are collocated with large  $|\nabla b|$ . The  $Ri^{-1}$  reaches 1.5 at 99 m, 0.5 at 299 m, 0.2 at 506 m, and 0.13 at 900 m. These large  $Ri^{-1}$  ( $\geq 0.1-0.2$ ) further highlight the ageostrophic nature of the ocean interior over the entire domain, known to be conducive to intense frontogenesis. Note that the thermal wind balance is a reasonable assumption that only breaks at a few locations south of the SAF and below the main thermocline. These locations can be identified by the negative values of the second component of the Ertel PV (Figs. 2g-i). A possible explanation for the thermal wind imbalance is the impact of IGWs, that are present below the main thermocline south of the SAF (Figs. 3c-d and 4c-d), and are associated with a temporal term that breaks the thermal wind balance, as suggested by Danioux et al. (2012). This can also be seen in the  $\omega-k$  spectrum of

the Ertel PV (Fig. 5f), where a part of the variance is captured by IGWs (above the dashed line).

Overall, these results highlight the generation mechanism of ageostrophic submesoscale fronts by mesoscale turbulence (Klein and Lapeyre 2009), not only within the ML but also in the ocean interior, as further detailed in the next section for two submesoscale fronts.

### c. Ageostrophic frontal dynamics

#### 1) CASE STUDY OF AGEOSTROPHIC FRONTAL DYNAMICS

In this section, frontal dynamics associated with  $|\nabla b|$  in the ocean interior are examined for two submesoscale fronts with a width of  $\sim 10$  km. One front is located at the SAF boundary (43.5°S, 71.3°E) and the other is on the edge of an elliptic mesoscale eddy in the northwest of the domain (41.8°S, 59.1°E), as inferred from SSH contours in Fig. 1. Both fronts are identified by the red arrows

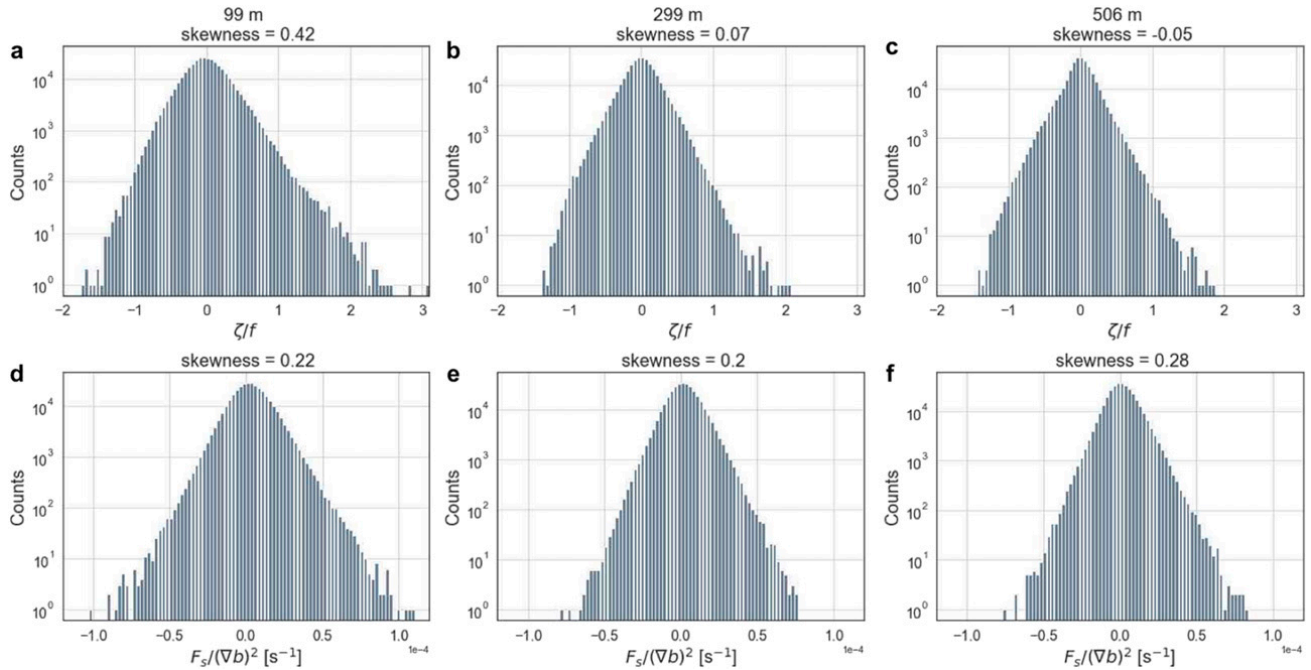


FIG. 11. Histograms of (a)–(c)  $|\zeta/f|$  and (d)–(f)  $F_s/(\nabla b)^2$  at (left) 99, (center) 299, and (right) 506 m over the entire domain for a randomly selected snapshot taken at 0200 UTC 28 Oct 2012.

on the vertical sections of Ertel PV in Fig. 3b and by the red lines on the horizontal map of Ertel PV in Fig. 2d. Their departure from QG is quantified in terms of the Rossby and Richardson numbers. The nature of the frontal dynamics is investigated with the frontogenesis function  $F_s$  defined as

$$F_s \equiv -\mathbf{Q} \cdot \nabla b, \quad (3)$$

where  $\mathbf{Q}$  is the frontogenetic vector of Hoskins et al. (1978), which can be expressed as

$$\mathbf{Q} = \begin{pmatrix} u_x & v_x \\ u_y & v_y \end{pmatrix} \cdot \begin{pmatrix} b_x \\ b_y \end{pmatrix}. \quad (4)$$

Since the equation of the evolution of a buoyancy gradient is given by

$$\frac{1}{2} \frac{d|\nabla b|^2}{dt} = F_s + \nabla w \cdot \nabla b, \quad (5)$$

with  $w$  being the vertical velocity field (Hoskins 1982). A positive  $F_s$  indicates the presence of frontogenesis, and a negative  $F_s$  indicates the presence of frontolysis (i.e., frontal destruction).

The exact location of the submesoscale fronts is apparent in the buoyancy anomaly field (blue curve in Fig. 13), which exhibits a sharp jump down to 299 m in both fronts. The fronts are associated  $\zeta/f$  (red curve) ranging from  $-1$  to  $2$  at 39 m, from  $-1$  to  $1$  at 99 m, from  $-0.75$  to  $0.75$  at 209 m, and from  $-0.5$  and  $0.5$  at

both 299 and 506 m. These high  $|\text{Ro}|$  ( $>0.5$ ) are the signature of an ageostrophic regime down to 506 m. In addition, both fronts are associated with high inverse Richardson number ( $\text{Ri}^{-1}$ ; green curve). Similar to  $\text{Ro}$ ,  $\text{Ri}^{-1}$  decreases with depth:  $\text{Ri}^{-1}$  reaches 0.3 and 0.6 at 39 m, 0.3 and 0.4 at 99 m, 0.25 and 0.4 at 209 m, 0.2 and 0.23 at 299 m, and only 0.05 and 0 at 506 m, for the front in the SAF and the one at the eddy's periphery, respectively. These high  $\text{Ri}^{-1}$  ( $\geq 0.2$ ) further confirm the ageostrophic character of deep-reaching submesoscale fronts. Last, the frontogenesis function  $F_s$  spikes at the location of these fronts, from the surface down to 299 m, highlighting their frontogenetic nature.  $F_s$  is on the order of  $10^{-18}$ – $10^{-17} \text{ s}^{-5}$ , which, when normalized by  $|\nabla b|^2$ , leads to rapid time scales from one to several hours. Interestingly, instance of frontolysis are often observed on one side of the front adjacent to frontogenesis (see at 99 m in Fig. 13c and at 299 m in Fig. 13h, for instance). Frontolysis alone also occurs (see at 506 m in Fig. 13i), indicating the front's total collapse. Furthermore, the slanted shape of submesoscale fronts discussed in the previous section is clearly visible in Fig. 13, as emphasized by the lateral shift of the fronts with depth.

A conspicuous asymmetry between the dense ( $b' < 0$ ) and light ( $b' > 0$ ) side of the fronts is present, not only at the surface, but also at depth. Cyclonic vorticities ( $\zeta/f > 0$ ; dense side) are considerably stronger than anticyclonic vorticities ( $\zeta/f < 0$ ; light side) and frontogenesis ( $F_s > 0$ ) occurs on the dense side of the front. Asymmetrical

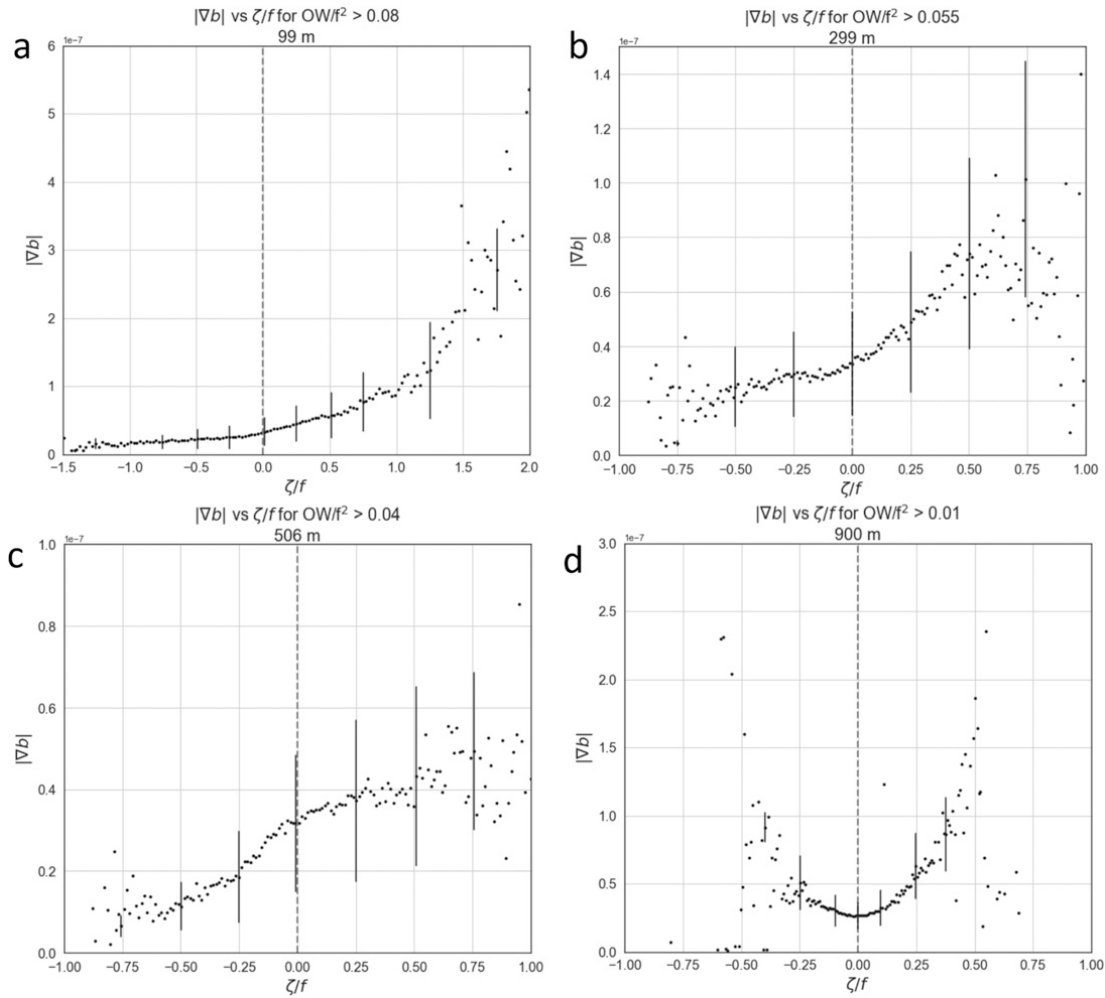


FIG. 12. Scatterplots of  $|\nabla b|$  and  $\zeta/f$  conditioned by Okubo–Weiss normalized by  $f^2$  such that  $\sim 20\%$  of the domain points are kept so as to capture the filaments and exclude the vortices, following the method described in Roulet and Klein (2010) (see main text and appendix C) at (a) 99, (b) 299, (c) 506, and (d) 900 m. The scatterplots are computed over the entire domain for a randomly selected snapshot taken at 0200 UTC 28 Oct 2012. Each point represents the average over each grid interval on the abscissa (that has a total of 200 grid intervals), and thin vertical lines show the std dev around the averages. A strong asymmetry between positive and negative  $\zeta/f$  and  $\nabla b$  is present down to 506 m, highlighting an ageostrophic regime. However, at 900 m the relation is symmetrical, suggesting a QG regime, as discussed in section 4.

frontogenesis is a distinctive characteristic of strongly ageostrophic flows (Hoskins 1982; McWilliams et al. 2009; Hakim and Keyser 2001; Capet et al. 2008) as it leads to a secondary circulation tilted along isopycnals, whereas the QG circulation cell is not tilted (Hakim and Keyser 2001). As a result, the vertical velocity field is negatively skewed, which further amplifies the skewness of  $Ro$  through the vorticity equation (Hoskins 1982; Hakim et al. 2002; Thomas et al. 2008).

The frontal dynamics considered here are complex because the fronts are not idealized nor isolated. Multiple submesoscale fronts of varying intensity are present in the vicinity of a stronger one, as can be seen in the successive occurrences of positive and negative  $Ro$  of different magnitudes (Fig. 13). Consequently, it is challenging to

derive a pointwise correspondence between the different quantities considered here, which was also the case for the nice results of Capet et al. (2008). However, we refer the reader to the idealized surface front presented in Fig. 4 of Thomas et al. (2008), where these relations are flabbergasting.

Overall, these results highlight the ageostrophic character of deep-reaching submesoscale fronts, characterized by large  $Ro$  and  $Ri^{-1}$  and positive  $F_s$ . These findings point to a positive skewness  $F_s$  associated with these fronts over the entire domain, as explored in the next section.

## 2) AGEOSTROPHIC FRONTOGENESIS

The 3D distribution of the frontogenesis function  $F_s$  closely resembles that of  $|\nabla b|$ . Strong  $F_s$  coincide with

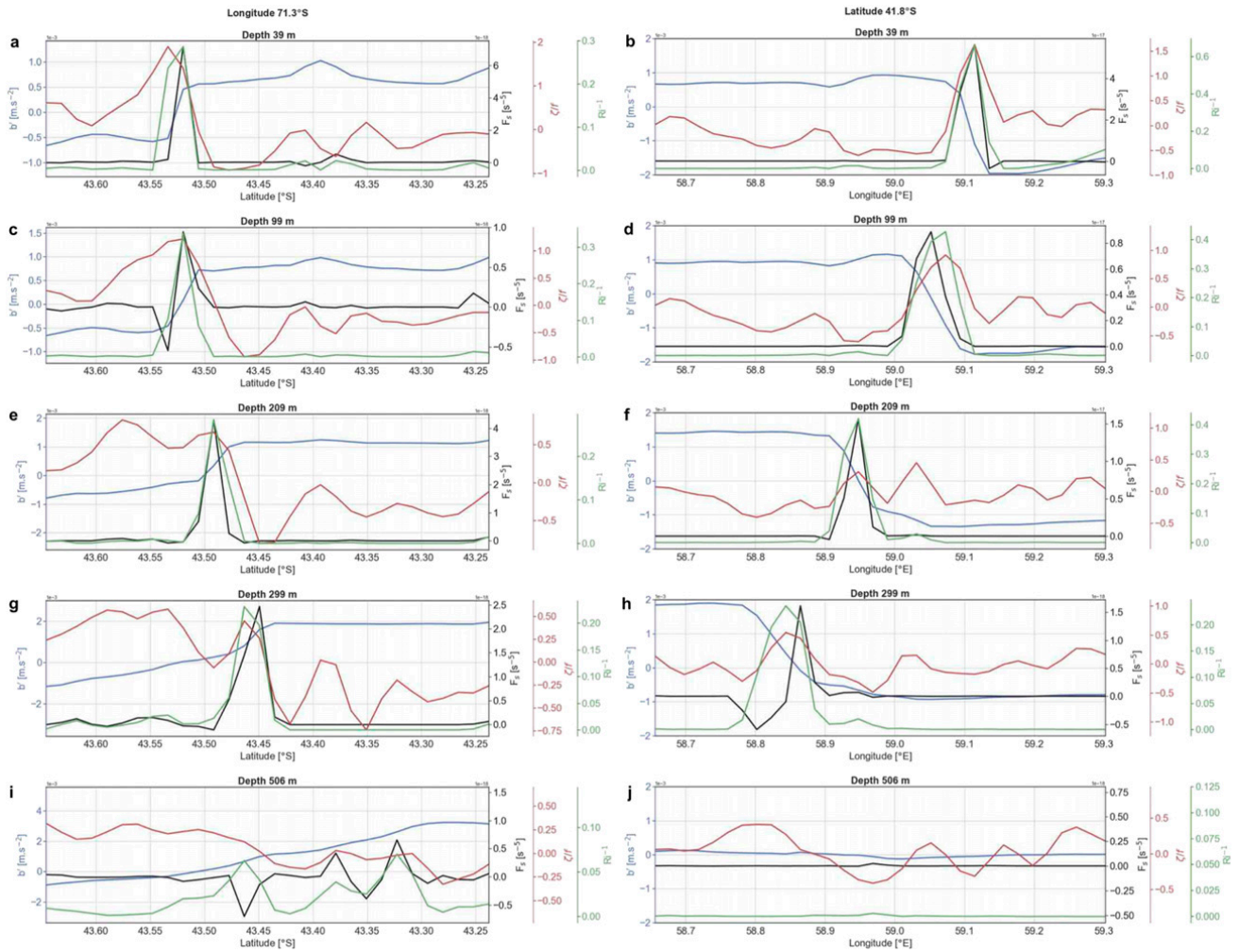


FIG. 13. Horizontal profiles across two individual submesoscale fronts at different depths, described in the main text: (a),(b) 39, (c),(d) 99, (e),(f) 209, (g),(h) 299, and (i),(j) 506 m. In all panels, the buoyancy anomaly  $b'$  is in blue, the frontogenesis function  $F_s$  is in black, the Rossby number  $\zeta/f$  is in red, and the inverse Richardson number  $Ri^{-1}$  is in green. These sections are shown by the red lines in Fig. 2d and the red arrows in Figs. 3c and 3d.

strong  $|\nabla b|$  at all depths and  $F_s$  is characterized by filamentary structures with a width of  $\sim 10$  km down to 299 m. At depth, filaments of  $F_s$  are concentrated along the SAF (Fig. 6). This spatial correspondence confirms that submesoscale fronts are generated by frontogenesis processes in the ocean interior.

The time scale associated to frontogenesis and frontolysis can be retrieved from  $F_s/(\nabla b)^2$  [Eq. (5)]. RMS values of  $F_s/(\nabla b)^2$  range from  $1.7 \times 10^{-5}$  to  $10^{-5} s^{-1}$  between the surface and 500 m, corresponding to time scales from 10 h to a day. Twenty percent of frontogenetic processes [ $F_s/(\nabla b)^2 > 0$ ] are larger than  $2 \times 10^{-5} s^{-1}$ —that is, 14 h—at 39 m and  $1 \times 10^{-5} s^{-1}$ —that is, a day—at 900 m (Fig. 8c). Similar results are obtained for frontolytic processes [ $F_s/(\nabla b)^2 < 0$ ] (Fig. 8c). These time scales are consistent with the strain rate, for which 20% of the values are larger than  $5 \times 10^{-5} s^{-1}$ —that is, 12 h—at 39 m and  $1.5 \times 10^{-5} s^{-1}$ —that is, 19 h—at 900 m (Fig. 8d).

The rms of positive  $F_s/(\nabla b)^2$  is greater than that of negative  $F_s/(\nabla b)^2$  by a factor of at least 1.4, regardless of depth, indicating that frontal creation is faster than frontal collapse. Similar to Ro,  $F_s/(\nabla b)^2$  is positively skewed, with skewness values of  $\sim 0.2$  down to 506 m (Figs. 11d–f), highlighting the dominance of frontogenesis over frontolysis in the ocean interior. Overall, the strong asymmetry of  $F_s$  in the upper 500 m emphasizes once again the ageostrophic character of frontogenesis in the ocean interior, which is known to be associated with enhanced vertical velocities and vertical heat fluxes.

#### d. Vertical velocities and vertical heat flux

Vertical sections of daily-averaged vertical velocities  $w$  reveal positive and negative  $w$  of up to  $500 m day^{-1}$  (Figs. 14a,c,e,g). Structures of  $w$  have a width of  $\sim 10$ – $20$  km. They are intensified in the ocean interior, below the mixed layer down to at least 900 m. Strong

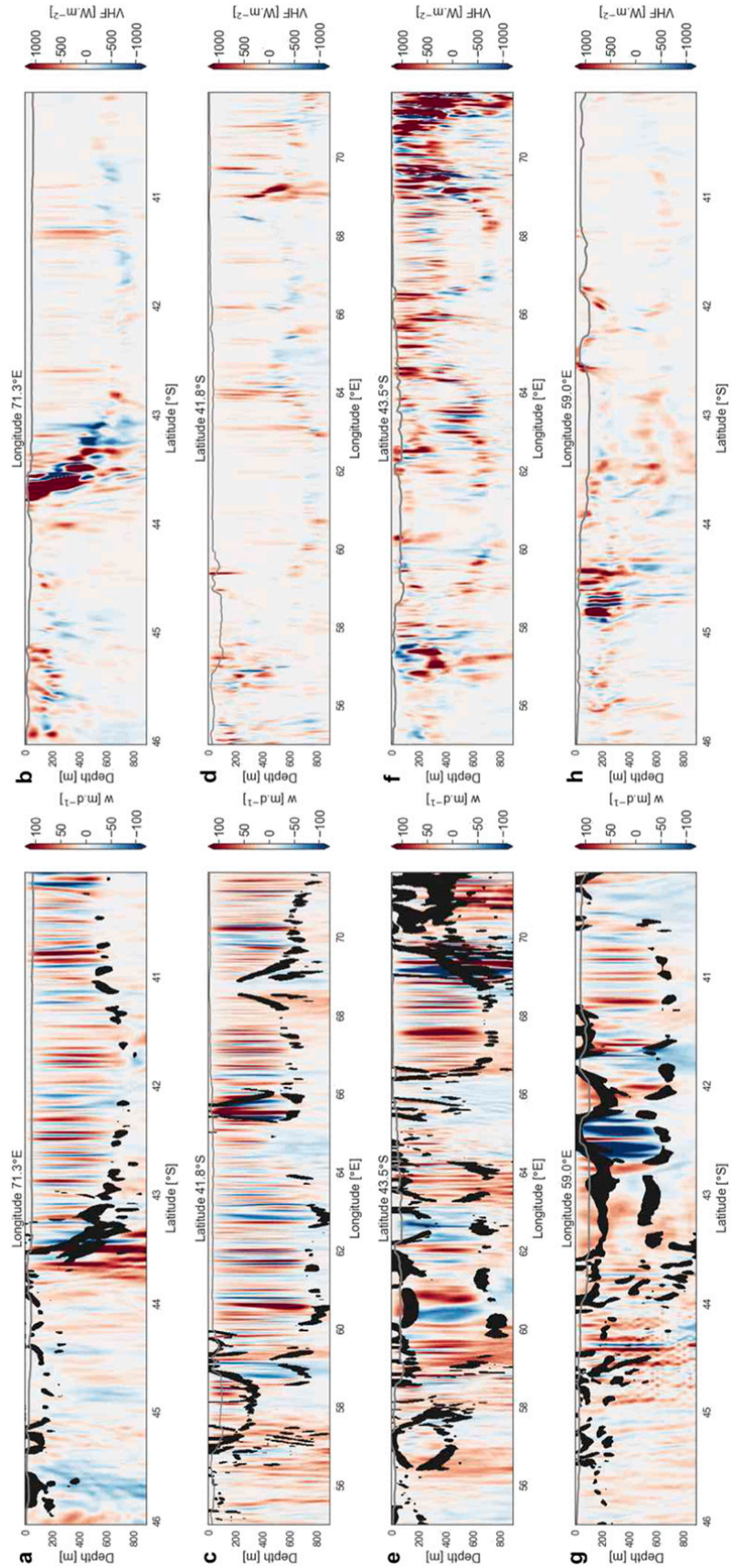


FIG. 14. Vertical sections of (left) vertical velocities  $w$  superimposed with  $|\nabla b| > 5 \times 10^{-8} \text{ s}^{-2}$  shown in black and (right) VHF for the zonal and meridional sections highlighted by the white dashed lines in Fig. 2b. The maps are for a randomly selected snapshot taken at 0200 UTC 28 Oct 2012. The mixed layer depth is shown in gray.

buoyancy gradients (in black in Figs. 14a,c,e,g) are collocated with large  $w$ . The signature of divergence is apparent as intensified and thin vertical features of  $w$  are collocated with  $\zeta$  in areas of weak vertical stratification (at 41°–43°S in Fig. 14a or at 68°E in Fig. 14c for example). Instances of strong  $w$  inside subsurface eddies also occur, with  $\nabla b$  acting as a barrier (at 42.5°S in Fig. 14g).  $w$  are impacted by IGWs, as can be seen at 44.5°S in Fig. 14g. The rms of  $w$  over the domain is maximal at 350 m with a value of 45 m day<sup>-1</sup> and is 20 m day<sup>-1</sup> at both 50 and 900 m (dashed blue curve in Fig. 15).

Vertical heat fluxes (VHF) are estimated from temperature and vertical velocity anomalies as  $\text{VHF} = \rho_0 C_p w' T'$ , where the prime refers to the anomaly with respect to the domain-averaged value and  $C_p = 3985 \text{ J kg}^{-1} \text{ K}^{-1}$  is the specific heat capacity of seawater (Figs. 14b,d,f,h). A positive or negative value respectively indicates an upward or downward heat flux. Positive values result from frontogenesis, whereas negative values arise from frontolysis. VHF have a local amplitude reaching 2000 W m<sup>-2</sup> down to at least 900 m. VHF are enhanced at the location of strong submesoscale fronts that border surface trapped, subsurface and deep mesoscale eddies. Time and domain-averaged VHF ( $\langle \text{VHF} \rangle$ ) are positive and enhanced in the ocean interior relative to the first 50 m, that is, below the ML (Fig. 15), shedding new light on the diabatic nature of the ocean interior. In the active submesoscale area (dashed rectangle in Fig. 6b),  $\langle \text{VHF} \rangle$  over 5 days reach values of up to 370 W m<sup>-2</sup> at 150 m and remain surprisingly large at depth; 260 W m<sup>-2</sup> at 500 m and 140 W m<sup>-2</sup> at 900 m (orange curve in Fig. 15). Over the entire domain and one month,  $\langle \text{VHF} \rangle$  reaches a maximal value of 260 W m<sup>-2</sup> at 120 m, 140 W m<sup>-2</sup> at 50 m, and 30 W m<sup>-2</sup> at 900 m (green curve in Fig. 15). These findings are consistent with the in situ observations of Siegelman et al. (2020). The  $\omega$ - $k$  cospectra (appendix C) corroborate these results and further show that, down to 299 m, VHF are explained by scales <50 km and frequencies corresponding to time scales from a few hours to a few days (Figs. 16a–c). At 506 m (Fig. 16d) and below (not shown), VHF are explained by scales of 30–150 km. A key and striking result is that linear IGWs do not impact VHF, which are predominantly explained by balanced motions. However, this does not fully exclude the impact of nonlinear IGWs and their interactions with balanced motions (Thomas 2017). These results shed light on the efficient pathway for the transport of heat from the ocean interior to the surface enabled by deep submesoscale fronts.

## 5. Summary and perspectives

The region considered in this study is a subdomain of the ACC, which is sufficiently large to capture ocean-scale

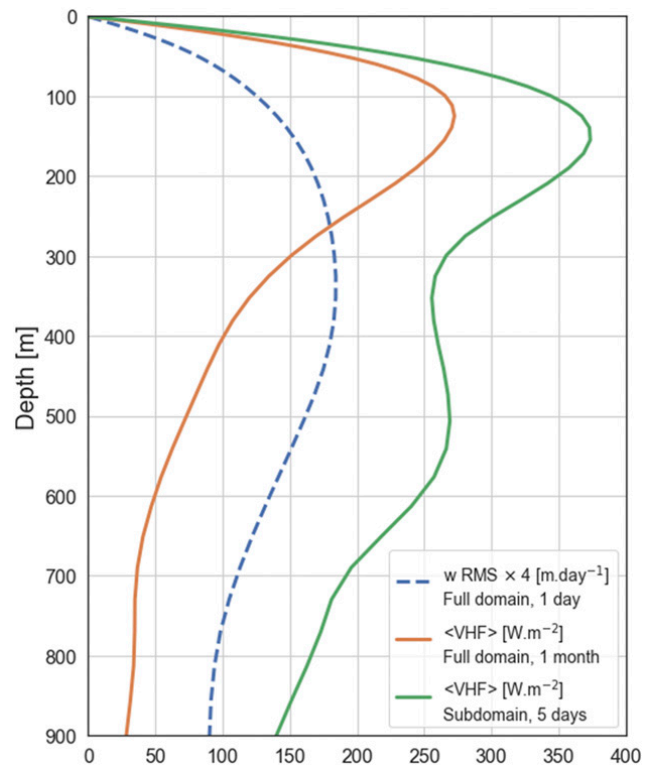


FIG. 15. RMS of daily-averaged vertical velocities over the entire domain on 28 Oct 2012 (dashed blue curve), along with domain-averaged vertical heat fluxes (VHF) over the entire domain and one month (15 Oct–15 Nov 2012) (orange curve) and over the active submesoscale area (dashed black rectangle in Fig. 6d) and 5 days (26–31 Oct 2012) (green curve). The  $\langle \text{VHF} \rangle$  are directed upward (positive values), and they are enhanced at depth, especially below the mixed layer.

interactions, from the large-scale meandering SAF, to multiple mesoscale eddies and numerous submesoscale fronts. Mesoscale eddies emanating from the SAF interact and coexist on both sides of the jet, down to a least 506 m. These surface-trapped, subsurface and deep mesoscale eddies are associated with submesoscale structures characterized by large  $|\text{Ro}|$  ( $>0.5$ ) dominated by cyclonic vorticity ( $\zeta/f > 0$ ). Intense gradients of Ertel PV, Ro, and buoyancy are located at their periphery, acting as ageostrophic dynamical barriers, which increase the eddies' coherence and lifetime (Mariotti et al. 1994). Note that the generation mechanism of these subsurface and deep eddies remains an open question that is out of the scope of this paper and will be the object of a future study.

Lateral gradients of buoyancy, resulting from the straining generated by mesoscale eddies, have a remarkable weak depth dependence, in stark contrast with QG dynamics but in close agreement with ageostrophic Boussinesq flows (Molemaker et al. 2010). Resulting frontogenesis is associated with rapid time scales from a few hours to a day, comparable to the background strain

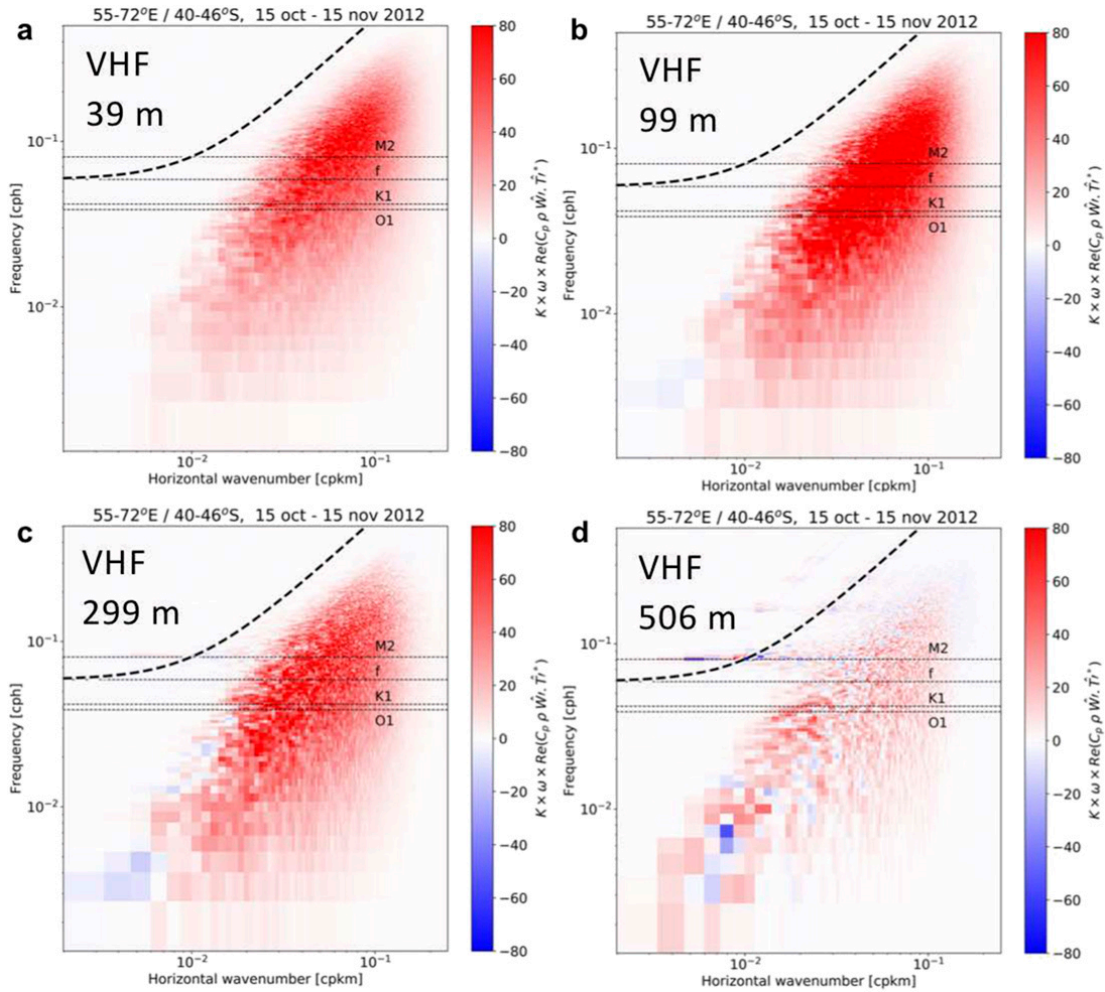


FIG. 16. Frequency–wavenumber cospectra of vertical velocities and temperature computed from 15 Oct to 15 Nov 2012 at (a) 39, (b) 99, (c) 299, and (d) 506 m. These cospectra are presented in a variance-preserving form, which allows one to directly compare the relative contribution of different time and spatial scales with the total variance (appendix B).

field. Frontogenesis is asymmetric, amplifying the positive skewness of  $Ro$ , which is the signature of ageostrophic dynamics. Consequently, frontogenesis statistically dominates frontolysis, consistent with the theoretical and idealized studies of Klein and Lapeyre (2009), Roulet and Klein (2010), and Molemaker et al. (2015). As a result, there is a net upward VHF at deep-reaching submesoscale fronts that is induced by the asymmetrical character of the ageostrophic frontogenesis (Molemaker et al. 2015). These VHF are larger in the ocean interior than within the ML, concordant with the in situ findings of Siegelman et al. (2020) and Yu et al. (2019), and suggesting the presence of an intensified oceanic restratification at depth.

Several caveats pertaining to the model resolution need to be mentioned. First, even though  $|\nabla b|$  are strong and associated with large  $|Ro|$  ( $>0.5$ ), they remain weaker than in the observations, especially in terms of  $Ri^{-1}$ . This is likely due to the fact that buoyancy gradients are

partly captured by higher vertical normal modes than those resolved by the model because of its coarse vertical resolution at depth (5 m at a depth of 49 m vs 45 m at 900 m). In comparison, the in situ data in Siegelman et al. (2020) have a constant vertical resolution of 1 m. This points to the need of choosing a vertical resolution able to adequately resolve higher vertical normal modes. In addition, the horizontal resolution of the model seems to lie at the edge of being submesoscale resolving, as can be seen in Fig. 13 where the sharp fronts are only captured by a single model grid point. As such, a higher 3D resolution is needed to fully represent the ageostrophic dynamics of the interior ocean, which are likely to be even stronger than what is reported here.

This study solely considers a region of the ACC in springtime. However, the vertical heat fluxes diagnosed here in the ocean interior are comparable to those obtained in the ML in winter on a global scale (Su et al. 2018).



As such, these results call for extended analyses of deep ageostrophic frontal dynamics at different seasons and throughout the World Ocean, in particular in other parts of the ACC, as well as in the Gulf Stream and Kuroshio Extension, in order to confirm the ageostrophic character of the ocean interior.

*Acknowledgments.* Thanks are given to Patrice Klein for his wise and always inspiring advices and to Andrew F. Thompson for stimulating discussions. Thanks are also given to Hector S. Torres for his invaluable assistance in navigating the tricks of NASA Advanced Supercomputing (NAS), to Dimitris Menemenlis for running the LLC4320 simulation, to Christopher Henze at NASA Ames Hyperwall, and to the MITgcm developers and NAS scientists that made available the model outputs. This research was carried out, in part, at the Jet Propulsion Laboratory, California Institute of Technology, under a contract with NASA. Author Siegelman is a NASA-JVSRP affiliate and is supported by a joint CNES–Région Bretagne doctoral fellowship. High-end computing resources for the numerical simulation were provided by the NAS Division at the Ames Research Center.

## APPENDIX A

### Details of the LLC4320 Simulation

The outputs of an ocean general circulation model, enabled by NASA Advanced Supercomputing Division, are used to investigate ocean dynamics down to the submesoscale. The model is based on a global, full-depth ocean and sea ice configuration of the Massachusetts Institute of Technology general circulation model (MITgcm) (Marshall et al. 1997; Hill et al. 2007) and uses a latitude–longitude–polar cap (LLC) grid (Forget et al. 2015). The MITgcm was spun up in a hierarchy of numerical simulations with increasing horizontal resolutions with 90 vertical levels. The simulation analyzed here is the highest resolution, the LLC4320 at  $1/48^\circ$ , with a time step of 25 s. The prognostic variables are saved as instantaneous snapshots at hourly intervals. Control and forcing files as well as details of the high-resolution LLC model setups are available online ([http://mitgcm.org/viewvc/MITgcm/MITgcm\\_contrib/llc\\_hires](http://mitgcm.org/viewvc/MITgcm/MITgcm_contrib/llc_hires)).

Surface fluxes are from the  $0.14^\circ$  European Centre for Medium-Range Weather Forecasting (ECMWF) atmospheric operational model analysis, starting in 2011. The model also includes tidal forcing for the 16 most significant components that are applied as additional atmospheric pressure forcing (Chaudhuri et al. 2013). Vertical mixing is parameterized based on the critical value of Richardson number and is implemented using

the  $K$ -profile parameterization (KPP) scheme (Large et al. 1994) that has been extensively used and evaluated in ocean modeling studies (Large et al. 1997; Fernández-Castro et al. 2014). More details on the LLC4320 simulation, in particular on its validation with observations, can be found in Torres et al. (2018).

## APPENDIX B

### Frequency–Wavenumber Spectrum and Cospectrum

The  $\omega$ – $k$  spectrum of a given variable  $\phi(x, y, t)$  is computed in a box of  $700 \text{ km} \times 700 \text{ km}$  and over 1 month. We refer the reader to Torres et al. (2018) for the full method. However, briefly, before computing the  $\omega$ – $k$  spectrum of a  $\phi(x, y, t)$ , its linear trend is removed and a 3D Hanning window is subsequently applied to the detrended  $\phi(x, y, t)$  (Qiu et al. 2018). A discrete 3D Fourier transform is then computed to retrieve  $\hat{\phi}(k, l, \omega)$ , where the caret indicates the Fourier transform,  $k$  is the zonal wavenumber,  $l$  is the meridional wavenumber, and  $\omega$  is the frequency. The 3D Fourier transform is used to compute a 2D spectral density  $|\hat{\phi}|^2(\kappa, \omega)$ , where  $\kappa$  is the isotropic wavenumber, defined as  $\kappa = (k^2 + l^2)^{1/2}$ . The transformation from an anisotropic spectrum to an isotropic spectrum is performed following the method described by Savage et al. (2017).

The dispersion relation curves for IGWs (Gill 1982) have been also estimated for each vertical normal mode (Torres et al. 2018). The curve related to the tenth baroclinic vertical mode, that is, the highest baroclinic mode resolved by the simulation, was found to be the most relevant to partition balanced motions (below the curve) and IGWs (above the curve). To better compare the variance explained by IGWs and BMs in different areas of the  $\omega$ – $\kappa$  space, the spectra are presented in a variance-preserving form, which is achieved by multiplying the  $\omega$ – $k$  spectra by  $\omega$  and  $\kappa$  (Torres et al. 2018).

The  $\omega$ – $k$  cospectra of vertical heat fluxes are computed similar to the  $\omega$ – $k$  spectrum, following the method described in Flexas et al. (2019). First, the Fourier transforms of vertical velocity  $\hat{W}(k, l, \omega)$  and temperature  $\hat{T}(k, l, \omega)$  are calculated. The cospectrum of vertical heat fluxes is then given by

$$\widehat{W \cdot T}(k, l, \omega) = \text{Re}[\hat{W} \cdot \hat{T}^*(k, l, \omega) + \hat{W}^* \cdot \hat{T}(k, l, \omega)],$$

where  $\text{Re}$  is the real part of the complex quantity and the asterisk indicates the complex conjugate. The 2D cospectrum  $\widehat{W \cdot T}(\kappa, \omega)$  is retrieved using the same method as before. The  $\omega$ – $k$  spectrum and cospectrum are presented in a variance-preserving form for easier comparison across the frequency–wavenumber domain.

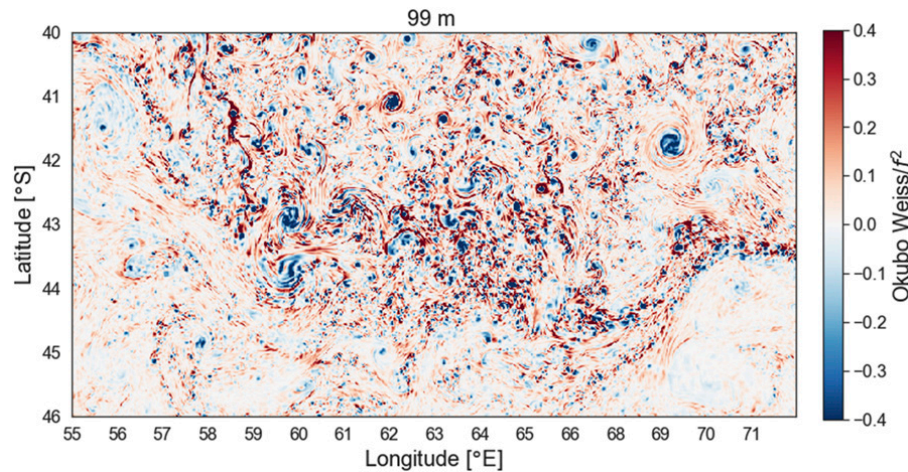


FIG. C1. Map of the Okubo–Weiss quantity  $\lambda$  normalized by  $f^2$  at 99 m. Vortex cores dominated by  $\zeta$  are in blue ( $\lambda < 0$ ), and filaments dominated by strain are in red ( $\lambda > 0$ ). Strain-dominated regions are particularly prone to the formation of submesoscale fronts because of the exponential growth of tracer gradients in this region of the flow.

## APPENDIX C

### Okubo–Weiss Quantity

The Okubo–Weiss quantity is defined as

$$\lambda = \frac{1}{4}(\sigma_n^2 + \sigma_s^2 - \zeta^2).$$

where  $\zeta = v_x - u_y$  is the relative vorticity,  $\sigma_n = u_x - v_y$  is the normal strain rate, and  $\sigma_s = v_x + u_y$  is the shear strain rate. The Okubo–Weiss quantity, derived by Okubo (1970) and Weiss (1991), is used to partition the fluid into regions with different dynamical properties, that is, elliptic regions dominated by  $\zeta$  ( $\lambda < 0$ ) from hyperbolic regions dominated by  $\sigma_n$  and  $\sigma_s$  ( $\lambda > 0$ ) (Fig. C1 and Fig. S2 in the online supplemental material). Under the assumption that the velocity gradient is slowly varying along a Lagrangian trajectory, the behavior of a tracer gradient can be determined by the sign of  $\lambda$  (Hua and Klein 1998). Indeed, tracer gradients do not grow in vortex cores where  $\lambda < 0$ . In this case, the gradient vector experiences a simple rotation. On the other hand, in strain-dominated areas where  $\lambda > 0$ , tracer gradients exponentially grow.

## REFERENCES

- Armi, L., D. Hebert, N. Oakey, J. Price, P. L. Richardson, T. Rossby, and B. Ruddick, 1988: The history and decay of a Mediterranean salt lens. *Nature*, **333**, 649–651, <https://doi.org/10.1038/333649a0>.
- Barbosa Aguiar, A., C. Ménesguen, S. Le Gentil, R. Schopp, and X. Carton, 2015: Cyclones and anticyclones in seismic imaging. *J. Phys. Oceanogr.*, **45**, 2436–2443, <https://doi.org/10.1175/JPO-D-15-0066.1>.
- Biescas, B., V. Sallarès, J. L. Pelegrí, F. Machín, R. Carbonell, G. Buffett, J. J. Dañobeitia, and A. Calahorrano, 2008: Imaging meddy finestructure using multichannel seismic reflection data. *Geophys. Res. Lett.*, **35**, L11609, <https://doi.org/10.1029/2008GL033971>.
- Callies, J., R. Ferrari, J. M. Klymak, and J. Gula, 2015: Seasonality in submesoscale turbulence. *Nat. Commun.*, **6**, 6862, <https://doi.org/10.1038/ncomms7862>.
- Capet, X., J. C. McWilliams, M. J. Molemaker, and A. Shchepetkin, 2008: Mesoscale to submesoscale transition in the California Current system. Part I: Flow structure, eddy flux, and observational tests. *J. Phys. Oceanogr.*, **38**, 29–43, <https://doi.org/10.1175/2007JPO3671.1>.
- Chassignet, E. P., and X. Xu, 2017: Impact of horizontal resolution (1/12 to 1/50) on Gulf Stream separation, penetration, and variability. *J. Phys. Oceanogr.*, **47**, 1999–2021, <https://doi.org/10.1175/JPO-D-17-0031.1>.
- Chaudhuri, A. H., R. M. Ponte, G. Forget, and P. Heimbach, 2013: A comparison of atmospheric reanalysis surface products over the ocean and implications for uncertainties in air–sea boundary forcing. *J. Climate*, **26**, 153–170, <https://doi.org/10.1175/JCLI-D-12-00090.1>.
- Danioux, E., J. Vanneste, P. Klein, and H. Sasaki, 2012: Spontaneous inertia-gravity-wave generation by surface-intensified turbulence. *J. Fluid Mech.*, **699**, 153–173, <https://doi.org/10.1017/jfm.2012.90>.
- Fernández-Castro, B., B. Mouriño-Carballido, V. Benítez-Barrios, P. Chouciño, E. Fraile-Nuez, R. Graña, M. Piedeleu, and A. Rodríguez-Santana, 2014: Microstructure turbulence and diffusivity parameterization in the tropical and subtropical Atlantic, Pacific and Indian Oceans during the Malaspina 2010 expedition. *Deep-Sea Res. I*, **94**, 15–30, <https://doi.org/10.1016/j.dsr.2014.08.006>.
- Flexas, M. M., A. F. Thompson, H. S. Torres, P. Klein, J. T. Farrar, H. Zhang, and D. Menemenlis, 2019: Global estimates of the energy transfer from the wind to the ocean, with emphasis on near-inertial oscillations. *J. Geophys. Res. Oceans*, **124**, 5723–5746, <https://doi.org/10.1029/2018JC014453>.
- Forget, G., J.-M. Campin, P. Heimbach, C. N. Hill, R. M. Ponte, and C. Wunsch, 2015: ECCO version 4: An integrated

- framework for non-linear inverse modeling and global ocean state estimation. *Geosci. Model Dev.*, **8**, 3071–3104, <https://doi.org/10.5194/GMD-8-3071-2015>.
- Fox-Kemper, B., R. Ferrari, and R. Hallberg, 2008: Parameterization of mixed layer eddies. Part I: Theory and diagnosis. *J. Phys. Oceanogr.*, **38**, 1145–1165, <https://doi.org/10.1175/2007JPO3792.1>.
- Gill, A. E., 1982: *Atmosphere–Ocean Dynamics*. Vol. 30. Academic Press, 662 pp.
- Gula, J., T. M. Blacic, and R. E. Todd, 2019: Submesoscale coherent vortices in the Gulf Stream. *Geophys. Res. Lett.*, **46**, 2704–2714, <https://doi.org/10.1029/2019GL081919>.
- Hakim, G. J., and D. Keyser, 2001: Canonical frontal circulation patterns in terms of Green’s functions for the Sawyer–Eliassen equation. *Quart. J. Roy. Meteor. Soc.*, **127**, 1795–1814, <https://doi.org/10.1002/qj.4971275717>.
- , C. Snyder, and D. J. Muraki, 2002: A new surface model for cyclone–anticyclone asymmetry. *J. Atmos. Sci.*, **59**, 2405–2420, [https://doi.org/10.1175/1520-0469\(2002\)059<2405:ANSMFC>2.0.CO;2](https://doi.org/10.1175/1520-0469(2002)059<2405:ANSMFC>2.0.CO;2).
- Haynes, P., and J. Anglade, 1997: The vertical-scale cascade in atmospheric tracers due to large-scale differential advection. *J. Atmos. Sci.*, **54**, 1121–1136, [https://doi.org/10.1175/1520-0469\(1997\)054<1121:TVSCIA>2.0.CO;2](https://doi.org/10.1175/1520-0469(1997)054<1121:TVSCIA>2.0.CO;2).
- Hill, C., D. Menemenlis, B. Ciotti, and C. Henze, 2007: Investigating solution convergence in a global ocean model using a 2048-processor cluster of distributed shared memory machines. *Sci. Program.*, **15**, 107–115, <https://doi.org/10.1155/2007/458463>.
- Holton, J. R., 1973: An introduction to dynamic meteorology. *Amer. J. Phys.*, **41**, 752–754, <https://doi.org/10.1119/1.1987371>.
- Hoskins, B. J., 1982: The mathematical theory of frontogenesis. *Annu. Rev. Fluid Mech.*, **14**, 131–151, <https://doi.org/10.1146/annurev.fl.14.010182.001023>.
- , and F. P. Bretherton, 1972: Atmospheric frontogenesis models: Mathematical formulation and solution. *J. Atmos. Sci.*, **29**, 11–37, [https://doi.org/10.1175/1520-0469\(1972\)029<0011:AFMMFA>2.0.CO;2](https://doi.org/10.1175/1520-0469(1972)029<0011:AFMMFA>2.0.CO;2).
- , I. Draghici, and H. C. Davies, 1978: A new look at the  $\omega$ -equation. *Quart. J. Roy. Meteor. Soc.*, **104**, 31–38, <https://doi.org/10.1002/qj.49710443903>.
- Hua, B. L., and D. B. Haidvogel, 1986: Numerical simulations of the vertical structure of quasi-geostrophic turbulence. *J. Atmos. Sci.*, **43**, 2923–2936, [https://doi.org/10.1175/1520-0469\(1986\)043<2923:NSOTVS>2.0.CO;2](https://doi.org/10.1175/1520-0469(1986)043<2923:NSOTVS>2.0.CO;2).
- , and P. Klein, 1998: An exact criterion for the stirring properties of nearly two-dimensional turbulence. *Physica D*, **113**, 98–110, [https://doi.org/10.1016/S0167-2789\(97\)00143-7](https://doi.org/10.1016/S0167-2789(97)00143-7).
- Kim, Y. S., and A. H. Orsi, 2014: On the variability of Antarctic Circumpolar Current fronts inferred from 1992–2011 altimetry. *J. Phys. Oceanogr.*, **44**, 3054–3071, <https://doi.org/10.1175/JPO-D-13-0217.1>.
- Klein, P., and G. Lapeyre, 2009: The oceanic vertical pump induced by mesoscale and submesoscale turbulence. *Annu. Rev. Mar. Sci.*, **1**, 351–375, <https://doi.org/10.1146/annurev.marine.010908.163704>.
- , A.-M. Treguier, and B. L. Hua, 1998: Three-dimensional stirring of thermohaline fronts. *J. Mar. Res.*, **56**, 589–612, <https://doi.org/10.1357/002224098765213595>.
- , and Coauthors, 2019: Ocean-scale interactions from space. *Earth Space Sci.*, **6**, 795–817, <https://doi.org/10.1029/2018EA000492>.
- Kundu, P. K., and I. Cohen, 2004: Application of complex variables. *Fluid Mechanics*, Academic Press, 157–158.
- Large, W. G., J. C. McWilliams, and S. C. Doney, 1994: Oceanic vertical mixing: A review and a model with a nonlocal boundary layer parameterization. *Rev. Geophys.*, **32**, 363–403, <https://doi.org/10.1029/94RG01872>.
- , G. Danabasoglu, S. C. Doney, and J. C. McWilliams, 1997: Sensitivity to surface forcing and boundary layer mixing in a global ocean model: Annual-mean climatology. *J. Phys. Oceanogr.*, **27**, 2418–2447, [https://doi.org/10.1175/1520-0485\(1997\)027<2418:STSFAB>2.0.CO;2](https://doi.org/10.1175/1520-0485(1997)027<2418:STSFAB>2.0.CO;2).
- Mahadevan, A., 2016: The impact of submesoscale physics on primary productivity of plankton. *Annu. Rev. Mar. Sci.*, **8**, 161–184, <https://doi.org/10.1146/annurev-marine-010814-015912>.
- Mariotti, A., B. Legras, and D. G. Dritschel, 1994: Vortex stripping and the erosion of coherent structures in two-dimensional flows. *Phys. Fluids*, **6**, 3954–3962, <https://doi.org/10.1063/1.868385>.
- Marshall, J., A. Adcroft, C. Hill, L. Perelman, and C. Heisey, 1997: A finite-volume, incompressible Navier Stokes model for studies of the ocean on parallel computers. *J. Geophys. Res.*, **102**, 5753–5766, <https://doi.org/10.1029/96JC02775>.
- McWilliams, J. C., 1984: The emergence of isolated coherent vortices in turbulent flow. *J. Fluid Mech.*, **146**, 21–43, <https://doi.org/10.1017/S0022112084001750>.
- , 2016: Submesoscale currents in the ocean. *Proc. Roy. Soc. London*, **472A**, 20160117, <https://doi.org/10.1098/RSPA.2016.0117>.
- , F. Colas, and M. Molemaker, 2009: Cold filamentary intensification and oceanic surface convergence lines. *Geophys. Res. Lett.*, **36**, L18602, <https://doi.org/10.1029/2009GL039402>.
- Menesguen, C., B. Hua, C. Papenberg, D. Klaeschen, L. Geli, and R. Hobbs, 2009: Effect of bandwidth on seismic imaging of rotating stratified turbulence surrounding an anticyclonic eddy from field data and numerical simulations. *Geophys. Res. Lett.*, **36**, L00D05, <https://doi.org/10.1029/2009GL039951>.
- Meunier, T., C. Ménesguen, R. Schopp, and S. Le Gentil, 2015: Tracer stirring around a meddy: The formation of layering. *J. Phys. Oceanogr.*, **45**, 407–423, <https://doi.org/10.1175/JPO-D-14-0061.1>.
- Molemaker, M. J., J. C. McWilliams, and I. Yavneh, 2005: Baroclinic instability and loss of balance. *J. Phys. Oceanogr.*, **35**, 1505–1517, <https://doi.org/10.1175/JPO2770.1>.
- , —, and X. Capet, 2010: Balanced and unbalanced routes to dissipation in an equilibrated eady flow. *J. Fluid Mech.*, **654**, 35–63, <https://doi.org/10.1017/S0022112009993272>.
- , —, and W. K. Dewar, 2015: Submesoscale instability and generation of mesoscale anticyclones near a separation of the California Undercurrent. *J. Phys. Oceanogr.*, **45**, 613–629, <https://doi.org/10.1175/JPO-D-13-0225.1>.
- Okubo, A., 1970: Horizontal dispersion of floatable particles in the vicinity of velocity singularities such as convergences. *Deep-Sea Res. Oceanogr. Abstr.*, **17**, 445–454, [https://doi.org/10.1016/0011-7471\(70\)90059-8](https://doi.org/10.1016/0011-7471(70)90059-8).
- Pedlosky, J., 2013a: *Geophysical Fluid Dynamics*. Springer Science and Business Media, 626 pp.
- , 2013b: *Waves in the Ocean and Atmosphere: Introduction to Wave Dynamics*. Springer Science and Business Media, 624 pp.
- Qiu, B., S. Chen, P. Klein, J. Wang, H. Torres, L.-L. Fu, and D. Menemenlis, 2018: Seasonality in transition scale from balanced to unbalanced motions in the World Ocean. *J. Phys. Oceanogr.*, **48**, 591–605, <https://doi.org/10.1175/JPO-D-17-0169.1>.
- Rosso, I., and Coauthors, 2014: Vertical transport in the ocean due to sub-mesoscale structures: Impacts in the Kerguelen region. *Ocean Modell.*, **80**, 10–23, <https://doi.org/10.1016/j.ocemod.2014.05.001>.
- Roulet, G., and P. Klein, 2010: Cyclone–anticyclone asymmetry in geophysical turbulence. *Phys. Rev. Lett.*, **104**, 218501, <https://doi.org/10.1103/PHYSREVLETT.104.218501>.

- Sasaki, H., P. Klein, B. Qiu, and Y. Sasai, 2014: Impact of oceanic-scale interactions on the seasonal modulation of ocean dynamics by the atmosphere. *Nat. Commun.*, **5**, 5636, <https://doi.org/10.1038/ncomms6636>.
- Savage, A. C., and Coauthors, 2017: Frequency content of sea surface height variability from internal gravity waves to mesoscale eddies. *J. Geophys. Res. Oceans*, **122**, 2519–2538, <https://doi.org/10.1002/2016JC012331>.
- Siegelman, L., M. O'Toole, M. Flexas, P. Rivière, and P. Klein, 2019: Submesoscale ocean fronts act as biological hotspot for southern elephant seal. *Sci. Rep.*, **9**, 5588, <https://doi.org/10.1038/s41598-019-42117-w>.
- , P. Klein, P. Rivière, A. F. Thompson, H. S. Torres, M. Flexas, and D. Menemenlis, 2020: Enhanced upward heat transport at deep submesoscale ocean fronts. *Nat. Geosci.*, **13**, 50–55, <https://doi.org/10.1038/S41561-019-0489-1>.
- Smith, K. S., and R. Ferrari, 2009: The production and dissipation of compensated thermohaline variance by mesoscale stirring. *J. Phys. Oceanogr.*, **39**, 2477–2501, <https://doi.org/10.1175/2009JPO4103.1>.
- Su, Z., J. Wang, P. Klein, A. F. Thompson, and D. Menemenlis, 2018: Ocean submesoscales as a key component of the global heat budget. *Nat. Commun.*, **9**, 775, <https://doi.org/10.1038/s41467-018-02983-w>.
- Thomas, L. N., 2017: On the modifications of near-inertial waves at fronts: Implications for energy transfer across scales. *Ocean Dyn.*, **67**, 1335–1350, <https://doi.org/10.1007/s10236-017-1088-6>.
- , A. Tandon, and A. Mahadevan, 2008: Submesoscale processes and dynamics. *Ocean Modeling in an Eddy Regime, Geophys. Monogr.*, Vol. 177, Amer. Geophys. Union, 17–38.
- Torres, H. S., P. Klein, D. Menemenlis, B. Qiu, Z. Su, J. Wang, S. Chen, and L.-L. Fu, 2018: Partitioning ocean motions into balanced motions and internal gravity waves: A modeling study in anticipation of future space missions. *J. Geophys. Res. Oceans*, **123**, 8084–8105, <https://doi.org/10.1029/2018JC014438>.
- Weiss, J., 1991: The dynamics of enstrophy transfer in two-dimensional hydrodynamics. *Physica D*, **48**, 273–294, [https://doi.org/10.1016/0167-2789\(91\)90088-Q](https://doi.org/10.1016/0167-2789(91)90088-Q).
- Yu, X., A. C. Naveira Garabato, A. P. Martin, C. E. Buckingham, L. Brannigan, and Z. Su, 2019: An annual cycle of submesoscale vertical flow and restratification in the upper ocean. *J. Phys. Oceanogr.*, **49**, 1439–1461, <https://doi.org/10.1175/JPO-D-18-0253.1>.

## 5 Submesoscale fronts as biological hotspot

In this chapter, the importance of submesoscale fronts for upper trophic levels is explored west of the Kerguelen Islands (Figure 1.2). The bio-physical dataset collected by a seal (tag 50, Figure 1.5) reveals a conspicuous increase in the seal’s foraging activity at the westernmost part of its trip, concomittant with a standing meander of the ACC. Thanks to the continuous high-resolution of the tag, that surpasses the present-day capabilities of other instruments, e.g. autonomous floats or gliders, we were able to propose a physical explanation for such high biological activity based on the study of submesoscale fronts. Indeed, these submesoscale fronts, with a size of 5–20 km, are enhanced at the standing meander site and reveal the presence of strong mixing. Our findings help explain why multiple marine top predators from the Kerguelen Islands and adjacent locations, ranging from elephant seals to macaroni penguins, recurrently head to this standing meander area.

**Siegelman, L.**, O’Toole, M., Flexas, M., Rivière, P. and Klein, P. (2019). Submesoscale ocean fronts act as biological hotspot for southern elephant seal. *Scientific reports*, 9(1), p.5588.

# SCIENTIFIC REPORTS

OPEN

## Submesoscale ocean fronts act as biological hotspot for southern elephant seal

Lia Siegelman<sup>1,2,3</sup>, Malcolm O'Toole<sup>4</sup>, Mar Flexas<sup>2</sup>, Pascal Rivière<sup>1</sup> & Patrice Klein<sup>2,3</sup>

The area west of the Kerguelen Islands (20–70°E/45–60°S) is characterized by a weak mesoscale activity except for a standing meander region of the Antarctic Circumpolar Current (ACC) localized between 20 and 40°E. A unique bio-physical dataset at high-resolution collected by a southern elephant seal (*Mirounga leonina*) reveals a conspicuous increase in foraging activity at the standing meander site up to 5 times larger than during the rest of her three-month trip west of the Kerguelen Islands. Here, we propose a physical explanation for such high biological activity based on the study of small-scale fronts with scales of 5 to 20 km, also called submesoscales. The standing meander is associated with intensified frontal dynamics at submesoscale, not observed in the rest of the region. Results shed new light on the spatial distribution of submesoscale fronts in the under-sampled area west of the Kerguelen plateau and emphasize their importance for upper trophic levels. Despite that most elephant seals target foraging grounds east of the Kerguelen Plateau, our findings suggest that excursions to the west are not accidental, and may be explained by the recurrently elevated physical and biological activity of the site. As such, other standing meanders of the ACC may also act as biological hotspots where trophic interactions are stimulated by submesoscale turbulence.

The Antarctic Circumpolar Current (ACC) hosts a small number of standing meanders localized in the lee of topographic features. These meandering large-scale jets trigger mesoscale eddies, with a size of 50 to 200 km, associated with hotspots of eddy kinetic energy of up to two orders of magnitude greater than in surrounding areas where the eddy activity is weak<sup>1–4</sup>. Thompson *et al.*<sup>2</sup> reported four such standing meander regions across the ACC, among which one is localized between 45–60°S/20–40°E (Fig. 1). This standing meander area, linked to the topographical feature of the Southwest Indian Ridge, is identifiable from climatological altimetry data<sup>2,5</sup> and has an average eddy kinetic energy value greater than 0.10 m<sup>2</sup> s<sup>-2</sup> over the duration of our study (from October 2014 to January 2015) (Fig. 2a).

Dynamical studies of the last decade further indicate that the flow shear, hereafter referred to as the strain field, associated to these mesoscale eddies generates submesoscale fronts with a size of 5 to 20 km in-between them and on their edges<sup>6–8</sup>. These structures, mainly thermohaline fronts, are now thought to capture most of the vertical velocities in the upper ocean and therefore to be the preferential pathway for the vertical exchange of heat, nutrients and other tracers between the surface and the deep ocean. In the iron-limited Southern Ocean, these dynamics have profound implications for phytoplankton production and biogeochemical systems<sup>9–11</sup>. However, these submesoscale dynamics are not well documented and poorly quantified in the ocean due to the lack of submesoscale-resolving *in situ* observations available over large domains. As a consequence, impacts on upper trophic levels remain largely unexplored. While numerous studies have identified mesoscale eddies as favorable feeding grounds for top predators such as elephant seals<sup>12–15</sup>, the relation between submesoscale turbulence and marine top predator's at-sea foraging behaviour has only been inferred from altimetry-derived Lagrangian diagnostics<sup>16,17</sup>. To date, this has been the only available approach to overcome the lack of bio-physical observations capable of resolving oceanic submesoscale features.

The present study focuses on the area west of the Kerguelen Islands (Indian sector of the Southern Ocean, Fig. 2) over the austral summer. The Kerguelen region is known to host a complex local circulation<sup>18,19</sup> due to the presence of strong bathymetric features, e.g. the Kerguelen Plateau and the Southwest Indian Ridge (Fig. 2b).

<sup>1</sup>Univ. Brest, CNRS, IRD, Ifremer, LEMAR, Plouzané, France. <sup>2</sup>California Institute of Technology, Pasadena, CA, USA.

<sup>3</sup>Jet Propulsion Laboratory, California Institute of Technology, Pasadena, CA, USA. <sup>4</sup>UWA Oceans Institute, Indian Ocean Marine Research Centre, University of Western Australia, Crawley, WA, 6009, Australia. Correspondence and requests for materials should be addressed to L.S. (email: [lsiegelman@caltech.edu](mailto:lsiegelman@caltech.edu))

Received: 16 November 2018

Accepted: 25 March 2019

Published online: 03 April 2019

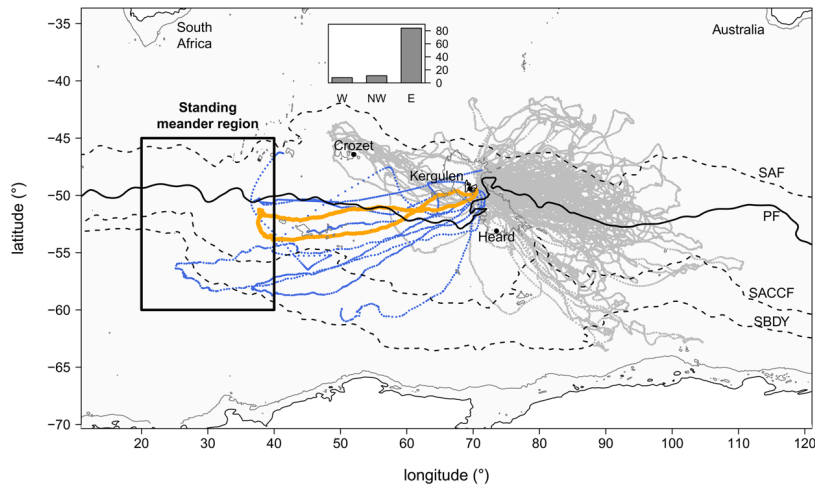


**Figure 1.** Spatial distribution of the 103 post-breeding female southern elephant seals tagged from the Kerguelen Islands since the beginning of the Marine Mammal Exploring the Ocean Pole-to-Pole consortium in 2004. Southern elephant seals are separated per region: west (W) in blue and east (E) and northwest (NW) in gray. Insert figure shows regional seal distribution. The high-resolution trajectory considered in this study is shown in orange. The region of the standing meander is identified by the black rectangle<sup>2</sup>. Climatological position of the Sub-Antarctic Front (SAF), Polar Front (PF), Southern Antarctic Circumpolar Current Front (SACCF) and Southern Boundary front (SBDY) are indicated in black according to Kim and Orsi<sup>70</sup>.

These features are likely to play a positive role for the marine fauna. Indeed, the Kerguelen Islands are home to large colonies of marine predators and, in particular, host the second largest population of Southern Elephant Seals (SES, *Mirounga leonina*). The southern elephant seal is a deep-diving, wide-ranging marine predator species<sup>20</sup> that forages in either one of three main habitats: the Antarctic continental shelf, the Kerguelen Plateau or deep open water regions<sup>21</sup>. Antarctic shelf waters provide prime habitat for both sexes, but females from Kerguelen use them less because advancing sea ice may impede their annual return to breed<sup>21</sup>. Instead, most female SES from Kerguelen forage in the open water regions and along the sea ice edge year round<sup>13,14,22,23</sup>. Over the last two decades, the post-breeding trips (from ~October to January) of 103 females have been recorded as part of the National Observing System MEMO (Mammifère Echantillonneurs du Milieu Océanique). More than 80% of these seals target the area east of the plateau (Fig. 1) where high eddy kinetic energy ( $>0.20 \text{ m}^2 \text{ s}^{-2}$ , Fig. 2a) and chlorophyll concentrations (Fig. 2b) are found. Alternatively, less than 10% of seals head west of Kerguelen Islands (Fig. 1) in a region of weak eddy kinetic energy ( $<0.02 \text{ m}^2 \text{ s}^{-2}$ , Fig. 2a) and low chlorophyll concentrations (Fig. 2b). However, feeding-like behaviour of southern elephant seals in the standing meander region west of Kerguelen Islands has previously been identified<sup>24</sup>. This particular region also appears as a biological hotspot for predators from adjacent colonies on Prince Edwards Islands (46.9°S, 37.7°E), including elephant seals<sup>25,26</sup> and macaroni penguins<sup>27</sup>.

The present work complements the research of other tagging programs that use animals as oceanographers to study animal behaviour in relation to characteristic water masses<sup>28</sup> and large- to meso-scale oceanic features<sup>29–32</sup>. However, this study focuses on submesoscale physics thanks to a unique dataset at unprecedented high-resolution collected *in situ* by a female southern elephant seal from the Kerguelen Islands. Unlike previous tags mounted on marine mammal, the one used in this study recorded for the first time every single dive realized by a seal during its journey (or over 6900 dives). This dataset advantageously contains both physical and behavioural data, which allow us to explore the submesoscale dynamics of the region west of the Kerguelen Islands as well as its relation with the foraging behaviour of the tagged seal. The seal's trajectory displays a similar excursion to the standing meander site as the ones discussed above. This excursion is accompanied by a significant increase in foraging behaviour up to 5 times greater than during the rest of the trip (Fig. 2b). Here, we propose for the first time a physical explanation for such a biologically active area based on the study of submesoscale dynamics in the vast domain sampled by the seal and broadly defined by 20–70°E/45–55°S, potentially explaining the other southern elephant seals western excursions observed in Fig. 1.

## Results

**Southern elephant seal observations at unprecedented high-resolution.** Results are inferred from a unique dataset of physical and biological observations collected by a female southern elephant seal (Fig. 2b). The seal was equipped with sensors measuring temperature, conductivity and pressure at a continuous high-frequency of 0.5 Hz and its travel was tracked through the Argos satellite system. Buoyancy, which is of opposite sign to the fluid density, and spiciness, which indicates thermohaline variations along constant density surfaces<sup>33</sup> (see Methods), are estimated from temperature and salinity observations. Both fields have a final vertical resolution of 1 m and a horizontal resolution of 1 km (see Methods). This gives access to a unique dataset of vertical sections ( $x-z$ ) of buoyancy and spiciness at very high-resolution over a long distance ( $>5000 \text{ km}$ ) and down to 600 m in the ocean interior. Simultaneously, the same device recorded animal behavioural information, based on the

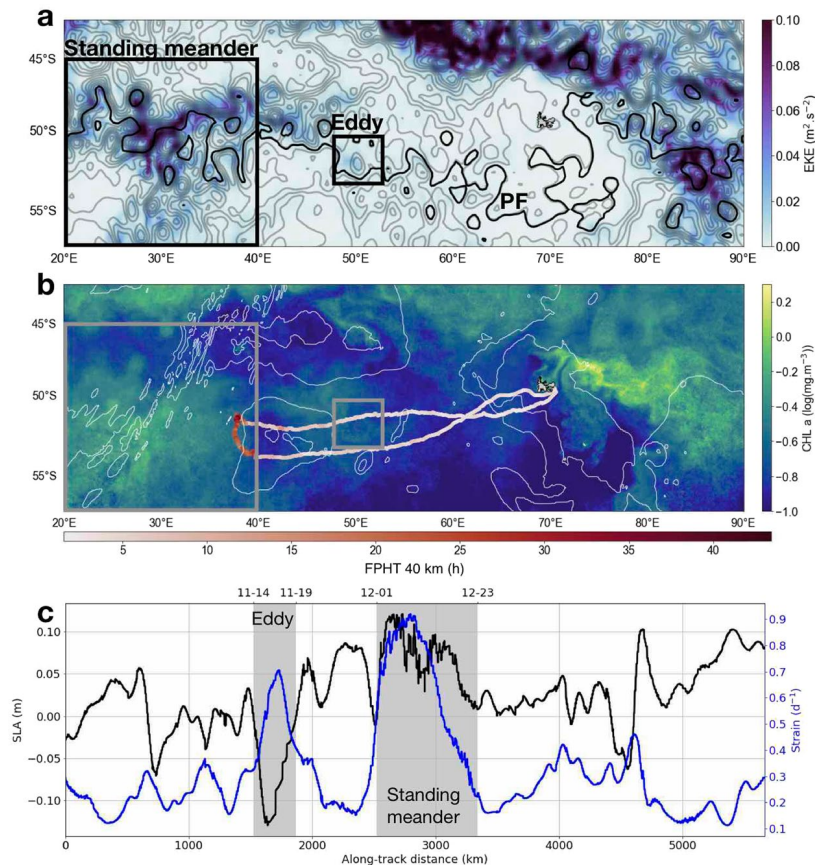


**Figure 2.** (a) Mean Eddy Kinetic Energy (EKE) over the seal's journey (27 Oct 2014 - 21 Jan 2015) superimposed with sea surface height contours at mid-trajectory (12 Dec 2014) ranging from  $-1.6$  to  $1.7$  m with  $0.1$  m increments obtained from AVISO satellite data. The Polar Front (PF) is indicated in bold black as the  $-0.61$  m contour according to Kim and Orsi<sup>70</sup>. (b) Mean chlorophyll a concentration obtained from satellite data during the seal's journey superimposed with the seal's trajectory colored by the First-Passage Hunting Time (FPHT) with a radius  $R = 40$  km, i.e. of the order of the first Rossby radius of deformation in the Kerguelen area. 2 and 4 km bathymetry contours from ETOPO5 are shown in white. On (a and b) black and white rectangles identify the standing meander area and cyclonic eddy discussed in the main text. (c) Lagrangian time series of Sea Level Anomaly (SLA, in black) and strain (in blue) along the seal's path derived from satellite data (see Methods).

premise a predator will maximize resource acquisition by adapting its movement in response to prey distribution and density<sup>34,35</sup>. More precisely, the seal's foraging behaviour is estimated through the computation of the First-Passage Hunting Time (FPHT), which combines the first passage time metric used in Bailleul *et al.*<sup>36</sup> and the sinuosity method of Heerah *et al.*<sup>37</sup>. FPHT advantageously takes into account the horizontal and vertical dive sinuosity in order to indicate the amount of time the seal spent hunting within an area of given radius. In this study, FPHT is computed at the radius  $R$  of 40 km, which is of the order of the local Rossby radius of deformation in terms of wavelength<sup>38</sup>, in order to capture the mesoscale features of the area. However, a sensitivity analysis demonstrates that the results are robust to the choice of  $R$  (see Methods and Supplementary Fig. S1).

During its three-month post-breeding round trip from the Kerguelen Islands in the austral summer (28 Oct 2014 to 21 Jan 2015), the seal traveled a distance of 5665 km. The seal's voyage can be divided into three distinct parts (Fig. 2b): two relatively straight transit lines back and forth between the Kerguelen Islands and the standing meander site—accounting for 85% of the total distance (4850 km) but only 67% of the total time—and the remaining 15% of the trip (815 km), accounting for a third of the time, spent in the standing meander region. The seal's foraging activity appears to be enhanced at the standing meander site, where FPHT reach values up to five times that of the rest of the trip (Fig. 2b). In order to understand this contrast, we study the underlying physics at meso- and sub-mesoscale.

**Submesoscale dynamics west of the Kerguelen Plateau.** During its 85 day trip, the seal encounters two well-defined mesoscale features: a cyclonic eddy and a meander located at the easternmost tip of the standing meander area (Fig. 2). The cyclonic eddy has a size of  $\sim 150$  km and is located north of an anticyclonic one, creating a dipole structure, which generates a westward jet of  $\sim 0.2$  m/s in between both eddies. The meander has an elongated shape with a length of  $\sim 350$  km and a width of  $\sim 50$  km. The local flow is directed southward with a magnitude of  $\sim 0.3$  m/s. In both structures, the seal travels in the same direction as the current. More precisely, the seal crosses the southern part of the cyclonic eddy, amounting to a cumulative distance of 350 km, in 6 days and



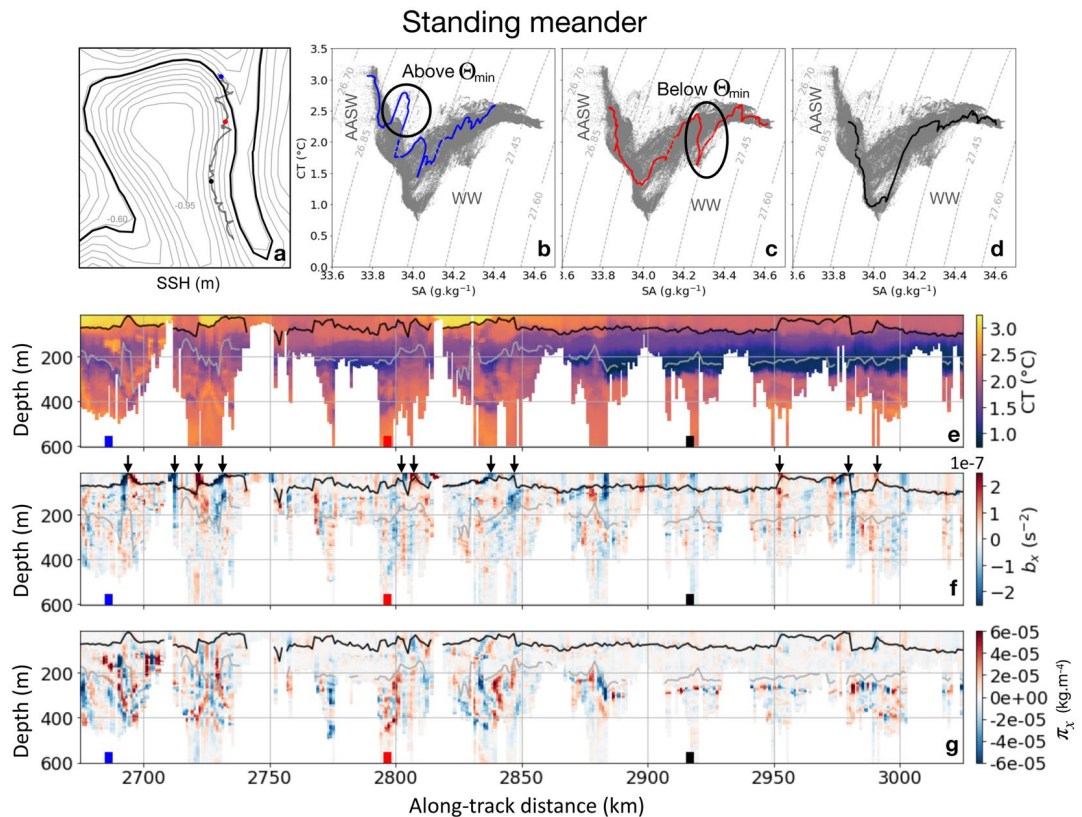


**Figure 3.** Key physical properties for a 350-km long section in the standing meander. (a) Snapshot of Sea Surface Height (SSH) on 2014/12/10 superimposed with the seal's trajectory from 2014/12/5–14. Blue, red and black dots indicate the profiles in the Temperature (CT)–Salinity (SA) diagrams. The Polar Front is indicated in bold black as the  $-0.61$  m contour according to Kim and Orsi<sup>70</sup>. Sea surface height contours are incremented by  $0.05$  m. (b) Temperature–salinity diagram highlighting a profile presenting intrusions above the temperature minimum ( $\Theta_{\min}$ ). (c) Temperature–salinity diagram highlighting a profile presenting intrusions below the temperature minimum. (d) Temperature–salinity diagram highlighting a profile presenting no intrusion. In (b–d), the gray profiles correspond to the rest of the transect in (a). (e) Vertical section of temperature for the transect in (a). (f) Vertical section of lateral gradient of buoyancy ( $b_x$ ) for the transect in (a). Black arrows indicate instances of mixed layer depth shoaling, concomitant with intense gradients of buoyancy. (g) Vertical section of lateral gradient of spiciness ( $\pi_x$ ) for the transect in (a). In (e–g), the profiles shown in (a–d) are indicated by blue, red and black squares at the bottom of the plots. The black line indicates the mixed layer depth and the gray line the depth of the temperature minimum.

corresponding to a speed of  $\sim 60$  km/day. In contrast, the seal spends 23 days on the edge of the meander over a cumulative distance of 815 km, which corresponds to a speed of  $\sim 35$  km/day, i.e. the seal reduces overall speed by roughly 40% in the meander in comparison with the cyclonic eddy. However, both mesoscale features, identified from satellite data of sea level anomaly (see Methods), are associated to a strong strain field reaching  $0.8$  day $^{-1}$  in the standing meander and  $0.6$  day $^{-1}$  in the cyclonic eddy (Fig. 2c). Since theoretical studies indicate that a turbulent mesoscale eddy field can drive and constrain submesoscale turbulence<sup>7,39</sup>, both areas are potentially favorable for the development of submesoscale features.

**Standing meander.** Seal observations clearly indicate that submesoscale buoyancy gradients with a width of 5 to 20 km are indeed present at the standing meander, extending from the surface down to 500 m and intensified within the mixed layer (Fig. 3f). A succession of large surface gradients coincides with instances of mixed layer depth shoaling on the edges of the meander as inferred from the comparison with sea surface height (black arrows in Fig. 3f). These events are presumably related to the seal zig-zagging through the standing meander and thus identify its edges. Gradient magnitudes reach values larger than  $2 \times 10^{-7}$  s $^{-2}$ , consistent with numerical and observational studies<sup>40–43</sup>. The mixed layer depth has an average value of 85 m (black line in Fig. 3e–g).

Similar patterns are observed for lateral gradients of spiciness, indicative of thermohaline intrusion occurring along isopycnals and thus of oceanic mixing. They also have a scale of 5 to 20 km and extend down to at least 500 m (Fig. 3g). However, the mixed layer is free of lateral gradients of spiciness, which are enhanced below the temperature minimum (see for example the gradient at the red square location in Fig. 3g). Although, several instances of large lateral gradients of spiciness occur above the temperature minimum, especially noticeable from 2675 to 2750 km (Fig. 3g, blue square). Strong lateral gradients of spiciness reach values of  $8 \times 10^{-5}$  km $^{-4}$ . Finally, strong lateral gradients of spiciness are not always associated with buoyancy ones (see for example between 2780

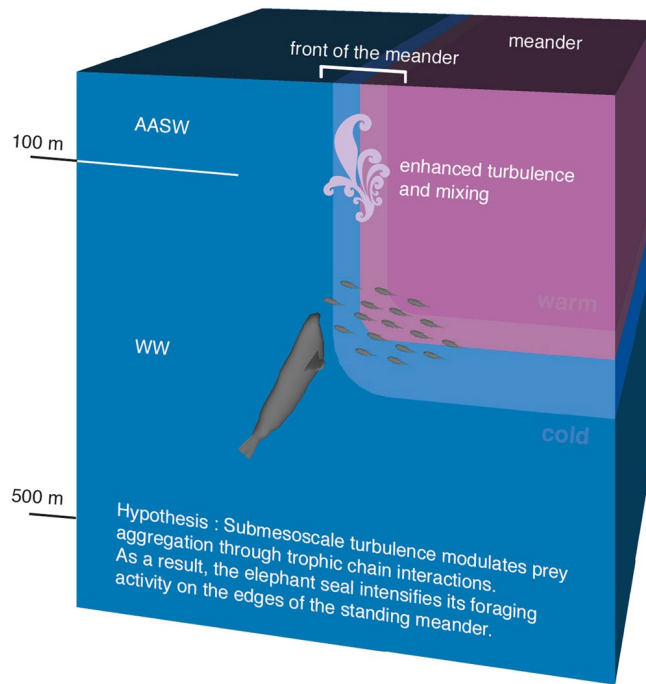


**Figure 4.** Schematic summarizing how submesoscale turbulence distributed on the edges of coherent mesoscale structures (here a standing meander of the ACC) affects the seal's foraging behaviour and featuring the water masses encountered by the seal; Antarctic Surface Water (AASW) and Winter Water (WW). Relative depths of water masses are provided as an indication only. Tandi Reason Dahl is the author of this image.

and 2850 km, red square in Fig. 3f–g). This happens when anomalies of temperature and salinity are stretched by the local strain field, which generates strong gradients of temperature and salinity at submesoscale that are however density compensated.

To further understand these water mass intrusions, we use temperature–salinity diagrams (Fig. 3b–d). The seal mainly encounters Winter Water, formed during the previous cold season, and characterized by the presence of a subsurface temperature minimum and shallow, warm and fresh Antarctic Surface Water sitting mainly above Winter Water (highlighted in Fig. 3b–d and schematized in Fig. 4). Temperatures are comprised between 0.6 and 3.2°C. Temperature–salinity profiles present numerous thermohaline intrusions localized at different depths (Fig. 3b–e). As previously mentioned, intrusions occur above the temperature minimum, as highlighted on the blue profile in Fig. 3b and below the temperature minimum, as shown on the red profile in Fig. 3c. For comparison, Fig. 3d highlights a profile presenting no such intrusion. These intrusions, as well the erosion of the temperature minimum at depth, are also reflected in the vertical section of temperature (Fig. 3e) presenting sharp variations at submesoscale. Overall these results highlight the intense submesoscale activity present along the edges of the meander where waters are being mixed.

**Cyclonic eddy.** The seal-sampled water masses (Antarctic Surface Water and Winter Water, Fig. 5) are characterized by temperatures between 0.4 and 2.4°C with warmer and colder waters north and south of the transect, respectively (Fig. 5a,b). The dives can be separated by temperature minima of 0.8, 1.25 and 1.5°C. Lateral gradients of buoyancy below the mixed layer are of the same order as those observed in the meander (Fig. 5d). However, a few differences are worth mentioning. First, the mixed layer is deeper in the cyclonic eddy with an average value of 115 m and, unlike in the meander, no lateral gradients of buoyancy are observed within it. More importantly, the cyclonic eddy is characterized by weak lateral gradients of spiciness seldom reaching  $2 \times 10^{-5} \text{ kg m}^{-4}$  (Fig. 5e) and systematically localized below the temperature minimum (see for example the black arrows in Fig. 5d). The absence of thermohaline intrusion is also reflected in the temperature–salinity diagram (Fig. 5b) that displays a remarkable fan-shape distribution with gaps between the different temperature minima, indicative of the clear separation between water types, and thus, stratification and absence of mixing.

**Entire transect.** Overall, the submesoscale characteristics along the entire trajectory (standing meander excluded) resemble those found in the cyclonic eddy; inferred from the time series of lateral gradients of buoyancy and spiciness presented in Fig. 6a,b. Lateral gradients of buoyancy within the mixed layer (shown at 15 m in Fig. 6a), and spiciness throughout the water column (shown at 150 m in Fig. 6b), are stronger inside than outside the standing meander. However, below the mixed layer, lateral gradients of buoyancy are homogeneous along the entire transect, with no clear intensification in the meander (not shown). In the first 80 m, the root mean square of the lateral gradient of buoyancy inside the standing meander is greater than outside of it by a factor  $>2$ . Below 80 m, this factor is  $<2$  and further decreases with depth (Fig. 6c). For lateral gradients of spiciness, the root mean square inside the standing meander is 1.5 to 3.2 times greater than outside the standing meander (Fig. 6d),

## Cyclonic eddy

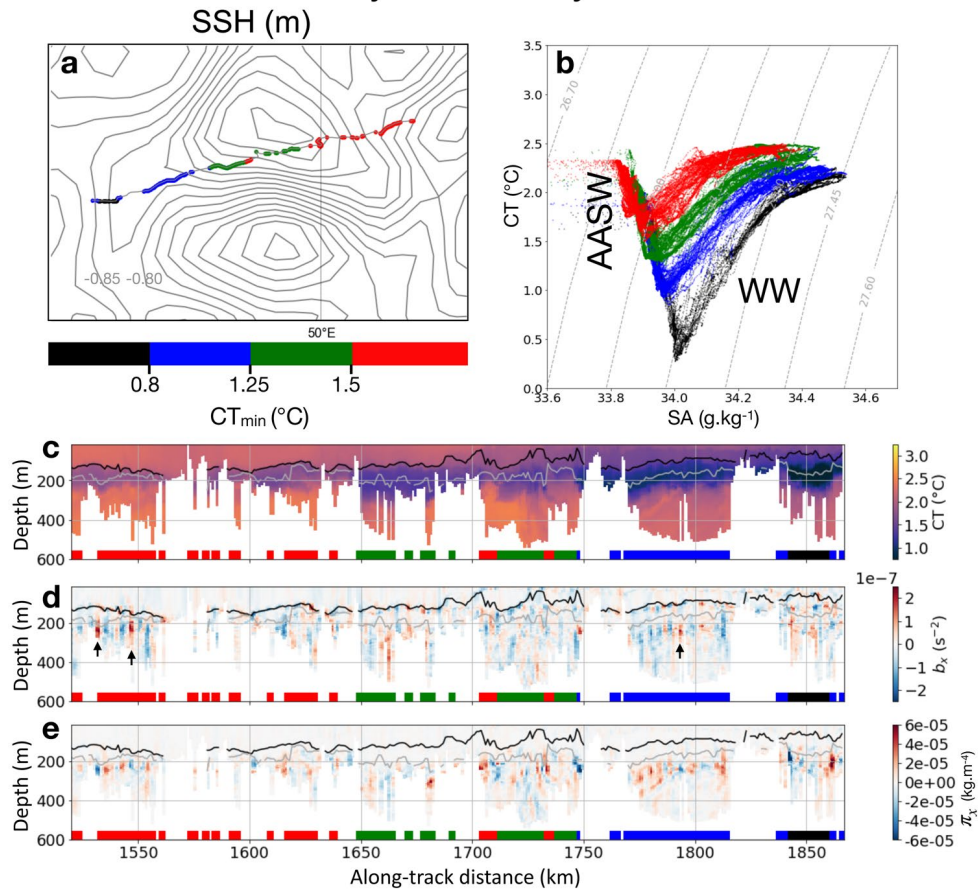


**Figure 5.** Key physical properties for the 350-km long section on the southern part of the cyclonic eddy. (a) Snapshot of Sea Surface Height (SSH) on 2014/11/16 superimposed with the seal's trajectory from 2014/11/14–19 colored by the dives subsurface temperature minimum ( $CT_{min}$ ). Sea surface height contours are incremented by 0.05 m. (b) Temperature (CT)–Salinity (SA) diagram for the transect in a. Same color code as (a). (c) Vertical section of temperature for the transect in (a). (d) Vertical section of lateral gradient of buoyancy ( $b_x$ ) for the transect in (a). The black arrows highlight a few lateral gradients of buoyancy localized below the temperature minimum. (e) Vertical section of lateral gradient of spiciness ( $\pi_x$ ) for the transect in a. In (c–e), the profiles shown in (a,b) are indicated by the colored squares at the bottom of the plots. The black line indicates the mixed layer depth and the gray line the depth of the temperature minimum.

highlighting the strong mixing occurring in the vicinity of the standing meander. Overall, the observed sub-mesoscale features are mostly located in regions of intense shear, consistent with theoretical studies<sup>7,39</sup> indicating that submesoscale frontal structures result from the mesoscale stirring field generated by co-interacting eddies.

**Impact of submesoscale dynamics on southern elephant seal behaviour.** The intense submesoscale fronts observed at the standing meander site suggest that the biological pump is stimulated via mixing and frontogenesis processes that contribute to the injection of nutrients from deeper layers to the euphotic zone where primary production occurs<sup>11</sup>. However, knowing how marine top predators respond to this submesoscale turbulence remains an open question.

Here, we investigate the seal's foraging activity and, in particular, relate submesoscale fronts to local foraging behaviour. To do so, we identify transitions in movement patterns (e.g. from transit behaviour to feeding) between mesoscale regions of 50 to 200 km-size along the seal's trajectory. As previously mentioned, we use the First-Hunting Passage Time (FPHT) with a radius  $R$  of 40 km, which captures the mesoscale features of the area, as a proxy for the seal's foraging activity (see Methods).

FPHT intensifies significantly at the standing meander site with values  $>20$  hours. The bimodal distribution of FPHT inside and outside of the standing meander further underscores this finding, with FPHT between 15 and 40+ hours inside the standing meander, while generally being  $<10$  hours outside of it with a median of 4 hours outside versus 23 hours inside (Fig. 6e). There is a good agreement between the time series of FPHT and both lateral gradient of spiciness at 150 m and lateral gradient of buoyancy at 15 m (Fig. 6a,b). This is particularly noticeable at the standing meander where strong gradients of buoyancy and spiciness are associated with greater FPHT (Fig. 6). For lateral gradients of spiciness, different depths lead to similar results. On the other hand, for

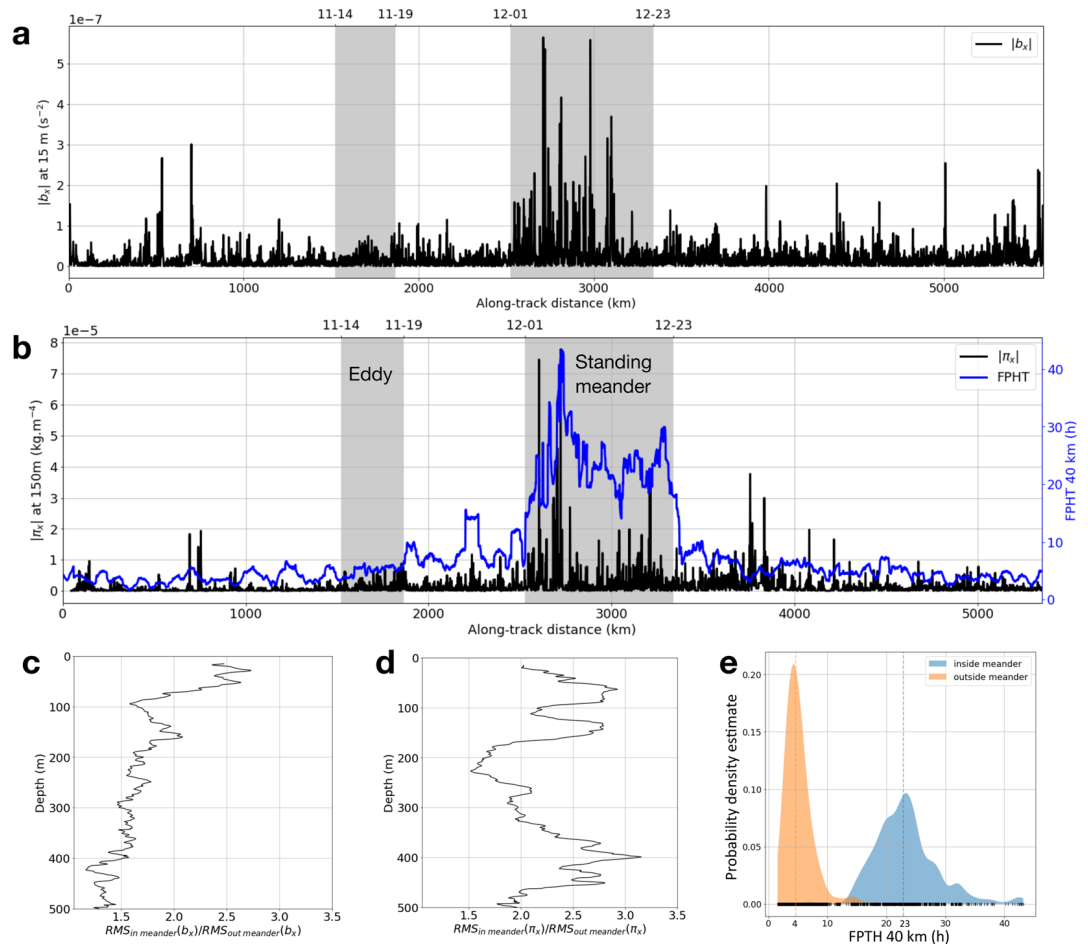


**Figure 6.** Lagrangian time series along the seal's track of (a) Lateral buoyancy gradient ( $|b_x|$ ) at 15 m. (b) Lateral gradient of spiciness ( $|\pi_x|$ ) at 150 m (in black) and First-Passage Hunting Time (FPHT) at 40 km (in blue) calculated as in Fig. 2b. The eddy and standing meander discussed in the main text and described in Figs 5 and 3 are indicated in gray. Root mean square (RMS) ratio inside/outside of the meander as a function of depth for (c) lateral buoyancy gradient. (d) lateral gradient of spiciness. (e) Probability density estimate of First-Passage Hunting Time (FPHT, in hour) inside (blue) and outside (orange) of the meander. Medians are indicated in dashed colored lines and a rug plot is shown on the bottom. Lateral gradients of buoyancy and spiciness, and First-Passage Hunting Time are significantly greater inside the meander.

lateral gradients of buoyancy, this results holds in the first 80 meters but not below. This is because at depth, lateral gradients of buoyancy are more homogeneously distributed along the seal's trajectory (Fig. 6c).

Generalized additive models corroborate the qualitative relationships observed between FPHT and key physical quantities (Figs 2 and 6). At mesoscale, FPHT is positively linked to the strain field (Fig. 7a), consistent with previous studies suggesting that elephant seals target energetic mesoscale structures<sup>16,17,21</sup>. At submesoscale, FPHT is also positively linked to lateral gradients of buoyancy at 15 m and lateral gradients of spiciness at 150 m (Fig. 7b,c). This last result highlights the seal's preference for submesoscale features, that are concentrated at the standing meander site. Moreover, the mixed layer depth is negatively linked to FPHT, highlighting the seal's preference for shallower mixed layer, which often occur on the edges of mesoscale structures, and thus correspond to areas of strong buoyancy gradients (Figs 3f and 7c). However, it is hard to disentangle the seasonal component from the spatial variability at submesoscale in the time series of the mixed layer depth.

These results emphasize that submesoscale frontal structures constitute favorable foraging habitats for top marine predators such as elephant seals (Fig. 4). The seal's foraging activity is significantly enhanced on the edges of the standing meander where most of the submesoscale features are located. The standing meander west of the Kerguelen Islands that hosts the vast majority of submesoscale features thus appears to be a physical and biological hotspot for apex marine predators.

## Conclusion and Discussion

Our results provide evidence that submesoscales, while dominant in winter time, are also active in the Southern Ocean during the summertime. This is consistent with recent observational findings obtained from gliders in the Drake passage in summer<sup>43</sup> and in the sub-Antarctic zone in spring<sup>42</sup>.

This work documents the spatial distribution of submesoscale features over a large oceanic domain (>5000 km) in the under sampled area west of the Kerguelen Islands. A clear partitioning of the physical

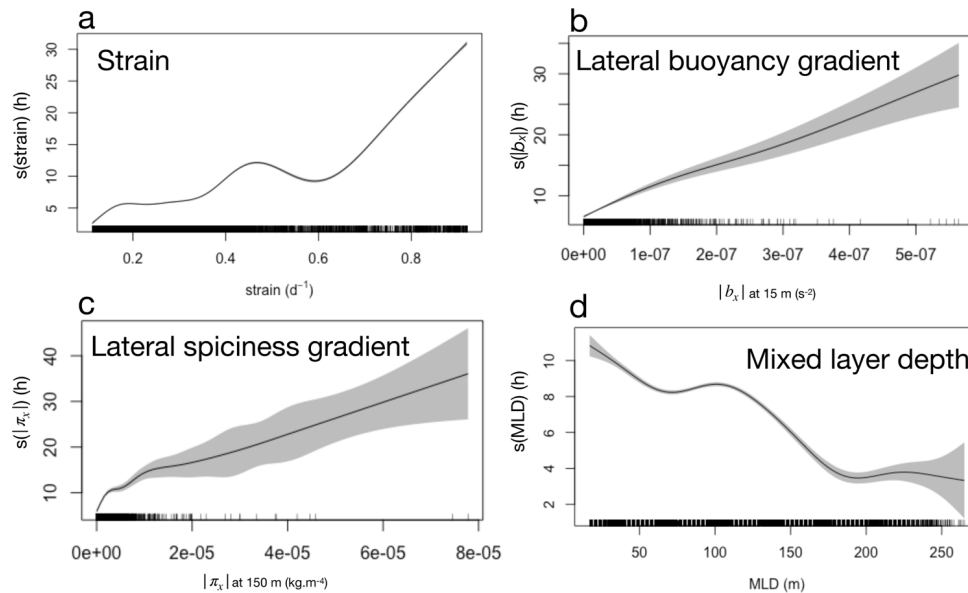


**Figure 7.** Effect of key physical properties on the seal’s foraging effort, quantified by First-Passage Hunting Time (FPHT) at 40 km, inferred from generalized additive models. **(a)** Strain derived from satellite data. **(b)** Lateral buoyancy gradient ( $|b_x|$ ) at 15 m derived from seal data. **(c)** Lateral spiciness gradient ( $|\pi_x|$ ) at 150 m derived from seal data. **(d)** Mixed Layer Depth (MLD) derived from seal data. Shaded grey polygons show 95% confidence interval. A rug plot is added to the bottom of each panel.

properties at submesoscale is observed: within the standing meander area, the mixed layer contains strong lateral gradients of buoyancy. Below the mixed layer, intense lateral gradients of spiciness are present down to 500 m, indicating the presence of strong thermohaline intrusions, also noticeable on temperature–salinity diagrams (Fig. 3). In comparison, the rest of the area, including the cyclonic eddy discussed in the results section, is characterized by weak lateral gradients of spiciness throughout the water column and tame lateral gradients of buoyancy within the mixed layer, which is deeper in the cyclonic eddy than in the meander. However, lateral gradients of buoyancy at depth are comparable and relatively weak over the entire domain. The weakness of these lateral gradients of buoyancy can be understood through their link with the mesoscale strain field. Indeed, the strain field associated to mesoscale eddies is known to stretch buoyancy (or density) anomalies, leading to the creation of strong gradients at submesoscale<sup>7</sup>. However, over the vast domain sampled by the seal, the mesoscale strain field is weak (apart in the standing meander and the cyclonic eddy), as inferred from the map of eddy kinetic energy (Fig. 2a) and the time series of the strain field (blue curve in Fig. 2c). As a consequence, lateral gradients of spiciness and buoyancy remain subdued in most of the domain. However, this contrast is also observed between the two distinct mesoscale features encountered by the seal: the standing meander and the cyclonic eddy. One simple hypothesis explaining this dichotomous distribution may be related to their respective sizes. While the meander is an elongated feature of  $\sim 350$  km of length, the cyclonic eddy has a smaller size of  $\sim 100$  km, which makes it statistically less likely to host mixing events and thus even less likely to observe it. Furthermore, our observational results confirm modelling studies of the last decade showing that submesoscale fronts are produced mostly at the edges and in-between mesoscale eddies<sup>39</sup>.

The abundance and strength of submesoscale features observed on the edges of the standing meander are of biological significance for upper trophic levels: the SES considered in this study spends significantly more time foraging in the vicinity of strong submesoscale features located on the edge of the meander where it also decreases its speed. This is consistent with the results of Della Penna *et al.*<sup>17</sup>, who found that SES adopt a “quasi planktonic behaviour”, i.e. are horizontally advected, on the edge of mesoscale features identified as favorable feeding grounds. At these locations, an intense foraging activity is however observed on the vertical, similar to the animal considered in this study. Our results are also consistent with recent findings of Hindell *et al.*<sup>21</sup> suggesting that rather than targeting one specific water mass, SES may simply be targeting areas of high mixing that are presumably concomitant with high prey concentrations due to the higher turnover of nutrients within the water column. Our findings are also consistent with previous work linking mesoscale features to SES behaviour. Indeed, numerous studies of the last decade have identified mesoscale eddies as favorable feeding grounds for SES with a preference for cold cyclonic structures and the edges of anticyclonic ones<sup>12–15</sup>. Both structures were reported to be enriched in organisms of different trophic levels<sup>44–46</sup>, and aggregate resources into narrower layers closer to the surface where they are more accessible to air-breathing SES<sup>47</sup>. Interestingly, when the seal encounters the standing meander, it most intensified his foraging behaviour at a depth of 220 m (Supplementary Fig. S2). Furthermore, hunting dive depth and maximum dive depth variances decrease (Supplementary Fig. S2). This relatively constant foraging dive depth of SES possibly reflects narrower prey fields associated with improved foraging success<sup>24,48</sup>, hinting that local dynamics creates predictable biological boundaries that facilitate prey accessibility.

Since the beginning of the bio-logging program in 2004, all but one of the five post-breeding females trajectories located west of the Kerguelen Islands present similar excursions to the standing meander site (Fig. 1). Even though the reason why SES transit west is presumably related to multiple factors, such as minimizing intra-specific competition<sup>49</sup> for instance, it is still necessary that they find optimal conditions for feeding. This suggests that western excursions to the standing meander region (Fig. 1) are not accidental, and may be explained by the recurrently elevated physical activity of the site. Furthermore, individual SES often return to the same broad scale foraging grounds over consecutive years, presumably because these habitats are reliable ‘oasis’ in a highly variable environment<sup>50,51</sup>. This site loyalty has been shown to be an effective strategy adopted by marine predators foraging in a dynamic and heterogeneous environment such as the Southern Ocean<sup>50,52,53</sup>. These findings are consistent with the fact that the standing meander region highlighted in this study is a permanent physical feature of the Southern Ocean, as described by Thompson *et al.*<sup>2</sup>. As such, the western trips observed in Fig. 1 are unlikely a temporary phenomenon, and are expected to be repeated by individuals as elephant seals have a high degree of individual foraging site fidelity over periods of up to 10 years<sup>50,54</sup>.

Within the Antarctic Circumpolar Current, other standing meanders and areas of high eddy kinetic energy may also act as physical and biological hotspot. For instance, the region east of the Kerguelen Islands located at ~80°E–50°S, analyzed in Siegelman *et al.* (submitted), is a homogeneous hotbed of eddy kinetic energy where a strongly turbulent mesoscale eddy field generates intense submesoscale motions associated to a vigorous vertical velocity field. In addition to the iron input from the Kerguelen plateau which sustains a recurrent plume of primary production near shore<sup>9</sup>, Siegelman *et al.* (submitted) show that the submesoscale turbulence, and its associated vigorous vertical velocities, may stimulate primary production in the open ocean. The combined intensity of submesoscale features, boosting the biological system and modulating prey aggregation<sup>15</sup>, and its proximity to the Kerguelen Islands may thus explain southern elephant seals’ statistical preference for the high eddy kinetic energy area east of the Kerguelen plateau (Figs 1 and 2) or maybe because the western standing meander region is much farther away.

Our study, limited to a region of the Southern Ocean, stresses the need for more submesoscale-resolving physical and biological observations across the globe and during different seasons. In particular, it would be interesting to repeat this analysis during wintertime when submesoscale features are known to be more abundant and energetic<sup>35</sup>. Ultimately, understanding how the behaviour of individual marine predators is modulated by surrounding structures is key for assessing the health and functioning of open ocean ecosystems and is instrumental in designing effective marine protection policies in a changing climate.

## Methods

**Satellite data.** 85 daily maps of gridded 0.25° × 0.25° L4 Sea Surface Height (SSH) and Seal Level Anomaly (SLA) were obtained from the AVISO Ssalto/Duacs products, covering the spatial and temporal extent of the seal observation data. The Lagrangian time series of SLA along the seal’s track was used to identify the standing meander site (the region of positive SLA between 2525 and 3340 km) and the cyclonic eddy (the region of negative SLA between 1520 and 1865 km) (Fig. 2).

Using the geostrophic approximation, geostrophic surface currents ( $u, v$ ) are derived as

$$u = \frac{g}{f} \frac{\partial SSH}{\partial x}, v = -\frac{g}{f} \frac{\partial SSH}{\partial y},$$

where  $g$  is gravity and  $f$  the Coriolis parameter<sup>56</sup>. The strain field  $\sigma$  is subsequently computed as

$$\sigma = \sqrt{(u_x - v_y)^2 + (v_x + u_y)^2},$$

where subscripts denote partial derivative.

In addition, the map of Chlorophyll *a* concentration level 2 data in Fig. 2b has been processed by CLS for the Kerguelen area. It corresponds to a time average of Chlorophyll *a* concentration over the 85 days of the seal’s journey.

**Southern Elephant Seal dataset.** High-resolution data was recorded by a seal-borne Conductivity-Temperature-Depth Satellite Relay Data Logger (CTD SRDL, Sea Mammal Research Unit, University of St Andrews) deployed on a post-breeding female southern elephant seal from the Kerguelen Islands (49°20’S, 70°20’E). The seal is tracked by the Argos satellite system and is equipped with sensors recording conductivity, temperature and pressure at a continuous frequency of 0.5 Hz between 27 October 2014 and 20 January 2015, with an accuracy of ±0.02 °C for temperature and ±0.03 g/kg for salinity<sup>57</sup>. Only the ascending phase of a dive is used because it is more uniform in speed and direction compared to the descent when the seal dives sinusoidally to forage. The dataset is comprised of 6942 dives, or over eighty dives per day, which corresponds to a cumulative length of 5665 km with a median spacing between two dives of 700 m (Supplementary Fig. S3). Dives can be as deep as 500 to 1000 m. They generally last less than 25 minutes and are separated by a few minutes surfacing, where the seal breathes without transiting. More than 85% of the dives reach a depth of at least 100 m, 45% reach 300 m and 25% are 400 m or deeper.

To ensure a better accuracy of the conductivity-derived salinity data, two additional steps are applied to the temperature and salinity fields. First temperature and salinity are corrected for a thermal cell effect, and then a density inversion removal algorithm is applied to the salinity field. Potential density is then calculated from corrected temperature and salinity with the TEOS-10 equation<sup>58</sup>. The correction procedure and accuracy of the dataset are presented in more details in Siegelman *et al.*<sup>57</sup>. The dataset has been made available to the community and can be found on the Marine Mammals Exploring the Oceans Pole to Pole database (<http://www.meop.net/>).

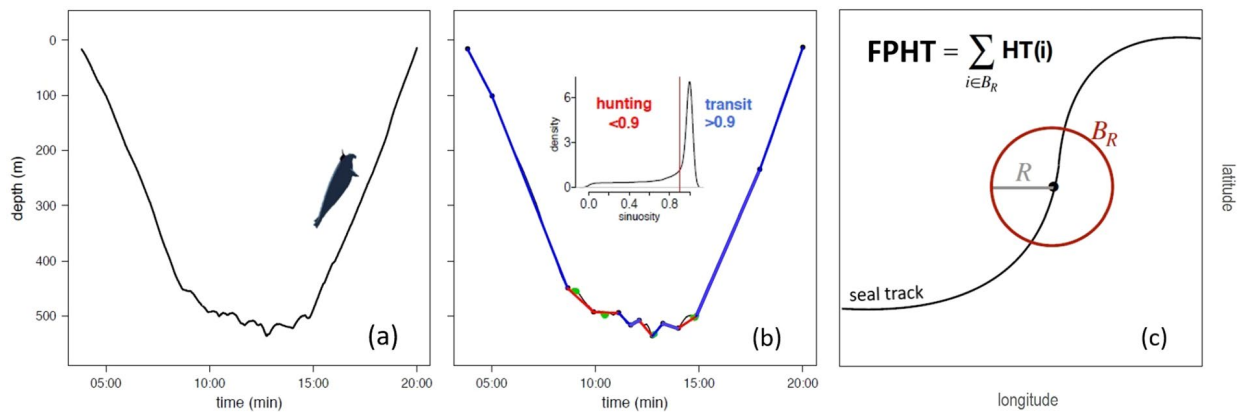


**Figure 8.** Schematic of First Passage Hunting Time (FPHT) calculation. (a) Typical dive profile recorded by the device deployed on the elephant seal. (b) The dive is separated into segments of hunting (red) and transit (blue) using the broken stick method (for details see Heerah *et al.*<sup>37</sup>). Hunting time (HT) is the summed total time of hunting segments in each dive. The number of prey encounter events detected by an on-board accelerometer (green) increased almost fourfold in hunting segments. (c) The First Passage Hunting Time at each point of the seal's trajectory is then calculated as the sum of Hunting Time within a radius  $R$ .

The animal in this study was handled in accordance with the Institut polaire francais Paul-Emile Victor (IPEV) ethical and Polar Environment Committees guidelines as part of the SNO-MEMO and IPEV program 109 (PI. H. Weimerskirch). The experimental protocols were approved by the Ethics Committee of IPEV and Polar Environment Committees.

**Buoyancy.** Along-track time series of buoyancy (in  $s^{-2}$ ),  $b = g(1 - \rho/\rho_0)$ , where  $g$  is gravity,  $\rho$  is potential density, and  $\rho_0 = 1025 \text{ kg m}^{-3}$  is a reference density reveals variability covering both meso- and submesoscales. For the analysis, in particular the calculation of lateral buoyancy gradients ( $b_x$ ), buoyancy was first linearly interpolated along the seal's path onto a regular grid of 100 m resolution, corresponding to the shortest along-track distance between two dives (Fig. S1). A moving average with a 1 km window was then applied such that the final dataset has a vertical resolution of 1 m and a horizontal resolution of 1 km. Buoyancy anomalies are resolved by multiple vertical profiles, such that the structures are not related to aliasing of the along-track data.

**Spiciness.** Spiciness (in  $\text{kg m}^{-3}$ ) is a state variable most sensitive to isopycnal thermohaline variations and least correlated with the density field<sup>33</sup>. Spiciness is conserved in isentropic motions and its value increases with increasing temperature and salinity. Positive (warm, salty) and negative (cold, fresh) subsurface spiciness anomalies can be generated by subsurface isopycnal advection across spiciness fronts<sup>59,60</sup>. As such, variation in spiciness is particularly useful to detect thermohaline intrusions characteristic of intense mixing. Spiciness is derived from salinity and temperature with the TEOS-10 equation<sup>58</sup>.

**Mixed layer depth.** The mixed layer depth (in m) is defined as the level of a  $0.03 \text{ kg m}^{-3}$  density increase with respect to the density at 15 m depth<sup>61</sup>.

**Quantify seal foraging activity.** Foraging activity is estimated from high-resolution dive data, recorded at the continuous sampling frequency of 0.5 Hz, by taking into account both the horizontal and vertical sinuosity of a dive. Indeed, a seal is expected to decrease its speed when feeding and move more sinuously along the horizontal axis, displaying what is effectively area-restricted search behaviour (ARS)<sup>13,62</sup>. However, adding the vertical dimension is also important<sup>36</sup>, and high-resolution dive data of female SES demonstrates how vertical sinuosity can significantly improve the predictive capacity of ARS as a proxy for foraging success<sup>24</sup>. This is backed by simulated diving tracks of beluga whales (*Delphinapterus leucas*) used to refined ARS in a 3D space<sup>63</sup>.

Here, we develop an index, the First-Passage Hunting Time (FPHT), which indicates the amount of time spent hunting in a region of given radius and includes the following steps. First, we compute the Hunting Time (HT) via an automated broken stick algorithm, which summarizes the vertical sinuosity of the dive data based on the optimized number of segments within each dive. Further details outlining this step are provided in Heerah *et al.*<sup>37</sup>. A behavioural state is then assigned to each dive segment based on visual inspection of dive segment sinuosity distribution: low sinuosity values ( $>0.9$ ) represent transit behaviour and high sinuosity values ( $<0.9$ ) represent hunting behaviour. To validate this method, prey encounter events were detected from an accelerometer<sup>64</sup> that, unfortunately, only recorded during the first three weeks of the seal's trip due to limited storage capacity. However, evidence suggests that elephant seals even exhibit high foraging success during the outward transit when movement was relatively rapid and direct<sup>65</sup>. Furthermore, most prey encounter events (79%) recorded during these initial three weeks occurred within hunting segments, which comforts the use of the accelerometer data as validation data throughout the entire seal's journey. This result is also consistent with the analyses of two post-breeding elephant seal trips in Heerah *et al.*<sup>37</sup>. Next, we modify the First-Passage Time approach (FPT)<sup>66</sup>, which is a scale-dependent foraging metric (i.e. ARS) that estimates how much time is required for an animal

to cross a given radius. Instead, we estimate how much time spent hunting is required for the seal to cross a given radius, referred hereafter as First-Passage Hunting Time (FPHT). Values of FPHT and FPT are similar across scales, but differences demonstrate how FPT cannot always account for vertical foraging activity (Fig. S1). Relatively speaking,  $FPHT > FPT$  is where more time is spent hunting within dives than is captured by the seal's horizontal movement and vice versa. This methodology is refined compared to Bailleul *et al.* (2008) who took the entire bottom phase time. Specifically, we sum the time spent in hunting segments and ignore the time spent in transit segments. A summary of FPHT derivation is presented in Fig. 8.

FPHT is computed at the radius  $R$  of 40 km in order to capture the mesoscale features of the area. However, results are robust to the choice of  $R$ . Indeed, although the behavioural pattern seems ambiguous at fine scale ( $r = 5$  km), it is generally consistent at broader scales ( $r > 10$  km): the seal transits west of Kerguelen for a month (low FPHT), followed by increased hunting activity at the standing meander (high FPHT), followed by a three-week transit return to Kerguelen (low FPHT) (Fig. S1).

**Generalized additive models.** Generalized Additive Models (GAMs) were used to explore relationships between key physical variables and FPHT using a Gaussian distribution with the identity link function. Time series of FPHT at 40 km were used as the response variable, and time series of the lateral gradient of buoyancy at 15 m, lateral gradient of spiciness at 150 m and mixed layer depth (from the seal's observations) and strain field (from satellite data) were used as explanatory variables. A summary table is presented in Supplementary Table S1. Model assumptions pertaining to GAMs, including normality and homogeneity of variance were checked using plots of residuals against fitted values<sup>67,68</sup>. GAMs were computed with the 'mgcv' package for R<sup>69</sup>.

### Data Availability

The marine mammal data were collected and made freely available by the International MEOP Consortium and the national programs that contribute to it (<http://www.meop.net>). The Ssalto/Duacs altimeter products were produced and distributed by the Copernicus Marine and Environment Monitoring Service (CMEMS) (<http://www.marine.copernicus.eu>).

### References

- Zika, J. D. *et al.* Vertical eddy fluxes in the southern ocean. *J. Phys. Oceanogr.* **43**, 941–955 (2013).
- Thompson, A. F. & Naveira Garabato, A. C. Equilibration of the antarctic circumpolar current by standing meanders. *J. Phys. Oceanogr.* **44**, 1811–1828 (2014).
- Rosso, I., Hogg, A. M., Kiss, A. E. & Gayen, B. Topographic influence on submesoscale dynamics in the southern ocean. *Geophys. Res. Lett.* **42**, 1139–1147 (2015).
- Youngs, M. K., Thompson, A. F., Lazar, A. & Richards, K. J. Acc meanders, energy transfer, and mixed barotropic–baroclinic instability. *J. Phys. Oceanogr.* **47**, 1291–1305 (2017).
- Kostianoy, A. G., Ginzburg, A. L., Lebedev, S. A., Frankignoulle, M. & Delille, B. Fronts and mesoscale variability in the southern indian ocean as inferred from the topex/poseidon and ers-2 altimetry data. *Oceanology C/C of Okeanologiya* **43**, 632–642 (2003).
- Klein, P. *et al.* Upper ocean turbulence from high-resolution 3d simulations. *J. Phys. Oceanogr.* **38**, 1748–1763 (2008).
- Klein, P. & Lapeyre, G. The oceanic vertical pump induced by mesoscale and submesoscale turbulence. *Annu. review. marine science* **1**, 351–375 (2009).
- McWilliams, J., Colas, F. & Molemaker, M. Cold filamentary intensification and oceanic surface convergence lines. *Geophys. Res. Lett.* **36** (2009).
- Blain, S. *et al.* Effect of natural iron fertilization on carbon sequestration in the southern ocean. *Nature* **446**, 1070 (2007).
- Perruche, C., Rivière, P., Lapeyre, G., Carton, X. & Pondaven, P. Effects of surface quasi-geostrophic turbulence on phytoplankton competition and coexistence. *J. marine research* **69**, 105–135 (2011).
- Lévy, M., Ferrari, R., Franks, P. J., Martin, A. P. & Rivière, P. Bringing physics to life at the submesoscale. *Geophys. Res. Lett.* **39** (2012).
- Campagna, C., Piola, A. R., Marin, M. R., Lewis, M. & Fernández, T. Southern elephant seal trajectories, fronts and eddies in the brazil/malvinas confluence. *Deep. Sea Res. Part I: Oceanogr. Res. Pap.* **53**, 1907–1924 (2006).
- Bailleul, F., Cotté, C. & Guinet, C. Mesoscale eddies as foraging area of a deep-diving predator, the southern elephant seal. *Mar. Ecol. Prog. Ser.* **408**, 251–264 (2010).
- Dragon, A.-C., Monestiez, P., Bar-Hen, A. & Guinet, C. Linking foraging behaviour to physical oceanographic structures: Southern elephant seals and mesoscale eddies east of kerguelen islands. *Prog. Oceanogr.* **87**, 61–71 (2010).
- Abrahms, B. *et al.* Mesoscale activity facilitates energy gain in a top predator. *Proc. R. Soc. B* **285**, 20181101 (2018).
- Cotté, C., d'Ovidio, F., Dragon, A.-C., Guinet, C. & Lévy, M. Flexible preference of southern elephant seals for distinct mesoscale features within the antarctic circumpolar current. *Prog. Oceanogr.* **131**, 46–58 (2015).
- Della Penna, A., De Monte, S., Kestenare, E., Guinet, C. & d'Ovidio, F. Quasi-planktonic behavior of foraging top marine predators. *Sci. reports* **5** (2015).
- Park, Y.-H., Fuda, J.-L., Durand, I. & Garabato, A. C. N. Internal tides and vertical mixing over the kerguelen plateau. *Deep Sea Research Part II: Topical Studies in Oceanography* **55**, 582–593 (2008).
- Bestley, S. *et al.* Ocean circulation and frontal structure near the southern kerguelen plateau: the physical context for the kerguelen axis ecosystem study. *Deep Sea Research Part II: Topical Studies in Oceanography* (2018).
- Hindell, M., Slip, D. & Burton, H. The diving behavior of adult male and female southern elephant seals, mirounga-leonina (pinnipedia, phocidae). *Aust. J. Zool.* **39**, 595–619 (1991).
- Hindell, M. A. *et al.* Circumpolar habitat use in the southern elephant seal: Implications for foraging success and population trajectories. *Ecosphere* **7**, e01213 (2016).
- Bailleul, F. *et al.* Successful foraging zones of southern elephant seals from the Kerguelen Islands in relation to oceanographic conditions. *Philos. Transactions Royal Soc. B: Biol. Sci.* **362**, 2169–2181 (2007).
- Labrousse, S. *et al.* Under the sea ice: Exploring the relationship between sea ice and the foraging behaviour of southern elephant seals in east antarctica. *Prog. Oceanogr.* **156**, 17–40 (2017).
- Vacquié-Garcia, J. *et al.* Predicting prey capture rates of southern elephant seals from track and dive parameters. *Mar. Ecol. Prog. Ser.* **541**, 265–277 (2015).
- Massie, P. P. *et al.* The role of eddies in the diving behaviour of female southern elephant seals. *Polar Biol.* **39**, 297–307 (2016).
- Tosh, C. A. *et al.* Marine habitats of juvenile southern elephant seals from marion island. In *SCAR XXXII & Open Science Conference* (2012).
- Whitehead, T. O., Kato, A., Ropert-Coudert, Y. & Ryan, P. G. Habitat use and diving behaviour of macaroni Eudyptes chrysolophus and eastern rockhopper E. chrysosome filholi penguins during the critical pre-moult period. *Marine Biol.* **163**, 19 (2016).



28. Biuw, M. *et al.* Variations in behavior and condition of a southern ocean top predator in relation to *in situ* oceanographic conditions. *Proc. Natl. Acad. Sci.* **104**, 13705–13710 (2007).
29. Charrassin, J.-B., Park, Y.-H., Maho, Y. L. & Bost, C.-A. Penguins as oceanographers unravel hidden mechanisms of marine productivity. *Ecol. Lett.* **5**, 317–319 (2002).
30. Boehme, L., Thorpe, S., Biuw, M., Fedak, M. & Meredith, M. Monitoring drake passage with elephant seals: Frontal structures and snapshots of transport. *Limnol. Oceanogr.* **53**, 2350–2360 (2008).
31. Charrassin, J.-B. *et al.* Southern ocean frontal structure and sea-ice formation rates revealed by elephant seals. *Proc. Natl. Acad. Sci.* **105**, 11634–11639 (2008).
32. Gove, J. M. *et al.* Near-island biological hotspots in barren ocean basins. *Nat. communications* **7**, 10581 (2016).
33. Flament, P. A state variable for characterizing water masses and their diffusive stability: spiciness. *Prog. Oceanogr.* **54**, 493–501 (2002).
34. Charnov, E. L. *et al.* Optimal foraging, the marginal value theorem. *Theor. Popul. Biol.* **9**, 129–136 (1976).
35. Fauchald, P., Erikstad, K. E. & Skarsfjord, H. Scale-dependent predator–prey interactions: the hierarchical spatial distribution of seabirds and prey. *Ecol.* **81**, 773–783 (2000).
36. Bailleul, F., Pinaud, D., Hindell, M., Charrassin, J. B. & Guinet, C. Assessment of scale-dependent foraging behaviour in southern elephant seals incorporating the vertical dimension: A development of the First Passage Time method. *J. Animal Ecol.* **77**, 948–957 (2008).
37. Heerah, K., Hindell, M., Guinet, C. & Charrassin, J.-B. A new method to quantify within dive foraging behaviour in marine predators. *PLoS One* **9**, e99329 (2014).
38. Chelton, D. B., Schlax, M. G. & Samelson, R. M. Global observations of nonlinear mesoscale eddies. *Prog. Oceanogr.* **91**, 167–216 (2011).
39. Lapeyre, G. & Klein, P. Impact of the small-scale elongated filaments on the oceanic vertical pump. *J. marine research* **64**, 835–851 (2006).
40. Rosso, I. *et al.* Vertical transport in the ocean due to sub-mesoscale structures: Impacts in the kerguelen region. *Ocean Model.* **80**, 10–23 (2014).
41. Thompson, A. F. *et al.* Open-ocean submesoscale motions: A full seasonal cycle of mixed layer instabilities from gliders. *J. Phys. Oceanogr.* **46**, 1285–1307 (2016).
42. du Plessis, M., Swart, S., Anson, I. & Mahadevan, A. Submesoscale processes promote seasonal restratification in the subantarctic ocean. *J. Geophys. Res. Ocean.* **122**, 2960–2975 (2017).
43. Viglione, G. A., Thompson, A. F., Flexas, M. M., Sprintall, J. & Swart, S. Abrupt transitions in submesoscale structure in southern drake passage: Glider observations and model results. *J. Phys. Oceanogr.* (2018).
44. Biggs, D. C. Nutrients, plankton, and productivity in a warm-core ring in the western gulf of Mexico. *J. Geophys. Res. Ocean.* **97**, 2143–2154 (1992).
45. Riande, V., Champalbert, G., Carlotti, F., Taupier-Letage, I. & Thibault-Botha, D. Zooplankton distribution related to the hydrodynamic features in the Algerian basin (western Mediterranean Sea) in summer 1997. *Deep Sea Res. Part I: Oceanogr. Res. Pap.* **52**, 2029–2048 (2005).
46. Landry, M. R., Decima, M., Simmons, M. P., Hannides, C. C. & Daniels, E. Mesozooplankton biomass and grazing responses to cyclone opal, a subtropical mesoscale eddy. *Deep Sea Res. Part II: Topical Studies in Oceanography* **55**, 1378–1388 (2008).
47. Le Bras, Y., Jouma'a, J., Picard, B. & Guinet, C. How Elephant Seals (*Mirounga leonina*) Adjust Their Fine Scale Horizontal Movement and Diving Behaviour in Relation to Prey Encounter Rate. *PLoS One* **11**, 1–23 (2016).
48. Guinet, C. *et al.* Southern elephant seal foraging success in relation to temperature and light conditions: Insight into prey distribution. *Mar. Ecol. Prog. Ser.* **499**, 285–301 (2014).
49. Field, I. C., Bradshaw, C. J. A., Burton, H. R., Sumner, M. D. & Hindell, M. A. Resource partitioning through oceanic segregation of foraging juvenile southern elephant seals (*Mirounga leonina*). *Oecologia* **142**, 127–135 (2005).
50. Bradshaw, C. J., Hindell, M. A., Sumner, M. D. & Michael, K. J. Loyalty pays: potential life history consequences of fidelity to marine foraging regions by southern elephant seals. *Animal Behaviour* **68**, 1349–1360 (2004).
51. Rodriguez, J. P. *et al.* Big data analyses reveal patterns and drivers of the movements of southern elephant seals. *Sci. reports* **7**, 112 (2017).
52. Authier, M., Bentaleb, I., Ponchon, A., Martin, C. & Guinet, C. Foraging fidelity as a recipe for a long life: Foraging strategy and longevity in male southern elephant seals. *PLoS One* **7** (2012).
53. Arthur, B. *et al.* Return customers: Foraging site fidelity and the effect of environmental variability in wide-ranging antarctic fur seals. *PLoS one* **10**, e0120888 (2015).
54. Robinson, P. W. *et al.* Foraging behavior and success of a mesopelagic predator in the northeast Pacific Ocean: insights from a data-rich species, the northern elephant seal. *PLoS one* **7**, e36728 (2012).
55. Callies, J., Ferrari, R., Klymak, J. M. & Gula, J. Seasonality in submesoscale turbulence. *Nat. communications* **6**, 6862 (2015).
56. Vallis, G. K. *Atmospheric and oceanic fluid dynamics* (Cambridge University Press, 2017).
57. Siegelman, L. *et al.* Correction and accuracy of high- and low-resolution CTD data from animal-borne instruments. *Journal of Atmospheric and Oceanic Technology* (2019).
58. Intergovernmental-Oceanographic-Commission *et al.* The international thermodynamic equation of seawater–2010: calculation and use of thermodynamic properties includes corrections up to 31st October 2015. *UNESCO* (2010).
59. Schneider, N. A decadal spiciness mode in the tropics. *Geophys. Res. Lett.* **27**, 257–260 (2000).
60. Kilpatrick, T., Schneider, N. & Di Lorenzo, E. Generation of low-frequency spiciness variability in the thermocline. *J. Phys. Oceanogr.* **41**, 365–377 (2011).
61. de Boyer Montégut, C., Madec, G., Fischer, A. S., Lazar, A. & Iudicone, D. Mixed layer depth over the global ocean: An examination of profile data and a profile-based climatology. *J. Geophys. Res. Ocean.* **109** (2004).
62. Kareiva, P. & Odell, G. Swarms of predators exhibit “preytaxis” if individual predators use area-restricted search. *The Am. Nat.* **130**, 233–270 (1987).
63. Bailleul, F., Lesage, V. & Hammill, M. O. Spherical First Passage Time: A tool to investigate area-restricted search in three-dimensional movements. *Ecol. Model.* **221**, 1665–1673 (2010).
64. Gallon, S. *et al.* Identifying foraging events in deep diving southern elephant seals, *Mirounga leonina*, using acceleration data loggers. *Deep-Sea Research Part II: Topical Studies in Oceanography* **88–89**, 14–22 (2013).
65. Thums, M., Bradshaw, C. J. & Hindell, M. A. *In situ* measures of foraging success and prey encounter reveal marine habitat-dependent search strategies. *Ecol.* **92**, 1258–1270 (2011).
66. Fauchald, P. & Tveraa, T. Using first-passage time in the analysis of area-restricted search and habitat selection. *Ecol.* **84**, 282–288 (2003).
67. Wood, S. N. *Generalized additive models: an introduction with R* (Chapman and Hall/CRC, 2006).
68. Zuur, A., Ieno, E., Walker, N., Saveliev, A. & Smith, G. *Mixed effects models and extensions in ecology with R*. Gail M., Krickeberg K., Samet J.M., Tsatis A., Wong W., editors (New York, NY, Springer Science and Business Media, 2009).
69. Wood, S. *Generalized Additive Models: An Introduction with R* 2nd edn (Chapman and Hall/CRC, 2017).
70. Kim, Y. S. & Orsi, A. H. On the variability of antarctic circumpolar current fronts inferred from 1992–2011 altimetry. *J. Phys. Oceanogr.* **44**, 3054–3071 (2014).

## Acknowledgements

This work was partly funded by the CNES (OSTST-OSIW) and the Laboratoire d'Excellence LabexMER (ANR-10-LABX-19). L.S. is a NASA-JPL JFSRP affiliate and is supported by a joint CNES-Région Bretagne doctoral grant. M.F. is supported by NASA grant NNX15AG42G. P.K. is supported by the NASA-CNES SWOT mission and a NASA Senior Fellowship. This study was also supported by the CNES-TOSCA project Elephant seals as Oceanographic Samplers of submesoscale features led by C. Guinet. The authors would like to thank the French Polar Institute (Institut Paul Emile Victor, IPEV) (Programs 109 and 1201) and CNES-TOSCA as well as Christophe Guinet and all the volunteers involved in the research program on southern elephant seals in Kerguelen. The authors would also like to thank Baptiste Picard for providing the elephant seal data, Tandi Reason Dahl for realizing the summary schematic (Figure 4) and two anonymous reviewers who considerably helped improve the manuscript.

## Author Contributions

L.S., M.O. and M.F. conceived and conducted the experiment and analyzed the results. L.S., M.O., M.F., P.R. and P.K. reviewed the manuscript.

## Additional Information

**Supplementary information** accompanies this paper at <https://doi.org/10.1038/s41598-019-42117-w>.

**Competing Interests:** The authors declare no competing interests.

**Publisher's note:** Springer Nature remains neutral with regard to jurisdictional claims in published maps and institutional affiliations.



**Open Access** This article is licensed under a Creative Commons Attribution 4.0 International License, which permits use, sharing, adaptation, distribution and reproduction in any medium or format, as long as you give appropriate credit to the original author(s) and the source, provide a link to the Creative Commons license, and indicate if changes were made. The images or other third party material in this article are included in the article's Creative Commons license, unless indicated otherwise in a credit line to the material. If material is not included in the article's Creative Commons license and your intended use is not permitted by statutory regulation or exceeds the permitted use, you will need to obtain permission directly from the copyright holder. To view a copy of this license, visit <http://creativecommons.org/licenses/by/4.0/>.

© The Author(s) 2019

## Conclusion and perspectives

Results, derived from *in situ* and model data, demonstrate that ageostrophic motions (i) are generated by the background mesoscale eddy field via frontogenesis processes, and (ii) are not solely confined to the ocean surface mixed layer but, rather, extend in the ocean interior down to depths of a thousand meters. As such, deep-reaching fronts at submesoscale provide an important, yet unexplored, pathway connecting the ocean interior to the surface. In terms of vertical heat fluxes (VHF), instantaneous values associated with these fronts reach  $\pm 2\,000\text{ W m}^{-2}$ . Furthermore, time and domain-averaged VHF over one month and  $\sim 500\text{ km} \times 500\text{ km}$  are directed upward regardless of depth, and have a magnitude of up to  $+350\text{ W m}^{-2}$  below the mixed layer (Siegelman et al., 2019a; Siegelman, pres). These results suggest revisiting current estimates of the Earth’s heat budget and stress the need to account for small-scale physics, not only within, but also below the ocean surface mixed layer, in the prediction of future climate states. In addition, the results of this dissertation may have a far greater scope as the evidence for intense vertical currents associated with deep-reaching submesoscale ocean fronts may also provide an efficient pathway for the transport of chemical and biological tracers, with potential major implications for biogeochemical systems.

Limitations of, and questions raised by, the present PhD work offer several routes for future work. First, the results of this dissertation suggest that an inaccurate representation of ageostrophic motions could considerably underestimate the amount of heat transferred from the ocean interior back to the surface and, as a consequence, potentially overestimate the amount of heat the ocean can absorb. However, the coupled ocean-atmosphere system is complex and regulated by two-way oceanic-atmospheric feedbacks. Thus, a central question that arises concerns the impact of deep VHF on the atmosphere, through air-sea fluxes for instance. Accurately answering this question from a modeling perspective requires a coupled ocean-atmosphere simulation at high resolution, such as the global one that is running as I write at the NASA Advanced Supercomputing Division at the Ames research center. However, recent results already indicate that sea surface temperature fronts associated with oceanic mesoscale eddies trigger a significant wind divergence, which leads to large latent heat and moisture release in the vicinity of oceanic

eddies. Consequently, mesoscale eddies in the Kuroshio Extension exert a distant influence on winter rainfalls along the U.S. Northern Pacific coast, leading to an increase of 20–25% of the total rainfall (Ma et al., 2015), and mesoscale eddies in the Gulf Stream impact the wintertime European blocking (O’Reilly et al., 2017). These results highlight that oceanic mesoscale eddies have the capacity to mediate intermittent air-sea interactions, suggesting that the influence of submesoscale turbulence on atmospheric storm tracks is potentially a lot greater than previously thought.

In the context of the upcoming NASA-CNES Surface Water Ocean Topography (SWOT) mission that will be launched in 2021, one may ask whether it is possible to diagnose ageostrophic dynamics in the ocean interior from space. It is known that the strain field associated with oceanic eddies governs tracer dispersion (Hua et al., 1998; Lapeyre et al., 1999) and that advection and stretching properties widely differ in the QG and ageostrophic regimes (Scott, 2006; Özgökmen et al., 2012; Foussard et al., 2017). On the one hand, in the QG regime, the  $k^{-3}$  KE spectrum slope implies that the stretching of small-scale filaments is driven by the largest eddies alone. In this case, tracer fluxes, from large to small scales, are associated with "non-local" scale interactions as the large scales control the small ones (Scott, 2006). On the other hand, in an ageostrophic regime, the  $k^{-2}$  KE spectrum slope implies that filament dynamics are controlled by both meso- and submesoscales. These interactions are now referred to as "local" as small-scale filaments can also be produced by the smallest eddies (Scott, 2006). Preliminary results indicate that FSLEs can be used to diagnose local and non-local advection properties of a tracer from space, as can be seen in Figure 5.1 for the Ertel PV (Siegelman et al., prep). When submesoscale motions are taken into account in addition to mesoscale ones alone, FSLE are characterized by smaller scales and larger magnitudes. These results are particularly relevant in the context of SWOT, which will resolve SSH at an unprecedented resolution of 15-km wavelength, i.e., ten times greater than current satellite altimeters. SWOT will give access for the first time to both meso- and submesoscales on a global scale, enabling the study of local and non-local advection from space. This opens the door to retrieve the vertical velocity field at both meso- and submesoscale from space, not only at the ocean surface but also in the ocean interior. A promising route to do so is based on the diagnostic omega equation, relating the strain field and lateral

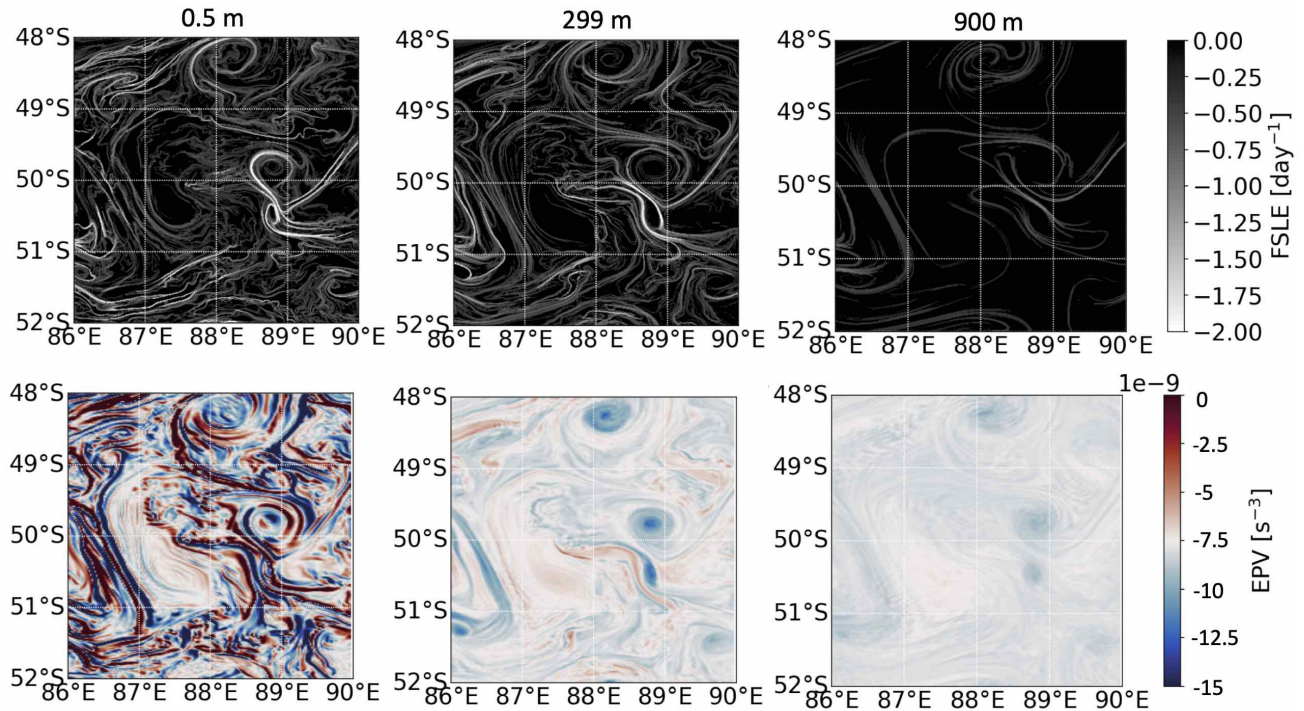


Figure 5.1: Snapshot of FSLE (top) and Ertel PV (bottom) at 0.5 m (left), 299 m (middle), and 900 m (right) in the Kerguelen area (Figure 1.11) on 2011-12-25 15:00:00 UTC, computed from the LLC4320 simulation (see section 1.3). From Siegelman et al. (prep).

gradients of buoyancy to vertical velocities (Chapter 2). This constitutes an on-going project with Pr. Bo Qiu (University of Hawaii, see submitted NASA SWOT proposal 2019) in the context of eSQG reconstruction methods of the vertical velocity field (Qiu et al., 2019). The current major limitation of the traditional eSQG method is that it can only retrieve the buoyancy, and thus the vertical velocity, field at mesoscale. To overcome this limitation, and similarly to what was done in Chapter 3, we intend to use FSLEs to derive the strain field from upcoming SWOT observations. More precisely, the idea is to add an extra step in the current eSQG method: at each depth, the buoyancy field computed with eSQG will be advected as a 2-D tracer by the velocity field, also derived from eSQG. This Lagrangian advection will allow buoyancy gradients at submesoscale to emerge due to the direct cascade of PE energy. This buoyancy field will then be compared/realigned with FSLEs diagnosed from SWOT, which should now take into account local and non-local straining dynamics as a function of depth. Finally, the vertical velocity field at submesoscale will be derived from the omega equation.

Throughout this dissertation, with the exception of the wavenumber-frequency spectra presented

in Chapter 4, interactions between IGWs and balanced motions (BM) have not been studied. However, although BMs and IGWs occupy distinct regions of the spectral space (Figure 5.2), they do interact (Chereskin et al., 2019). Many studies have revealed that IGW propagation is polarized by the sign of relative vorticity and stratification anomaly of mesoscale eddies (Kunze, 1985; Young and Jelloul, 1997; Danioux et al., 2011; Joyce et al., 2013; Zaron and Egbert, 2014; Grisouard and Thomas, 2015; Ponte and Klein, 2015; Whitt and Thomas, 2015; Dunphy et al., 2017; Thomas, 2017). As a result, IGWs are preferentially trapped within anticyclonic eddies and expelled from cyclonic eddies, and

their frequencies and wavenumbers significantly increase during this process (Whitt and Thomas, 2015). Thus, the scattering and dispersive impacts of BMs on IGWs may ultimately lead to intensified (reduced) mixing in anticyclonic (cyclonic) eddies. Besides driving localized mixing, recent studies suggest that interactions between IGWs and BMs may also stimulate submesoscale fronts and their associated vertical velocities (Xie and Vanneste, 2015; Taylor and Straub, 2016; Wagner and Young, 2016; Barkan et al., 2017; Thomas, 2017; Rocha et al., 2018).

As such, the propagation direction and velocity of IGWs trapped in a balanced strain field may be considerably modified, leading to non-zero momentum and buoyancy fluxes associated with IGWs (Thomas, 2017). These fluxes represent an energy transfer from mesoscale KE to wave PE, with this energy being subsequently transferred to submesoscale fronts with high frequencies, i.e.,

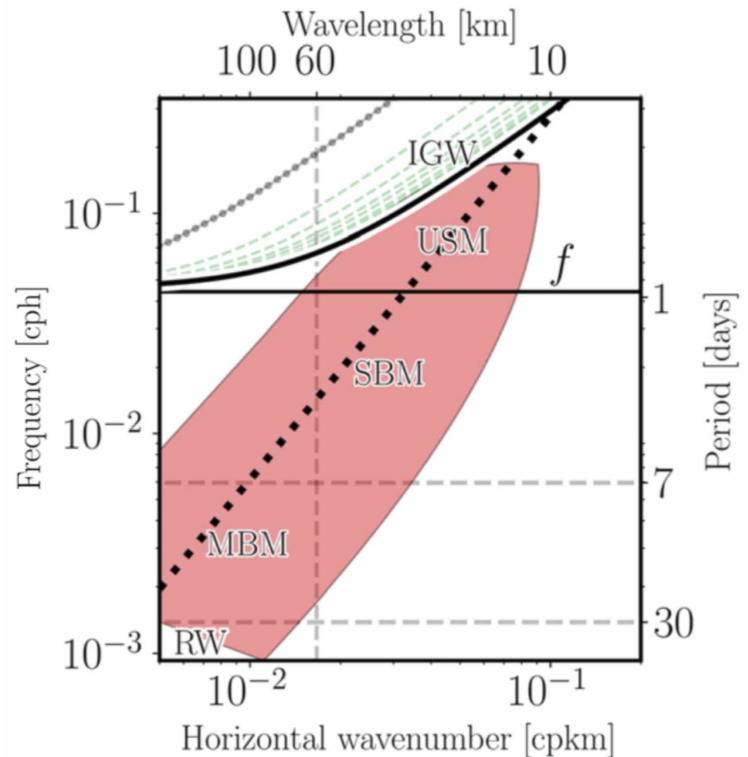


Figure 5.2: Wavenumber-frequency spectrum schematic displaying the multiple dynamical regimes: RW stands for Rossby waves, MBM for mesoscale balanced motions, SBM for submesoscale balanced motions, USM for unbalanced submesoscale motions, and IGW for internal gravity waves. The dispersion relations for the first ten baroclinic modes are shown: mode 1 in gray dotted line, mode 2–9 in green dashed lines, and mode 10 in black. The non-dispersive line  $\omega - ck = 0$  is drawn for an eddy speed  $c$  of  $10 \text{ m s}^{-1}$ . From Torres et al. (2018).

the USM area in Figure 5.2. This mechanism, referred to as stimulated imbalance, increases the vertical velocity field associated with submesoscale fronts and therefore vertical advective fluxes of tracers (Barkan et al., 2017; Thomas, 2017; Rocha et al., 2018). To date, these energy transfers have mainly been studied in idealized models (Xie and Vanneste, 2015; Taylor and Straub, 2016; Wagner and Young, 2016; Barkan et al., 2017; Thomas, 2017; Rocha et al., 2018) and remain largely unknown and unexplored in the real ocean. This constitutes an active area of research that is of interest to me (see the studies of Klein et al. (2019) presented in Appendix A and Torres et al. (2019) in Appendix B that I co-authored) and a route that I would like to pursue during my upcoming postdoctoral position. In particular, it remains to be determined whether high-frequency IGWs can lead, in addition to irreversible mixing, to a substantial increase of vertical advective tracer fluxes, as found in Su et al. (2018) and Su (*pers. comm.*). Note that the on-going Near Inertial Shear and Kinetic Energy in the North Atlantic Experiment (NISKINE) promises to provide the first direct observations of these processes from ship-based and autonomous floats (Rainville et al., 2019), and should serve as a baseline for future *in situ* experiments aimed at studying the interactions between IGWs and BMs in other regions of the world ocean.

Regarding *in situ* campaigns, I would also like to suggest potential strategies for the study of ageostrophic dynamics in the ocean interior:

- In order to sample submesoscale motions, it appears crucial to target areas of intense mesoscale activity, i.e., strain-dominated areas of the flow field, which can be diagnosed from space. In order to do so, one can imagine a similar setup to the one implemented in the POMME experiment by Legal et al. (2007). In this experiment, a ship equipped with an ADCP and a SeaSoar closely followed regions of negative Okubo-Weiss (OW, i.e., strain-dominated areas of the flow field) where a radiator pattern across the frontal region was executed. Instead of tracking the OW quantity, which tends to be noisy (Figure 2.5), especially when derived from altimeter data (not shown), I suggest to use FSLEs. FSLEs have the advantage of being at finer-scale for a similar initial SSH field (Figure 1.10). In addition, FSLEs take into account the rotation of the strain tensor axis (Lapeyre et al.,

1999) and thus the time evolution of the Lagrangian strain field, whereas OW does not.

- Another rich, yet under-looked, approach to study meso- and submesoscale turbulence in the ocean interior is through seismic reflection profiling. This technique originated in the oil industry and was first used for oceanographic purposes to observe internal waves (Gonella and Michon, 1988). More recently, seismic reflection has been used to study oceanographic fronts in relation to thermohaline structures in the northern Atlantic (Holbrook et al., 2003; Nandi et al., 2004) as well as mesoscale eddies and submesoscale filaments in the ocean interior (Pinot et al., 1996; Holbrook and Fer, 2005; Biescas et al., 2008; Krahnmann et al., 2008; Klaeschen et al., 2009; Quentel et al., 2010, 2011; Ménesguen et al., 2012). Seismic data also allow the detection of submesoscale eddies that hydrographic sections rarely capture (Menesguen et al., 2009; Quentel et al., 2010; Ménesguen et al., 2012; Gula et al., 2019), as can be seen in Figure 5.3.

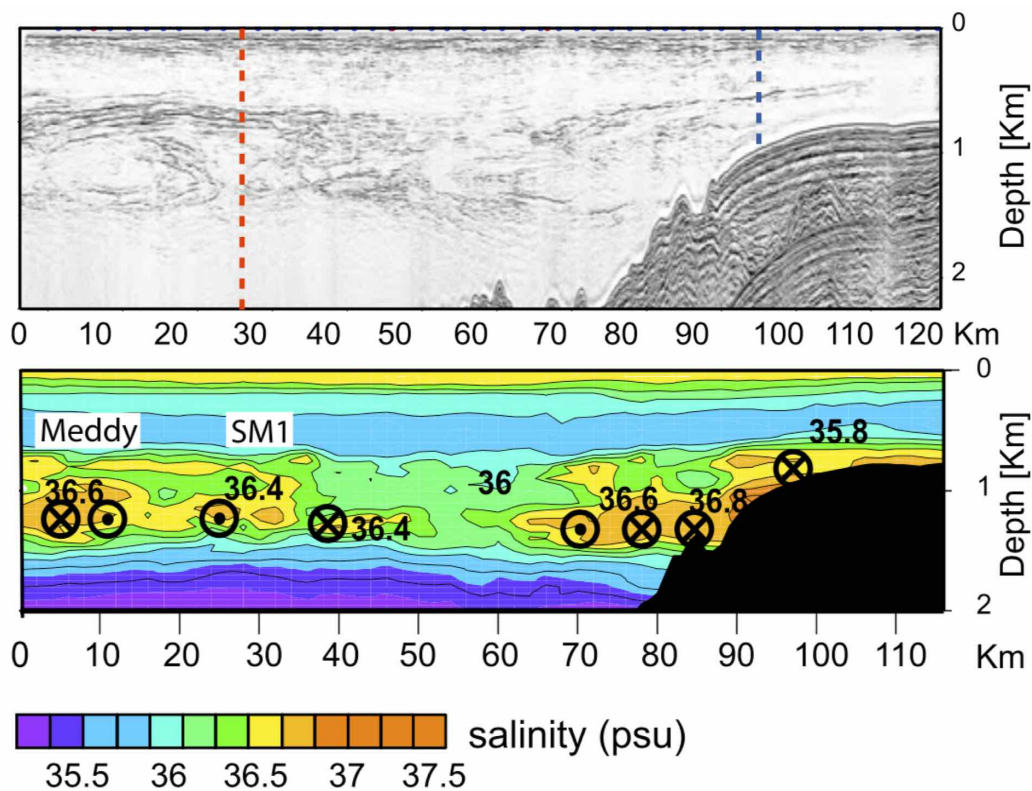


Figure 5.3: Vertical section of seismic reflection (top) and salinity (bottom). Velocity vectors on the bottom panel (black bolt cross, velocities directed to the east; black bold dot, velocities directed to the west) indicate an anticyclonic mesoscale eddy (Meddy), a cyclonic submesoscale eddy (SM1). Adapted from Quentel et al. (2010).



## References

- Arbic, B. K., Richman, J. G., Shriver, J. F., Timko, P. G., Metzger, E. J., and Wallcraft, A. J. (2012). Global modeling of internal tides: Within an eddying ocean general circulation model. *Oceanography*, 25(2):20–29.
- Aref, H. (1984). Stirring by chaotic advection. *Journal of fluid mechanics*, 143:1–21.
- Armi, L., Hebert, D., Oakey, N., Price, J., Richardson, P. L., Rossby, T., and Ruddick, B. (1988). The history and decay of a mediterranean salt lens. *Nature*, 333(6174):649.
- Barbosa Aguiar, A., Ménesguen, C., Le Gentil, S., Schopp, R., and Carton, X. (2015). Cyclones and anticyclones in seismic imaging. *Journal of Physical Oceanography*, 45(9):2436–2443.
- Barkan, R., Winters, K. B., and McWilliams, J. C. (2017). Stimulated imbalance and the enhancement of eddy kinetic energy dissipation by internal waves. *Journal of Physical Oceanography*, 47(1):181–198.
- Basdevant, C. and Philipovitch, T. (1994). On the validity of the “weiss criterion” in two-dimensional turbulence. *Physica D: Nonlinear Phenomena*, 73(1-2):17–30.
- Biescas, B., Sallarès, V., Pelegrí, J. L., Machín, F., Carbonell, R., Buffett, G., Dañobeitia, J. J., and Calahorrano, A. (2008). Imaging meddy finestructure using multichannel seismic reflection data. *Geophysical Research Letters*, 35(11).
- Boccaletti, G., Ferrari, R., and Fox-Kemper, B. (2007). Mixed layer instabilities and restratification. *Journal of Physical Oceanography*, 37(9):2228–2250.
- Boehme, L., Lovell, P., Biuw, M., Roquet, F., Nicholson, J., Thorpe, S. E., Meredith, M. P., and Fedak, M. (2009). Animal-borne ctd-satellite relay data loggers for real-time oceanographic data collection. *Ocean Science*.
- Boyer, T. P., Antonov, J. I., Baranova, O. K., Coleman, C., Garcia, H. E., Grodsky, A., Johnson, D. R., Locarnini, R. A., Mishonov, A. V., O’Brien, T. D., et al. (2013). World ocean database 2013.
- Callies, J. and Ferrari, R. (2013). Interpreting energy and tracer spectra of upper-ocean turbulence in the submesoscale range (1–200 km). *Journal of Physical Oceanography*, 43(11):2456–2474.
- Callies, J., Flierl, G., Ferrari, R., and Fox-Kemper, B. (2016). The role of mixed-layer instabilities in submesoscale turbulence. *Journal of Fluid Mechanics*, 788:5–41.
- Capet, X., McWilliams, J. C., Molemaker, M. J., and Shchepetkin, A. (2008). Mesoscale to submesoscale transition in the california current system. part i: Flow structure, eddy flux, and observational tests. *Journal of physical oceanography*, 38(1):29–43.
- Chaudhuri, A. H., Ponte, R. M., Forget, G., and Heimbach, P. (2013). A comparison of atmospheric reanalysis surface products over the ocean and implications for uncertainties in air–sea boundary forcing. *Journal of Climate*, 26(1):153–170.
- Chelton, D. B., Schlax, M. G., and Roger, M. S. (2011). Global observations of nonlinear mesoscale eddies. *Progress in Oceanography*, 91(2):167–216.
- Chereskin, T. K., Rocha, C. B., Gille, S. T., Menemenlis, D., and Passaro, M. (2019). Characterizing the transition from balanced to unbalanced motions in the southern california current. *Journal of Geophysical Research: Oceans*, 124(3):2088–2109.
- Danioux, E., Klein, P., Hecht, M. W., Komori, N., Roullet, G., and Le Gentil, S. (2011). Emergence of wind-driven near-inertial waves in the deep ocean triggered by small-scale eddy vorticity structures. *Journal of Physical Oceanography*, 41(7):1297–1307.
- Davis, C. A. (1992). Piecewise potential vorticity inversion. *Journal of the atmospheric sciences*, 49(16):1397–1411.

- Deremble, B., Wienders, N., and Dewar, W. (2014). Potential vorticity budgets in the north atlantic ocean. *Journal of Physical Oceanography*, 44(1):164–178.
- d’Ovidio, F., Fernández, V., Hernández-García, E., and López, C. (2004). Mixing structures in the mediterranean sea from finite-size lyapunov exponents. *Geophysical Research Letters*, 31(17).
- Dunphy, M., Ponte, A. L., Klein, P., and Le Gentil, S. (2017). Low-mode internal tide propagation in a turbulent eddy field. *Journal of Physical Oceanography*, 47(3):649–665.
- Fernández-Castro, B., Mouriño-Carballido, B., Benítez-Barrios, V., Chouciño, P., Fraile-Nuez, E., Graña, R., Piedeleu, M., and Rodríguez-Santana, A. (2014). Microstructure turbulence and diffusivity parameterization in the tropical and subtropical atlantic, pacific and indian oceans during the malaspina 2010 expedition. *Deep Sea Research Part I: Oceanographic Research Papers*, 94:15–30.
- Ferrari, R. (2011). A frontal challenge for climate models. *Science*, 332(6027):316–317.
- Ferrari, R. and Wunsch, C. (2009). Ocean circulation kinetic energy: Reservoirs, sources, and sinks. *Annual Review of Fluid Mechanics*, 41.
- Forget, G., Campin, J.-M., Heimbach, P., Hill, C. N., Ponte, R. M., and Wunsch, C. (2015). Ecco version 4: An integrated framework for non-linear inverse modeling and global ocean state estimation. *Geosci. Model Dev.*
- Foussard, A., Berti, S., Perrot, X., and Lapeyre, G. (2017). Relative dispersion in generalized two-dimensional turbulence. *Journal of Fluid Mechanics*, 821:358–383.
- Fox-Kemper, B., Ferrari, R., and Hallberg, R. (2008). Parameterization of mixed layer eddies. part i: Theory and diagnosis. *Journal of Physical Oceanography*, 38(6):1145–1165.
- Fox-Kemper, B. and Menemenlis, D. (2008). Can large eddy simulation techniques improve mesoscale rich ocean models. *Ocean modeling in an eddying regime*, 177:319–337.
- Garrett, C. (1983). On the initial streakiness of a dispersing tracer in two-and three-dimensional turbulence. *Dynamics of Atmospheres and Oceans*, 7(4):265–277.
- Gent, P. R. and McWilliams, J. C. (1983). Consistent balanced models in bounded and periodic domains. *Dynamics of Atmospheres and Oceans*, 7(2):67–93.
- Gill, A. E. (1982). Atmosphere. *Ocean dynamics*, 30:662.
- Gonella, J. and Michon, D. (1988). Ondes internes profondes revelees par sismique reflexion au sein des masses d’eau en atlantique-est. *Comptes rendus de l’Académie des sciences. Série 2, Mécanique, Physique, Chimie, Sciences de l’univers, Sciences de la Terre*, 306(12):781–787.
- Grisouard, N. and Thomas, L. N. (2015). Critical and near-critical reflections of near-inertial waves off the sea surface at ocean fronts. *Journal of Fluid Mechanics*, 765:273–302.
- Gula, J., Blacic, T. M., and Todd, R. E. (2019). Submesoscale coherent vortices in the gulf stream. *Geophysical Research Letters*, 46(5):2704–2714.
- Hakim, G. and Keyser, D. (2001). Canonical frontal circulation patterns in terms of green’s functions for the sawyer-eliasen equation. *Quarterly Journal of the Royal Meteorological Society*, 127:1795–1814.
- Haller, G. and Sapsis, T. (2011). Lagrangian coherent structures and the smallest finite-time lyapunov exponent. *Chaos: An Interdisciplinary Journal of Nonlinear Science*, 21(2):023115.
- Hansen, J., Sato, M., Kharecha, P., and Schuckmann, K. v. (2011). Earth’s energy imbalance and implications. *Atmospheric Chemistry and Physics*, 11(24):13421–13449.
- Haynes, P. and McIntyre, M. (1990). On the conservation and impermeability theorems for potential vorticity. *Journal of the atmospheric sciences*, 47(16):2021–2031.

- Haza, A. C., Ozgokmen, T. M., Griffa, A., Garraffo, Z. D., and Piterbarg, L. (2012). Parameterization of particle transport at submesoscales in the gulf stream region using lagrangian subgridscale models. *Ocean Modelling*, 42(1):31–49.
- Hill, C., Menemenlis, D., Ciotti, B., and Henze, C. (2007). Investigating solution convergence in a global ocean model using a 2048-processor cluster of distributed shared memory machines. *Scientific Programming*, 15(2):107–115.
- Hindell, M. A., McMahon, C. R., Bester, M. N., Boehme, L., Costa, D., Fedak, M. A., Guinet, C., Herraiz-Borreguero, L., Harcourt, R. G., Huckstadt, L., et al. (2016). Circumpolar habitat use in the southern elephant seal: implications for foraging success and population trajectories. *Ecosphere*, 7(5):e01213.
- Hogg, A. M., Meredith, M. P., Chambers, D. P., Abrahamsen, E. P., Hughes, C. W., and Morrison, A. K. (2015). Recent trends in the southern ocean eddy field. *Journal of Geophysical Research: Oceans*, 120(1):257–267.
- Holbrook, W. S. and Fer, I. (2005). Ocean internal wave spectra inferred from seismic reflection transects. *Geophysical Research Letters*, 32(15).
- Holbrook, W. S., Páramo, P., Pearse, S., and Schmitt, R. W. (2003). Thermohaline fine structure in an oceanographic front from seismic reflection profiling. *Science*, 301(5634):821–824.
- Holton, J. R. (1973). An introduction to dynamic meteorology. *American Journal of Physics*, 41(5):752–754.
- Hoskins, B. J. (1982). The mathematical theory of frontogenesis. *Annual review of fluid mechanics*, 14(1):131–151.
- Hoskins, B. J. and Bretherton, F. P. (1972). Atmospheric frontogenesis models: Mathematical formulation and solution. *Journal of the Atmospheric Sciences*, 29(1):11–27.
- Hoskins, B. J., Draghici, I., and Davies, H. C. (1978). A new look at the  $\omega$ -equation. *Quarterly Journal of the Royal Meteorological Society*, 104(439):31–38.
- Hoskins, B. J., McIntyre, M. E., and Robertson, A. W. (1985). On the use and significance of isentropic potential vorticity maps. *Quarterly Journal of the Royal Meteorological Society*, 111(470):877–946.
- Hua, B. and Klein, P. (1998). An exact criterion for the stirring properties of nearly two-dimensional turbulence. *Physica D: Nonlinear Phenomena*, 113(1):98–110.
- Hua, B. L., McWilliams, J. C., and Klein, P. (1998). Lagrangian accelerations in geostrophic turbulence. *Journal of Fluid Mechanics*, 366:87–108.
- Joyce, T. M., Toole, J. M., Klein, P., and Thomas, L. N. (2013). A near-inertial mode observed within a gulf stream warm-core ring. *Journal of Geophysical Research: Oceans*, 118(4):1797–1806.
- Klaeschen, D., Hobbs, R., Krahnemann, G., Papenberg, C., and Vsemirnova, E. (2009). Estimating movement of reflectors in the water column using seismic oceanography. *Geophysical Research Letters*, 36(24).
- Klein, P. and Lapeyre, G. (2009). The oceanic vertical pump induced by mesoscale and submesoscale turbulence. *Annual review of marine science*, 1:351–375.
- Klein, P., Lapeyre, G., Siegelman, L., Qiu, B., Fu, L.-L., Torres, H., Su, Z., Menemenlis, D., and Le Gentil, S. (2019). Ocean-scale interactions from space. *Earth and Space Science*.
- Klein, P., Treguier, A.-M., and Hua, B. L. (1998). Three-dimensional stirring of thermohaline fronts. *Journal of marine research*, 56(3):589–612.
- Krahnemann, G., Brandt, P., Klaeschen, D., and Reston, T. (2008). Mid-depth internal wave energy off the iberian peninsula estimated from seismic reflection data. *Journal of Geophysical Research: Oceans*, 113(C12).
- Kunze, E. (1985). Near-inertial wave propagation in geostrophic shear. *Journal of Physical Oceanography*, 15(5):544–565.

- Lapeyre, G. (2002). Characterization of finite-time lyapunov exponents and vectors in two-dimensional turbulence. *Chaos: An Interdisciplinary Journal of Nonlinear Science*, 12(3):688–698.
- Lapeyre, G., Hua, B., and Klein, P. (2001). Dynamics of the orientation of active and passive scalars in two-dimensional turbulence. *Physics of Fluids*, 13(1):251–264.
- Lapeyre, G., Klein, P., and Hua, B. (1999). Does the tracer gradient vector align with the strain eigenvectors in 2d turbulence? *Physics of fluids*, 11(12):3729–3737.
- Large, W. G., Danabasoglu, G., Doney, S. C., and McWilliams, J. C. (1997). Sensitivity to surface forcing and boundary layer mixing in a global ocean model: Annual-mean climatology. *Journal of Physical Oceanography*, 27(11):2418–2447.
- Large, W. G., McWilliams, J. C., and Doney, S. C. (1994). Oceanic vertical mixing: A review and a model with a nonlocal boundary layer parameterization. *Reviews of Geophysics*, 32(4):363–403.
- Large, W. G. and Yeager, S. (2009). The global climatology of an interannually varying air–sea flux data set. *Climate dynamics*, 33(2-3):341–364.
- Large, W. G. and Yeager, S. G. (2004). Diurnal to decadal global forcing for ocean and sea-ice models: the data sets and flux climatologies. *NCAR Tech. Note*.
- Ledwell, J. R., Watson, A. J., and Law, C. S. (1993). Evidence for slow mixing across the pycnocline from an open-ocean tracer-release experiment. *Nature*, 364(6439):701.
- Legal, C., Klein, P., Tréguier, A. M., and Paillet, J. (2007). Diagnosis of the vertical motions in a mesoscale stirring region. *Journal of Physical Oceanography*, 37(5):1413–1424.
- Lehahn, Y., d’Ovidio, F., Lévy, M., and Heifetz, E. (2007). Stirring of the northeast atlantic spring bloom: A lagrangian analysis based on multisatellite data. *Journal of Geophysical Research: Oceans*, 112(C8).
- Lévy, M., Klein, P., and Treguier, A.-M. (2001). Impact of sub-mesoscale physics on production and subduction of phytoplankton in an oligotrophic regime. *Journal of marine research*, 59(4):535–565.
- Lévy, M., Klein, P., Tréguier, A.-M., Iovino, D., Madec, G., Masson, S., and Takahashi, K. (2010). Modifications of gyre circulation by sub-mesoscale physics. *Ocean Modelling*, 34(1-2):1–15.
- Losch, M., Menemenlis, D., Campin, J.-M., Heimbach, P., and Hill, C. (2010). On the formulation of sea-ice models. part 1: Effects of different solver implementations and parameterizations. *Ocean Modelling*, 33(1-2):129–144.
- Ma, X., Chang, P., Saravanan, R., Montuoro, R., Hsieh, J.-S., Wu, D., Lin, X., Wu, L., and Jing, Z. (2015). Distant influence of kuroshio eddies on north pacific weather patterns? *Scientific reports*, 5:17785.
- Mariotti, A., Legras, B., and Dritschel, D. G. (1994). Vortex stripping and the erosion of coherent structures in two-dimensional flows. *Physics of Fluids*, 6(12):3954–3962.
- Marshall, J., Adcroft, A., Hill, C., Perelman, L., and Heisey, C. (1997). A finite-volume, incompressible navier stokes model for studies of the ocean on parallel computers. *Journal of Geophysical Research: Oceans*, 102(C3):5753–5766.
- McWilliams, J. C. (2016). Submesoscale currents in the ocean. *Proc. R. Soc. A*, 472(2189):20160117.
- Ménesguen, C., Hua, B., Carton, X., Klingelhoefer, F., Schnürle, P., and Reichert, C. (2012). Arms winding around a meddy seen in seismic reflection data close to the morocco coastline. *Geophysical Research Letters*, 39(5).
- Ménesguen, C., Hua, B., Papenberg, C., Klaeschen, D., Geli, L., and Hobbs, R. (2009). Effect of bandwidth on seismic imaging of rotating stratified turbulence surrounding an anticyclonic eddy from field data and numerical simulations. *Geophysical Research Letters*, 36(24).

- Mensah, V., Roquet, F., Siegelman, L., Picard, B., Pauthenet, E., and Guinet, C. (2018). A correction for the thermal mass-induced errors of ctd tags mounted on marine mammals. *Journal of atmospheric and oceanic technology*, 35(6):1237–1252.
- Molemaker, J., McWilliams, J., and Yavneh, I. (2005). Baroclinic instability and loss of balance. *Journal of physical oceanography*, 35:1505–1517.
- Molemaker, M. J., McWilliams, J. C., and Capet, X. (2010). Balanced and unbalanced routes to dissipation in an equilibrated eady flow. *Journal of Fluid Mechanics*, 654:35–63.
- Muraki, D. J., Snyder, C., and Rotunno, R. (1999). The next-order corrections to quasigeostrophic theory. *Journal of the atmospheric sciences*, 56(11):1547–1560.
- Nandi, P., Holbrook, W. S., Pearse, S., Páramo, P., and Schmitt, R. W. (2004). Seismic reflection imaging of water mass boundaries in the norwegian sea. *Geophysical Research Letters*, 31(23).
- Okubo, A. (1970). Horizontal dispersion of floatable particles in the vicinity of velocity singularities such as convergences. *Deep sea research and oceanographic abstracts*, 17(3):445–454.
- Ollitrault, M., Gabillet, C., and De Verdiere, A. C. (2005). Open ocean regimes of relative dispersion. *Journal of Fluid Mechanics*, 533:381–407.
- O’Reilly, C. H., Minobe, S., Kuwano-Yoshida, A., and Woollings, T. (2017). The gulf stream influence on wintertime north atlantic jet variability. *Quarterly Journal of the Royal Meteorological Society*, 143(702):173–183.
- Özgökmen, T. M., Poje, A. C., Fischer, P. F., Childs, H., Krishnan, H., Garth, C., Haza, A. C., and Ryan, E. (2012). On multi-scale dispersion under the influence of surface mixed layer instabilities and deep flows. *Ocean Modelling*, 56:16–30.
- Pauthenet, E. (2018). *Unraveling the thermohaline structure of the Southern Ocean using functional data analysis*. PhD thesis, Department of Meteorology, Stockholm University.
- Pedlosky, J. (2013). *Geophysical fluid dynamics*. Springer Science & Business Media.
- Pierrehumbert, R. T., Held, I. M., and Swanson, K. L. (1994). Spectra of local and nonlocal two-dimensional turbulence. *Chaos, Solitons & Fractals*, 4(6):1111–1116.
- Pinot, J.-M., Tintoré, J., and Wang, D.-P. (1996). A study of the omega equation for diagnosing vertical motions at ocean fronts. *Journal of marine research*, 54(2):239–259.
- Ponte, A. L. and Klein, P. (2015). Incoherent signature of internal tides on sea level in idealized numerical simulations. *Geophysical Research Letters*, 42(5):1520–1526.
- Qiu, B., Chen, S., Klein, P., Sasaki, H., and Sasai, Y. (2014). Seasonal mesoscale and submesoscale eddy variability along the north pacific subtropical countercurrent. *Journal of Physical Oceanography*, 44(12):3079–3098.
- Qiu, B., Chen, S., Klein, P., Torres, H., Wang, J., Fu, L.-L., and Menemenlis, D. (2019). Reconstructing upper ocean vertical velocity field from sea surface height in the presence of unbalanced motion. *Journal of Physical Oceanography*, (2019).
- Quentel, E., Carton, X., and Gutscher, M. A. (2011). Structure and temporal variability of mediterranean water in hydrological and marine seismic data south of portimao canyon (gulf of cadiz), from 1999 to 2002. *International Journal of Geosciences*, 2(03):185.
- Quentel, E., Carton, X., Gutscher, M.-A., and Hobbs, R. (2010). Detecting and characterizing mesoscale and submesoscale structures of mediterranean water from joint seismic and hydrographic measurements in the gulf of cadiz. *Geophysical Research Letters*, 37(6).

- Rainville, L., Girton, J., Lund, B., Savage, A., Thomas, L., Whalen, C., Bertero, L., Burnett, J., Cole, D., Gobat, J., Goheen, S., Jokinen, B., and Snyder, A. (2019). Near-inertial shear and kinetic energy in the north atlantic experiment (niskine). Technical report, AR35-03 cruise report.
- Rio, M.-H., Santoleri, R., Bourdalle-Badie, R., Griffa, A., Piterbarg, L., and Taburet, G. (2016). Improving the altimeter-derived surface currents using high-resolution sea surface temperature data: A feasibility study based on model outputs. *Journal of Atmospheric and Oceanic Technology*, 33(12):2769–2784.
- Rocha, C. B., Chereskin, T. K., Gille, S. T., and Menemenlis, D. (2016a). Mesoscale to submesoscale wavenumber spectra in drake passage. *Journal of Physical Oceanography*, 46(2):601–620.
- Rocha, C. B., Gille, S. T., Chereskin, T. K., and Menemenlis, D. (2016b). Seasonality of submesoscale dynamics in the kuroshio extension. *Geophysical Research Letters*, 43(21):11–304.
- Rocha, C. B., Wagner, G. L., and Young, W. R. (2018). Stimulated generation: extraction of energy from balanced flow by near-inertial waves. *Journal of Fluid Mechanics*, 847:417–451.
- Roquet, F., Boehme, L., Block, B., Charrassin, J. B., Costa, D., Guinet, C., Harcourt, R. G., Hindell, M. A., Hückstädt, L. A., McMahon, C. R., et al. (2017). Ocean observations using tagged animals. *Oceanography*.
- Roquet, F., Charrassin, J.-B., Marchand, S., Boehme, L., Fedak, M., Reverdin, G., and Guinet, C. (2011). Delayed-mode calibration of hydrographic data obtained from animal-borne satellite relay data loggers. *Journal of Atmospheric and Oceanic Technology*, 28(6):787–801.
- Roquet, F., Williams, G., Hindell, M. A., Harcourt, R., McMahon, C., Guinet, C., Charrassin, J.-B., Reverdin, G., Boehme, L., Lovell, P., et al. (2014). A southern indian ocean database of hydrographic profiles obtained with instrumented elephant seals. *Scientific data*, 1:140028.
- Sasaki, H., Klein, P., Qiu, B., and Sasai, Y. (2014). Impact of oceanic-scale interactions on the seasonal modulation of ocean dynamics by the atmosphere. *Nature communications*, 5:6636.
- Scott, R. (2006). Local and nonlocal advection of a passive scalar. *Physics of Fluids*, 18(11):116601.
- Siegelman, L. (in pres). Energetic submesoscale dynamics in the ocean interior. *Journal of Physical Oceanography*.
- Siegelman, L., Klein, P., Rivière, P., Thompson, A. F., Torres, H. S., Flexas, M., and Menemenlis, D. (2019a). Enhanced upward heat transport at deep submesoscale ocean fronts. *Nature Geoscience*, pages 1–6.
- Siegelman, L., Klein, P., Torres, H. S., Thompson, A. F., and Menemenlis, D. (in prep). Local and non-local advection of erTEL potential vorticity from space. *Geophysical Research Letters*.
- Siegelman, L., Roquet, F., Mensah, V., Rivière, P., Pauthenet, E., Picard, B., and Guinet, C. (2019b). Correction and accuracy of high-and low-resolution ctd data from animal-borne instruments. *Journal of Atmospheric and Oceanic Technology*, 36(5):745–760.
- Smith, K. S. and Ferrari, R. (2009). The production and dissipation of compensated thermohaline variance by mesoscale stirring. *Journal of Physical Oceanography*, 39(10):2477–2501.
- Spall, S. and Richards, K. (2000). A numerical model of mesoscale frontal instabilities and plankton dynamics—i. model formulation and initial experiments. *Deep Sea Research Part I: Oceanographic Research Papers*, 47(7):1261–1301.
- Su, Z., Wang, J., Klein, P., Thompson, A. F., and Menemenlis, D. (2018). Ocean submesoscales as a key component of the global heat budget. *Nature communications*, 9(1):775.
- Taylor, S. and Straub, D. (2016). Forced near-inertial motion and dissipation of low-frequency kinetic energy in a wind-driven channel flow. *Journal of Physical Oceanography*, 46(1):79–93.
- Thomas, L. and Ferrari, R. (2008). Friction, frontogenesis, and the stratification of the surface mixed layer. *Journal of Physical Oceanography*, 38(11):2501–2518.

- Thomas, L. N. (2017). On the modifications of near-inertial waves at fronts: implications for energy transfer across scales. *Ocean Dynamics*, 67(10):1335–1350.
- Thomas, L. N., Tandon, A., and Mahadevan, A. (2008). Submesoscale processes and dynamics. *Ocean modeling in an Eddying Regime*, 177(1):17–38.
- Thomas, L. N., Taylor, J. R., Ferrari, R., and Joyce, T. M. (2013). Symmetric instability in the gulfstream. *Deep-Sea Research II*, 91:96–110.
- Thompson, A. F., Lazar, A., Buckingham, C., Naveira Garabato, A. C., Damerell, G. M., and Heywood, K. J. (2016). Open-ocean submesoscale motions: A full seasonal cycle of mixed layer instabilities from gliders. *Journal of Physical Oceanography*, 46(4):1285–1307.
- Torres, H., Klein, P., Siegelman, L., Qiu, B., Chen, S., Ubelman, C., Wang, J., Menemenlis, D., and Fu, L.-L. (2019). Diagnosing ocean-wave-turbulence interactions from space. *Geophysical Research Letters*.
- Torres, H. S., Klein, P., Menemenlis, D., Qiu, B., Su, Z., Wang, J., Chen, S., and Fu, L.-L. (2018). Open-ocean submesoscale motions: A full seasonal cycle of mixed layer instabilities from gliders. *Journal of geophysical research*, page doi.org/10.1029/2018JC014438.
- Treasure, A. M., Roquet, F., Ansoerge, I. J., Bester, M. N., Boehme, L., Bornemann, H., Charrassin, J.-B., Chevallier, D., Costa, D. P., Fedak, M. A., et al. (2017). Marine mammals exploring the oceans pole to pole: a review of the meop consortium. *Oceanography*, 30(2):132–138.
- Tulloch, R., Marshall, J., Hill, C., and Smith, K. S. (2011). Scales, growth rates, and spectral fluxes of baroclinic instability in the ocean. *Journal of Physical Oceanography*, 41(6):1057–1076.
- Tulloch, R. and Smith, K. S. (2009). A note on the numerical representation of surface dynamics in quasi-geostrophic turbulence: Application to the nonlinear eady model. *Journal of the Atmospheric Sciences*, 66(4):1063–1068.
- Ubelmann, C., Klein, P., and Fu, L. L. (2015). Dynamic interpolation of sea surface height and potential applications for future high-resolution altimetry mapping. *Journal of Atmospheric and Oceanic Technology*, 32(1):177–184.
- Vallis, G. K. (2017). *Atmospheric and oceanic fluid dynamics*. Cambridge University Press.
- Wagner, G. L. and Young, W. R. (2016). A three-component model for the coupled evolution of near-inertial waves, quasi-geostrophic flow and the near-inertial second harmonic. *Journal of Fluid Mechanics*, 802:806–837.
- Waugh, D. W. and Abraham, E. R. (2008). Stirring in the global surface ocean. *Geophysical Research Letters*, 35(20).
- Weiss, J. (1981). Report lji-tn-81-121. *La Jolla Inst., San Diego, CA*.
- Weiss, J. (1991). The dynamics of enstrophy transfer in two-dimensional hydrodynamics. *Physica D: Nonlinear Phenomena*, 48(2-3):273–294.
- Whitt, D. B. and Thomas, L. N. (2015). Resonant generation and energetics of wind-forced near-inertial motions in a geostrophic flow. *Journal of Physical Oceanography*, 45(1):181–208.
- Xie, J.-H. and Vanneste, J. (2015). A generalised-lagrangian-mean model of the interactions between near-inertial waves and mean flow. *Journal of Fluid Mechanics*, 774:143–169.
- Young, W. and Jelloul, M. B. (1997). Propagation of near-inertial oscillations through a geostrophic flow. *Journal of marine research*, 55(4):735–766.
- Yu, X., Naveira Garabato, A. C., Martin, A. P., Buckingham, C. E., Brannigan, L., and Su, Z. (2019). An annual cycle of submesoscale vertical flow and restratification in the upper ocean. *Journal of Physical Oceanography*, 49(6):1439–1461.
- Zaron, E. D. and Egbert, G. D. (2014). Time-variable refraction of the internal tide at the hawaiian ridge. *Journal of Physical Oceanography*, 44(2):538–557.

## A Ocean-scale interactions from space

Klein, P., Lapeyre, G., **Siegelman, L.**, Qiu, B., Fu, L.L., Torres, H.S., Su, Z., Menemenlis, D. and Le Gentil, S. (2019). Ocean-Scale Interactions From Space. *Earth and Space Science*, 6(5), pp.795-817.





## RESEARCH ARTICLE

10.1029/2018EA000492

## Ocean-Scale Interactions From Space

## Special Section:

Nonlinear Systems in Geophysics:  
Past Accomplishments and Future  
Challenges

## Key Points:

- Twenty-five years of satellite altimeter observations and recent numerical studies highlight that all the oceans are fully turbulent
- This turbulence involves energetic ocean-scale interactions over a broad range of scales, from 1 to 5,000 km
- These interactions control the ocean kinetic energy budget, heat storage, biodiversity, and air-sea exchanges

## Correspondence to:

P. Klein,  
patrice.klein@ifremer.fr

## Citation:

Klein, P., Lapeyre, G., Siegelman, L., Qiu, B., Fu, L.-L., Torres, H., et al. (2019). Ocean-scale interactions from space. *Earth and Space Science*, 6, 795–817. <https://doi.org/10.1029/2018ea000492>

Received 5 OCT 2018

Accepted 3 APR 2019

Accepted article online 10 APR 2019

Published online 22 MAY 2019

©2019. The Authors.

This is an open access article under the terms of the Creative Commons Attribution-NonCommercial-NoDerivs License, which permits use and distribution in any medium, provided the original work is properly cited, the use is non-commercial and no modifications or adaptations are made.

Patrice Klein<sup>1,2,3</sup> , Guillaume Lapeyre<sup>4</sup> , Lia Siegelman<sup>1,2,5</sup> , Bo Qiu<sup>6</sup> , Lee-Lueng Fu<sup>1</sup> , Hector Torres<sup>1</sup> , Zhan Su<sup>2</sup> , Dimitris Menemenlis<sup>1</sup> , and Sylvie Le Gentil<sup>3</sup><sup>1</sup>Jet Propulsion Laboratory (NASA), California Institute of Technology, Pasadena, CA, USA, <sup>2</sup>Department of Environmental Science and Engineering, California Institute of Technology, Pasadena, CA, USA, <sup>3</sup>LOPS-Ifremer/CNRS, Brest, France, <sup>4</sup>LMD/IPSL, CNES, ENS, PSLRU, Paris, France, <sup>5</sup>LEMAR/IUEM/CNRS, Brest, France, <sup>6</sup>Department of Oceanography, University of Hawai'i, Honolulu, HI, USA

**Abstract** Satellite observations of the last two decades have led to a major breakthrough emphasizing the existence of a strongly energetic mesoscale turbulent eddy field in all the oceans. This ocean mesoscale turbulence is characterized by cyclonic and anticyclonic eddies (with a 100- to 300-km size and depth scales of ~500–1,000 m) that capture approximately 80% of the total kinetic energy and is now known to significantly impact the large-scale ocean circulation, the ocean's carbon storage, the air-sea interactions, and therefore the Earth climate as a whole. However, ocean mesoscale turbulence revealed by satellite observations has properties that differ from those related to classical geostrophic turbulence theories. In the last decade, a large number of theoretical and numerical studies has pointed to submesoscale surface fronts (1–50 km), not resolved by satellite altimeters, as the key suspect explaining these discrepancies. Submesoscale surface fronts have been shown to impact mesoscale eddies and the large-scale ocean circulation in counterintuitive ways, leading in particular to up-gradient fluxes. The ocean engine is now known to involve energetic scale interactions, over a much broader range of scales than expected one decade ago, from 1 to 5,000 km. New space observations with higher spatial resolution are however needed to validate and improve these recent theoretical and numerical results.

## 1. Introduction

In 1992, a satellite with a high-precision altimeter, Topex/Poseidon (T/P, CNES/NASA), was launched in space to observe the sea surface height (SSH) in all oceans over a range of scales from 100 km to more than 5,000 km. SSH observations, a proxy of surface pressure, were used to retrieve oceanic surface motions using the geostrophic approximation (that assumes an equilibrium between Coriolis and pressure gradients forces). First analyses of T/P observations profoundly revolutionized the field of oceanography. They showed that General Ocean Circulation Models (OGCM) with low spatial resolution were strongly deficient in estimating the kinetic energy (KE) of oceanic motions (Fu & Smith, 1996; Stammer et al., 1996). Walter Munk, testifying before the U.S. Commission on Ocean Policy in April 2002, emphasized that T/P was “the most successful ocean experiment of all time”. In September 2018, over 300 ocean scientists attended a 5-day symposium in Ponta Delgada (Azores Archipelago) to celebrate 25 years of Progress in satellite radar altimetry. Ocean monitoring over more than two decades, using T/P and other satellite altimeters (Figure 1), has led to a major scientific breakthrough responsible of a paradigm shift: all the oceans are now known to be populated by numerous coherent eddies at mesoscale (100–300 km) as illustrated by Figure 2a. Altimeter observations further emphasize these eddies capture almost 80% of the total oceanic KE of the ocean (Chelton et al., 2011; Ferrari & Wunsch, 2009; Morrow & Le Traon, 2012; Wunsch, 2002, 2009). Although energetic eddies are present everywhere, they are intensified in hot spots associated with major oceanic currents such as the Gulf Stream, the Kuroshio Extension, and the Antarctic Circumpolar Current (see Figure 2b). This vision of a strongly turbulent ocean at mesoscale has been confirmed by recent numerical OGCMs performed with high resolution of a few kilometers (see Figure 3).

Due to the high vertical stratification of the open ocean and the Earth rotation, oceanic motions at scales larger than 100 km are geostrophic and quasi-horizontal (Vallis, 2017); that is, vertical motions at these scales are very weak. So it is not surprising that the ocean mesoscale turbulence (OMT) revealed by satellite altimeters was then expected to obey the properties of geostrophic turbulence (GT), described in many



**Figure 1.** Existing and future satellite altimeters (see <https://sealevel.jpl.nasa.gov/>).

theoretical and numerical studies starting with Charney (1971; see, e.g., Hua et al., 1998; Hua & Haidvogel, 1986; McWilliams, 1989; Rhines, 1975, 1979).

Because of the specific impacts of the rotation and vertical stratification, GT properties strongly differ from the classical 3-D turbulence properties (Tennekes & Lumley, 1974). A first difference is the existence in GT of an inverse KE cascade, driven by the nonlinear interactions between eddies, such that KE fluxes from the scales of eddy sources (mostly explained by baroclinic instability) toward larger scales (for which Rossby wave dispersion starts to dominate and nonlinear interactions weaken). Such inverse KE cascade is concomitant with the nonlinear merging between coherent eddies giving rise to larger ones (Vallis, 2017). As a consequence, the resulting eddy fluxes significantly increase the total KE and further strengthen large geostrophic eddies by making them more coherent with a longer life time and ultimately leading to the emergence of zonal jets when Rossby wave dispersion becomes significant (Panetta, 1993; Rhines, 1975). Such inverse KE cascade is not observed in 3-D turbulence that only experiences a direct KE cascade from KE sources to smaller scales and therefore to dissipation scales (Tennekes & Lumley, 1974). A second difference is the direct cascade of dynamically passive or active tracers toward small scales driven by geostrophic eddies (Lapeyre et al., 2001). Through the action of stretching and folding, geostrophic eddies generate long and thin filaments of tracers (as illustrated in the ocean by the chlorophyll or Ertel potential vorticity maps; see Figures 4a and 4b) that eventually mix with their surrounding environment (Ledwell et al., 1993; Pierrehumbert et al., 1994). Maps of Finite Size Lyapunov Exponents, or FSLE, are a usual index to materialize these stretching and folding processes (see Figure 4c). The associated mechanisms, called chaotic advection (Aref, 1984; Lapeyre, 2002), make mixing much more efficient than expected from the classical diffusion paradigm used in 3-D turbulence, by at least 2 to 3 orders of magnitude (Garrett, 1983).

Using the GT framework has been illuminating to understand how oceanic mesoscale eddies, observed by satellite, control the global meridional heat transport (Hausmann & Czaja, 2012) and how they shape the large-scale ocean circulation through the inverse KE cascade (Hurlburt & Hogan, 2000). The GT framework has also been used to understand how OMT drives the three-dimensional dispersion and mixing of

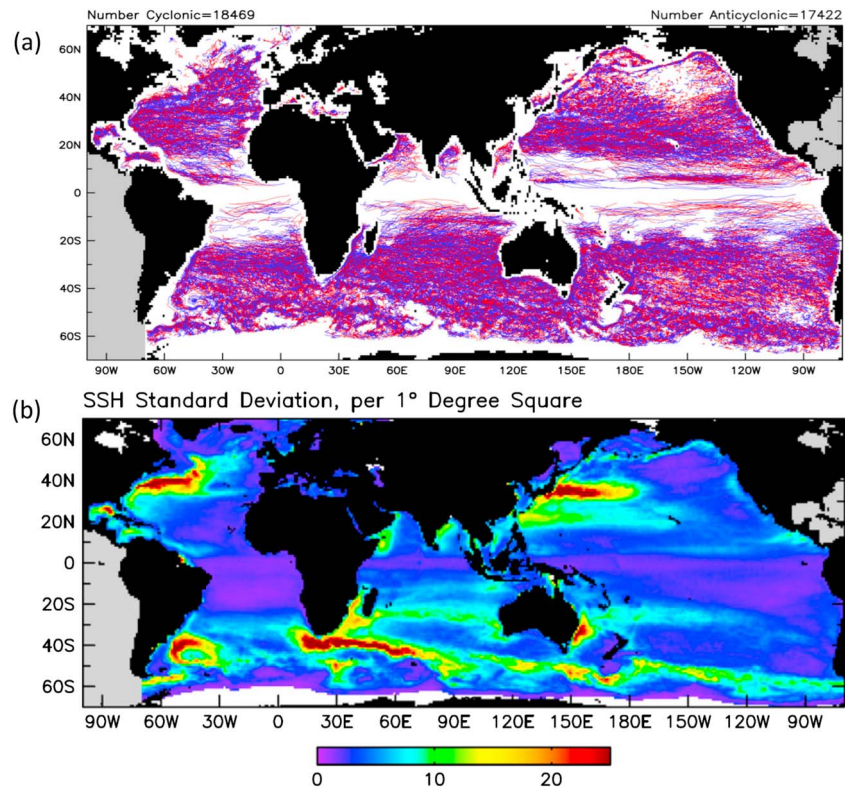


**Figure 2.** (a) Trajectories of cyclonic (blue lines) and anticyclonic (red lines) eddies (estimated from altimeter data) over the 16-year period, October 1992 to December 2008, for lifetimes >16 weeks (from Chelton et al., 2011). (b) Map of the standard deviation of eddy SSH amplitude (in centimeters; from Chelton et al., 2011, used with permission.) SSH = sea surface height.

tracers, such as nutrients and therefore the biological diversity and carbon storage (d’Ovidio et al., 2010; McGillicuddy Jr, 2016). Mezic et al. (2010) applied GT ideas to improve the forecast of pollutants dispersion using altimeter observations. They used these ideas for the forecast of the oil spill dispersion after the Deep Water Horizon accident in the Gulf of Mexico (see also Poje et al., 2014). Assimilation of satellite altimeter observations and in situ global data sets (such as the ARGO float dataset) in numerical models has led to the fast development of operational oceanography (Chassignet et al., 2018; Le Traon, 2013). Some assimilation techniques make use of the GT framework to better represent the OMT impacts on tracers. For example, Gaultier et al. (2012) proposed to assimilate the stretching (or strain) field (i.e., the second-order spatial derivatives of SSH) instead of simply assimilating SSH. These authors showed how this idea helped to much better predict the chlorophyll dispersion by mesoscale eddies.

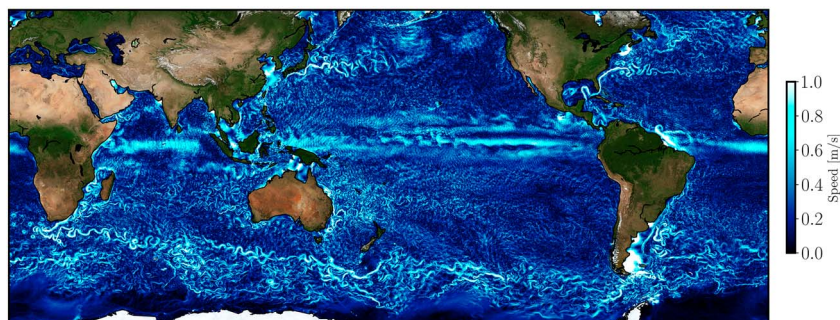


**Figure 3.** Instantaneous snapshot of the kinetic energy in the global ocean, from a global Estimating the Circulation and Climate of the Ocean (ECCO) numerical simulation ((1/48)<sup>o</sup> degree resolution in the horizontal and 90 vertical levels). (See <https://science.jpl.nasa.gov/projects/ECCO-ICES/>).

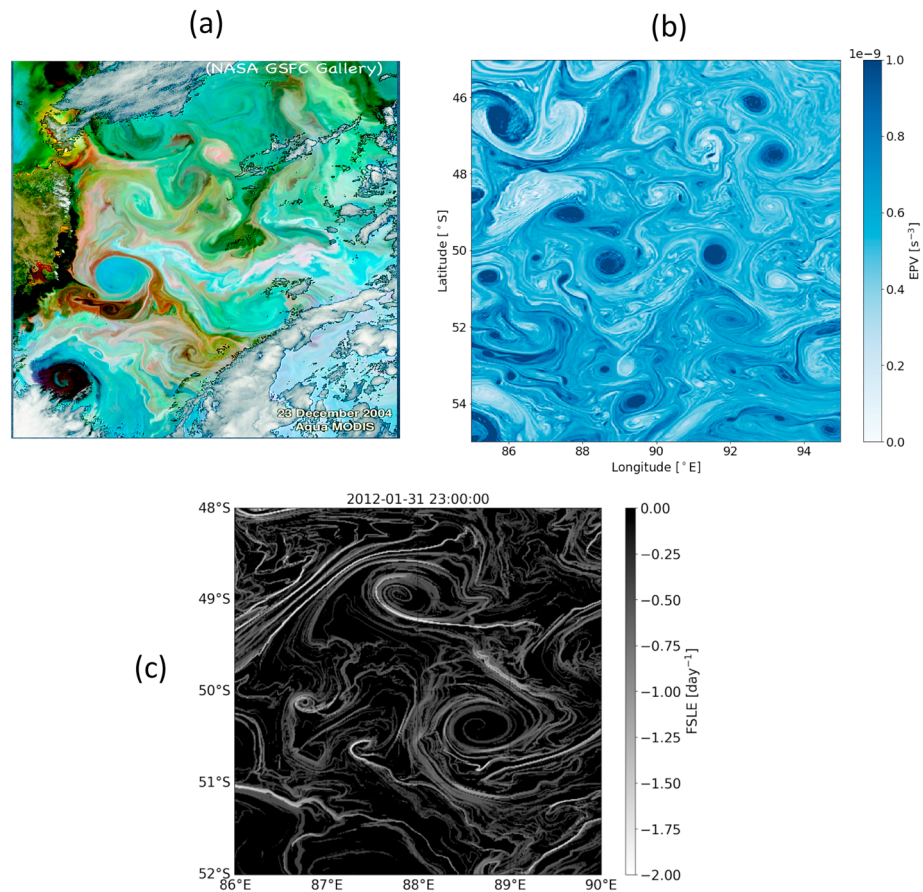


**Figure 4.** (a) Satellite image of the chlorophyll in the Southern Ocean (see <https://earthobservatory.nasa.gov/>). (b) Map of the Ertel potential vorticity in the Southern Ocean from the global ECCO numerical simulation (see above). Ertel potential vorticity is a dynamical active tracer conserved on a 3-D Lagrangian trajectory. (c) Map of the Finite Size Lyapunov Exponents (FSLE) in the Southern Ocean estimated using sea surface height from the global ECCO numerical simulation ((1/48)<sup>o</sup> resolution in the horizontal and 90 vertical levels; see <https://science.jpl.nasa.gov/projects/ECCO-1cES/>). FSLE are an index of the dispersion of tracers and particles by geophysical eddies (with a size of less than 100 km on this map; see more details about FSLE in d’Ovidio et al., 2010).

Still, some disconcerting discrepancies between OMT properties diagnosed from SSH observations and what is expected from GT theory are not fully understood (Morrow & Le Traon, 2012) as detailed in section 2. One of the key suspects, highlighted by numerical models with high spatial resolution, is the impact of smaller scales not resolved by existing satellite altimeters, in particular surface frontal structures with a 1- to 50-km width (called submesoscales in the present paper) for which the geostrophic approximation still works, but only at zero leading order. The numerous numerical and theoretical studies devoted to submesoscales and their interactions with mesoscale eddies of the past 15 years have led to startling discoveries discussed in section 3. One of them points to the extension of the inverse KE cascade to scales down to 30 km, that is, in a regime where frontal processes are beginning to take place. This suggests that the oceans are even less diabatic and more inertial than we thought; that is, fluxes of any quantities (including KE) are much less controlled by diffusivity or viscosity (which leads to irreversible downgradient fluxes) and more by nonlinear interactions that can lead to reversible up and downgradient fluxes. Mesoscale and submesoscale motions with scales down to 30 km should be observable by the forthcoming Surface Water and Ocean Topography (SWOT) altimeter mission (Fu & Ferrari, 2008) described in section 4. However, one challenge to meet to analyze these future observations is that balanced motions (BMs) with scales smaller than 100 km are entangled with another class of motions, the internal gravity waves (IGWs), as discussed in section 5.

The most recent results using numerical models with the highest spatial resolution allowed by available petascale computers (Chassignet & Xu, 2017, Lévy et al., 2010, Su et al., 2018, Torres et al., 2018; Figure 3) highlight that ocean-scale interactions, involving scales down to 1 km, affect the ocean dynamics in counter-

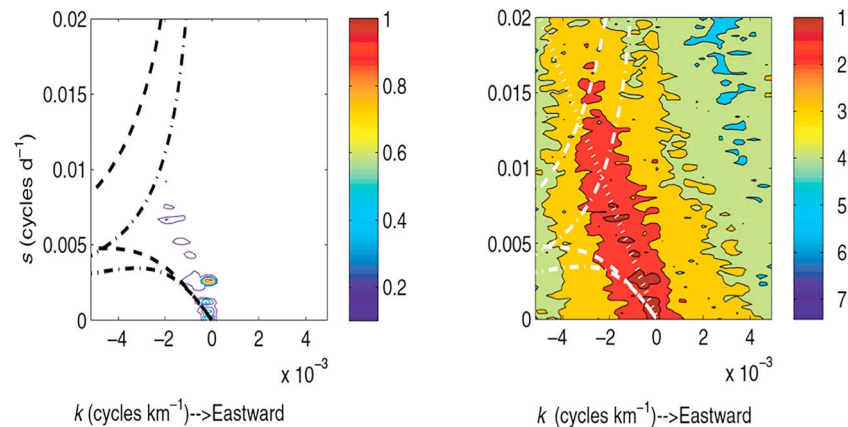


**Figure 5.** Frequency (cycle/day) and zonal wavenumber (cycles/km) spectrum of sea surface height variance estimated from altimeter data. (left) A two-dimensional spectrum plotted on a linear power scale, smoothed in frequency and zonal wavenumber. (right) The logarithm of the power. Dashed curves indicate the barotropic and first baroclinic mode dispersion curves of Rossby waves. Dash-dotted lines are the corresponding curves for the unit aspect ratio. The “nondispersive line” defined in the text lies along the ridge of maximum energy density and is closely approximated by the dotted white line (in the red area of the right panel) with a slope of 4 km/day (from Wunsch, 2009, 2010, © La Societe Canadienne de Meteorologie et d’Oceanographie, reprinted by permission of Taylor & Francis Ltd, www.tandfonline.com on behalf of La Societe Canadienne de Meteorologie et d’Oceanographie.).

intuitive ways, as illustrated by some examples in section 6. Submesoscale structures in one region not only impact ocean dynamics locally but also impact ocean dynamics in remote regions (Chassignet & Xu, 2017; Lévy et al., 2010). The implication is that understanding how the ocean engine works, over such a large range of scales, requires a numerical strategy involving large domains and employing the highest spatial resolution. However, as Carl Wunsch put it during the OSTST meeting in Lisbon in 2010: “Increased resolution in ocean models needs to be accompanied by higher resolution observations” on a global scale, which is presently a real challenge, as discussed in section 7. Such observations are indeed highly needed to question theories and models in order to improve our understanding of the ocean dynamics, which eventually will lead to new theories and models. The synergy of using observations from different satellite missions should help to better understand the dynamics involved in this broad range of scales, as discussed in section 7.

The purpose of this paper is not to provide a thorough and comprehensive review of the important contribution of satellite altimeters to the knowledge of the OMT but rather to point to the missing mechanisms that can potentially improve this knowledge. The paper mostly focuses on the upper ocean (from the surface down to ~1,000 m) in extra-equatorial latitudes. Equatorial dynamics are discussed in another paper in this issue (see Menesguen et al., 2019).

## 2. Ocean Mesoscale Turbulence and Theory of Geostrophic Turbulence

Present altimeter observations concern spatial scales (larger than 70–100 km) for which the associated motions are characterized by a Rossby number (defined as  $Ro \equiv U/fL$  with  $U$  and  $L$ , respectively, a velocity and length scales, and  $f$  the Coriolis frequency) smaller than 1. This means that these surface motions are either in geostrophic balance (i.e., a balance between Coriolis and horizontal pressure forces leading to  $-f\vec{k} \times U = -g\nabla SSH$ , with  $\vec{k}$  the vertical vector) or in gradient wind balance (a balance that, in addition, involves the nonlinear terms, i.e.,  $U \cdot \nabla U - f\vec{k} \times U = -g\nabla SSH$ ; Vallis, 2017).

BMs diagnosed from satellite altimeter observations now concur with the idea that the oceans are fully turbulent, involving strongly interacting mesoscale eddies and giving rise to significant energy transfers across scales. This turbulent character was revealed by one of the first  $\omega$ - $k$  spectrum (with  $\omega$  the frequency and  $k$  the horizontal wavenumber) of ocean variability estimated from SSH observations (Wunsch, 2009, 2010). As illustrated in Figure 5, the maximum of the SSH variance does not follow the dispersion relation curves associated with linear Rossby waves. Rather, it lies approximately along a “nondispersive” line,  $c.k + \omega = 0$  (with  $k < 0$ ), corresponding to an eddy propagation speed of  $c \approx 4.6$  cm/s (close to the values found independently by Fu, 2009). This finding highlights the strong nonlinear character of mesoscale eddies, confirmed later on by the study of Chelton et al. (2011). All these results point to the existence of an energetic OMT expected

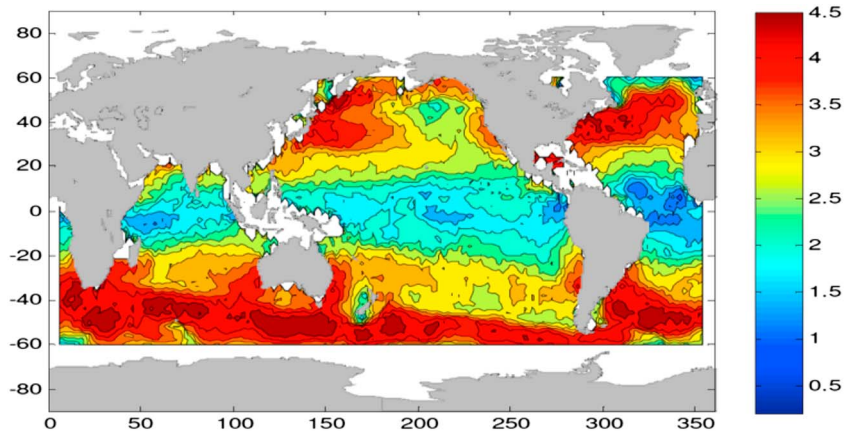


**Figure 6.** Global distribution of the spectral slopes ( $k^{-n}$ ) of sea surface height wavenumber spectrum in the wavelength band of 70–250 km estimated from the Jason-1 altimeter measurements. The color scale is related to values of  $n$  (from Xu & Fu, 2012, © American Meteorological Society. Used with permission.).

to share the GT properties described in Charney (1971), Hua and Haidvogel (1986), McWilliams (1989), and Hua et al. (1998). However, some intriguing discrepancies between OMT and GT properties quickly emerged. Let us comment on two of them.

The first one concerns the KE spectral slope estimated from satellite altimetry. Based on GT theory, the KE spectrum should scale in  $k^{-3}$  (Charney, 1971). However, KE spectra deduced from altimeter observations using the geostrophic balance do display a linear slope in log-log space in the scale range 100–300 km, but with a power law varying between  $k^{-2}$  and  $k^{-3}$ . This discrepancy, early noted by Fu (1983), was first attributed to altimeter noise. But more careful estimations, using a larger set of altimeter observations, by Le Traon et al. (2008), confirmed the  $k^{-2}$  slope. Such slope for the KE spectrum suggests that smaller eddies resolved by satellite altimeters are more energetic than predicted by GT. Xu and Fu (2012) recently highlighted an even more complex picture displaying a strong regional dependency of the SSH spectral slope (Figure 6). On one hand, in many high KE regions, the resulting KE spectral slopes vary between  $k^{-3}$  and  $k^{-2}$ . On the other hand, in low KE regions, such as in the eastern part of ocean basins, the spectral slope is even flatter than  $k^{-2}$ , which is unrealistic in terms of geostrophic motions (Xu & Fu, 2012). The consensus that presently emerges is that this diversity of spectral slopes is not due to altimeter noise but is due to physical mechanisms other than those involved in GT that vary seasonally and regionally (Dufau et al., 2016; Xu & Fu, 2012).

Another discrepancy concerns the KE fluxes or the inverse KE cascade. As mentioned before, GT theory suggests that mesoscale geostrophic eddies should experience an inverse KE cascade, with KE fluxing from the scales of eddy sources (50–100 km for the ocean) to the scales of the most energetic eddies ( $L_e \sim 250$ –300 km for oceanic mesoscale eddies; Charney, 1971; Hua & Haidvogel, 1986; Hua et al., 1998; McWilliams, 1989; Rhines, 1975. Studies by Smith, 2007 and Tulloch et al. 2011), using altimeter observations and in situ data, confirmed the factor 3 to 4 between the eddy source scales and scales of the most energetic eddies, suggesting an inverse KE cascade over a broad scale range. However, the first KE fluxes estimated from altimeter observations by Scott and Wang (2005) were not consistent with this picture. Rather, these authors found an inverse KE cascade over a narrower scale range, that is, starting only at wavelengths larger than 150 km, the smaller wavelengths (including the eddy source scales) experiencing a direct KE cascade (Figure 7a). Some studies, such as Arbic et al. (2012) and Arbic et al. (2013), questioned the contribution of smaller scales, unresolved by altimeter observations, for the transfer of energy between scales. Using an OGCM with a  $(1/32)^\circ$  spatial resolution, they showed that the scale range and magnitude of the inverse KE cascade are strongly sensitive to the resolution of small scales: when small scales are taken into account, the inverse KE cascade involves a much broader scale range involving smaller scales. Thus, KE at scales unresolved by satellite altimeters may contribute to KE fluxes that strengthen eddies resolved by altimetry through the inverse KE cascade. This contribution of unresolved scales seems to be in agreement with the  $\sim k^{-2}$  spectral slope previously mentioned and as further detailed in section 3. Note that, in terms of inverse KE cascade, Arbic et al. (2012) are the first authors to show that OMT experiences an inverse KE cascade in frequency as well.

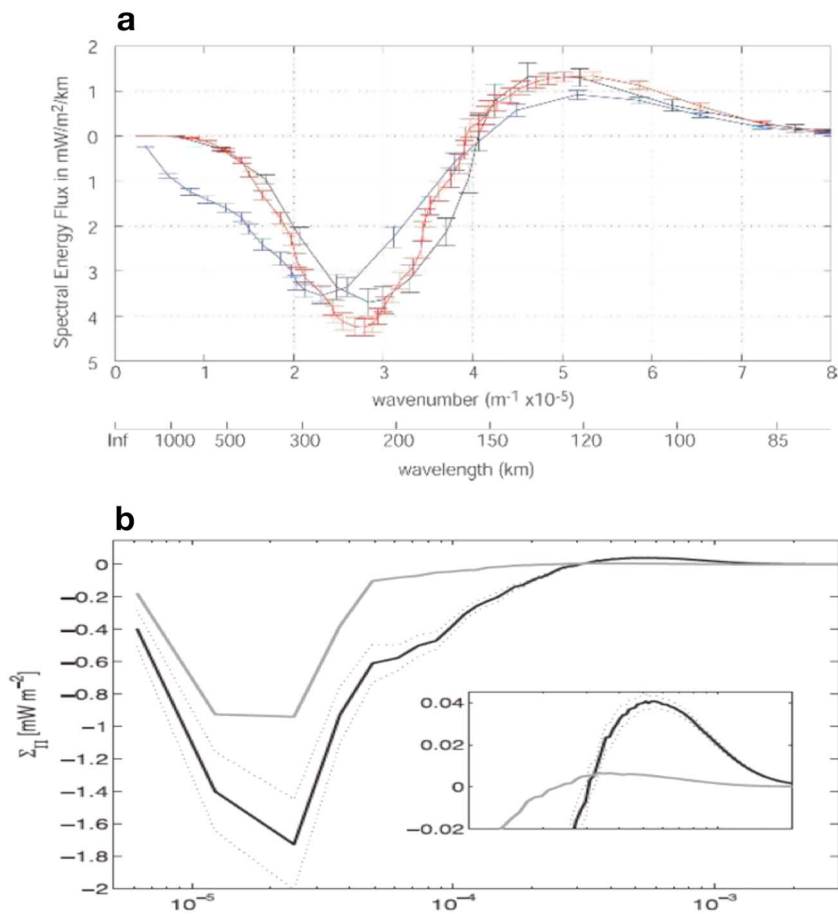


**Figure 7.** (a) Spectral kinetic energy flux versus total wavenumber estimated from altimeter data. Black curve using sea surface height on a  $32 \times 32$  grid, red curve using sea surface height on a  $64 \times 64$  grid, blue curve using velocity on a  $64 \times 64$  grid. Positive slope reveals a source of energy. The larger negative lobe reveals a net inverse cascade to lower wavenumber. Error bars represent standard error. (From Scott & Wang, 2005, © American Meteorological Society. Used with permission.) (b) Spectral kinetic energy flux (from numerical simulations) integrated over the upper 200 m for a flow forced by the Charney instability (and therefore involving submesoscale frontal structures; solid black) and a flow forced by Phillips instability (and therefore with no submesoscale structure; solid gray). Uncertainty is represented as dotted lines based on the assumption that the 360-day run corresponds to 12 independent realizations. In the inset, the vertical axis is zoomed in the range of large wavenumbers to better emphasize the forward cascade. (from Capet et al., 2016, © American Meteorological Society. Used with permission.) Similar results are found in Sasaki et al. (2014).

For larger scales, OMT properties appear to match GT properties. One example concerns the arrest of the inverse KE cascade which leads, from GT, to the emergence of alternating zonal jets with a width close to the Rhines scale, that is, the scale at which the Rossby wave dispersion starts to dominate and the nonlinear interactions weaken (Hua & Haidvogel, 1986; Panetta, 1993; Rhines, 1975; Vallis, 2017). Maximenko et al. (2005, 2008) tested their existence using satellite altimeter observations averaged over more than 10 years (which filters out mesoscale eddies). Results reveal the presence of multiple zonal jets, with an east-west velocity direction alternating with latitude, in many parts of the world oceans (Maximenko et al., 2005, 2008). At midlatitudes, jets have often a meridional wavelength close to or larger than 300 km, that is, close to the Rhines scale.

The second example concerns the vertical eddy scale. The combination of SSH and moorings observations (Wunsch, 2009, 2010; Wortham & Wunsch, 2014) shows that roughly 40% of the KE at mesoscale is barotropic in nature, with about another 40% lying in the first baroclinic mode. Since the buoyancy frequency,  $N(z)$ , in the ocean is surface intensified, the KE contribution of the first baroclinic mode is also intensified there, leading to the conclusion that KE inferred from altimeter observations is primarily (but not wholly) in the first baroclinic mode (Hua et al., 1985; Wunsch, 2010). In other words, KE at mesoscale concentrates in the first 500–1,000 m below the surface in agreement with the GT theory and numerical studies

of Fu and Flierl (1980), Hua and Haidvogel (1986), and Smith and Vallis (2001). As found by these studies, the energy is rapidly transferred from high to lower baroclinic modes, leading to an inverse KE cascade that is not only 2-D but also 3-D in space.

As a summary, altimeter observations reveal that OMT shares some similarities with GT but also point to some discrepancies. Present studies indicate that many of these discrepancies, in particular in high KE regions, are likely explained by the missing contribution of unresolved small scales of BMs that concern submesoscale density fronts at the ocean surface as discussed in section 3. On the other hand, discrepancies in low KE regions seem to be due to the contribution of IGWs, as discussed in section 5.

### 3. Ocean Mesoscale/Submesoscale Turbulence: A New Paradigm Involving Submesoscale Fronts

It has been acknowledged for a long time that the formation and development of atmospheric storms (the equivalent of ocean mesoscale eddies) can only be understood by taking into account density fronts with smaller scales at the troposphere's boundaries (i.e., the Earth surface and the tropopause). The turbulence associated with this boundary frontal dynamics (Hoskins, 1976) was first studied by Blumen (1978) who developed a surface quasi-geostrophic (SQG) theory. SQG theory assumes zero potential vorticity in the fluid interior with the flow being driven by the time evolution of density at the boundaries, leading to intense fronts at scales smaller than the Rossby radius of deformation (Held et al., 1995). SQG turbulence was used to explain the dynamics of the atmospheric tropopause by Juckes (1994) and Hakim et al. (2002).

The impact of surface density fronts at submesoscale on the OMT started to be questioned only in the early 2000s. Subsequent studies were based on the theoretical results obtained for the atmosphere and in particular on the SQG theory. Although it has obvious limitations and shortcomings, such as an underprediction of the amplitude of subsurface velocities (see LaCasce, 2012 for example), SQG dynamics coupled with GT à la Charney (Tulloch & Smith, 2006) has been a helpful dynamical framework to understand the interactions between submesoscale dynamics and mesoscale eddies. But later studies have revealed a more complex picture as detailed below.

#### 3.1. Surface Frontal Dynamics

Within the oceanic context, early 2000s numerical models (Lévy et al., 2001) that resolved scales down to 10 km pointed to an appealing property of surface density fronts at submesoscales. These fronts are intimately associated with large vertical velocities extending from surface down to a depth of at least 300–500 m, with values much larger than those reported for 3-D GT but close to those reported for SQG turbulence (Klein & Lapeyre, 2009). Two other properties of SQG turbulence that address the discrepancies mentioned before, led to studies focused on near-surface fronts at submesoscales and their interactions with mesoscale eddies using the SQG paradigm (starting in 2006 with LaCasce and Mahadevan (2006), Lapeyre and Klein (2006) and Lapeyre et al. (2006)): the first property is the  $k^{-5/3}$  KE spectrum of SQG turbulence (Blumen, 1978; Held et al., 1995), instead of a  $k^{-3}$  spectrum for 3-D GT or 2-D turbulence. The second property is that an SQG flow experiences an inverse KE cascade (Capet et al., 2008), starting at submesoscale, indicating that submesoscale fronts may energize larger scales.

Later on, a large number of studies quickly revealed that the production of oceanic submesoscale fronts and their interactions with mesoscale eddies may result from mechanisms different from SQG. Thus, Boccaletti et al. (2007) and Fox-Kemper et al. (2008), among others, revisited previous results from Stone (1966) who described baroclinic instabilities within atmospheric boundary layers. They showed that similar instabilities occur within the oceanic surface mixed layer during winter when it is deep. These mixed-layer instabilities lead to the production of numerous intensified submesoscale fronts during this period. Seasonality of submesoscale fronts has been confirmed by in situ observations in the North Atlantic (Callies et al., 2015; Thompson et al., 2016; see Figure 8a) and further detailed by several oceanic numerical models at a basin scale (Chassignet & Xu, 2017; Mensa et al., 2013; Qiu et al., 2014; Rocha, Gille, et al., 2016; Sasaki et al., 2014 and also, J. Le Sommer, personal communication, June, 2018). Klein et al. (2008), Roulet et al. (2012), Qiu et al. (2014), and Capet et al. (2016) pointed to another mechanism, a coupled surface/interior baroclinic instability (the so-called Charney, 1947, instability), able to produce submesoscale fronts near the surface (a mechanism also emphasized by Tulloch et al., 2011). Recently, Barkan et al. (2017) further discussed how the high-frequency part of the wind forcing can also trigger frontal instabilities at submesoscale.



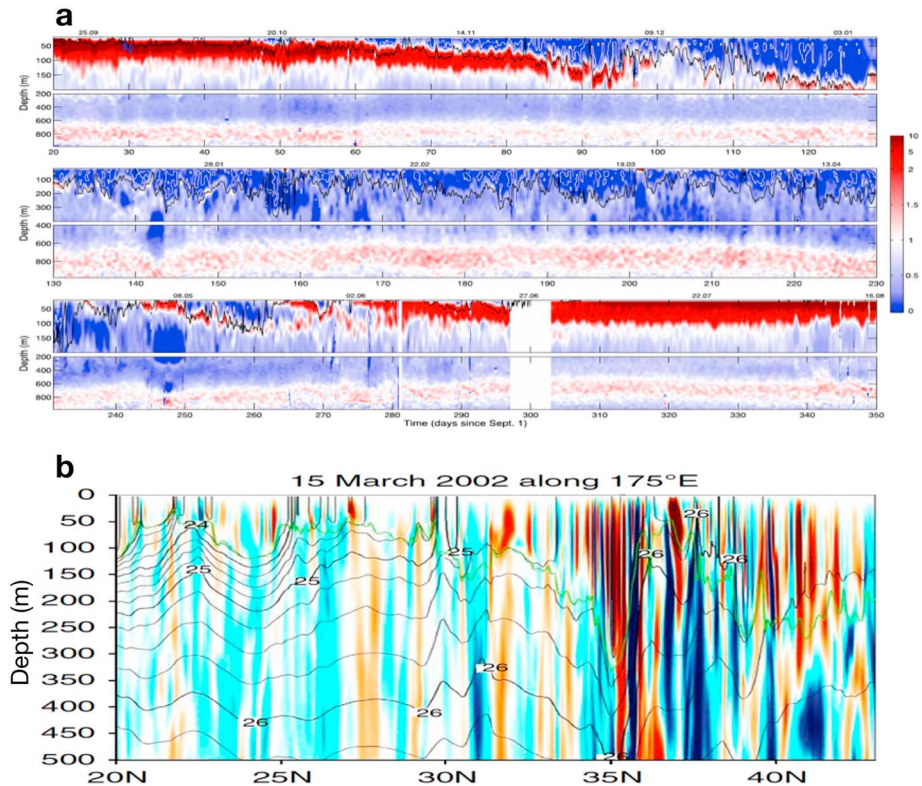


**Figure 8.** (a) Yearlong time series of Ertel potential vorticity ( $10^{-9} \text{ s}^{-3}$ ), calculated from glider data in the Northeastern Atlantic ocean. The time series is divided into (top) fall, (middle) winter, and (bottom) spring-summer periods; calendar dates (dd.mm) are provided along the top of the panels. The black contour is the mixed layer depth. (from Thompson et al., 2016, © American Meteorological Society. Used with permission.) (b) Meridional section of vertical velocity in the Northwestern Pacific (from a numerical simulation): vertical velocity (color, m/day), potential density (black contour), and Mixed-Layer Depth (MLD) (green line). (from Sasaki et al., 2014).

In most of these studies, the driving mechanism for the production of submesoscale fronts is the action of the geostrophic strain on the surface buoyancy gradients which leads to intensified horizontal fronts and strong vertical motions. It turns out that these fronts, whatever mechanisms that produce them, have properties close to SQG turbulence, such as a tight relation between buoyancy and relative vorticity (see Figure 7 of Klein et al., 2008) and an  $\sim k^{-2}$  (i.e., close to  $k^{-5/3}$ ) KE spectrum slope associated with an inverse KE cascade starting at submesoscales. Some extensive reviews have been recently dedicated to surface frontal dynamics at submesoscale in the oceans such as those by McWilliams (2016) and Lapeyre (2017).

### 3.2. Coupling Between Surface Frontal Turbulence and OMT: A New Energy Route Involving Submesoscales

Whereas mesoscale eddies capture most of the horizontal motions (horizontal KE), submesoscale fronts are now known to capture most of the vertical velocity field (vertical KE) in the upper ocean, that is, in the first 500–1,000 m below the surface (Klein et al., 2008; McWilliams, 2016; Thompson et al., 2016; see also Figure 8b). This important property, that can be demonstrated using SQG and QG arguments (see Figure 10 in Klein & Lapeyre, 2009), has been confirmed by several numerical models at a basin or global scale (Sasaki et al., 2014; Su et al., 2018; see Figure 8b). As Ferrari (2011) puts it “these small-scale surface fronts are the equivalents of the thin ducts in the lung called aveoli that facilitate the rapid exchange of gases when breathing.” Near-surface submesoscale fronts are now thought to be the preferential path of heat, nutrient, and other gas exchanges between the ocean interior and surface. In addition, vertical velocity associated with submesoscale fronts impacts the energy route. Indeed, vertical fluxes of buoyancy (or density) driven by submesoscale frontogenesis near the ocean surface correspond to a transformation of potential energy (PE) into KE that scales as  $\overline{w\rho} \propto |\nabla\rho|^2$  with  $w$  the vertical velocity and  $\rho$  the density (see Capet et al., 2008; Fox-Kemper et al., 2008; Lapeyre et al., 2006 for this scaling). Since the density spectrum near the surface has a  $k^{-2}$  slope (Fox-Kemper et al., 2008; Sasaki et al., 2014), and therefore  $\nabla\rho$  has a flat spectrum, this means

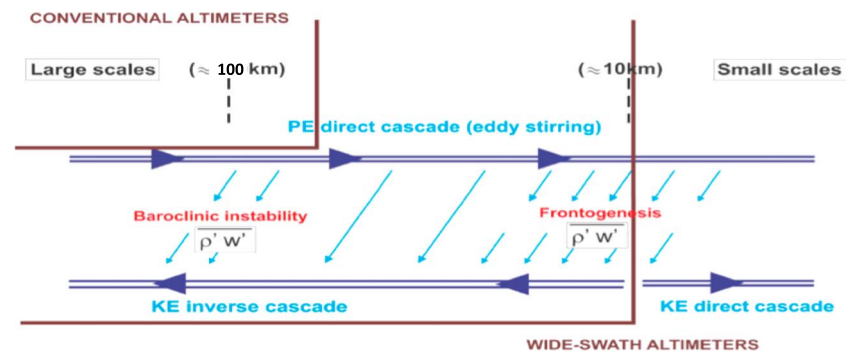


**Figure 9.** Schematic of the energy route involving mesoscales and submesoscales. PE is known to experience a direct cascade from large to small scales because of the eddy stirring (see upper line). The new energy pathway involving submesoscales includes a transformation of PE into KE at fine scale ( $\sim 10\text{--}20$  km) due to frontogenesis and an inverse KE cascade over a wide spectral range (see lower line). Conventional satellite altimeters only capture the classical energy pathway involving interior baroclinic instability at mesoscale (down to 100 km). Future wide-swath altimeters, such as Surface Water and Ocean Topography, should capture the energy pathway involving finer scales (down to  $\sim 10\text{--}20$  km). PE = potential energy; KE = kinetic energy.

that  $\overline{w\rho}$  is captured by the smallest scales (Klein & Lapeyre, 2009). In terms of energy exchanges, the picture that emerges is a tight interaction between oceanic mesoscale eddies and submesoscale motions that lead to more energetic mesoscale eddies. Indeed, as sketched in Figure 9 (upper part), mesoscale eddies stir and stretch the surface density field leading to the production of surface density anomalies at smaller and smaller scales (a process called direct PE cascade) and therefore to the production of fronts at submesoscale. These submesoscale fronts give rise to vertical fluxes of density, and therefore to a transformation of PE into KE at submesoscale. A large part of this KE at submesoscale is then transferred to mesoscale eddies through the inverse KE cascade (Capet et al., 2016; see Figure 7b and lower part of Figure 9).

The energy route involving submesoscale density fronts can be coupled with the energy route à la Salmon (Salmon, 1980), that is, the one associated with GT involving a transformation of PE into KE at the Rossby radius of deformation (i.e., at mesoscale) through baroclinic instability, as sketched in Figure 9. Such coupling has been proposed by several studies (Callies et al., 2016; Tulloch & Smith, 2006). The resulting energy route and the associated ocean-scale interactions now include a much broader range of scales (Figure 9) with the inverse KE cascade now starting at submesoscales, as shown by Capet et al. (2016; Figure 7b). This inverse KE cascade over a broad scale range reconciles with the findings of Smith (2007) and Tulloch et al. (2011) and is also consistent with the results from Arbic et al. (2013) mentioned before. As sketched in Figure 9, future wide-swath satellite altimeters (such as SWOT; see section 4) should resolve not only the eddy generation scales but also a large part of submesoscales and therefore this inverse KE cascade.

The inverse KE cascade over such a broad scale range has been questioned when the strong ageostrophic character of submesoscale fronts is taken into account (see Molemaker et al., 2010 for a discussion). So far, most numerical models at a basin or a global scale, using primitive equations with resolution up to 1–3 km (Capet et al., 2016; Mensa et al., 2013; Qiu et al., 2014; Rocha, Chereskin, et al., 2016; Rocha, Gille, et al., 2016; Sasaki et al., 2014; Su et al., 2018), take into account this ageostrophic character. They point to a transition scale, between the inverse and the direct KE cascade, close to 20–30 km in terms of wavelength depending on the season and the oceanic region (see again Figure 7b). Many of these studies further show how energetic submesoscale fronts in winter can impact the mesoscale eddy field in spring and summer because of the time lag associated with the inverse KE cascade (see Qiu et al., 2014; Sasaki et al., 2014). Thus, mixed-layer instabilities at submesoscale in winter appear to provide an explanation of the puzzling seasonality of mesoscale KE (displaying a KE peak in spring/summer) observed in altimeter observations (Sasaki et al., 2014; Zhai et al., 2008). Numerical models also reveal a significant seasonality of the velocity wavenumber spectrum, displaying a  $k^{-2}$  slope in winter and  $k^{-3}$  slope in summer. These results are consistent with the in situ data analysis of Callies et al. (2015) in the Gulf Stream region, of Qiu et al. (2017) in the Western Pacific, and with the results from Xu and Fu (2012) and Dufau et al. (2016) based on a reanalysis of conventional altimeter observations.

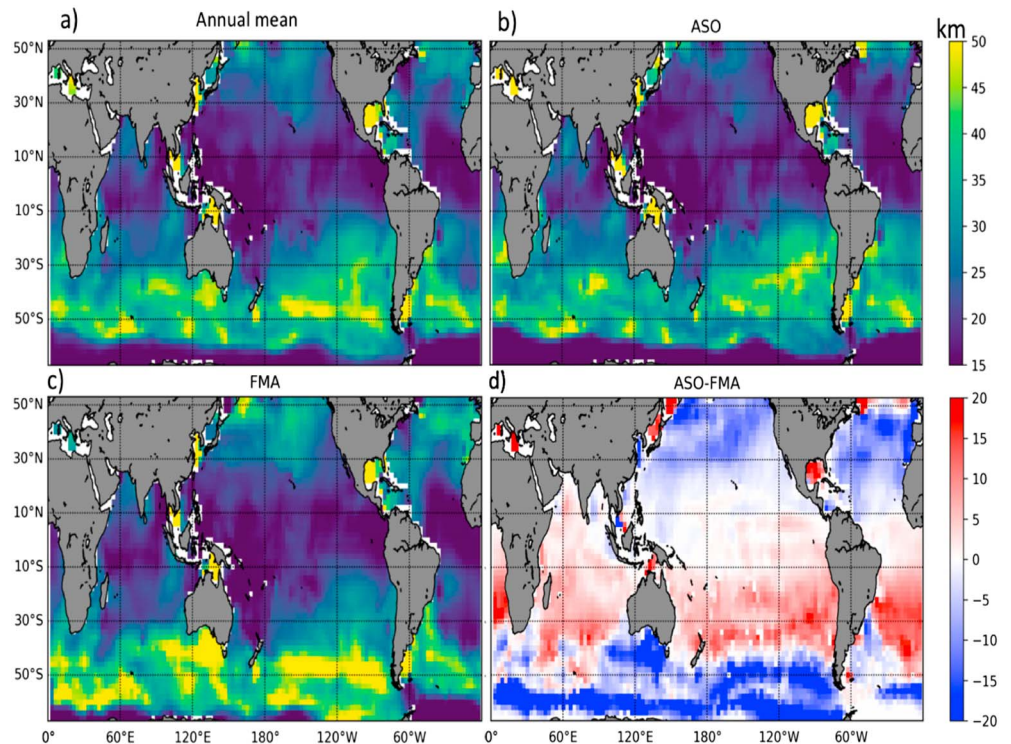


**Figure 10.** The minimum wavelengths (km),  $L_s$ , expected to be resolved by Surface Water and Ocean Topography (a), in ASO (b), and in FMA (c). The seasonal change (ASO-FMA) is shown in panel (d). These wavelengths have been estimated using a numerical simulation (from Wang et al., 2019, © American Meteorological Society. Used with permission.) ASO = August-September-October; FMA = February-March-April.

#### 4. Observational Challenges Using Future Satellite Altimetry (SWOT)

The theoretical and numerical results, of the last decade, on submesoscale BMs and their impacts on mesoscale eddies, need to be confronted and confirmed by observations. Since these results emphasize a strong regionality and seasonality, observations have to be global in space and continuous in time over several years. Only satellite altimetry can achieve this goal. Existing conventional radar altimetry has, however, two limitations. First, the instrument noise exceeds signal strength at wavelengths shorter than 50–70 km. Second, only one-dimensional SSH is profiled along the satellite ground tracks. To advance the observational capability, and in particular to capture a broader scale range of BMs, a wide-swath altimeter mission, SWOT, has been designed to observe SSH with a higher spatial resolution and in two dimensions (Fu & Ferrari, 2008). This is possible using the radar interferometry technique (Fu & Uebelmann, 2014; Rodríguez et al., 2018). The SWOT resolution is expected to be about 15 km over 68% of the ocean, assuming 2-m significant wave height, along a swath with a  $\sim 120$  km width (see <https://swot.jpl.nasa.gov/mission.htm>).

However, before diagnosing BMs at scales smaller than 50–70 km using SWOT observations, several challenges have to be met. First, the measurement noise increases with significant height of surface waves and this noise is known to be seasonally and geographically dependent. Second, at wavelengths shorter than  $\sim 100$  km, the SSH signals of internal tides and IGWs may become comparable to those of submesoscale BMs. This entanglement of the balanced and wave motions is discussed in more details in the next section. It leads to a complicated spatial and temporal variability of the scales of BMs resolvable by SWOT (Qiu et al., 2018). Using an OGCM with a high spatial resolution (similar to the one leading to Figure 3), Wang et al. (2019) studied the scales expected to be resolved by SWOT after taking into account the noise issues. Shown in Figure 10 are global maps of the minimum wavelengths,  $L_s$ , possibly resolvable by SWOT. In the tropics, the measurement noise is generally the lowest owing to the small height of surface waves, leading to the highest resolution ( $L_s < 20$  km), which is also attributable to the shallow spectral slope of the SSH (Xu & Fu, 2012). In regions of the Southern Ocean with moderate mesoscale KE, the measurement noise is the worst owing to the large height of surface waves, which leads to the poorest resolution ( $L_s \sim 40$ –50 km).

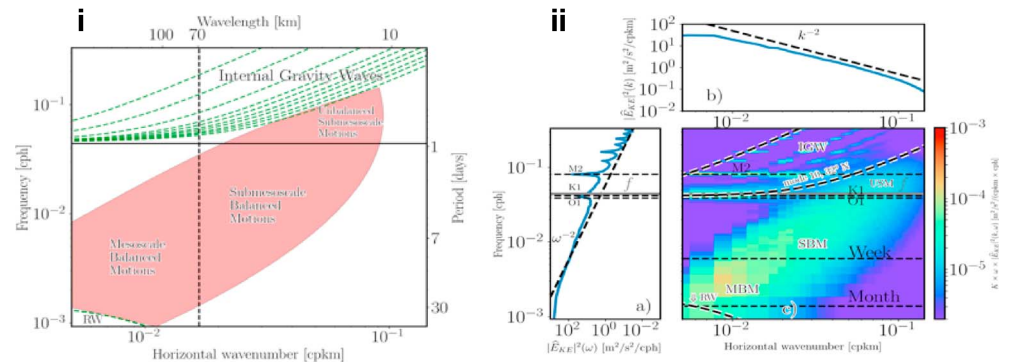


**Figure 11.** (From Torres et al., 2018). (i) Schematic spectrum displaying the multiple dynamical regimes: Mesoscale Balanced Motions (MBM), Submesoscale Balanced Motions (SBMs), “Unbalanced Submesoscale Motions” (USMs) and IGWs. Additionally, the scheme shows the linear dispersion relations of the first 10 baroclinic modes for IGWs (in green, upper part) and of baroclinic mode one for Rossby waves (in green, lower left corner). (ii) Frequency-wavenumber spectra of KE ( $EKE [m^2/s^2/(cpkm \times cph)]$ ) corresponding to the Kuroshio-Extension region, in winter. The spectrum, estimated from a numerical simulation, is multiplied by  $k$  and  $\omega$ . (ii) (a) Frequency spectra. (b) Wavenumber spectra. (c) Frequency-wavenumber spectra (from Torres et al., 2018). Three horizontal bands with frequencies close to tidal (semidiurnal and diurnal) and inertial frequencies span a larger range in the small scales band. Integrating this  $\omega - k$  spectrum over the  $k$  range or  $\omega$  range leads to the frequency spectrum (a) or the wavenumber spectrum (b), respectively.

However, in other regions of the Southern Ocean with strong mesoscale and submesoscale eddies, such as downstream the Kerguelen Plateau, the resolution is much better ( $L_s < 30$  km). As shown in Figure 10d, during the winter seasons, the resolution is generally poorer than summer north of  $40^\circ S$  because of the effects of surface waves. The situation south of  $40^\circ S$  is different. During winter, the mesoscale energy is so high that the signal strength overcomes the increased noise, leading to higher resolution than summer.

In addition to the variability of the spatial resolution, the temporal sampling of SWOT is also challenging. Owing to the 120-km swath, it will take 21 days to map the world oceans, with the number of repeat observations varying from two in the tropics to six at latitudes of  $60^\circ$ . Given the short time scales of the ocean variability at small scales, this temporal sampling poses another challenge to reconstruct coherent patterns of SSH over time. To meet this challenge, it is desirable to make use of high-resolution assimilative models guided by geophysical fluid dynamics argument (Ubelmann et al., 2015) and also by an a priori knowledge of the relative contribution of BMs and IGWs (see Qiu et al., 2018; Torres et al., 2018). These last two studies should help analyze the regionality and seasonality of observations at submesoscales. Given the global high-resolution measurements of SSH signals down to  $O(15$  km), the SWOT mission should provide us with unprecedented information about the evolution of small-mesoscale and submesoscale features and the possibility to reconstruct the upper ocean circulation such as relative vorticity and vertical velocity associated with BMs (Klein et al., 2009; Qiu et al., 2016). By disentangling the SSH signals of BMs versus IGWs (see section 5 below), the SWOT-measured SSH data may also allow us to potentially explore interactions between the balanced and unbalanced motions.

### 5. BMs and IGWs

As mentioned before, ocean currents with scales equal to or less than 300 km involve not only BMs but also IGWs whose properties significantly differ from BMs. IGWs include wind-forced near-inertial waves, with frequencies close to  $f$  and coherent internal tides with diurnal and semidiurnal frequencies (Alford et al., 2016; Müller et al., 2015). IGWs also include a continuum of motions with frequencies higher than  $f$  and spatial scales smaller than 100 km (see Figures 11i and 11ii). IGWs, unlike BMs, are characterized by a fast propagation and are mostly driven by weakly nonlinear interactions (Müller et al., 2015), with almost zero potential vorticity (see Alford et al., 2016 for a review). These characteristics explain why, contrary to BMs, IGWs have almost no direct impact on vertical and horizontal advective fluxes of any quantity. On the other hand, IGWs are known to drive a large part of the ocean mixing through a direct KE cascade toward the smallest scales (Polzin & Lvov, 2011). As a consequence, they trigger irreversible diffusive fluxes and

therefore represent an important pathway for the route to dissipation of KE. However, studies of the last 3 years emphasize that characteristics of this pathway depend on how BMs and IGWs interact.

### 5.1. Ocean-Scale Interactions Involving BMs and IGWs

Although BMs and IGWs occupy distinct regions in the spectral space (see Figure 11), they do interact (Chereskin et al., 2019). Since Kunze (1985), many studies have revealed that IGW propagation is polarized by the sign of the relative vorticity and the sign of the stratification anomaly (or stretching) of mesoscale eddies (Danioux et al., 2011; Dunphy et al., 2017; Grisouard & Thomas, 2015; Joyce et al., 2013; Kunze, 1985; Young & Jelloul, 1997; Ponte & Klein, 2015; Thomas, 2017; Whitt & Thomas, 2015; Zaron & Egbert, 2014). As a result, these waves may become trapped within anticyclonic eddies and expelled from cyclonic ones with their frequencies and wavenumbers significantly increasing during this process (see Whitt & Thomas, 2015 for a short review). In other words, the scenario that emerges is that the scattering and dispersive impacts of BMs on IGWs may ultimately lead to intensified mixing in anticyclonic structures and reduced mixing in cyclonic ones which, in turn, modifies the OMT properties (Klein et al., 2003).

Besides driving localized mixing, more recent studies suggest that the interactions between IGWs and BMs may stimulate submesoscale fronts and their associated vertical velocity field (Barkan et al., 2017; Rocha et al., 2018; Taylor & Straub, 2016; Thomas, 2017; Wagner & Young, 2016; Xie & Vanneste, 2015). Thus, IGWs caught up in a balanced strain field may experience considerable modifications to their propagation direction and speed, leading to nonzero momentum and buoyancy fluxes associated with these waves (Thomas, 2017). These fluxes represent an energy transfer from mesoscale KE to the wave PE, this energy being subsequently transferred to submesoscale fronts with high frequencies. Such mechanism, also called stimulated imbalance, leads to increase the vertical velocity field associated with submesoscale fronts and therefore the vertical advective fluxes of any quantities (Barkan et al., 2017; Rocha et al., 2018; Thomas, 2017). These energy transfers are still not well understood, and whether they can explain the energy observed in the region of “unbalanced motions” displayed in Figure 11, panel i, is unclear. Their confirmation by future studies will indicate whether high-frequency IGWs can lead, in addition to irreversible mixing, to a substantial increase of vertical advective fluxes of any quantity (Su et al., 2018).

In summary, understanding the interactions between BMs and IGWs, and the consequences on ocean mixing, is still in its infancy but is progressing quickly. Results obtained so far on this topic have been mostly obtained from numerical models. They need to be confirmed or infirmed by observations. As a preliminary, the question is how to partition motions into BMs and IGWs in the global ocean from observations.

### 5.2. Partition of Motions Into BMs and IGWs in the Global Ocean

BMs can be diagnosed from SSH for scales down to at least 100 km. Coherent tidal motions have an impact on SSH at specific wavenumbers. These tidal peaks explain the shallow SSH spectrum slope (much shallower than  $k^{-4}$ ) found by Xu and Fu (2012) in low KE regions (Richman et al., 2012; Savage et al., 2017a; J. Callies, personal communication, November, 2018). Tidal motions can be retrieved from long time series of SSH observations (that filter out mesoscale eddies; Egbert et al., 1994; Ray & Mitchum, 1997; Ray & Zaron, 2016; Stammer et al., 2014). Near-inertial waves have no impact on SSH (Gill et al., 1974) but can be retrieved from surface drifters (Lumpkin & Elipot, 2010). Diagnosing the IGW continuum with higher frequencies and higher wavenumbers (scales smaller than 100 km) from observations is still a challenge because of the strong entanglement of BMs and IGWs at these scales. Recent studies indicate this challenge may be partially met using satellite observations.

Using OGCMs with tides, several studies in the last 3 years have documented the spatial distribution of BMs and IGWs in the world ocean (Rocha, Gille, et al., 2016; Savage et al., 2017a, 2017b; see Figures 11 to 16 in 2017b). Qiu et al. (2018) and Torres et al. (2018) have further analyzed when and where IGWs with scales smaller than 100 km have a dominant imprint on the surface fields observable from space. One important property exploited by Qiu et al. (2018) and Torres et al. (2018; see also Savage et al., 2017a; Savage et al., 2017b) is that IGWs and BMs occupy two distinct regions in the  $\omega$ - $k$  spectral space, separated by the dispersion relation curve for the highest baroclinic mode of IGWs (see the schematic in Figure 11, panel i). The region above this curve (that includes frequencies equal to or higher than  $f$ ) is associated with IGWs and exhibits discrete bands aligned with the linear dispersion relation of the different baroclinic modes, suggesting weakly nonlinear interactions (see Figure 11, panel ii; Rocha, Chereskin, et al., 2016; Savage et al., 2017a; Torres et al., 2018). On the other hand, the region below the highest baroclinic mode is associated

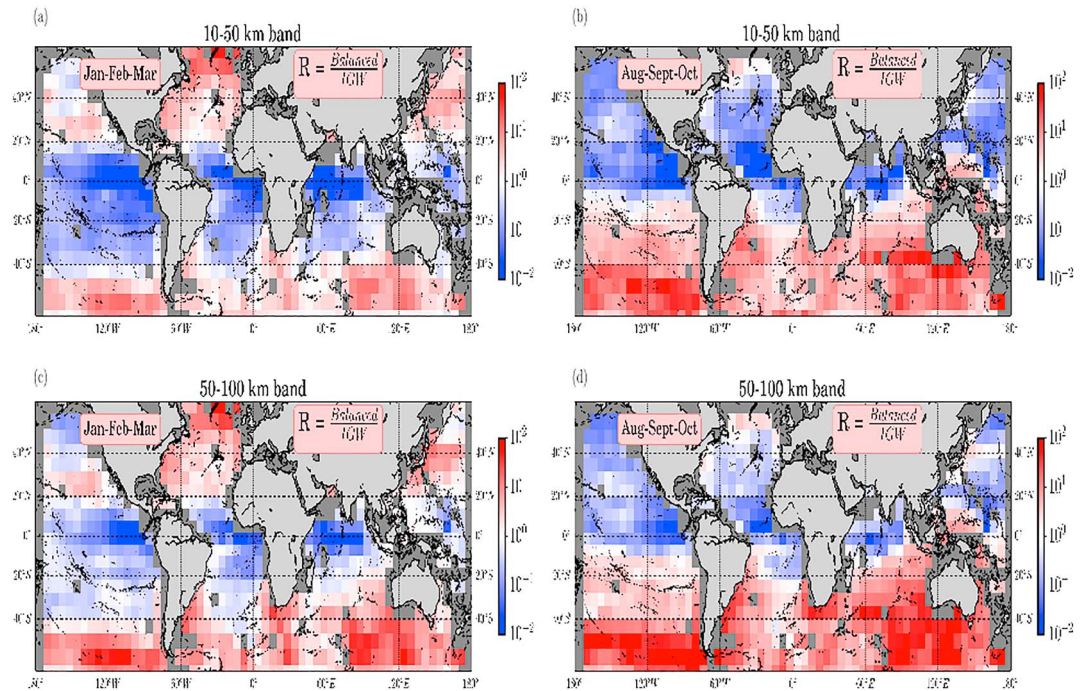


**Figure 12.** Global maps of the ratio  $R$  (see below) for kinetic energy at the ocean surface (estimated from a numerical simulation): Top panels stand for submesoscale range (10–50 km); bottom panels stand for mesoscale range (50–100 km). Left panels are for January to March (winter in the Northern Hemisphere and summer in the Southern Hemisphere), and right panels are for August to September (summer in the Northern Hemisphere and winter in the Southern Hemisphere). For a given range of spatial scales, the variance above the dispersion relation curve for internal gravity waves (IGWs) corresponding to the highest baroclinic mode has been associated with IGWs and the one below this curve associated with balanced motions (BMs).  $R$  is the ratio between the variance associated with BMs and that associated with IGWs:  $R = \frac{\text{BM variance}}{\text{IGW variance}}$ . So for a given spatial-scale band,  $R > 1$  means that the variability of the flow is explained by BMs, and  $R < 1$  means that the variability of the flow is explained by IGWs. These panels emphasize the strong seasonality of the partition of kinetic energy into IGWs and BMs for scales smaller than 100 km and the strong regional diversity and differences between Northern and Southern Hemispheres (from Torres et al., 2018).

with BMs and has energy continuously spread out in the  $\omega$ - $k$  space, suggesting strong energy exchanges through nonlinear interactions (Figure 11, panel ii).

Qiu et al. (2018) and Torres et al. (2018) defined a criterion to discriminate BMs and IGWs for two scale ranges (10–50 and 50–100 km). Their criterion  $R$  makes use of a  $\omega$ - $k$  spectrum (see caption of Figure 12 for the definition of  $R$ ). From the definition of  $R$ , BMs dominate for  $R > 1$  and IGWs for  $R < 1$ . Based on 12,000  $\omega$ - $k$  spectra that cover the global ocean, their results highlight that IGWs dominate BMs in many regions (region in blue in Figure 12). Results emphasize not only a strong seasonality (with BMs dominating in winter and IGWs in summer) but also a strong regional variability. These two studies further revealed that, in summer, the IGW impacts on SSH lead to a significant slope discontinuity on the SSH wavenumber spectrum, at scales smaller than 100 km, a discontinuity not observed on the KE spectrum. On the other hand, IGWs were found to have no impact on sea surface temperature (SST) and Sea Surface Salinity (SSS). These very different signatures of IGWs on SSH, KE, SST, and SSS indicate that exploiting the synergy of using different satellite observations should help to discriminate IGWs and BMs in the global ocean (Torres et al., 2018). In that context, it is important to mention that, in addition to the SWOT mission, a future Wind and Current Mission (WaCM), still under development, aims to produce simultaneous observations of wind stress and surface oceanic currents at high resolution (Rodríguez et al., 2018). The strong potential of WaCM will be to observe not only surface currents but also the wind work (i.e., the dot product of the wind stress and surface currents) and therefore to identify the wind-driven near-inertial motions that have no signature in SSH (Gill et al., 1974).

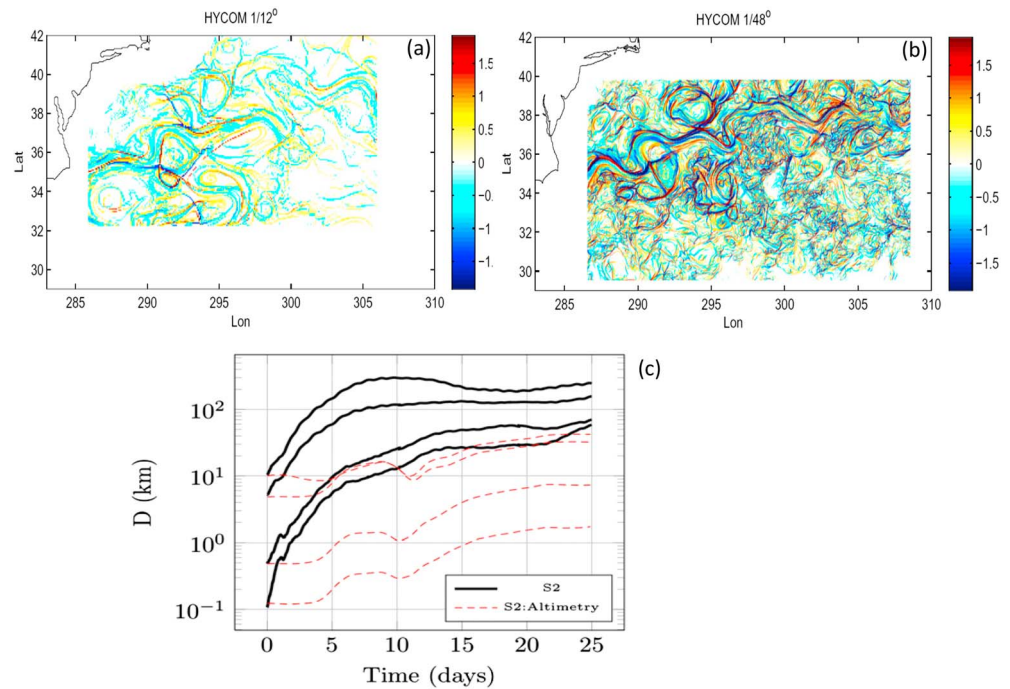


**Figure 13.** Finite Size Lyapunov Exponent from a simulation without (a) and with submesoscales (b). The color panels indicate Finite Size Lyapunov Exponent in day<sup>-1</sup>. Blue colors show inflowing/stable trajectories from forward in time, and red colors show outflowing/unstable trajectories from backward in time particle advection. (from Haza et al., 2012, used with permission.) (c) Separation distance of a particle pair as a function of time,  $D(t)$ , estimated in the Gulf of Mexico using (1) high-resolution data from 300 drifters (black curves) and (2) low-resolution AVISO sea surface height data (red). Dispersion is found to be 10–100 times larger when high-resolution data are used (from Poje et al., 2014, used with permission.).

## 6. Impact of Ocean Mesoscale/Submesoscale Turbulence on the Earth Climate

BMs (including mesoscale and submesoscale motions) are now known to have a strong impact on the large-scale ocean circulation, the ocean biology, and on the coupled ocean-atmosphere system, through the vertical and horizontal fluxes of any quantities. Recent studies, based on satellite altimeter products combined with in situ observations and on results from numerical simulations within large domains at high resolution, have highlighted the ocean turbulence contribution to the transport of heat, mass, chemical constituents of seawater, and air-sea interactions. In this section, we discuss some examples related to the impacts of this turbulence (that includes submesoscale fronts) on ocean dynamics and air-sea interactions. Impacts on ocean biology and carbon storage are discussed in recent review papers such as Lévy et al. (2012), Mahadevan (2016), and McGillicuddy Jr (2016).

### 6.1. Stirring and Mixing Properties

The stretching (or strain) field and the Lagrangian accelerations associated with geostrophic eddies determine the properties of the dispersion of tracers and particles (Hua & Klein, 1998; Lapeyre et al., 1999). In GT, the  $k^{-3}$  KE spectrum slope implies that only by the largest eddies are responsible of the stretching of small-scale filaments. The tracer fluxes from large to small scales are associated with “nonlocal” scale interactions as the large scales control the small scales (Scott, 2006). However, when the KE spectrum slope is in  $k^{-2}$ , such as when energetic submesoscale fronts/eddies are present, filament dynamics are controlled by all eddies (including submesoscale eddies). Such interactions are called “local” since small-scale filaments can be produced by the smallest eddies (Scott, 2006). In that case the dispersion properties are much different from those driven by GT (Foussard et al., 2017; Özgökmen et al., 2012; Scott, 2006). Differences between local and nonlocal properties are well highlighted by maps of Finite Size Lyapunov Exponents as displayed in Figures 13a and 13b (from Haza et al., 2012). When submesoscale fronts/eddies are taken into account, FSLE are characterized by scales much smaller and magnitudes much larger (i.e., more intense stirring) than when submesoscale fronts/eddies are not taken into account.

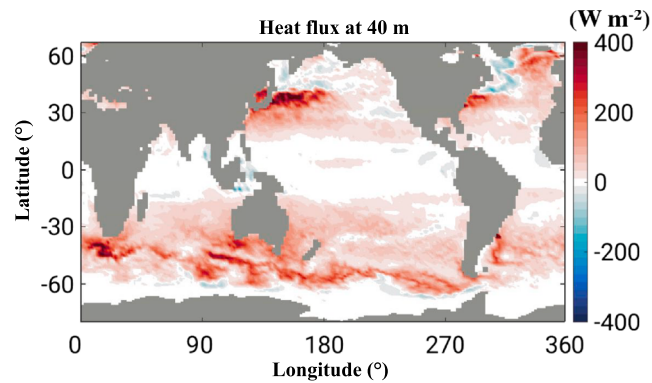


**Figure 14.** Global patterns of vertical heat transport (estimated from a numerical simulation) explained by submesoscales ( $<50$  km) in winter (January–March for the Northern Hemisphere and July–September for the Southern Hemisphere). Values are spatially smoothed over  $3^\circ \times 3^\circ$  square boxes; positive values indicate upward. In most area of midlatitudes, vertical heat transport at submesoscales is  $\sim 20$ – $200$   $\text{W}/\text{m}^2$  and is systematically upward (adapted from Su et al., 2018, used with permission).

Figure 13c (from Poje et al., 2014) issued from the analysis of high-resolution observations from surface drifters (that take into account submesoscale fronts and eddies) and SSH observations (that do not resolve submesoscale fronts and eddies) further quantifies the contribution of submesoscale fronts/eddies on the particle dispersion: particle dispersion is larger by at least 1 order of magnitude when estimated from high-resolution observations that include submesoscales (black curves in Figure 13c) than with observations that do not include submesoscales (such as those from AVISO SSH; see the red dashed curves in Figure 13c).

### 6.2. Horizontal Heat Transport

Hausmann and Czaja (2012) analyzed the relationship between satellite microwave SST and altimeter SSH observations. In regions of large SSH variability, SST and SSH mesoscale anomalies are nearly in-phase, involving intense warm-top anticyclones and cold-top cyclones. In quieter regions, weaker SST signatures are almost in quadrature with eddy SSH. These authors found that eddies flux heat poleward in the mixed-layer over a broad range of oceanic regimes. Magnitude of this heat transport, particularly significant in the Antarctic Circumpolar Current region, attains  $\sim 0.2$  PW, a value similar to that found by other studies using different observations, in particular the ARGO float data set (see Dong et al., 2014; Qiu & Chen, 2005) and studies using numerical simulations (Lévy et al., 2010). However, Hausmann and Czaja (Hausmann & Czaja, 2012) found that the poleward (equatorward) propagation of warm anticyclones (cold cyclones) produces a much weaker poleward heat transport in the mixed layer than the horizontal fluxes resulting from the westward phase shift between SST and SSH fluctuations. In other words, the meridional heat transport is not so much due to individual eddies transporting temperature anomalies, but it is principally due to horizontal heat fluxes resulting from the stirring of temperature anomalies by mesoscale eddies. This finding points to the importance of the phase shift between SSH and SST mesoscale anomalies for the estimation of the meridional heat fluxes. Lévy et al. (2010) further revealed that taking into account the impact of the submesoscale structures, in addition to that of mesoscale eddies, does not lead to a systematic increase of the total meridional heat transport. Rather, impacts of submesoscale structures lead to significantly decrease this transport in some regions and increase it in others (see their Figure 12).

### 6.3. Vertical Heat Transport

Submesoscale frontal dynamics are known to be characterized by  $O(1)$  Rossby number and to capture most of the vertical velocity field in the upper ocean (Klein & Lapeyre, 2009; McWilliams, 2016; Mensa et al., 2013; Sasaki et al., 2014; Thompson et al., 2016). One consequence, revealed by Hakim et al. (2002) and confirmed by Lapeyre and Klein (2006) and McWilliams et al. (2009; see also Fox-Kemper et al., 2008, 2011), is that these submesoscale fronts are associated with positive vertical heat fluxes, that is, upgradient (from deep cold waters to surface warm waters) and not downgradient. This adiabatic property has been highlighted in a recent paper by Su et al. (2018) using an OGCM at unprecedented high spatial resolution (2 km in the horizontal and 90 vertical levels). Results indicate that upper ocean submesoscale turbulence produces a systematically upward heat transport that is 5 to 10 times larger than the vertical heat transport explained by mesoscale eddies! Wintertime magnitudes of these submesoscale heat fluxes are up to  $200$   $\text{W}/\text{m}^2$  for mid-



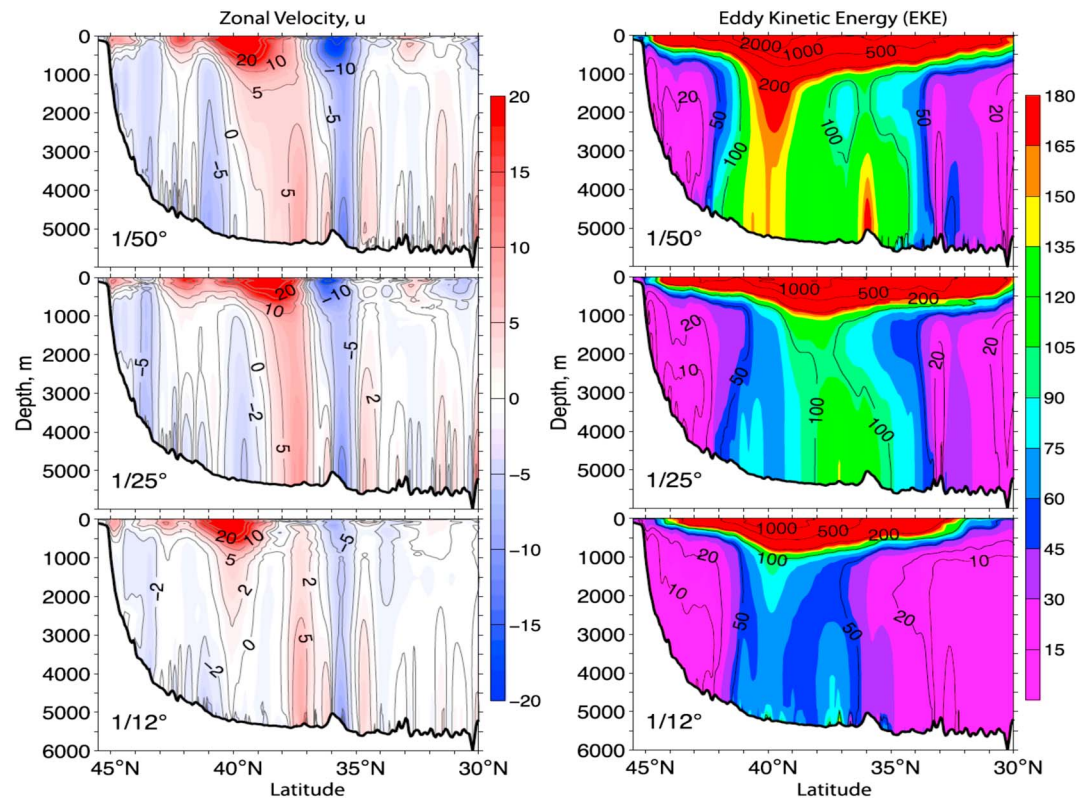


**Figure 15.** Vertical distribution of the modeled (left column) zonal velocity (cm/s) and (right column) eddy kinetic energy ( $\text{cm}^2/\text{s}^2$ ) along  $55^\circ\text{W}$  for the  $(1/50)^\circ$ ,  $(1/25)^\circ$ , and  $(1/12)^\circ$  numerical simulations (from Chassignet & Xu, 2017, © American Meteorological Society. Used with permission).

latitudes (when averaged over 3 months and in boxes of 300-km size; see Figure 14). These vertical heat fluxes warm the sea surface by up to  $0.3^\circ\text{C}$  annually and produce an upward annual-mean air-sea heat flux anomaly of  $4\text{--}10\text{ W/m}^2$  at midlatitudes (Su et al., 2018). Such results indicate that submesoscale BMs associated with submesoscale frontal structures are critical to the vertical transport of heat between the ocean interior and the atmosphere and are thus a key component of the Earth’s climate. Noting that submesoscale fronts are preconditioned by mesoscale eddies, the results from Su et al. (2018) further highlight the impacts of the ocean-scale interactions on the Earth Climate.

#### 6.4. Impact of Submesoscale Fronts on the Large-Scale Ocean Circulation

The impact of submesoscale frontal physics on the large-scale ocean circulation has been examined by Lévy et al. (2010) and Chassignet and Xu (2017). To test this impact, these authors used several numerical models at a basin scale, each one with a different spatial resolution. After a reasonable spin-up period (10–20 years), the large-scale ocean circulation and the mean structure of the ventilated thermocline strongly differ when the resolution increased from 10 to 2 km (which highlights the impact of submesoscales). Changes involve the emergence of a denser and more energetic eddy population at the 2-km resolution, occupying most of the basin and sustained by submesoscale physics. Taking into account submesoscale dynamics leads to “regional” and “remote” effects. Regional effects occur through the inverse KE cascade that strongly intensifies zonal jets such as in the Gulf Stream region. This intensification subsequently leads to isopycnals steepening (through the thermal wind balance), which significantly counterbalances and locally overcomes the eddy-driven heat transport that tends to flatten isopycnals (Lévy et al., 2010). Chassignet and Xu (2017) further note that, when the spatial resolution is increased, the representation of the Gulf Stream penetration and associated recirculating gyres changes from unrealistic to realistic (in terms of comparison with observations) and that the penetration into the deep ocean drastically increases (see Figure 15). Remote effects occur through the resulting general equilibration of the main thermocline that shifts zonal jets at midlatitudes southward by a few degrees, significantly altering the shape and position of the gyres. Consequence is that the deep convection in high latitudes is reduced, leading to a significant modification of the meridional overturning circulation. Thus, results from Lévy et al. (2010) and Chassignet and Xu (2017) emphasize

that the impact of submesoscale fronts on the mean circulation and mean transport at a basin scale cannot be ignored anymore. There is a need to repeat these two numerical experiments in larger domains with an even higher spatial resolution (J. Callies, personal communication), in particular on the vertical, using the coming exascale computers.

### 6.5. Air-Sea Interaction

Chelton et al. (2004) discovered a remarkably strong positive correlation between surface winds and SST at mesoscale (i.e., 100–300 km) using a combination of radar scatterometers and SST observations. As shown later by Frenger et al. (2013), mesoscale eddies are characterized by a positive correlation between SST, SSH, cloudiness, and precipitation rate. Similar correlations were found between air-sea heat fluxes and SST (Bôas et al., 2015; Byrne et al., 2015; Ma et al., 2015). An arising question concerns the impact of OMT at the scale of the atmospheric storm track (i.e.,  $O(5,000\text{--}10,000\text{ km})$ ). Ma et al. (2015) and Foussard et al. (2019) showed that increased air-sea heat fluxes at the ocean surface, due to oceanic eddies, could lead to a nonlocal response associated with a modification of the atmospheric circulation far from the oceanic eddying region.

In parallel, using numerical models with spatial resolution accounting for scales as small as 50 km, Minobe et al. (2008) showed that local SST fronts in the Gulf Stream could impact the entire troposphere. These authors found a conspicuous signal in their atmospheric general circulation model, indicating a wind convergence over the warm flank of the oceanic front up to 12 km in altitude (i.e., close to the tropopause). One important characteristic is that the wind convergence was found to be proportional to the SST Laplacian (a second-order derivative that involves small scales). This sensitivity to small scales explains why past numerical models, with lower resolution, were unable to represent such dynamics (Bryan et al., 2010). Since then, numerous studies with higher spatial resolution have highlighted the importance of such SST gradients, with scales down to the submesoscales, for the tropospheric storm tracks (Deremble et al., 2012; Foussard et al., 2019; Nakamura et al., 2008). These results have led to a renewed interest in understanding the role played by SST anomalies at scales down to 5–10 km in atmosphere dynamics.

Although the ocean current magnitude is much smaller than the atmospheric wind speed, a large number of numerical studies, at least in the last two decades, have shown that oceanic currents at mesoscales and submesoscales can also significantly impact the wind stress. In terms of ocean dynamics, the resulting effects on the wind work lead to a net KE transfer from the ocean to the atmosphere. This transfer corresponds to a decay of almost 30% of the ocean KE at mesoscale at midlatitudes (Eden & Dietze, 2009) and less than 20% for oceanic submesoscales (Renault et al., 2018). In terms of atmospheric dynamics, the wind stress curl and divergence resulting from the ocean current impacts should affect the vertical velocity in the atmosphere. A recent in situ experiment has been carried out in the Gulf of Mexico using a Doppler Scatterometer to observe simultaneously the surface currents and wind stress at very high resolution ( $\sim 2.5\text{ km}$ ). The results reveal and confirm the strong correlation between the wind stress curl and the relative vorticity associated with oceanic submesoscales (E. Rodriguez, personal communication, November, 2018). Magnitude of the wind stress curl is such that the wind divergence in the atmosphere is 1 order of magnitude larger than found by Minobe et al. (2008).

These results further confirm that oceanic mesoscale eddies and submesoscales structures can significantly impact the atmospheric boundary layer and the whole troposphere. There is still some work to do to further quantify these impacts and the consequences on the atmospheric storm tracks.

## 7. Discussion and Conclusion

Analysis of altimeter observations collected in the last 25 years and results obtained from OGCMs with high spatial resolution emphasize that all the oceans are fully turbulent, involving a broad range of scales from at least 2 km to 5,000 km. All these scales are now known to strongly interact, leading to significant energy exchanges between scales, in particular in the upper ocean. Resulting ocean-scale interactions impact the Earth climate in counterintuitive ways. For instance, the smallest scales render mesoscale eddies more coherent with a longer lifetime and can also trigger significant upgradient and not downgradient vertical fluxes of any quantity. A better understanding of the IGWs impacts may lead to a more complex vision depending on how much they interact with BMs. Overall, results highlight that the oceanic fluid is much less diabatic and much more inertial than thought 25 years ago (i.e., again with fluxes much less controlled by diffusivity or viscosity and more by nonlinear interactions that lead to reversible upgradient and downgradient fluxes). Numerous studies now emphasize that these ocean-scale interactions are crucial for the

ocean's KE budget, the meridional heat transport, the air-sea interactions, and more generally for the Earth climate.

Running numerical models with high resolution is a powerful approach to assess ocean-scale interactions but only when they are performed with the highest spatial resolution (down to at least 1 km) and on a global scale in order to take into account, both, the local and nonlocal interactions. This strategy is the only one capable to assess the wealth of ocean-scale interactions over a broad range of scales. Such ocean numerical models as well as atmosphere-ocean coupled models with similar resolutions can be run on the present petascale computers. Future numerical models, with a higher resolution than presently considered, will certainly challenge the results presented in this paper, by revealing new and unsuspected impacts of smaller scales presently unresolved. These models will undoubtedly improve our understanding of the ocean engine.

Numerical findings need however to be confirmed or infirmed by high-resolution observations on a global scale and over several years, as already pointed out by Carl Wunsch in 2010. As emphasized in this paper, BMs and internal gravity waves have different impacts in terms of fluxes on the KE budget, which points to the need to discriminate them from observations. In that respect, future wide-swath altimeter missions, such as the SWOT mission (Fu & Ferrari, 2008), will be critical to make major advances. These observations are the only ones capable to diagnose correctly BMs down to scales of 30–50 km. However, these future SSH observations will have to be combined with existing satellite observations as well as with those from missions under development to retrieve other IGWs. The latter missions include WaCM (Rodríguez et al., 2018), already mentioned, that will observe simultaneously the wind stress and oceanic currents at very high resolution and therefore give access to near-inertial waves and smaller IGWs. They also include other missions such as the Surface KInematic Monitoring mission (Ardhuin et al., 2018) and the Wavemill mission (Martin et al., 2016) aiming to observe surface currents with high resolution. An optimal strategy to better capture the subtleties of ocean turbulence would be to exploit the synergy of analyzing all these satellite observations in combination with in situ data on a global scale, such as the ones collected by surface drifters (Lumpkin et al., 2017) and ARGO floats (Le Traon, 2013) deployed in all oceans.

The importance, for the Earth climate, of fully taking into account the ocean-scale interactions is further emphasized by recent geophysical studies on the Earth atmosphere and oceans. The Earth atmosphere involves cyclones and anticyclones (although with larger scales than in the oceans) that strongly interact the so-called atmospheric storm tracks. However, if geophysical turbulence refers to an inverse KE cascade over a broad inertial range (defined as the scale range between the eddy source scale and the scale of the most energetic eddies), the atmosphere is found much less turbulent than the oceans (Jansen & Ferrari, 2012). The atmosphere is indeed characterized by an inverse KE cascade over a very small inertial range compared to the oceans (Merlis & Schneider, 2009; Schneider & Walker, 2006). Scales of the atmospheric cyclones and anticyclones are close to their source scales (scales of the baroclinic instability). On the other hand, as pointed out several times in this paper, the OMT is characterized by an inverse KE cascade over a broad inertial range (Hua & Haidvogel, 1986; Hua et al., 1998). The consequence, as discussed by Jansen and Ferrari (2012), is that the atmospheric response to external forcings is much faster and much less inertial than the ocean response, which should impact the dynamics of the coupled ocean-atmosphere system. These differences between the ocean and atmosphere turbulent properties emphasize the importance of the future developments on ocean-scale interactions for studies of climate and climate change (Jansen & Ferrari, 2012).

## References

- Alford, M. H., MacKinnon, J. A., Simmons, H. L., & Nash, J. D. (2016). Near-inertial internal gravity waves in the ocean. *Annual Review of Marine Science*, 8, 95–123.
- Arbic, B. K., Polzin, K. L., Scott, R. B., Richman, J. G., & Shriver, J. F. (2013). On eddy viscosity, energy cascades, and the horizontal resolution of gridded satellite altimeter products. *Journal of Physical Oceanography*, 43(2), 283–300.
- Arbic, B. K., Scott, R. B., Flierl, G. R., Morten, A. J., Richman, J. G., & Shriver, J. F. (2012). Nonlinear cascades of surface oceanic geostrophic kinetic energy in the frequency domain. *Journal of Physical Oceanography*, 42(9), 1577–1600.
- Ardhuin, F., Aksenov, Y., Benetazzo, A., Bertino, L., Brandt, P., Caube, A. P., et al. (2018). Measuring currents, ice drift, and waves from space: The sea surface kinematics multiscale monitoring (SKIM) concept. *Ocean Science*, 14, 337–354.
- Aref, H. (1984). Stirring by chaotic advection. *Journal of Fluid Mechanics*, 143, 1–21.
- Barkan, R., Winters, K. B., & McWilliams, J. C. (2017). Stimulated imbalance and the enhancement of eddy kinetic energy dissipation by internal waves. *Journal of Physical Oceanography*, 47(1), 181–198.
- Blumen, W. (1978). Uniform potential vorticity flow: Part I. Theory of wave interactions and two-dimensional turbulence. *Journal of the Atmospheric Sciences*, 35(5), 774–783.

## Acknowledgments

We dedicate this study to our colleague and friend Bach Lien Hua who was the first woman to give a Lorenz Conference (in 2006) and who made so many significant and insightful contributions to the understanding of oceanic turbulence. We thank the two reviewers for their constructive comments and in particular Eric Chassignet for his advices during the revision process. We also thank Jinbo Wang for his insightful comments. This study was carried out at the Jet Propulsion Laboratory, California Institute of Technology, under contract with the National Aeronautics and Space Administration (NASA), at the Laboratoire de Météorologie Dynamique and at the Courant Institute. P. K. is supported by a NASA Senior Fellowship and the SWOT mission. G. L. is supported by the CNES-SWOT mission. L. S. is a JPL JVS RP affiliate and is supported by a joint CNES-Région Bretagne doctoral grant. B. Q. and L. L. F. acknowledge support from the NASA SWOT mission (NNX16AH66G). H. T. and D.M. are supported by NASA Physical Oceanography (PO) and Modeling, Analysis, and Prediction (MAP) Programs. Z. S. has been supported by NASA NPP postdoc fellowship and NASA grant NNX15AG42G. This work is partly funded by CNES (OSTST-OSIW grant). Data used in this paper can be found in the NASA website (<https://science.jpl.nasa.gov/projects/ECCO-IcES/>).

- Bóas, A. V., Sato, O., Chaigneau, A., & Castelão, G. (2015). The signature of mesoscale eddies on the air-sea turbulent heat fluxes in the South Atlantic Ocean. *Geophysical Research Letters*, *42*, 1856–1862. <https://doi.org/10.1002/2015GL063105>
- Boccaletti, G., Ferrari, R., & Fox-Kemper, B. (2007). Mixed layer instabilities and restratification. *Journal of Physical Oceanography*, *37*(9), 2228–2250.
- Bryan, F. O., Tomas, R., Dennis, J. M., Chelton, D. B., Loeb, N. G., & McClean, J. L. (2010). Frontal scale air-sea interaction in high-resolution coupled climate models. *Journal of Climate*, *23*(23), 6277–6291.
- Byrne, D., Papritz, L., Frenger, I., Münnich, M., & Gruber, N. (2015). Atmospheric response to mesoscale sea surface temperature anomalies: Assessment of mechanisms and coupling strength in a high-resolution coupled model over the South Atlantic. *Journal of the Atmospheric Sciences*, *72*(5), 1872–1890.
- Callies, J., Ferrari, R., Klymak, J. M., & Gula, J. (2015). Seasonality in submesoscale turbulence. *Nature Communications*, *6*, 6862.
- Callies, J., Flierl, G., Ferrari, R., & Fox-Kemper, B. (2016). The role of mixed-layer instabilities in submesoscale turbulence. *Journal of Fluid Mechanics*, *788*, 5–41.
- Capet, X., Klein, P., Hua, B., Lapeyre, G., & McWilliams, J. (2008). Surface kinetic and potential energy transfer in SQG dynamics. *Journal of Fluid Mechanics*, *604*, 165–174.
- Capet, X., Roulet, G., Klein, P., & Maze, G. (2016). Intensification of upper-ocean submesoscale turbulence through Charney baroclinic instability. *Journal of Physical Oceanography*, *46*(11), 3365–3384.
- Charney, J. G. (1947). The dynamics of long waves in a baroclinic westerly current. *Journal of Meteorology*, *4*(5), 136–162.
- Charney, J. G. (1971). Geostrophic turbulence. *Journal of the Atmospheric Sciences*, *28*(6), 1087–1095.
- Chassignet, E., Pascual, A., Tintore, J., & Verron, J. (2018). *New Frontiers in Operational Oceanography*. Tallahassee, FL: GODAE OceanView.
- Chassignet, E., & Xu, X. (2017). Impact of horizontal resolution (1/12° to 1/50°) on Gulf Stream separation, penetration, and variability. *Journal of Physical Oceanography*, *47*, 1999–2021.
- Chelton, D. B., Schlax, M. G., Freilich, M. H., & Milliff, R. F. (2004). Satellite measurements reveal persistent small-scale features in ocean winds. *science*, *303*(5660), 978–983.
- Chelton, D. B., Schlax, M. G., & Samelson, R. M. (2011). Global observations of nonlinear mesoscale eddies. *Progress in Oceanography*, *91*(2), 167–216.
- Chereskin, T. K., Rocha, C. B., Gille, S. T., Menemenlis, D., & Passaro, M. (2019). Characterizing the Transition From Balanced to Unbalanced Motions in the Southern California Current. *Journal of Geophysical Research: Oceans*, *124*. <https://doi.org/10.1029/2018JC014583>
- d'Ovidio, F., DeMonte, S., Alvain, S., Dandonneau, Y., & Levy, M. (2010). Fluid dynamical niches of phytoplankton types. *Proceeding of the National Academy of Sciences*, *107*, 18,366–18,370. <https://doi.org/10.1073/pnas.1004620107>
- Danioux, E., Klein, P., Hecht, M. W., Komori, N., Roulet, G., & Le Gentil, S. (2011). Emergence of wind-driven near-inertial waves in the deep ocean triggered by small-scale eddy vorticity structures. *Journal of Physical Oceanography*, *41*(7), 1297–1307.
- Deremble, B., Lapeyre, G., & Ghil, M. (2012). Atmospheric dynamics triggered by an oceanic SST front in a moist quasigeostrophic model. *Journal of the Atmospheric Sciences*, *69*(5), 1617–1632.
- Dong, C., McWilliams, J. C., Liu, Y., & Chen, D. (2014). Global heat and salt transports by eddy movement. *Nature Communications*, *5*, 3294.
- Dufau, C., Orszynowicz, M., Dibarbour, G., Morrow, R., & Le Traon, P.-Y. (2016). Mesoscale resolution capability of altimetry: Present and future. *Journal of Geophysical Research: Oceans*, *121*, 4910–4927. <https://doi.org/10.1002/2015JC010904>
- Dunphy, M., Ponte, A. L., Klein, P., & Le Gentil, S. (2017). Low-mode internal tide propagation in a turbulent eddy field. *Journal of Physical Oceanography*, *47*(3), 649–665.
- Eden, C., & Dietze, H. (2009). Effects of mesoscale eddy/wind interactions on biological new production and eddy kinetic energy. *Journal of Geophysical Research*, *114*, C05023. <https://doi.org/10.1029/2008JC005129>
- Egbert, G. D., Bennett, A. F., & Foreman, M. G. (1994). Topex/poseidon tides estimated using a global inverse model. *Journal of Geophysical Research*, *99*(C12), 24,821–24,852.
- Ferrari, R. (2011). A frontal challenge for climate models. *Science*, *332*(6027), 316–317.
- Ferrari, R., & Wunsch, C. (2009). Ocean circulation kinetic energy: Reservoirs, sources, and sinks. *Annual Review of Fluid Mechanics*, *41*, 253–282.
- Foussard, A., Berti, S., Perrot, X., & Lapeyre, G. (2017). Relative dispersion in generalized two-dimensional turbulence. *Journal of Fluid Mechanics*, *821*, 358–383.
- Foussard, A., Lapeyre, G., & R. Plougonven (2019). Storm tracks response to oceanic eddies in idealized atmospheric simulations. *Journal of Climate*, *32*, 445–463.
- Fox-Kemper, B., Danabasoglu, G., Ferrari, R., Griffies, S., Hallberg, R., Holland, M., et al. (2011). Parameterization of mixed layer eddies. III: Implementation and impact in global ocean climate simulations. *Ocean Modelling*, *39*(1-2), 61–78.
- Fox-Kemper, B., Ferrari, R., & Hallberg, R. (2008). Parameterization of mixed layer eddies. Part I: Theory and diagnosis. *Journal of Physical Oceanography*, *38*(6), 1145–1165.
- Frenger, I., Gruber, N., Knutti, R., & Münnich, M. (2013). Imprint of Southern Ocean eddies on winds, clouds and rainfall. *Nature Geoscience*, *6*(8), 608.
- Fu, L.-L. (1983). On the wave number spectrum of oceanic mesoscale variability observed by the SEASAT altimeter. *Journal of Geophysical Research*, *88*(C7), 4331–4341.
- Fu, L.-L. (2009). Pattern and velocity of propagation of the global ocean eddy variability. *Journal of Geophysical Research*, *114*, C11017. <https://doi.org/10.1029/2009JC005349>
- Fu, L.-L., & Ferrari, R. (2008). Observing oceanic submesoscale processes from space. *Eos, Transactions American Geophysical Union*, *89*(48), 488–488.
- Fu, L.-L., & Flierl, G. R. (1980). Nonlinear energy and enstrophy transfers in a realistically stratified ocean. *Dynamics of Atmospheres and Oceans*, *4*, 219–246.
- Fu, L.-L., & Smith, R. D. (1996). Global ocean circulation from satellite altimetry and high-resolution computer simulation. *Bulletin of the American Meteorological Society*, *77*(11), 2625–2636.
- Fu, L.-L., & Ubelmann, C. (2014). On the transition from profile altimeter to swath altimeter for observing global ocean surface topography. *Journal of Atmospheric and Oceanic Technology*, *31*, 560–568.
- Garrett, C. (1983). On the initial streakiness of a dispersing tracer in two- and three-dimensional turbulence. *Dynamics of Atmospheres and Oceans*, *7*, 265–277.
- Gaultier, L., Verron, J., Brankart, J. M., Titau, O., & Brasseur, P. (2012). On the inversion of submesoscale tracer fields to estimate the surface ocean circulation. *Journal of Marine Systems*, *126*, 33–42. <https://doi.org/10.1016/j.jmarsys.2012.02.014>

- Gill, A., Green, J., & Simmons, A. (1974). Energy partition in the large-scale ocean circulation and the production of mid-ocean eddies. *Deep-Sea Research*, 21(7), 499–528.
- Grisouard, N., & Thomas, L. N. (2015). Critical and near-critical reflections of near-inertial waves off the sea surface at ocean fronts. *Journal of Fluid Mechanics*, 765, 273–302.
- Hakim, G. J., Snyder, C., & Muraki, D. J. (2002). A new surface model for cyclone-anticyclone asymmetry. *Journal of the Atmospheric Sciences*, 59(16), 2405–2420.
- Hausmann, U., & Czaja, A. (2012). The observed signature of mesoscale eddies in sea surface temperature and the associated heat transport. *Deep Sea Research Part I: Oceanographic Research Papers*, 70, 60–72.
- Haza, A. C., Ozgokmen, T. M., Griffa, A., Garraffo, Z. D., & Piterbarg, L. (2012). Parameterization of particle transport at submesoscales in the Gulf Stream region using lagrangian subgridscale models. *Ocean Modelling*, 42, 31–49.
- Held, I. M., Pierrehumbert, R. T., Garner, S. T., & Swanson, K. L. (1995). Surface quasi-geostrophic dynamics. *Journal of Fluid Mechanics*, 282, 1–20.
- Hoskins, B. (1976). Baroclinic waves and frontogenesis. Part I: Introduction and eady waves. *Quarterly Journal of the Royal Meteorological Society*, 102(431), 103–122.
- Hua, B., & Haidvogel, D. (1986). Numerical simulations of the vertical structure of quasi-geostrophic turbulence. *Journal of the Atmospheric Sciences*, 43(23), 2923–2936.
- Hua, B. L., & Klein, P. (1998). An exact criterion for the stirring properties of nearly two-dimensional turbulence. *Physica D*, 113, 98–110.
- Hua, B., McWilliams, J. C., & Klein, P. (1998). Lagrangian accelerations in geostrophic turbulence. *Journal of Fluid Mechanics*, 366, 87–108.
- Hua, B.-L., McWilliams, J. C., & Owens, B. (1985). An objective analysis of the polymode local dynamics experiment. Part ii: Streamfunction and potential vorticity fields during the extensive period. *Journal of Physical Oceanography*, 16, 506–522.
- Hurlburt, H. E., & Hogan, P. J. (2000). Impact of 1/8 to 1/64 resolution on gulf stream model-data comparisons in basin-scale subtropical atlantic ocean models. *Dynamics of Atmospheres and Oceans*, 32(3-4), 283–329.
- Jansen, M., & Ferrari, R. (2012). Macroturbulent equilibration in a thermally forced primitive equation system. *Journal of the Atmospheric Sciences*, 69(2), 695–713.
- Joyce, T. M., Toole, J. M., Klein, P., & Thomas, L. N. (2013). A near-inertial mode observed within a gulf stream warm-core ring. *Journal of Geophysical Research: Oceans*, 118, 1797–1806. <https://doi.org/10.1002/jgrc.20141>
- Juckles, M. (1994). Quasigeostrophic dynamics of the tropopause. *Journal of the Atmospheric Sciences*, 51(19), 2756–2768.
- Klein, P., Hua, B.-L., & Carton, X. (2003). Emergence of cyclonic structures due to the interactions of near-inertial oscillations with mesoscale eddies. *Quarterly Journal of the Royal Meteorological Society*, 129, 1–20.
- Klein, P., Hua, B. L., Lapeyre, G., Capet, X., Le Gentil, S., & Sasaki, H. (2008). Upper ocean turbulence from high-resolution 3D simulations. *Journal of Physical Oceanography*, 38(8), 1748–1763.
- Klein, P., Isern-Fontanet, J., Lapeyre, G., Roulet, G., Danioux, E., Chapron, B., et al. (2009). Diagnosis of vertical velocities in the upper ocean from high resolution sea surface height. *Geophysical Research Letters*, 36, L12603. <https://doi.org/10.1029/2009GL038359>
- Klein, P., & Lapeyre, G. (2009). The oceanic vertical pump induced by mesoscale and submesoscale turbulence. *Annual Review of Marine Science*, 1, 351–375.
- Kunze, E. (1985). Near-inertial wave propagation in geostrophic shear. *Journal of Physical Oceanography*, 15(5), 544–565.
- LaCasce, J. (2012). Surface quasigeostrophic solutions and baroclinic modes with exponential stratification. *Journal of Physical Oceanography*, 42, 549–580.
- LaCasce, J., & Mahadevan, A. (2006). Estimating subsurface horizontal and vertical velocities from sea-surface temperature. *Journal of Marine Research*, 64(5), 695–721.
- Lapeyre, G. (2002). Characterization of finite-time Lyapunov exponents and vectors in two-dimensional turbulence. *Chaos: An Interdisciplinary Journal of Nonlinear Science*, 12(3), 688–698.
- Lapeyre, G. (2017). Surface quasi-geostrophy. *Fluids*, 2(1), 7.
- Lapeyre, G., Hua, B., & Klein, P. (2001). Dynamics of the orientation of active and passive scalars in two-dimensional turbulence. *Physics of Fluids*, 13(1), 251–264.
- Lapeyre, G., & Klein, P. (2006). Dynamics of the upper oceanic layers in terms of surface quasigeostrophy theory. *Journal of Physical Oceanography*, 36(2), 165–176.
- Lapeyre, G., Klein, P., & Hua, B. (1999). Does the tracer gradient vector align with the strain eigenvectors in 2D turbulence? *Physics of Fluids*, 11(12), 3729–3737.
- Lapeyre, G., Klein, P., & Hua, B.-L. (2006). Oceanic restratification forced by surface frontogenesis. *Journal of Physical Oceanography*, 36(2), 1577–1590.
- Le Traon, P.-Y. (2013). From satellite altimetry to argo and operational oceanography: three revolutions in oceanography. *Ocean Science*, 9, 901–915.
- Le Traon, P.-Y., Klein, P., Hua, B. L., & Dibarboure, G. (2008). Do altimeter wavenumber spectra agree with the interior or surface quasigeostrophic theory? *Journal of Physical Oceanography*, 38(5), 1137–1142.
- Ledwell, J. R., Watson, A. J., & Law, C. S. (1993). Evidence for slow mixing across the pycnocline from an open-ocean tracer-release experiment. *Nature*, 364(6439), 701.
- Lévy, M., Ferrari, R., Franks, P. J., Martin, A. P., & Rivière, P. (2012). Bringing physics to life at the submesoscale. *Geophysical Research Letters*, 39, L14602. <https://doi.org/10.1029/2012GL052756>
- Lévy, M., Klein, P., & Treguier, A.-M. (2001). Impact of sub-mesoscale physics on production and subduction of phytoplankton in an oligotrophic regime. *Journal of Marine Research*, 59(4), 535–565.
- Lévy, M., Klein, P., Tréguier, A.-M., Iovino, D., Madec, G., Masson, S., & Takahashi, K. (2010). Modifications of gyre circulation by sub-mesoscale physics. *Ocean Modelling*, 34(1-2), 1–15.
- Lumpkin, R., & Elipot, S. (2010). Surface drifter pair spreading in the North Atlantic. *Journal of Geophysical Research*, 115, C12017. <https://doi.org/10.1029/2010JC006338>
- Lumpkin, R., Özgökmen, T., & Centurioni, L. (2017). Advances in the application of surface drifters. *Annual Review of Marine Science*, 9, 59–81.
- Ma, J., Xu, H., Dong, C., Lin, P., & Liu, Y. (2015). Atmospheric responses to oceanic eddies in the Kuroshio Extension region. *Journal of Geophysical Research: Atmospheres*, 120, 6313–6330. <https://doi.org/10.1002/2014JD022930>
- Mahadevan, A. (2016). The impact of submesoscale physics on primary productivity of plankton. *Annual Review of Marine Science*, 8, 161–184.

- Martin, A. C. H., Gommenginger, C., Marquez, J., Doody, S., Navarro, V., & Buck, C. (2016). Wind-wave-induced velocity in ATI SAR ocean surface currents: First experimental evidence from airborne campaign. *Journal of Geophysical Research: Oceans*, *21*, 1640–1653. <https://doi.org/10.1002/2015JC011459>
- Maximenko, N. A., Bang, B., & Sasaki, H. (2005). Observational evidence of alternating zonal jets in the world ocean. *Geophysical Research Letters*, *32*, L12607. <https://doi.org/10.1029/2005GL022728>
- Maximenko, N. A., Oleg, V. M., Pearn, P. N., & Hideharu, S. (2008). Stationary mesoscale jet-like features in the ocean. *Geophysical Research Letters*, *35*, L08603. <https://doi.org/10.1029/2008GL033267>
- McGillicuddy Jr, D. J. (2016). Mechanisms of physical-biological-biogeochemical interaction at the oceanic mesoscale. *Annual Review of Marine Science*, *8*, 125–159.
- McWilliams, J. C. (1989). Statistical properties of decaying geostrophic turbulence. *Journal of Fluid Mechanics*, *198*, 199–230.
- McWilliams, J. C. (2016). Submesoscale currents in the ocean. *Proceedings of the Royal Society A*, *472*(2189), 20160117.
- McWilliams, J., Colas, F., & Molemaker, M. (2009). Cold filamentary intensification and oceanic surface convergence lines. *Geophysical Research Letters*, *36*, L18602. <https://doi.org/10.1029/2009GL039402>
- Meneguen, C., Delpech, A., Marin, F., Cravatte, S., Schopp, R., & Morel, Y. (2019). Observations and mechanisms for the formation of deep equatorial and tropical circulation. *Earth and Space Science*, *6*, 370–386. <https://doi.org/10.1029/2018EA000438>
- Mensa, J. A., Garraffo, Z., Griffa, A., Özgökmen, T. M., Haza, A., & Veneziani, M. (2013). Seasonality of the submesoscale dynamics in the Gulf Stream region. *Ocean Dynamics*, *63*(8), 923–941.
- Merlis, T. M., & Schneider, T. (2009). Scales of linear baroclinic instability and macroturbulence in dry atmospheres. *Journal of the Atmospheric Sciences*, *66*, 1821–1833.
- Mezic, I., Loire, S., Fonoberov, V., & Hogan, P. (2010). A new mixing diagnostic and gulf oil spill movement. *Science*, *330*, 486–489.
- Minobe, S., Kuwano-Yoshida, A., Komori, N., Xie, S.-P., & Small, R. J. (2008). Influence of the Gulf Stream on the troposphere. *Nature*, *452*(7184), 206.
- Molemaker, M. J., McWilliams, J. C., & Capet, X. (2010). Balanced and unbalanced routes to dissipation in an equilibrated easy flow. *Journal of Fluid Mechanics*, *654*, 35–63.
- Morrow, R., & Le Traon, P.-Y. (2012). Recent advances in observing mesoscale ocean dynamics with satellite altimetry. *Advances in Space Research*, *50*(8), 1062–1076.
- Müller, M., Arbic, B. K., Richman, J. G., Shriver, J. F., Kunze, E. L., Scott, R. B., et al. (2015). Toward an internal gravity wave spectrum in global ocean models. *Geophysical Research Letters*, *42*, 3474–3481. <https://doi.org/10.1002/2015GL063365>
- Nakamura, H., Sampe, T., Goto, A., Ohfuchi, W., & Xie, S.-P. (2008). On the importance of midlatitude oceanic frontal zones for the mean state and dominant variability in the tropospheric circulation. *Geophysical Research Letters*, *35*, L15709. <https://doi.org/10.1029/2008GL034010>
- Özgökmen, T. M., Poje, A. C., Fischer, P. F., Childs, H., Krishnan, H., Garth, C., et al. (2012). On multi-scale dispersion under the influence of surface mixed layer instabilities and deep flows. *Ocean Modelling*, *56*, 16–30.
- Panetta, R. L. (1993). Zonal jets in wide baroclinically unstable regions: Persistence and scale selection. *Journal of the Atmospheric Sciences*, *50*(14), 2073–2106.
- Pierrehumbert, R. T., Held, I. M., & Swanson, K. L. (1994). Spectra of local and nonlocal two-dimensional turbulence. *Chaos, Solitons & Fractals*, *4*, 1111–1116.
- Poje, A. C., Özgökmen, T. M., Lipphardt Jr., B. L., Haus, B. K., Ryan, E. H., Haza, A. C., et al. (2014). Submesoscale dispersion in the vicinity of the deepwater horizon spill. *Proceeding of the National Academy of Sciences*, *111*(35), 12,693–12,698.
- Polzin, K. L., & Lvov, Y. V. (2011). Toward regional characterizations of the oceanic internal wavefield. *Review of Geophysics*, *49*, RG4003. <https://doi.org/10.1029/2010RG000329>
- Ponte, A. L., & Klein, P. (2015). Incoherent signature of internal tides on sea level in idealized numerical simulations. *Geophysical Research Letters*, *42*, 1520–1526. <https://doi.org/10.1002/2014GL02583>
- Qiu, B., & Chen, S. (2005). Eddy-induced heat transport in the subtropical North Pacific from Argo, TMI and altimetry measurements. *Journal of Physical Oceanography*, *35*, 458–473.
- Qiu, B., Chen, S., Klein, P., Sasaki, H., & Sasai, Y. (2014). Seasonal mesoscale and submesoscale eddy variability along the North Pacific subtropical countercurrent. *Journal of Physical Oceanography*, *44*(12), 3079–3098.
- Qiu, B., Chen, S., Klein, P., Ubelmann, C., Fu, L.-L., & Sasaki, H. (2016). Reconstructibility of three-dimensional upper-ocean circulation from SWOT sea surface height measurements. *Journal of Physical Oceanography*, *46*, 947–963.
- Qiu, B., Chen, S., Klein, P., Wang, J., Torres, H., Fu, L.-L., & Menemenlis, D. (2018). Seasonality in transition scale from balanced to unbalanced motions in the World Ocean. *Journal of Physical Oceanography*, *48*(3), 591–605.
- Qiu, B., Nakano, T., Chen, S., & Klein, P. (2017). Submesoscale transition from geostrophic flows to internal waves in the northwestern Pacific upper ocean. *Nature Communications*, *8*, 14055.
- Ray, R. D., & Mitchum, G. T. (1997). Surface manifestation of internal tides in the deep ocean: Observations from altimetry and island gauges. *Progress in Oceanography*, *40*(1-4), 135–162.
- Ray, R. D., & Zaron, E. D. (2016). M2 internal tides and their observed wavenumber spectra from satellite altimetry. *Journal of Physical Oceanography*, *46*(1), 3–22.
- Renault, L., McWilliams, J. C., & Gula, J. (2018). Dampening of submesoscale currents by air-sea stress coupling in the Californian upwelling system. *Scientific Reports*, *8*, 13388.
- Rhines, P. B. (1975). Waves and turbulence on a beta-plane. *Journal of Fluid Mechanics*, *69*(3), 417–443.
- Rhines, P. B. (1979). Geostrophic turbulence. *Annual Review of Fluid Mechanics*, *11*, 401–441.
- Richman, J. G., Arbic, B. K., Shriver, J. F., Metzger, E. J., & Wallcraft, A. J. (2012). Inferring dynamics from the wavenumber spectra of an eddying global ocean model with embedded tides. *Journal of Geophysical Research*, *117*, C12012. <https://doi.org/10.1029/2012JC008364>
- Rocha, C. B., Chereskin, T. K., Gille, S. T., & Menemenlis, D. (2016). Mesoscale to submesoscale wavenumber spectra in drake passage. *Journal of Physical Oceanography*, *46*(2), 601–620.
- Rocha, C. B., Gille, S. T., Chereskin, T. K., & Menemenlis, D. (2016). Seasonality of submesoscale dynamics in the Kuroshio Extension. *Geophysical Research Letters*, *43*, 11–304. <https://doi.org/10.1002/2016GL071349>
- Rocha, C. B., Wagner, G. L., & Young, W. R. (2018). Stimulated generation: Extraction of energy from balanced flow by near-inertial waves. *Journal of Fluid Mechanics*, *847*, 417–451.
- Rodríguez, E., Wineteer, A., Perkovic-Martin, D., Gál, T., Stiles, B. W., Niamsuwan, N., & Monje, R. R. (2018). Estimating ocean vector winds and currents using a Ka-band pencil-beam doppler scatterometer. *Remote Sensing*, *10*(4), 576.
- Roulet, G., McWilliams, J. C., Capet, X., & Molemaker, M. J. (2012). Properties of steady geostrophic turbulence with isopycnal outcropping. *Journal of Physical Oceanography*, *42*(1), 18–38.

- Salmon, R. (1980). Baroclinic instability and geostrophic turbulence. *Geophysical & Astrophysical Fluid Dynamics*, 15(1), 167–211.
- Sasaki, H., Klein, P., Qiu, B., & Sasai, Y. (2014). Impact of oceanic-scale interactions on the seasonal modulation of ocean dynamics by the atmosphere. *Nature Communications*, 5, 6636.
- Savage, A. C., Arbic, B. K., Alford, M. H., Ansong, J. K., Farrar, J. T., Menemenlis, D., et al. (2017a). Spectral decomposition of internal gravity wave sea surface height in global models. *Journal of Geophysical Research: Oceans*, 122, 7803–7821. <https://doi.org/10.1002/2017JC013009>
- Savage, A. C., Arbic, B. K., Richman, J. G., Shriver, J. F., Alford, M. H., Buijsman, M. C., et al. (2017b). Frequency content of sea surface height variability from internal gravity waves to mesoscale eddies. *Journal of Geophysical Research: Oceans*, 122, 2519–2538. <https://doi.org/10.1002/2016JC012331>
- Schneider, T., & Walker, C. C. (2006). Self-organization of atmospheric macroturbulence into critical states of weak nonlinear eddy-eddy interactions. *Journal of the Atmospheric Sciences*, 63, 1569–1586.
- Scott, R. (2006). Local and nonlocal advection of a passive scalar. *Physics of Fluids*, 18(11), 116601.
- Scott, R. B., & Wang, F. (2005). Direct evidence of an oceanic inverse kinetic energy cascade from satellite altimetry. *Journal of Physical Oceanography*, 35(9), 1650–1666.
- Smith, K. S. (2007). The geography of linear baroclinic instability in Earth's oceans. *Journal of Marine Research*, 65(5), 655–683.
- Smith, K. S., & Vallis, G. K. (2001). The scales and equilibration of midocean eddies: Freely evolving flow. *Journal of Physical Oceanography*, 31(2), 554–571.
- Stammer, D., Ray, R., Andersen, O. B., Arbic, B., Bosch, W., Carrère, L., et al. (2014). Accuracy assessment of global barotropic ocean tide models. *Reviews of Geophysics*, 52, 243–282. <https://doi.org/10.1002/2014RG000450>
- Stammer, D., Tokmakian, R., Semtner, A., & Wunsch, C. (1996). How well does a 1/4° global circulation model simulate large-scale oceanic observations? *Journal of Geophysical Research*, 101(C11), 25,779–25,811.
- Stone, P. H. (1966). Frontogenesis by horizontal wind deformation fields. *Journal of the Atmospheric Sciences*, 23(5), 455–465.
- Su, Z., Wang, J., Klein, P., Thompson, A. F., & Menemenlis, D. (2018). Ocean submesoscales as a key component of the global heat budget. *Nature Communications*, 9(1), 775.
- Taylor, S., & Straub, D. (2016). Forced near-inertial motion and dissipation of low-frequency kinetic energy in a wind-driven channel flow. *Journal of Physical Oceanography*, 46(1), 79–93.
- Tennekes, H., & Lumley, J. L. (1974). *A first course in turbulence*. Cambridge: MIT Press.
- Thomas, L. N. (2017). On the modifications of near-inertial waves at fronts: Implications for energy transfer across scales. *Ocean Dynamics*, 67(10), 1335–1350.
- Thompson, A. F., Lazar, A., Buckingham, C., Naveira Garabato, A. C., Damerell, G. M., & Heywood, K. J. (2016). Open-ocean submesoscale motions: A full seasonal cycle of mixed layer instabilities from gliders. *Journal of Physical Oceanography*, 46(4), 1285–1307.
- Torres, H., Klein, P., Menemenlis, D., Qiu, B., Su, Z., Wang, J., et al. (2018). Partitioning ocean motions into balanced motions and internal gravity waves from space. *Journal of Geophysical Research: Oceans*, 123, 8084–8105. <https://doi.org/10.1029/2018JC014438>
- Tulloch, R., Marshall, J., Hill, C., & Smith, K. S. (2011). Scales, growth rates, and spectral fluxes of baroclinic instability in the ocean. *Journal of Physical Oceanography*, 41(6), 1057–1076.
- Tulloch, R., & Smith, K. (2006). A theory for the atmospheric energy spectrum: Depth-limited temperature anomalies at the tropopause. *Proceedings of the National Academy of Sciences*, 103(40), 14,690–14,694.
- Ubelmann, C., Klein, P., & Fu, L.-L. (2015). Dynamic interpolation of sea surface height and potential applications for future high-resolution altimetry mapping. *Journal of Atmospheric and Oceanic Technology*, 32, 177–184.
- Vallis, G. K. (2017). *Atmospheric and oceanic fluid dynamics*. Cambridge, UK: Cambridge University Press.
- Wagner, G., & Young, W. (2016). A three-component model for the coupled evolution of near-inertial waves, quasi-geostrophic flow and the near-inertial second harmonic. *Journal of Fluid Mechanics*, 802, 806–837.
- Wang, J., Fu, L.-L., Torres, H., Chen, S., Qiu, B., & Menemenlis, D. (2019). On the spatial scale to be resolved by the surface water and ocean topography Ka-band radar interferometer. *Journal of Atmospheric and Oceanic Technology*, 36, 87–99.
- Whitt, D. B., & Thomas, L. N. (2015). Resonant generation and energetics of wind-forced near-inertial motions in a geostrophic flow. *Journal of Physical Oceanography*, 45(1), 181–208.
- Wortham, C., & Wunsch, C. (2014). A multidimensional spectral description of ocean variability. *Journal of Physical Oceanography*, 44(3), 944–966.
- Wunsch, C. (2002). Ocean observations and the climate forecast problem. *International Geophysics Series*, 83, 233–248.
- Wunsch, C. (2009). The oceanic variability spectrum and transport trends. *Atmosphere-Ocean*, 47(4), 281–291.
- Wunsch, C. (2010). Toward a midlatitude ocean frequency-wavenumber spectral density and trend determination. *Journal of Physical Oceanography*, 40(10), 2264–2281.
- Xie, J.-H., & Vanneste, J. (2015). A generalised-lagrangian-mean model of the interactions between near-inertial waves and mean flow. *Journal of Fluid Mechanics*, 774, 143–169.
- Xu, Y., & Fu, L.-L. (2012). The effects of altimeter instrument noise on the estimation of the wavenumber spectrum of sea surface height. *Journal of Physical Oceanography*, 42(12), 2229–2233.
- Young, W., & Jelloul, M. B. (1997). Propagation of near-inertial oscillations through a geostrophic flow. *Journal of Marine Research*, 55(4), 735–766.
- Zaron, E. D., & Egbert, G. D. (2014). Time-variable refraction of the internal tide at the hawaiian ridge. *Journal of Physical Oceanography*, 44(2), 538–557.
- Zhai, X., Greatbatch, R. J., & Kohlmann, J.-D. (2008). On the seasonal variability of eddy kinetic energy in the gulf stream region. *Geophysical Research Letters*, 35, L24609. <https://doi.org/10.1029/2008GL036412>

## B Diagnosing ocean-wave-turbulence interactions from space

Torres, H.S., Klein, P., **Siegelman, L.**, Qiu, B., Chen, S., Ubelman, C., Wang, J., Menemenlis, D. and Fu, L.L. (2019). Diagnosing ocean-wave-turbulence interactions from space. *Geophysical Research Letters*, 46(15), pp.8933-8942.



# Geophysical Research Letters

## RESEARCH LETTER

10.1029/2019GL083675

### Key Points:

- We exploit spectral characteristics of sea surface height (SSH) to partition ocean motions into balanced motions and internal gravity waves
- We use a simple shallow-water model to diagnose internal gravity wave motions from SSH
- We test a dynamical framework to recover the interactions between internal gravity waves and balanced motions from SSH

### Supporting Information:

- Supporting Information S1
- Figure S1
- Figure S2
- Figure S3
- Figure S4
- Figure S5
- Figure S6
- Figure S7
- Figure S8

### Correspondence to:

H. S. Torres,  
hector.torres.gutierrez@jpl.nasa.gov

### Citation:

Torres, H. S., Klein, P., Siegelman, L., Qiu, B., Chen, S., Ubelmann, C., et al. (2019). Diagnosing ocean-wave-turbulence interactions from space. *Geophysical Research Letters*, 46. <https://doi.org/10.1029/2019GL083675>








Received 14 MAY 2019

Accepted 25 JUL 2019

Accepted article online 30 JUL 2019

©2019. American Geophysical Union.  
All Rights Reserved.

## Diagnosing Ocean-Wave-Turbulence Interactions From Space

H. S. Torres<sup>1</sup> , P. Klein<sup>1,2</sup> , L. Siegelman<sup>1,3</sup> , B. Qiu<sup>4</sup> , S. Chen<sup>4</sup> , C. Ubelmann<sup>5</sup>, J. Wang<sup>1</sup> , D. Menemenlis<sup>1</sup> , and L.-L. Fu<sup>1</sup> 

<sup>1</sup>Jet Propulsion Laboratory, California Institute of Technology, Pasadena, CA, USA, <sup>2</sup>LOPS/IFREMER, Plouzane, France, <sup>3</sup>LEMAR, Plouzane, France, <sup>4</sup>Department of Oceanography, University of Hawaii at Manoa, Honolulu, HI, USA, <sup>5</sup>Collecte Localisation Satellites, Ramonville St-Agne, France

**Abstract** Numerical studies indicate that interactions between ocean internal gravity waves (especially those <100 km) and geostrophic (or balanced) motions associated with mesoscale eddy turbulence (involving eddies of 100–300 km) impact the ocean's kinetic energy budget and therefore its circulation. Results from these studies have never been confirmed by observations in regional or basin-scale domains. Here we show that internal gravity waves have a spectral signature on sea surface height during summer that significantly differs from that of balanced motions. These spectral differences lead us to propose a new dynamical framework that quantifies the interactions between internal gravity waves and balanced motions in physical space from sea surface height snapshots, and in particular the energy exchanges between them. Our results, using this dynamical framework, highlight the strong potential of future satellite altimeter missions to make critical advances in assessing the ocean's kinetic energy budget from observations in large domains.

### 1. Introduction

Two classes of motions dominate ocean kinetic energy (KE): balanced motions (BMs) and internal gravity waves (IGWs). BMs considered in this study involve motions associated with mesoscale eddy turbulence, such as mesoscale eddies (with a 100- to 300-km size) and also smaller-scale structures with horizontal scales down to 10 km (Ferrari & Wunsch, 2009). BMs are principally in geostrophic balance (balance between pressure forces and Coriolis forces), with their frequencies smaller than or close to the Coriolis frequency,  $f$ . They are mostly energetic in turbulent regions such as the Gulf Stream, the Kuroshio Extension, and the Antarctic Circumpolar Current. BMs account for almost 80% of the total ocean KE and explain most of the advective horizontal and vertical transport of heat and any tracers (Ferrari & Wunsch, 2009). IGWs, on the other hand, are waves with frequencies close to or larger than  $f$  and spatial scales from hundreds of kilometers to tens of meters. Unlike BMs, IGWs are weakly nonlinear and characterized by a fast propagation (Alford et al., 2016). They include coherent internal tides, wind-driven near-inertial waves, and an IGW continuum with higher frequencies and much smaller spatial scales than the coherent internal tides and near-inertial waves. In turbulent regions, KE at scales larger than 100 km is principally dominated by BMs (Ferrari & Wunsch, 2009). KE at smaller scales is usually dominated by BMs in winter and IGWs in summer (Callies et al., 2015; Qiu et al., 2018; Rocha, Gille, et al., 2016; Torres et al., 2018).

The motivation for partitioning motions into BMs and IGWs is that they impact the ocean KE budget differently (Klein et al., 2019). BMs mostly experience an inverse KE cascade, with KE fluxing from sources (starting from ~30- to 50-km wavelength) toward larger scales, which contributes to sustain mesoscale eddy turbulence (Arbic et al., 2012; Qiu et al., 2014; Sasaki et al., 2014). IGWs, on the other hand, and in particular the IGW continuum, experience a direct KE cascade with KE fluxing toward smaller scales, ultimately leading to irreversible mixing (Polzin & Lvov, 2011). As such, IGWs map out an important path in the route to KE dissipation that affects mesoscale eddy turbulence.

However, BMs and IGWs do not evolve independently but strongly interact, and their interaction further impacts the ocean KE budget. Numerous studies, starting with Kunze (1985) and Young and Jelloul (1997), have shown that IGWs at large scales are scattered and dispersed by mesoscale eddies, leading to waves with smaller spatial scales and higher frequencies, trapped within anticyclonic eddies and expelled from cyclonic ones (Danioux et al., 2008; Whitt & Thomas, 2015). More recent theoretical and numerical

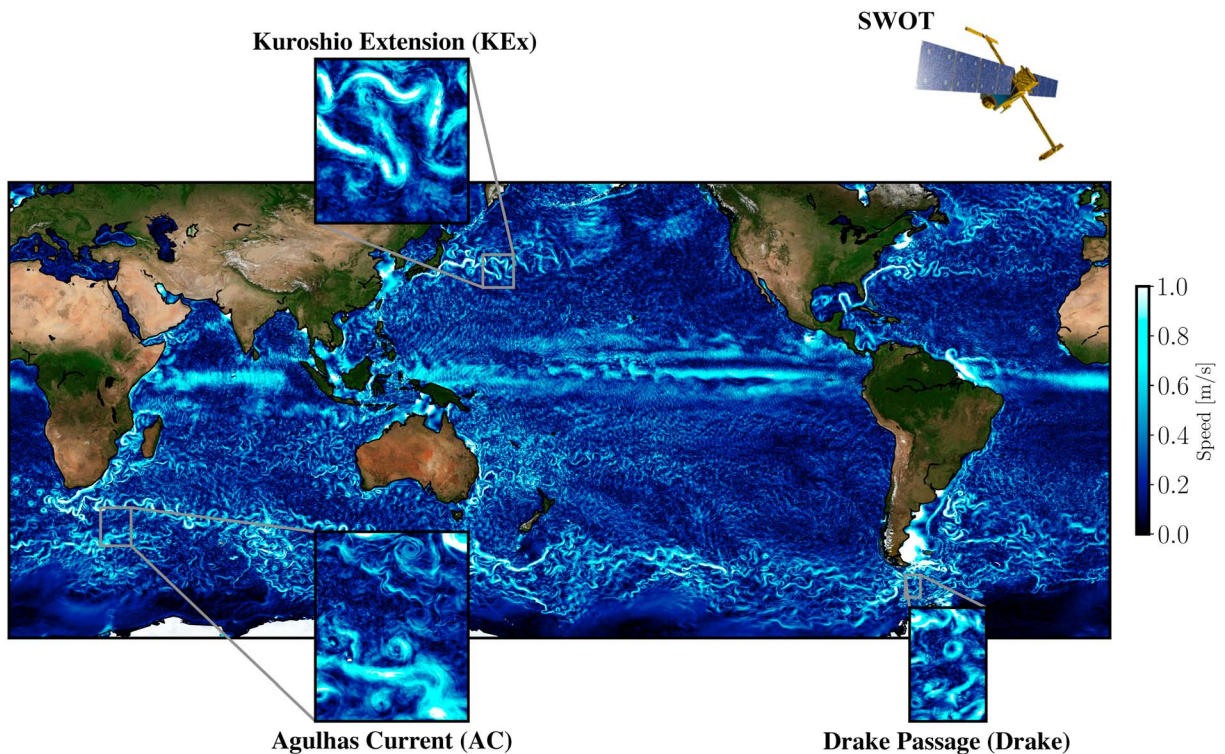


**Figure 1.** Map of surface speed in the world ocean from the OGCM (see Methods, section A). The zooms correspond to the three regions considered in this study, namely the Kuroshio-Extension [KEx, 30°N, 156°E], the Agulhas Current [AC, 40°S, 30°E] and the Drake Passage [Drake, 62°S, 67°W].

studies emphasize that these scattering mechanisms facilitate the energy exchanges between BMs and IGWs, exacerbating the cyclone-anticyclone asymmetry and eventually further dissipating mesoscale eddies (Barkan et al., 2017; Rocha et al., 2018; Taylor & Straub, 2016; Thomas, 2017). These theoretical and numerical results have never been confirmed by in situ and/or space observations in regional or basin-scale domains.

The present study addresses this observational challenge in the context of the upcoming Surface Water and Ocean Topography satellite mission, SWOT (Fu & Ferrari, 2008). Starting in 2021, SWOT will provide observations of the SSH, interpreted as a stream function or surface pressure, with unprecedented spatial resolution (up to ~10 km) on a global scale. In the meantime, to assess the potential of these observations, our study uses as a testbed the numerical outputs of an ocean global circulation model (OGCM), tidal resolving and with a very high-resolution (1/48° in the horizontal and 90 vertical levels) (see section A in supporting information for a detailed description of the model). Our results indicate that SSH observations at high resolution can be used to monitor the BM-IGW interactions and in particular the energy exchanges between BMs and IGWs, making a critical advance in assessing the potential for monitoring the KE budget of the world's oceans from space.

Our study exploits one SSH characteristic pointed out in Rocha, Chereskin, et al. (2016) and subsequent studies [see Torres et al., 2018, and references herein]: The SSH wave number spectrum displays, in summer, a significant slope discontinuity at a scale in the 50- to 100-km range. The shallower spectral slope at smaller scales within that range is explained by IGWs and the steeper slope at larger scales by BMs (Qiu et al., 2018; Torres et al., 2018). This SSH characteristic motivated us to develop a dynamical framework to diagnose BMs and IGWs directly from SSH snapshots and to recover the IGW-BM energy exchanges. We focus on three energetic regions during summer (Figure 1), namely, the Kuroshio Extension (August-September-October), the Agulhas Current (January-February-March), and the Drake Passage (January-February-March). The dynamical framework and the resulting diagnosis method are detailed in section 2 (see also section B in supporting information). The diagnosis method is then tested in section 3. Results illustrate the performance to recover from SSH snapshots, not only IGWs and BMs in physical space but also the KE exchanges between BMs and IGWs. Although our study is a first attempt, these results emphasize the

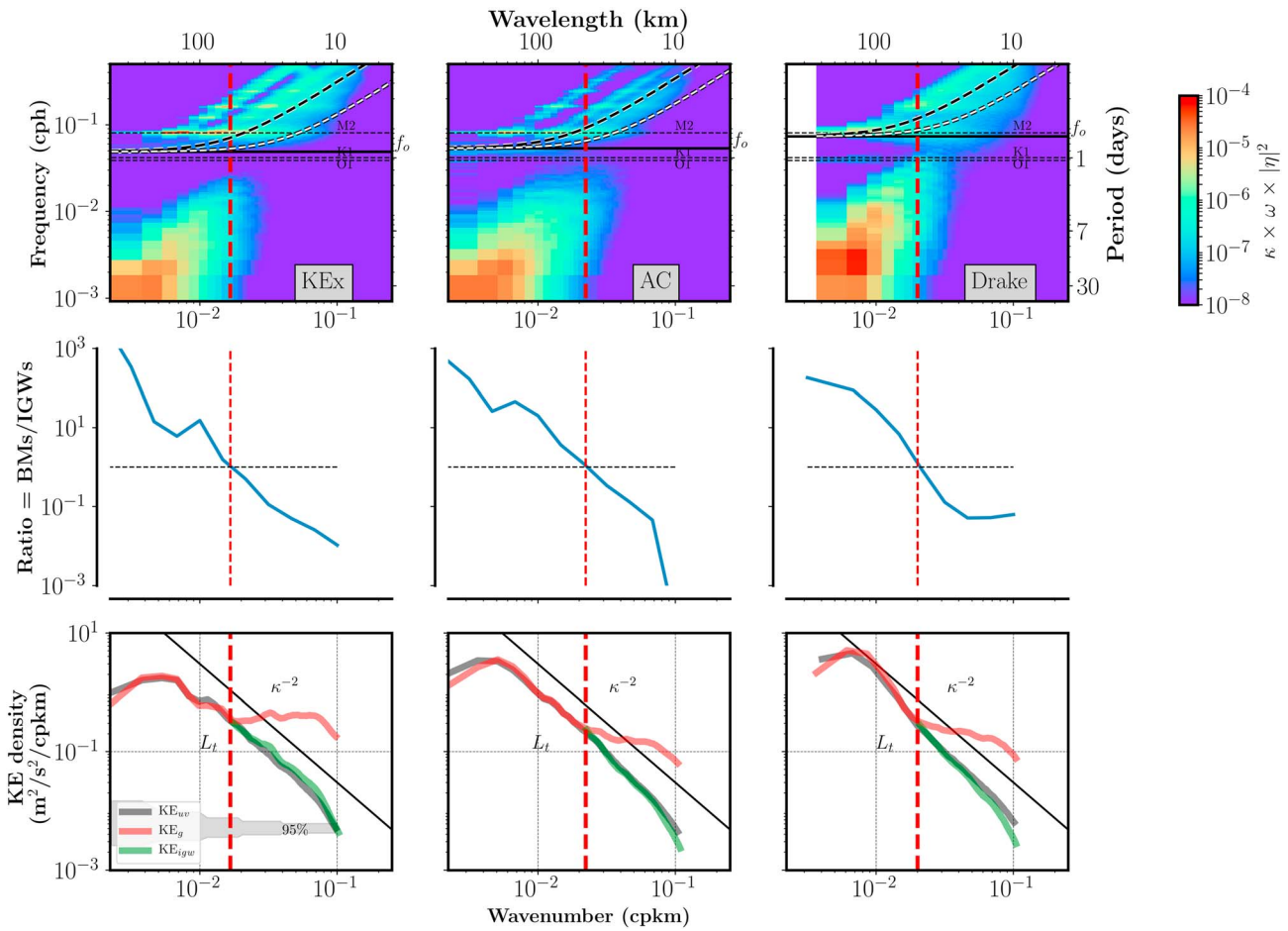


**Figure 2.** (top panels) The  $\omega - \kappa$  spectra of sea surface height (SSH) from the ocean global circulation model (see Methods) for the three targeted regions. The white (black) thick dashed curve stands for the dispersion relation of internal gravity waves for baroclinic mode-10 (mode-3). The red dashed lines mark the transition  $L_t = K_i^{-1}$  between BMs and IGWs dominance. (middle panels) Ratio  $[R(\kappa)]$  between BMs and IGWs variances as a function of wave number,  $\kappa$ . (bottom panels)  $KE_g$  (red lines): Geostrophic kinetic energy spectra diagnosed (using B3) from the SSH wave number spectra (estimated from the  $\omega - \kappa$  spectra integrated over all frequencies),  $KE_{uv}$  (gray lines): Kinetic energy spectra deduced from  $u$  and  $v$ , and  $KE_{igw}$  (green lines): internal gravity wave kinetic energy diagnosed from SSH (using B8). From left to right, each panel refers, respectively, to the Kuroshio-Extension [KEx, 30°N, 156°E], the Agulhas Current [AC, 40°S, 30°E] and the Drake Passage [Drake, 62°S, 67°W]. IGWs = internal gravity waves; BMs = balanced motions; KE = kinetic energy.

unexpected strong potential of future wide-swath satellite altimeters to monitor BM-IGW interactions from SSH in energetic oceanic regions. The last section discusses the caveats related to our framework.

## 2. A Dynamical Framework to Diagnose IGWs and BMs From SSH

### 2.1. Partitioning BMs and IGWs in Spectral Space

One approach to partition motions into BMs and IGWs, using numerical outputs from an OGCM (see section A in supporting information), is to move to the frequency ( $\omega$ )-wave number ( $\kappa$ ) domain. Indeed, as explained in Qiu et al. (2018) and Torres et al. (2018), the dispersion relation curve associated with the highest baroclinic mode taken into account in the model (the 10th baroclinic mode in the model we use, see dashed white line in Figure 2, top panels) separates IGWs located above this curve and the BMs located below (Figure 2, top panels). A more quantitative approach to infer the dominance of BMs over IGWs is to calculate for each wave number the ratio between the SSH variance below the dashed white line (i.e., BMs) and SSH variance above this line (i.e., IGWs) [Qiu et al., 2018 and Torres et al., 2018]. This ratio,  $R(\kappa) = BM_{\text{variance}}/IGW_{\text{variance}}$ , plotted on Figure 2 (middle panels), highlights the existence of a wave number,  $K_i$  (red dashed lines on Figure 2), that clearly separates the region with smaller wave numbers where BMs dominate (with  $R(\kappa) \gg 1$ ) from the one with larger wave numbers where IGWs dominate (with  $R(\kappa) \ll 1$ ). The wave number,

$K_i$ , corresponds to wavelengths close to 55, 50, and 40 km, respectively, for the Kuroshio Extension, the Agulhas Current, and the Drake Passage.

## 2.2. Spectral Relationships Between SSH Variance and KE for BMs and IGWs

Oceanic observations do not give access to a full  $\omega - \kappa$  spectrum. They give access only to either a frequency spectrum (as mooring observations) or a wave number spectrum (as SSH observations). The present study makes use of SSH observations and in particular exploits a conspicuous property of the SSH wave number spectrum in summer. It concerns a significant spectral slope discontinuity between a steep slope (in a  $\kappa^{-4} - \kappa^{-5}$ ) for small wave numbers and a shallower slope (in a  $\kappa^{-2}$ ) for larger wave numbers (Rocha, Chereskin, et al., 2016, Torres et al., 2018). Integration of the  $\omega - \kappa$  spectra of Figure 2 (top panels) over all frequencies reveals, in each region, an SSH wave number spectrum (not shown) with such a spectral slope discontinuity at exactly the same wave number,  $K_i$ , as the one revealed by the ratio,  $R(\kappa)$ . To further check whether this spectral slope discontinuity allows to partition motions into BMs and IGWs, we have diagnosed the KE from SSH using the classical relationship between SSH and BMs and using an appropriate relationship between SSH and IGWs motions (see section B in supporting information for details). The diagnosed KE spectra are then compared with the one deduced from surface motions.

If we apply the classical relationship between SSH and BMs (that makes use of the geostrophic balance) to the full SSH spectrum, we get the red curves ( $KE_g$ -spectra) displayed in Figure 2 (bottom panels). These curves exhibit in all regions a slope discontinuity at the same wave number as the one revealed by the ratio  $R(\kappa)$ , that is,  $\kappa = K_i$ . Compared with the KE spectrum estimated from surface motions (i.e.,  $KE_{uv}$ , gray curves in Figure 2, bottom panels), there is a quantitative agreement in the three regions for  $\kappa < K_i$ , which validates the geostrophic approximation. However, for  $\kappa > K_i$ , a breakdown of the geostrophic balance is observed since  $KE_g$ -spectra display a flat slope in this scale range, whereas  $KE_{uv}$ -spectra have still a  $\kappa^{-2}$  spectral slope.

We now choose an appropriate relationship between SSH and IGW motions for the wave number range  $\kappa > K_i$ . As detailed in the section B in supporting information, this relationship (equation B8 in supporting information) is based on a simple linear shallow-water model (LSWM). Choosing such a model assumes that the largest part of the IGWs is captured by only one baroclinic mode. Using matching conditions to guarantee the continuity of the SSH and KE spectra at  $\kappa = K_i$  (see section B in supporting information), we have found that this baroclinic mode is directly related to the wave number  $K_i$  and is very close to the third baroclinic mode for the three regions (black dashed curves on top panels in Figure 2). The  $KE_{igw}$ -spectra diagnosed from SSH using this relationship, shown by the green lines in Figure 2 (bottom panels), are very close to the  $KE_{uv}$  spectra in the three regions.

The good correspondence between the  $KE_g$  spectra (for  $\kappa < K_i$ ) and the  $KE_{igw}$  spectra (for  $\kappa > K_i$ ) with the  $KE_{uv}$  spectra in the three regions indicates that the slope discontinuity in the SSH wave number spectrum in summer clearly separates IGWs at small scales from BMs at larger scales. More importantly, our approach indicates that the wave number corresponding to this discontinuity further identifies the baroclinic mode that captures the largest part of the IGWs, leading to an adequate relationship between SSH and IGW motions in summer.

## 2.3. A Methodology to Diagnose Separately BMs and IGWs in Physical Space

The success of the approach described in the preceding section—using the geostrophic approximation for BMs and a single LSWM for IGWs to retrieve the full KE spectrum from a seasonal SSH spectrum—opens the possibility to diagnose the two-dimensional surface velocity field of both BMs and of IGWs in physical space from two-dimensional SSH snapshots.

To test this possibility, the following methodology is used. We consider a single snapshot of the SSH field,  $\eta(x,y)$ . We define a domain with double periodic conditions by multiplying  $\eta(x,y)$  by a two-dimensional Hanning window (see section C in supporting information) and, then, we apply a two-dimensional Fourier transform to the resulting  $\eta(x,y)$  field to get  $\hat{\eta}(k, l)$ , where the symbol  $\hat{\cdot}$  refers to the Fourier transform and  $k$  and  $l$  the wave number components. This field is partitioned as follows:  $\hat{\eta}(k, l) = \hat{\eta}_g(k, l) \Big|_{\kappa^2 = k^2 + l^2 < K_i^2} + \hat{\eta}_{igw}(k, l) \Big|_{\kappa^2 = k^2 + l^2 > K_i^2}$  (see section B in supporting information). Next, we diagnose BMs and IGWs in the spectral space using the appropriate relationships for BM and IGW motions (relations B2 and B7 in section B in supporting information). Finally, we recover BMs and IGWs in physical space using an inverse Fourier transform.

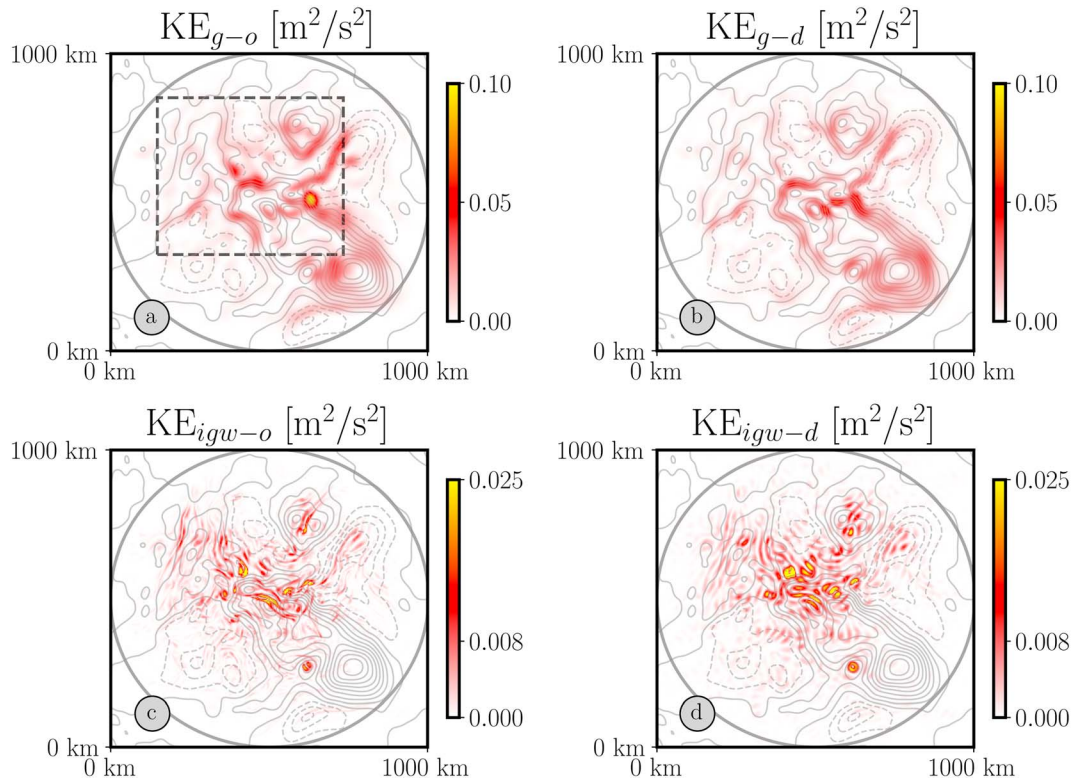


**Figure 3.** Two-dimensional kinetic energy field for the Kuroshio Extension. Top panels, (a) mesoscale kinetic energy,  $KE_{g-o}$  deduced from  $u$  and  $v$ , (c) internal gravity wave kinetic energy  $KE_{igw-o}$  deduced from  $u$  and  $v$ . Bottom panels, (b) geostrophic kinetic energy,  $KE_{g-d}$  diagnosed from sea surface height (SSH) and (d) internal gravity wave kinetic energy  $KE_{igw-d}$  diagnosed from SSH. The light gray lines stand for SSH contours. Note that for a pointwise comparison with the diagnosed fields,  $u(x,y)$  and  $v(x,y)$  have been multiplied by a two-dimensional Hanning window before estimating the observed KE, that is,  $KE_{g-o}$  and  $KE_{igw-o}$ . The gray circle delineates the region of influence of the Hanning window. Correlation between  $KE_{g-o}$  and  $KE_{g-d}$  is 0.9 and 0.7 between  $KE_{igw-o}$  and  $KE_{igw-d}$ . KE = kinetic energy; IGWs = internal gravity waves.

### 3. Results

#### 3.1. Diagnosing BMs and IGWs in Physical Space

We test the preceding methodology using our numerical simulation (section A in supporting information). We consider a two-dimensional SSH snapshot [i.e.,  $\eta(x,y)$ ], extracted from the numerical simulation outputs. Then, we diagnose separately BMs and IGWs in physical space using the methodology described before. Results, in terms of the KE explained by BMs ( $KE_{g-d}$ ) and IGWs ( $KE_{igw-d}$ ) with subscript d for diagnosed, are shown in Figures 3b and 3d for the Kuroshio Extension (see also Figures S2 and S3 in the supporting information, respectively, for the Agulhas Current and the Drake Passage). Note that the color bar for BMs is 4 times larger than that for IGWs. BMs have larger spatial scales than IGWs, as expected. We compare these diagnosed KE fields with those observed in the OGCM, that is,  $KE_{g-o}$  and  $KE_{igw-o}$  (with subscript o for observed), in Figures 3a and 3c, respectively (see also Figures S2 and S3).  $KE_{g-o}$  and  $KE_{igw-o}$  are estimated from  $u(x,y)$  and  $v(x,y)$  using high-pass and low-pass filters involving  $K_t^{-1}$ .

Comparison between Figures 3a and 3b indicates a strong similarity between  $KE_{g-o}$  and  $KE_{g-d}$ . For the Kuroshio Extension, the mean value for  $KE_{g-d}$  is close to  $0.056 \text{ m}^2/\text{s}^2$ , consistent with  $KE_{g-o}$  value,  $0.055 \text{ m}^2/\text{s}^2$ . Similar results are found for other regions. The  $KE_{g-o}$  and  $KE_{g-d}$  fields display smooth patterns intensified on the eddy edges (identified by SSH contours). Peaks in the  $KE_{g-d}$  field are at the same location as those in the  $KE_{g-o}$  field, with the same intensity. This similitude is confirmed by a pointwise comparison that leads to a correlation between  $KE_{g-d}$  and  $KE_{g-o}$  of 0.9, 0.87, and 0.85, respectively, for the Kuroshio Extension, the Agulhas Current, and the Drake Passage. Comparison of the velocity vectors observed in the simulation with the one diagnosed from SSH (first row in Figure 4, see also Figures S4 and S5) is quite good, as expected, except in the Drake Passage (Figure S5 where BMs might be in gradient wind balance (Vallis, 2017) instead of geostrophic balance.

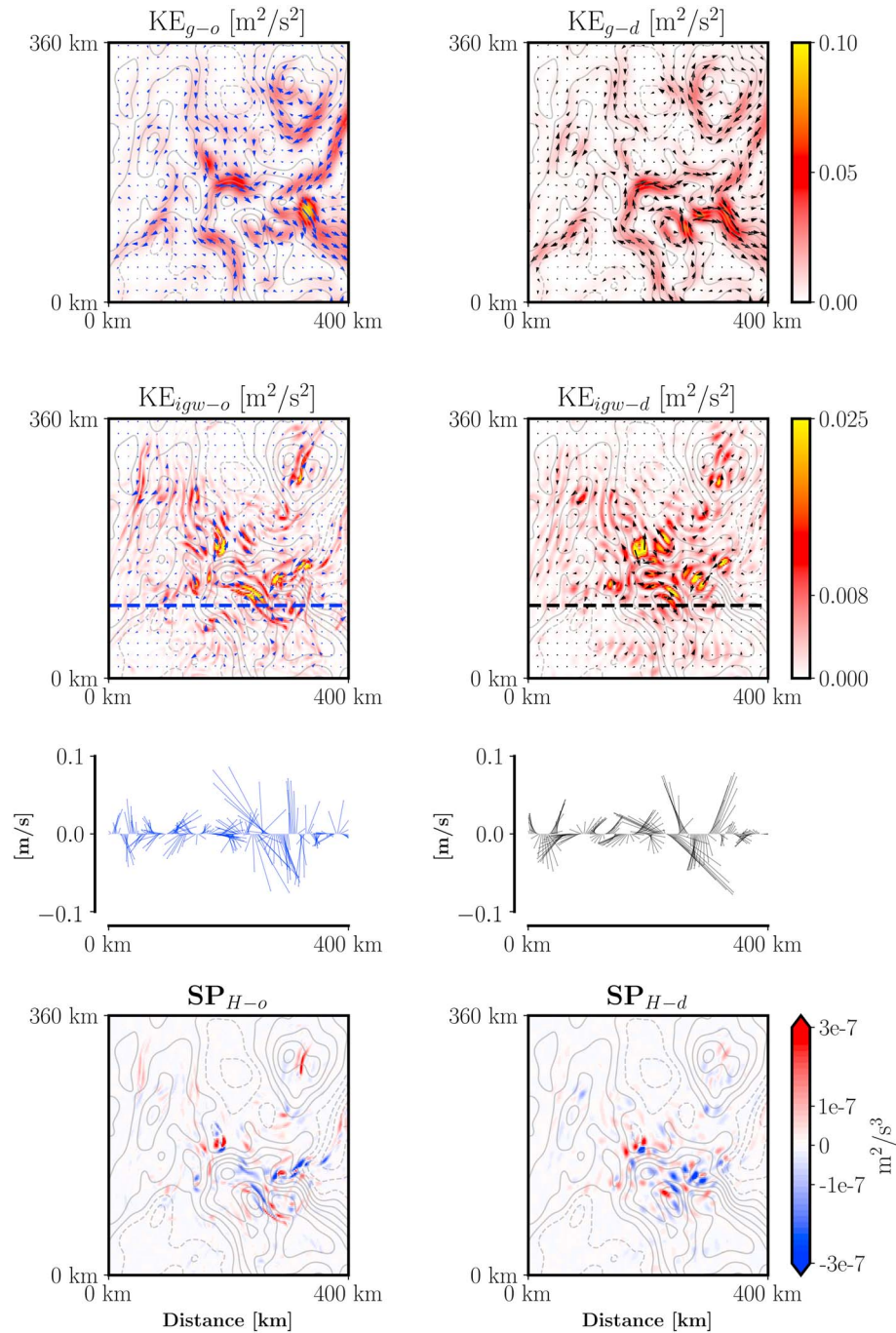


**Figure 4.** ZOOMS of the two-dimensional kinetic energy field and velocity vectors for the Kuroshio Extension. From top to bottom: first row; (left) mesoscale kinetic energy,  $KE_{g-o}$  deduced from  $u$  and  $v$ ; right) geostrophic kinetic energy  $KE_{g-d}$  diagnosed from sea surface height (SSH). Second row; (left) Internal gravity wave kinetic energy,  $KE_{igw-o}$ , deduced from  $u$  and  $v$ ; right) internal gravity wave kinetic energy,  $KE_{igw-d}$ , diagnosed from SSH. The light gray lines stand for SSH contours. Third row; stick diagram of velocity vector for IGWs corresponding to the dashed lines displayed in the middle panels. Fourth row; Kinetic energy exchange between BMs and IGWs by the shear production term,  $SP$  (see equation (1)), in the Kuroshio Extension: deduced from  $u$  and  $v$  ( $SP_{H-o}$ , left panel) and diagnosed from SSH ( $SP_{H-d}$ , right panel). Correlation coefficient between  $SP_{H-o}$  and  $SP_{H-d}$  is 0.45. The mean value of the shear production estimated from  $u$  and  $v$  is  $-1.17 \times 10^{-9} \text{ m}^2/\text{s}^3$  and the mean value of the shear production estimated from SSH is  $-2.5 \times 10^{-9} \text{ m}^2/\text{s}^3$ .

Next, we compare IGWs observed in the simulation with those diagnosed from SSH (see panels c [ $KE_{igw-o}$ ] and d [ $KE_{igw-d}$ ] in Figures 3, S2, and S3). A first comment is that  $KE_{igw-o}$  patterns differ much from  $KE_{g-o}$  patterns. Besides having smaller scales, their locations and geometries totally differ. IGW patterns are often located not only on the eddy edges but also inside the eddies (as in the Drake Passage, Figure S3). Sometimes,

they look like radial patterns on the eddy edges as in the Agulhas Current region (Figure S2), a reminder of some recent studies (see Figure 3 in Rocha et al., 2018). The Root-Mean-Square (RMS) value of the  $KE_{igw-d}$  field ( $0.025 \text{ m}^2/\text{s}^2$ ) is close to the one for  $KE_{igw-o}$  ( $0.024 \text{ m}^2/\text{s}^2$ ). Similar results are found in other regions (Figures S2 and S3).  $KE_{igw-d}$  is intensified at the same locations as  $KE_{igw-o}$ , although this intensification seems to be larger in the  $KE_{igw-d}$  field. The geometry of the  $KE_{igw-d}$  patterns is quite similar to  $KE_{igw-o}$  patterns. Scales of  $KE_{igw-d}$  are slightly larger than those observed in the simulation. The correlation value between  $KE_{igw-o}$  and  $KE_{igw-d}$  is 0.7 instead of 0.9 for the BM fields. Lower correlations are found for other regions (0.66 and 0.48, respectively, for the Agulhas Current and the Drake Passage). However, considering that  $KE_{igw-o}$  has a magnitude lower than  $KE_{g-o}$  and IGW scales are smaller than BM scales, even such a moderate correlation is encouraging. Finally, we compare the IGW velocity vectors observed in the simulation with those diagnosed from SSH (see second row in Figures 4, S4, and S5). Again, the resemblance between the two fields, in terms of magnitude and direction, is remarkable, although not as good as for BMs. For a better comparison, we have plotted two zonal sections of the IGW velocity vectors (third row in Figures 4, S4, and S5). The amplitudes and directions of these vectors compare well in the Kuroshio Extension and in the Agulhas Current, but not as well in the Drake Passage. IGW velocity vectors are often aligned with the  $KE_{igw-o}$  or  $KE_{igw-d}$  patterns, in particular, when these patterns are radial with respect to eddies. This alignment suggests an energy exchange between BMs and IGWs (Thomas, 2017).

### 3.2. Recovering BM-IGW Interactions From Space

BM-IGW interactions might lead to significant energy exchanges between these two classes of motions (Barkan et al., 2017; Rocha et al., 2018; Taylor & Straub, 2016; Thomas, 2017). The results of the previous section have encouraged us to test the possibility of inferring these exchanges from SSH observations. One quantity we have considered is the KE exchange between BMs and IGWs. From the KE equation (see, e.g., Barkan et al., 2017), the expression of this term (the shear production term, or  $SP_H$ ) is

$$SP_H = - \left[ u_{igw}^2 - v_{igw}^2 \right] \frac{\partial U_g}{\partial x} + u_{igw} v_{igw} \left[ \frac{\partial V_g}{\partial x} + \frac{\partial U_g}{\partial y} \right]. \quad (1)$$

A positive (negative)  $SP_H$  value means a KE transfer from BMs (IGWs) to IGWs (BMs). We have estimated  $SP_H$  using the velocity field from the numerical outputs (Figure 4, first and second rows, left panels) and the one diagnosed from SSH (Figure 4, first and second rows, right panels). For the Kuroshio Extension region, the resulting fields  $SP_{H-o}$  (observed) and  $SP_{H-d}$  (diagnosed) are shown on Figure 4 (fourth row, left and right panels, respectively). The  $SP_{H-o}$  field displays positive and negative patterns located in regions where  $KE_{igw-o}$  is large (Figure 3c). The magnitude of  $SP_{H-o}$  is consistent with the magnitude of  $KE_{igw-o}$  and  $KE_{g-o}$ . The diagnosed shear production term,  $SP_{H-d}$ , (Figure 4, fourth row, right panel) is remarkably similar to the observed one. The correlation between  $SP_{H-d}$  and  $SP_{H-o}$  is close to 0.5 in the Kuroshio Extension and the Agulhas Current but poor for the Drake Passage (Figures S7 and S8). Values of  $SP_{H-o}$  and  $SP_{H-d}$  averaged over the whole domain are close to  $10^{-9} \text{ m}^2/\text{s}^3$  for the three regions: For instance, in the Kuroshio Extension, the mean value of the shear production estimated from  $u$  and  $v$  is  $-1.17 \times 10^{-9} \text{ m}^2/\text{s}^3$ , and the mean value of the shear production estimated from SSH is  $-2.5 \times 10^{-9} \text{ m}^2/\text{s}^3$ . These magnitudes are close to those reported in recent studies although we have applied a double Hanning window on the variables (see section C in supporting information). These results emphasize that SSH observations can help to infer not only the IGWs' spatial organization by BMs but also the energy transfer between these two classes of motions.

One important question is whether  $KE_{igw}$  patterns and KE exchanges between IGWs and BMs evolve on a fast time scale (i.e., the propagation time scale of the waves, or  $\omega^{-1}$ ). If the answer is yes, we would need frequent SSH snapshots to monitor IGW-BM interactions. We have performed some sensitivity tests. Although IGW frequencies are larger than  $f$  (section B in supporting information),  $KE_{igw}$  patterns do not change within 1 or 2 days (cf. Figures 3 and S6). This is true also for the KE exchanges between IGWs and BMs (not shown). Actually, the time evolution of the interactions and KE exchanges appear to follow that of BMs. This means that frequent SSH snapshots are not needed. SSH snapshots with a few days' intervals should be enough to diagnose the spatial organization of IGWs by BMs. This result can be understood within the framework of Young and Jelloul (1997). These authors demonstrated that BMs impact the IGW dispersion on a time scale larger than the IGW oscillating time scale ( $\omega^{-1}$ ) and close to the BMs time scale. Thus,

although  $u_{igw}$  and  $v_{igw}$  and in particular their direction evolves with a fast time scale,  $KE_{igw}$  and the KE exchanges between BMs and IGWs evolve only on a slow time scale.

#### 4. Discussion and Perspectives

Recent theoretical and numerical results have emphasized the key role of BM-IGW interactions for the ocean KE budget and therefore for ocean general circulation. These results need to be confirmed by observations in regional or basin-scale domains and over long periods, which is a major challenge. The present study has exploited some spectral properties of BMs and IGWs to understand whether future wide-swath satellite altimeters with high spatial resolution might help to meet this challenge. Although this is a first attempt, results are encouraging and indicate that space observations can help to monitor BM-IGW interactions in the world's oceans. This monitoring will represent a new and major step for our understanding of ocean circulation. There are, however, several caveats to emphasize and some future extensions to mention.

- (i) The dynamical framework presented in this study is valid only when the SSH spectrum exhibits a clear slope discontinuity that separates IGWs at small scales from BMs at larger scales. Numerical studies indicate this should be the case in summer in many energetic regions, including the Gulf Stream, the Kuroshio Extension, and the Agulhas Current, where coherent internal tides have a weaker impact on SSH than do BMs (Qiu et al., 2018; Richman et al., 2012; Rocha, Gille, et al., 2016; Torres et al., 2018). But the slope discontinuity still needs to be confirmed by real SSH observations at high spatial resolution, which will be available after SWOT launches in 2021. However, IGWs' dominance in summer, in the small-scale range, has been reported by recent studies using Acoustic Doppler Current Profiler observations. Callies et al. (2015) showed that, in the Gulf Stream recirculation region, IGWs dominate the KE spectrum at scales smaller than 50 km. Qiu et al. (2017) reported similar results in the Kuroshio Extension region. In both studies, the KE spectrum slope in the small-scale range is either similar to, or shallower than, the slope in the larger-scale range. This means that, when using an SSH-KE spectral relationship similar to B8 (section B in supporting information), the resulting SSH spectral slope should be shallower (with a  $\kappa^{-2} - \kappa^{-3}$  slope) at smaller scales than at larger scales (usually a  $\kappa^{-4} - \kappa^{-5}$  slope), leading to a significant slope discontinuity.
- (ii) Our approach, using an LSWM, assumes that IGWs are explained by one dominant baroclinic mode, intimately related to the wave number at which the SSH spectrum exhibits a slope discontinuity. The third baroclinic mode found for the three regions is consistent not only with the findings of Rocha, Gille, et al. (2016) for the Kuroshio Extension but also with the more recent study from Lahaye et al. (2019) for the world ocean in summer. Both studies indicate that the dominance of the third baroclinic mode is explained by shallow mixed layers in summer. Using an LSWM implies a direct relationship between IGW frequencies and wave numbers, that is,  $\omega = \omega(\kappa)$ , or  $\kappa = \kappa(\omega)$ . This means all frequencies are supposed to be captured by one spatial snapshot of SSH. Farrar and Durland (2012) relied on a similar relationship [ $\omega = \omega(k)$ ] to retrieve SSH from mooring data, but considered several baroclinic modes. A future extension of this study should be considering several baroclinic modes by following the approach used in Farrar and Durland (2012).
- (iii) Our numerical tests emphasize that IGW-BM interactions involve slow time scale compared with the fast time scales associated with wave frequencies: Within 1 or 2 days, the  $KE_{igw}$  and SP patterns do not change significantly, meaning that no frequent SSH observations are needed. This slow time evolution can be explained by invoking the linear relationship between IGW frequencies and wave numbers mentioned before. Indeed, considering several wavelengths, as is done when going back to physical space, is equivalent to averaging over different wave periods.
- (iv) IGW-BM interactions involving wave numbers  $\kappa < K_i$  are not considered in our approach. IGWs at these scales (larger than 50–100 km), which include coherent internal tides and near-inertial waves, represent more than 50% of the total IGW KE in the three regions considered (see also Figure S1). Such IGWs might impact the IGW-BM interactions, in particular, in coastal areas in the presence of a steep topography (Flexas et al., 2015). However, previous studies (Barkan et al., 2017; Rocha et al., 2018; Taylor & Straub, 2016; Thomas, 2017) suggest that it is principally the IGW-BM interactions involving IGW scales smaller than 50–100 km that impact the KE exchanges between IGWs and BMs in energetic regions.



Despite these caveats, results of this study highlight the strong potential of future altimeter missions, such as SWOT, that aim to observe SSH with an unprecedented spatial resolution (~10 km) in two dimensions (wide swath of 120 km) over 68% of the world's ocean. The expected slope discontinuity in the SSH spectrum is such that the small-scale part of the spectrum should be above the noise level, which is likely to be true for high-KE regions of the world's ocean (Wang et al., 2019). SWOT observations will have a repeat period of 21 days. This means interpolation techniques, such as those proposed in Ubelmann et al. (2015), will be needed to produce daily SSH fields. Finally, exploiting the synergy of using SWOT observations with in situ surface drifters will enhance our ability to diagnose BM-IGW interactions in the near future and therefore their impact on the KE budget and ocean general circulation.

### Acknowledgments

This work was performed at the Jet Propulsion Laboratory, California Institute of Technology, under contract with the National Aeronautics and Space Administration (NASA). H. T. and D. M. were supported by NASA Physical Oceanography (PO) and Modeling, Analysis, and Prediction (MAP) Programs. P. K. was supported by a NASA Senior Fellowship and by a CNES (OSTST-OSIW grant). L. S. is a NASA-JVSRP affiliate and is supported by a joint CNES-Région Bretagne doctoral grant. B. Q. and S. C. were supported by NASA SWOT mission (NNX16AH66G). J. W. and L. L. Fu were supported by the SWOT mission. High-end computing resources were provided by the NASA Advanced Supercomputing (NAS) Division at the Ames Research Center. We are particularly grateful to C. Henze, B. Nelson, and D. Ellsworth for development of interactive visualization tools that helped us to explore the LLC4320 simulation. We thank the two reviewers for their positive and insightful comments. Instructions for obtaining LLC4320 model output are here: [http://ecco2.org/llc\\_hires](http://ecco2.org/llc_hires).

### References

- Alford, M. H., MacKinnon, J. A., Simmons, H. L., & Nash, J. D. (2016). Near-inertial internal gravity waves in the ocean. *Annual Review of Marine Science*, 8, 95–123. <https://doi.org/10.1146/annurev-marine-010814-015746>
- Arbic, B., Scott, R. B., Flierl, G. R., Morten, A. J., Richman, J. G., & Shriver, J. F. (2012). Nonlinear cascades of surface oceanic geostrophic kinetic energy in the frequency domain. *Journal of Physical Oceanography*, 42, 1577–1600. <https://doi.org/10.1175/JPO-D-11-0151.1>
- Barkan, R., Winters, K. B., & McWilliams, J. C. (2017). Stimulated imbalance and the enhancement of eddy kinetic energy dissipation by internal waves. *Journal of Physical Oceanography*, 47, 181–198. <https://doi.org/10.1175/jpo-d-16-0117.1>
- Callies, J., Ferrari, R., Klymak, J. M., & Gula, J. (2015). Seasonality in submesoscale turbulence. *Nature Communications*, 6(1), 6862. <https://doi.org/10.1038/ncomms7862>
- Danioux, E., Klein, P., & Riviere, P. (2008). Propagation of wind energy into the deep ocean through a fully turbulent mesoscale eddy field. *Journal of Physical Oceanography*, 38(10), 2224–2241. <https://doi.org/10.1175/2008JPO3821.1>
- Farrar, T. J., & Durland, T. S. (2012). Wavenumber–frequency spectra of inertia–gravity and mixed Rossby–gravity waves in the equatorial Pacific Ocean. *Journal of Physical Oceanography*, 42(11), 1859–1881. <https://doi.org/10.1175/JPO-D-11-0235.1>
- Ferrari, R., & Wunsch, C. (2009). Ocean circulation kinetic energy: Reservoirs, sources, and sinks. *Annual Review of Fluid Mechanics*, 41(1), 253–282. <https://doi.org/10.1146/annurev.fluid.40.111406.102139>
- Flexas, M., Schodlok, M. P., Padman, L., Menemenlis, D., & Orsi, A. H. (2015). Role of tides on the formation of the Antarctic slope front at the Weddell-Scotia confluence. *Journal of Geophysical Research: Oceans*, 120, 3658–3680. <https://doi.org/10.1002/2014JC010372>
- Fu, L.-L., & Ferrari, R. (2008). Observing oceanic submesoscale processes from space. *Eos, Transactions of the American Geophysical Union*, 89(48), 488. <https://doi.org/10.1029/2008EO480003>
- Klein, P., Lapeyre, G., Siegelman-Charbit, L., Smith, S., Torres, H., & Su, Z. (2019). Ocean scale interactions from space. *Earth and Space Science*, 6, 795–817. <https://doi.org/10.1029/2018EA000492>
- Kunze, E. (1985). Near-inertial wave propagation in geostrophic shear. *Journal of Physical Oceanography*, 15(5), 544–565. [https://doi.org/10.1175/1520-0485\(1985\)015<0544:NIWPIG>2.0.CO;2](https://doi.org/10.1175/1520-0485(1985)015<0544:NIWPIG>2.0.CO;2)
- Lahaye, N., Gula, J., & Roulet, G. (2019). Sea surface signature of internal tides. *Geophysical Research Letters*, 46(7), 3880–3890. <https://doi.org/10.1029/2018GL081848>
- Polzin, K. L., & Lvov, Y. (2011). Toward regional characterizations of the oceanic internal wavefield. *Reviews of Geophysics*, 49, RG4003. <https://doi.org/10.1029/2010RG000329>
- Qiu, B., Chen, S., Klein, P., Sasaki, H., & Sasai, Y. (2014). Seasonal mesoscale and submesoscale eddy variability along the North Pacific subtropical countercurrent. *Journal of Physical Oceanography*, 44, 3079–3098. <https://doi.org/10.1175/JPO-D-14-0071.1>
- Qiu, B., Chen, S., Klein, P., Wang, J., Torres, H., Fu, L.-L., & Menemenlis, D. (2018). Seasonality in transition scale from balanced to unbalanced motions in the world ocean. *Journal of Physical Oceanography*, 48, 591–605. <https://doi.org/10.1175/JPO-D-17-0169.1>
- Qiu, B., Nakano, T., Chen, S., & Klein, P. (2017). Submesoscale transition from geostrophic flows to internal waves in the northwestern Pacific upper ocean. *Nature Communications*, 8, 14055. <https://doi.org/10.1038/ncomms14055>
- Richman, J. G., Arbic, B. K., Shriver, J. F., Metzger, E. J., & Wallcraft, A. J. (2012). Inferring dynamics from the wavenumber spectra of an eddying global ocean model with embedded tides. *Journal of Geophysical Research*, 117, C12012. <https://doi.org/10.1029/2012JC008364>
- Rocha, C. B., Chereskin, T. K., Gille, S. T., & Menemenlis, D. (2016). Mesoscale to submesoscale wavenumber spectra in Drake Passage. *Journal of Physical Oceanography*, 46, 601–620. <https://doi.org/10.1175/JPO-D-15-0087.1>
- Rocha, C. B., Gille, S. T., Chereskin, T. K., & Menemenlis, D. (2016). Seasonality of submesoscale dynamics in the Kuroshio Extension. *Geophysical Research Letters*, 43, 11,304–11,311. <https://doi.org/10.1002/2016GL071349>
- Rocha, C. B., Wagner, G. L., & Young, W. R. (2018). Stimulated generation: Extraction of energy from balanced flow by near-inertial waves. *Journal of Fluid Mechanics*, 847, 417–451. <https://doi.org/10.1017/jfm.2018.308>
- Sasaki, H., Klein, P., Qiu, B., & Sasai, Y. (2014). Impact of oceanic-scale interactions on the seasonal modulation of ocean dynamics by the atmosphere. *Nature Communications*, 5, 5636. <https://doi.org/10.1038/ncomms6636>
- Taylor, S., & Straub, D. (2016). Forced near-inertial motion and dissipation of low-frequency kinetic energy in a wind-driven channel flow. *Journal of Physical Oceanography*, 46, 79–93. <https://doi.org/10.1175/JPO-D-15-0060.1>
- Thomas, L. N. (2017). On the modifications of near-inertial waves at fronts: Implications for energy transfer across scales. *Ocean Dynamics*, 67, 1335–1350. <https://doi.org/10.1007/s10236-017-1088-6>
- Torres, H. S., Klein, P., Menemenlis, D., Qiu, B., Su, Z., Wang, J., et al. (2018). Partitioning ocean motions into balanced motions and internal gravity waves: A modelling study in anticipation of future space missions. *Journal of Geophysical Research: Oceans*, 123, 8084–8105. <https://doi.org/10.1029/2018JC014438>
- Ubelmann, C., Klein, P., & Fu, L. L. (2015). Dynamic interpolation of sea surface height and potential applications for future high-resolution altimetry mapping. *Journal of Atmospheric and Oceanic Technology*, 32, 177–184. <https://doi.org/10.1175/JTECH-D-14-00152.1>
- Vallis, G. K. (2017). *Atmospheric and oceanic fluid dynamics*. Cambridge: Cambridge University Press. <https://doi.org/10.1017/9781107588417>

- Wang, J., Fu, L.-L., Torres, H. S., Chen, S., Qiu, B., & Menemenlis, D. (2019). On the spatial scales to be resolved by the surface water and ocean topography KA-band radar interferometer, Accepted in. *Journal of Atmospheric and Oceanic Technology*, *36*, 87–99. <https://doi.org/10.1175/JTECH-D-18-0119.1>
- Whitt, D. B., & Thomas, L. N. (2015). Resonant generation and energetics of wind-forced near-inertial motions in a geostrophic flow. *Journal of Physical Oceanography*, *45*, 181–208. <https://doi.org/10.1175/JPO-D-14-0168.1>
- Young, W., & Jelloul, M. B. (1997). Propagation of near-inertial oscillations through a geostrophic flow. *Journal of Marine Research*, *55*(4), 735–766. <https://doi.org/10.1357/0022240973224283>

**Titre :** Dynamique agéostrophique dans l'océan intérieur

**Mots clés :** Agéostrophie, océan intérieur, sous-mésoséchelle, éléphants de mer instrumentés, altimètre satellite, simulation numérique

**Résumé :** L'océan est le plus grand réservoir d'énergie solaire de notre planète. La quantité de chaleur qu'il est capable de stocker est modulée par sa circulation complexe, opérant sur une vaste gamme d'échelles allant du centimètre à la dizaine de milliers de kilomètres. Cette thèse s'intéresse à deux types de processus océaniques: les tourbillons de mésoéchelle, d'une taille de 100 à 300 km, et les fronts de sous-mésoséchelle, d'une taille inférieure à 50 km. L'idée communément admise est que les mouvements agéostrophiques de sous-mésoséchelle sont principalement confinés à la couche de mélange océanique de surface et sont faibles dans l'océan intérieur. Cette vision classique de la dynamique océanique repose sur l'hypothèse que l'océan intérieur est en équilibre quasi-géostrophique, empêchant la formation de forts gradients de densité en profondeur. Cette thèse remet en question ce paradigme en se basant sur des observations CTD *in situ* à haute résolution collectées par des éléphants de mer instrumentés, des images satellite d'élévation de la surface de l'océan, et des sorties de modèle à haute résolution dans le Courant Circumpolaire Antarctique.

Les résultats indiquent que les mouvements agéostrophiques sont (i) générés par le champ tourbillonnaire de mésoéchelle via des processus de frontogenèse, et (ii) ne sont pas limités à la couche de mélange de surface ; bien au contraire, ils pénètrent dans l'océan intérieur jusqu'à 1000 m de profondeur. Ces fronts agéostrophiques de sous-mésoséchelle sont associés à d'importants flux de chaleur dirigés de l'intérieur de l'océan vers la surface, d'une amplitude comparable aux flux air-mer. Cet effet peut potentiellement altérer la capacité de stockage de chaleur de l'océan et devrait être le plus fort dans les zones tourbillonnaires telles que le Courant Circumpolaire Antarctique, le Kuroshio et le Gulf Stream, les trois courants clefs du système climatique. Il apparaît ainsi que les fronts agéostrophiques de sous-mésoséchelle représentent une voie importante, mais encore largement méconnue, pour le transport de chaleur, de nutriments et de gaz entre l'intérieur et la surface de l'océan, avec des répercussions potentiellement majeures pour les systèmes biogéochimique et climatique.

**Title:** Ageostrophic dynamics in the ocean interior

**Keywords:** Ageostrophy, interior ocean, submesoscale, instrumented elephant seal, satellite altimetry, numerical simulation

**Abstract:** The ocean is the largest solar energy collector on Earth. The amount of heat it can store is modulated by its complex circulation, which spans a broad range of spatial scales, from centimeters to thousands of kilometers. This dissertation investigates two types of physical processes: mesoscale eddies (100-300 km size) and submesoscale fronts ( $\leq 50$  km size). To date, ageostrophic submesoscale motions are thought to be mainly trapped within the ocean surface mixed layer, and to be weak in the ocean interior. This is because, in the classical paradigm, motions below the mixed layer are broadly assumed to be in quasi-geostrophic balance, preventing the formation of strong buoyancy gradients at depth. This dissertation introduces a paradigm shift; based on a combination of high-resolution *in situ* CTD data collected by instrumented elephant seals, satellite observations of sea surface height, and high-resolution model outputs in the Antarctic Circumpolar Current, we show that

ageostrophic motions (i) are generated by the background mesoscale eddy field via frontogenesis processes, and (ii) are not solely confined to the ocean surface mixed layer but, rather, can extend in the ocean interior down to depths of 1 000 m. Deep-reaching ageostrophic fronts are shown to drive an anomalous upward heat transport from the ocean interior back to the surface that is larger than other contributions to vertical heat transport and of comparable magnitude to air-sea fluxes. This effect can potentially alter oceanic heat uptake and will be strongest in eddy-rich regions such as the Antarctic Circumpolar Current, the Kuroshio Extension, and the Gulf Stream, all of which are key players in the climate system. As such, ageostrophic fronts at submesoscale provide an important, yet unexplored, pathway for the transport of heat, chemical and biological tracers, between the ocean interior and the surface, with potential major implications for the biogeochemical and climate systems.